

**STRUCTURAL AND FUNCTIONAL CHARACTERIZATION
OF THE RNA EXOSOME FROM *S. CEREVISIAE***

by

Elizabeth V. Wasmuth

A Dissertation

Presented to the Faculty of the Louis V. Gerstner, Jr.

Graduate School of Biomedical Sciences,

Memorial Sloan Kettering Cancer Center

in Partial Fulfillment of the Requirements for the Degree of

Doctor of Philosophy

New York, NY

July, 2015

Christopher D. Lima, PhD
Dissertation Mentor

Date

Copyright by Elizabeth V. Wasmuth 2015 ©

DEDICATION

This work is dedicated to those young people who look past the fences and see the vast landscape beyond, who do not see the boundaries and their limitations but see opportunities for growth and adventure.

And in memory of M.R. Wasmuth for her example of perseverance, dignity, and selflessness.

ABSTRACT

The RNA exosome is an essential, multisubunit complex found in eukaryotes that houses 3' to 5' exoribonuclease and endoribonuclease activities. It is a major player in a diverse set of processes, including, but not limited to, normal RNA turnover, quality control, biogenesis and maturation pathways in the cytoplasm, nucleus, and nucleolus. Its 9 subunit non-catalytic core (Exo9) is composed of a two-stacked ring, featuring a prominent central channel. Two enzymes, Rrp44 and Rrp6, associate with Exo9, both possessing 3' to 5' exoribonuclease activity. The exosome was first discovered and its constituents described in 1997 – soon after, it became clear that different compositions of exosomes exist in various cellular compartments – for example, in the cytoplasm of *S. cerevisiae*, Rrp44 associates with Exo9, while Exo9, Rrp44 and Rrp6 form the nuclear exosome. It has been thought that various flavors of exosomes exist to allow targeting of distinct RNA substrates, but how a common Exo9 core could impart very different activities to its associated ribonucleases had not been well understood.

Chapter 1 of this dissertation begins by describing the findings of biochemical and genetic studies that probed the functions of the exosome, namely that Exo9 regulates both Rrp44 and Rrp6, that Rrp6 significantly activates Rrp44 in the 11 subunit nuclear exosome, and that all three enzymatic activities rely on the integrity of the Exo9 central channel.

Chapter 2 then focuses on addressing questions regarding Rrp6-associated exosomes. Specifically, 1) how does Rrp6 bind to the Exo9 core, 2) how does the Rrp6 exosome engage RNA (or any member of bacterial RNase D for that matter), and 3) how does the Rrp6 activation of Rrp44 in the nuclear exosome occur? Discussion will be centered on insights gained from the crystal structure of a Rrp6-Exo9 exosome engaged with polyA RNA, a decay substrate in the nucleus, and on subsequent structure-function analysis. Briefly, the highly conserved catalytic module of Rrp6 rests atop the Exo9 core

and central channel on one face of the S1/KH ring, with its non-catalytic C-terminus tethering Rrp6 to the core. The 3' end of the RNA is engaged in the Rrp6 active site, then threads into the S1/KH ring of the Exo9 core. With both Rrp44 and Rrp6 active sites positioned on opposite ends of the Exo9 central channel and using partially overlapping yet distinct paths for RNA decay, it is now appreciated that the basis for 3' to 5' directionality rests solely on Rrp6 and Rrp44 active sites, with Exo9 bearing no specificity for 3' ends.

The final two chapters will focus on the large contribution of small, disordered regions to greater exosome function – a polypeptide stretch dubbed the Rrp6 “lasso” in Chapter 3, and a basic protein cofactor, Mpp6, in Chapter 4. Using a combination of biochemical and genetic techniques, the Rrp6 lasso has been found to have an integral role in recruiting RNA towards the exosome, directing its path of ingress, and in facilitating decay by all three ribonuclease activities of the exosome. Mpp6, meanwhile, primarily modulates Rrp6 activity in an exosome-dependent fashion. Biochemical and preliminary structural results will be discussed to elucidate how Mpp6 stimulates exosome decay.

ACKNOWLEDGMENTS

Harold Varmus, a former president of Sloan Kettering, once mentioned the importance of a gate keeper in shaping the future of a young person. In his case, the gate keeper in his life was a former science mentor whose example inspired the young Varmus to change his career path, turning him on to experimental science, asking the “hows” and the “whys” rather than the “whats” of life. This story resonated with me because I did not grow up wanting to be a scientist – on the contrary, it was a paleontologist digging the bones of extinct animals, and then a veterinarian fixing the bones of living animals. I had no desire to question existing protocol. I was happy to read textbooks, accepting the dogma of whatever it was I read. This has radically changed.

Here I wish to acknowledge the gate keepers in my life, who have positively impacted me and inspired me to do the same for others. In all cases, their influence extends beyond just science, and for this, I am forever grateful.

I first wish to thank my parents, Scott and Victorina, and sisters Abigail and Christine, for their infinite support and advice in life decisions, and for grounding me with good values. To my grandparents William and Norma, for their progressiveness, and examples in juggling politics in academics while maintaining integrity.

To my high school English teacher, Don Delo, who angered and challenged me by his then accurate statement that I am a “black and white” thinker. I’d like to think he’d be pleased with my current color palette.

To my physician-scientist friend, Shahrukh Ali, whose love for science first eluded me from high school through college, but whose advice to do a summer undergraduate research fellowship in the lab of crystallographer, Dr. Mair Churchill at UC Denver changed my career path.

To Mair Churchill, and my mentor, Doug Donham, who gave a very green undergraduate a summer in their lab, despite constraints on their time, budget and

patience. During this formative time, I was shaken by the power of science, specifically structural biology, to explain mechanistic concepts I blandly swallowed in undergraduate biochemistry. Furthermore, I learned I could find these answers with my own hands; results – both positive and negative – were gratifying.

To Xingen Lei at Cornell University, who appointed me as a technician in his lab, giving me an unprecedented amount of responsibility and trust in managing a project, and fantastic mentorship and great appreciation.

To Forbes Porter and Christopher Wassif, whose genetics lab I worked at the NIH. From Chris I learned to think about the end goal of an experiment, and how to disassociate the negative results of science from life.

To Sasha Serganov, with whom I was privileged to work, who encouraged me to question the actual setup of failed experiments, not solely myself.

To my committee member, Dinshaw Patel, for his support and advocacy throughout the years, and his ability to challenge me by inquiring about the status of my project, and noting the possibility of doing the “impossible” when the Conti lab published the first yeast exosome structure.

To my committee member, Scott Keeney, for his mentorship from day one, and his dedication to strengthening my character and scientific abilities. Were it not for him, I would not be where I am now.

To Elena Conti, academically a competitor, but personally a mentor and source of inspiration. I am grateful for her advice, and her willingness to provide it, throughout the years.

To the members of the Lima lab, both past and present for their collegiality and friendships. The lab has been an ideal environment to work and grow mainly because of the wonderful people in it. I'd like to highlight my baymates, Agni Ghosh and Laurent Cappadocia for their constant advice, and for serving as role models in providing

mentorship in an infinitely patient manner. Shaun Olsen for his friendship, scientific and career support, and unconventionality. Nancy Arango, Chuck Streich, Xavier Mascle, Zac Hann and Selom Doamekpor for their help. And the exosome team: current members John Zinder and Kurt Januszyk, and previous members Jaclyn Greimann and Victor Liu.

Finally to Christopher Lima, for taking a gamble on a non-specialized, maverick graduate student, and entrusting her with his extremely challenging, competitive and personal project. My scientific and personal growth has been immense these years because of the environment he has provided me. It was a privilege and honor to work with him in the trenches during the exciting moments of discovery earlier on - these times are some of the fondest in my life. I also thank him for later giving me extreme independence. I am confident that I am leaving his lab a better scientist, thinker, and person, and look forward to tackling the challenges that lie ahead.

TABLE OF CONTENTS

LIST OF TABLES.....	xii
LIST OF FIGURES	xiii
INTRODUCTION	1
Discovery of the RNA exosome	3
Global architecture of the eukaryotic exosome core	4
RNase PH-like domains comprise a PH-like ring in eukaryotic exosomes	5
S1 and KH domains cap the PH-like ring.....	6
Rrp44, a hydrolytic endoribonuclease and processive exoribonuclease	8
Rrp44 and the 10-component exosome.....	12
Rrp6, a eukaryotic exosome subunit with distributive hydrolytic activities	13
Rrp44, Rrp6 and the 11-component nuclear exosome	15
MATERIALS AND METHODS	27
Yeast exosome subunit purification and complex reconstitution.....	27
Ribonuclease Assays.....	30
UV-RNA crosslinking.....	32
Fluorescence polarization	33
Yeast strains and complementation by plasmid shuffle	34
RNA analysis by qPCR	36
Crystallization and structure determination	37
CHAPTER 1	39
Exo- and endoribonucleolytic activities of yeast cytoplasmic and nuclear RNA exosomes are dependent on the non-catalytic core and central channel.....	39
1.1 Introduction	39

1.2 The exosome core modulates Rrp44 and Rrp6 activities in ten-subunit exosomes	40
1.3 Rrp6 and Rrp44 activities in the eleven-subunit exosome	43
1.4 RNA-protein interactions in exosomes containing Rrp6 and Rrp44	45
1.5 The exosome central channel is essential in vivo	46
1.6 Channel occluding mutations inhibit Rrp44 and Rrp6 activities in vitro	48
1.7 Functional consequences of channel occlusion in vivo	51
1.8 Conclusion	52
CHAPTER 2	86
Structure of an Rrp6-RNA Exosome Complex Bound to PolyA RNA	86
2.1 Introduction	86
2.2 Global architecture of Exo10 ^{Rrp6} -polyA RNA	87
2.3 RNA passes through the S1/KH ring to reach the Rrp6 active site	90
2.4 The central channel widens in Exo10 ^{Rrp6}	93
2.5 Conclusions	95
CHAPTER 3	119
RNA Recruitment by the RNA Exosome: Redefining the Rrp6 C-terminal Domain..	119
3.1 Introduction	119
3.2 The Rrp6 CTD is composed of two independent modules: an Exosome Associating Region (EAR), and a “lasso” region that recruits RNA	120
3.3 The Rrp6 Lasso Promotes RNA Binding and Decay Activities of Rrp6 and Rrp44 in 10- and 11-Component Exosomes	122
3.4 The Rrp6 Lasso Facilitates the Decay of Longer RNAs	125
3.5 The Rrp6 Lasso Feeds RNA into the Exo9 Central Channel	126

3.6 The Rrp6 Lasso Stimulates Rrp6 and Rrp44 Activities Independent of the EAR	127
3.7 In vivo Consequences of Lasso Deletion	128
3.8 RNA Ingress in Rrp6-Containing 10- and 11-Component Exosomes	129
3.9 Conclusions	131
CHAPTER 4	151
Insight to Exosome Stimulation by its Nuclear Cofactor, Mpp6	151
4.1 Introduction	151
4.2 Mpp6 is a disordered protein that binds nucleic acid	151
4.3 Mpp6 primarily stimulates Rrp6 in an Exo9-dependent manner	152
4.4 Mpp6 facilitates decay of both PolyA and PolyU RNAs	154
4.5 RNA ingresses through the S1/KH ring to Rrp6 in Exo10 ⁶ in the presence of Mpp6	155
4.6 Identification of a minimal region of Mpp6 sufficient for exosome binding and stimulation	158
4.7 Crystallization of Mpp6 Exosomes	160
4.8 A Diversion about a Divergent RNA Path to Rrp44	162
4.9 Mpp6 Associates with the S1/KH ring Subunit, Rrp40	165
4.10 Cooperativity between the Rrp6 Lasso and Mpp6	168
4.11 Conclusions	169
DISCUSSION	203
BIBLIOGRAPHY	204

LIST OF TABLES

Table 1. <i>E. coli</i> expression constructs used in Chapter 1.....	55
Table 2. Oligonucleotides used for qPCR.....	56
Table 3. Characterized Exosome Subunits and Complexes.....	57
Table 4. Initial rates for Rrp44 exoribonuclease activity	58
Table 5. Apparent K_d values	59
Table 6. Initial rates for Rrp44 endoribonuclease activity	60
Table 7. Initial rates for Rrp6 exoribonuclease activity	61
Table 8. Data collection and refinement statistics for Exo10 ⁶	97

LIST OF FIGURES

Figure 1. Schematics of eukaryotic exosomes.	16
Figure 2. Exosome complexes and their various known protein cofactors	17
Figure 3. Structure of the human nine-subunit exosome core.	18
Figure 4. The human PH-like subunit ring.	19
Figure 5. The human S1/KH protein ring.	20
Figure 6. The endo- and exoribonuclease Rrp44.	22
Figure 7. Structural comparison of RNA paths in murine Dis3L2, bacterial RNase II, and yeast Rrp44.....	24
Figure 8. The exoribonuclease Rrp6.....	26
Figure 9. ΔN_{128} Rrp6 can associate with exosomes and has similar activity to full-length Rrp6.	62
Figure 10. The Exo9 core alters exoribonuclease, endoribonuclease and RNA binding activities of Rrp44.	63
Figure 11. Experimental data used to derive apparent dissociation constants for various exosome subunits and complexes on AU-rich and PolyA RNAs.....	66
Figure 12. RNase activities associated with the exosome are modulated by the Exo9 core.	68
Figure 13. The Exo9 core alters Rrp6 exoribonuclease activity and RNA binding.	69
Figure 14. Exo10 ^{6exo-} and Exo10 ^{44exo-} form RNA crosslinks with the cap proteins and Rrp41 while Exo10 ^{44exo-} also crosslinks with the PH-like subunits in the Exo9 core.	71
Figure 15. UV-RNA cross-linking reveals exosome-RNA contacts.....	72
Figure 16. Channel-lining loop insertions fail to rescue the essential functions of the exosome <i>in vivo</i> , but do not interfere with exosome assembly <i>in vivo</i> or <i>in vitro</i>	74
Figure 17. The exosome central channel is essential <i>in vivo</i>	75

Figure 18. Channel occlusion inhibits RNA binding and RNase activities of Rrp44 and Rrp6.	77
Figure 19. All three RNase activities associated with the exosome are attenuated by channel occlusion by loop insertions.	80
Figure 20. Rrp6 is more dependent on the upper portion of the channel to access RNA.	81
Figure 21. Loop insertions placed towards the bottom of the channel (Exo10 ^{6exo-} Rrp41WT/Rrp45L) enhance UV-RNA crosslinks in Exo10 ^{6exo-} , while insertions placed towards the top of the channel (Exo10 ^{6exo-} Rrp41L/Rrp45WT) attenuate UV-RNA crosslinks relative to channel open complexes.	84
Figure 22. Channel occlusion results in aberrant RNA processing in vivo.	85
Figure 23. View highlighting electron densities covering RNA bound to Rrp6, Rrp4, Rrp40 and Csl4 within the Exo10 ^{Rrp6} -polyA structure.	98
Figure 24. Overall structure of a RNA bound Rrp6 exosome.	100
Figure 25. Rrp6 features within Exo10 ^{Rrp6}	101
Figure 26. Rrp6 contacts with the S1/KH ring and RNA.	103
Figure 27. The Rrp6 CTD is required for interaction with yeast Exo9.	106
Figure 28. RNA interactions within the Rrp6 active site.	108
Figure 29. Rrp6 activities depend on the integrity of the S1/KH ring.	109
Figure 30. Central channel mutations and their impact on Rrp6 degradation of AU-rich RNA.	111
Figure 31. Distinct but overlapping RNA paths to Rrp6 and Rrp44.	112
Figure 32. UV crosslinking with 36 nt RNAs for yeast exosome complexes using 4-thioU RNA substrates.	114
Figure 33. RNA paths to Rrp6 and Rrp44.	117
Figure 34. Widening of the S1/KH ring in Exo10 ^{Rrp6}	118

Figure 35. A 10 kilodalton region of the Rrp6 C-terminus in Exo10 ⁶ is vulnerable to limited proteolysis, in the absence or presence of RNA.	134
Figure 36. The Rrp6 CTD is composed of two modules – an Exosome Associating Region (EAR) and a disordered “lasso” that binds RNA.	135
Figure 38. The Rrp6 lasso enhances RNA binding and the rate of decay in Exo10 ⁶	138
Figure 39. The Rrp6 lasso stimulates all three ribonuclease activities of the nuclear exosome, Exo11 ^{44/6}	140
Figure 40. The Rrp6 lasso facilitates efficient decay of longer RNA.	141
Figure 41. Ribonuclease A protection of single-stranded RNA by Exo10 ^{6exo-}	142
Figure 42. Exo10 ⁶ binding to different length RNAs.....	143
Figure 43. The Rrp6 lasso recruits RNA through the Exo9 S1/KH ring in Exo10 ⁶	144
Figure 44. The Rrp6 lasso stimulates Rrp6 and Rrp44 activities independent of the EAR through a conserved mechanism.	145
Figure 45. The importance of the Rrp6 lasso <i>in vivo</i>	147
Figure 46. An identified route of RNA ingress in Exo10 ⁶ and Exo11 ^{44/6}	149
Figure 47. The Rrp6 lasso is poorly conserved by primary sequence in candidate eukaryotes but highly conserved in its physiochemical properties.	150
Figure 48. Mpp6 is a small, positively charged and disordered protein with poor sequence conservation.	172
Figure 49. Mpp6 is a disordered protein that binds RNA.	173
Figure 50. Exo9 is sufficient for Mpp6 association.....	174
Figure 51. Mpp6 stimulates Rrp6 activity in Exo10 ⁶ and Exo11 ^{44/6}	175
Figure 52. Mpp6 effect on Rrp44 decay in Exo11 ^{44/6}	176
Figure 53. Mpp6 and Rrp47 similarly stimulate Rrp6 in full-length Exo11 ^{44/6} and do not display additive effects <i>in vitro</i>	177
Figure 54. Mpp6 does not stimulate Rrp44 or Rrp6 outside of the exosome.....	178

Figure 55. Mpp6 greatly stimulates Rrp6 decay of single-stranded polyU RNA.	179
Figure 56. Effect of Exo9 channel mutations on Mpp6 stimulation.	180
Figure 57. Mpp6 exosomes use similar surfaces as Exo10 ⁶ for RNA binding.	181
Figure 58. Domain deletion analysis of Mpp6.	184
Figure 59. Global architecture of Mpp6 exosomes bound to RNA.	185
Figure 60. RNA path in Exo12 ^{44/6/Mpp6}	186
Figure 61. The “direct access” route to Rrp44 and implications for decay of small RNAs.	189
Figure 62. Density likely corresponding to Mpp6 is found primarily on acidic, conserved surfaces of Rrp40.	190
Figure 63. Mpp6 binding surface evaluation.	192
Figure 64. Mpp6 association induces the rotation of the Rrp6 catalytic module away from the Exo9 central channel.	194
Figure 65. The molecular basis for the Rrp6 catalytic module conformational change upon Mpp6 association.	197
Figure 66. Mpp6 can bypass inhibitory mutations in the Rrp4/Mtr3/Rrp42/Csl4 region of Exo9.	198
Figure 67. The Rrp6 CTD/Rrp43 NTD interaction takes an alternative route in crystal structures of Mpp6 exosomes.	200
Figure 68. The Rrp6 lasso and Mpp6 cooperatively stimulate Rrp6 and Rrp44 exoribonuclease activities.	201
Figure 69. Model of RNA decay by the Mpp6-associated nuclear exosome.	202

INTRODUCTION

3' to 5' RNA decay is an evolutionarily conserved process in all known kingdoms of life and the family of enzymes that catalyze RNA decay share mechanistic and structural relationships. In eukaryotes, nuclear and cytoplasmic 3' to 5' decay is catalyzed by an essential multi-subunit complex termed the RNA exosome^{1,2} (Figure 1). The RNA exosome includes a non-catalytic core formed by six subunits (Rrp41, Rrp45, Rrp42, Rrp43, Mtr3 and Rrp46) that share similarity to bacterial RNase PH and three subunits (Csl4, Rrp4 and Rrp40) that share similarity to proteins containing S1/KH RNA binding domains. The exosome core associates with two hydrolytic endo- and exoribonucleases (Rrp44 and Rrp6) that catalyze processive and distributive 3' to 5' exoribonuclease activities as well as endoribonuclease activities.

The RNA exosome is essential in budding yeast and its subunit composition is largely conserved from yeast to human³⁻⁵. In yeast, nuclear RNA exosomes include the nine-subunit exosome core, Rrp44 and Rrp6, while cytoplasmic exosomes appear to include only the exosome core and Rrp44^{6,3}. Interestingly, human encodes two Rrp44 homologs as well as Rrp6, and while each can associate with the RNA exosome core they exhibit distinct subcellular localizations⁷. This observation suggests that RNA exosome subunit composition may be dynamically regulated or that distinct exosomes exist for distinct functions. For instance, subcellular localization patterns suggest the existence of a nucleolar human exosome that includes the RNA exosome core and Rrp6.

Components of the eukaryotic RNA exosome share evolutionary relationships to bacterial and archaeal factors that catalyze 3'-5' RNA decay. In bacteria 3' to 5' RNA decay is catalyzed by RNase II and RNase R, two processive hydrolytic enzymes that

share similarity to Rrp44; RNase D, a distributive hydrolytic enzyme that is homologous to Rrp6; and PNPase, a processive phosphorolytic exoribonuclease that shares similarities to the non-catalytic eukaryotic RNA exosome core^{8,9}. PNPase is a multi-domain protein that homooligomerizes as a trimer to form a two-ring structure that features a prominent central channel. The top ring is formed by S1/KH domains while the bottom ring is formed by PH-domains that harbor the 3' to 5' processive phosphorolytic active sites. RNA must pass through the central channel to enter the phosphorolytic chamber¹⁰.

Archaeal exosomes are also processive phosphorolytic enzymes¹¹ but are composed of up to four individually encoded proteins that oligomerize to form a two-ring structure analogous to PNPase. In this case six PH-domain subunits form the bottom ring while three S1/KH domain proteins form the top ring^{12,13}. No RNase II or RNase D family members have yet been identified in archaea^{14,15}. Also, no Rrp40 homolog exists in archaea; rather Csl4 and Rrp4 homologs form the S1/KH cap. Analogous to PNPase, archaeal exosome rings possess a central channel that guides RNA substrates into the phosphorolytic chamber and active sites¹⁶.

The eukaryotic RNA exosome core is structurally related to bacterial PNPase and archaeal exosomes although it is composed of nine distinct subunits. Furthermore, unlike PNPase and archaeal exosomes, the nine-subunit eukaryotic exosome core is devoid of catalytic activities^{17,18}. Therefore it seems that the RNA exosome core has diverged mechanistically from its bacterial and archaeal cousins, dropping phosphorolytic capacity in its core in favor of interactions with the hydrolytic endo- and exoribonuclease Rrp44 and the hydrolytic exoribonuclease Rrp6 as well as protein cofactors such as Rrp47, Mpp6, and the TRAMP and SKI complexes² which presumably add additional layers of regulation to 3' to 5' decay pathways in eukaryotes (Figure 2).

This introduction will focus on the literature regarding RNA exosome structure and function primarily before the studies described in this dissertation were initiated.

Discovery of the RNA exosome

The RNA exosome was discovered in *S. cerevisiae* during the 1990s rather serendipitously by the group of David Tollervey and others. During this time, Tollervey and his group were interested in elucidating the steps of ribosomal RNA biogenesis; however, this proved to be complicated because depletion of the factors involved led to global loss of rRNA, thus making it challenging to assign a particular molecular function to each player. Thus, they focused on isolating enzymes whose depletion resulted in accumulation of pre-rRNAs at specific steps along the rRNA pathway, rather than those that resulted in a global loss of rRNA. Through these genetic screens, temperature sensitive lethal yeast strains of exosome core subunit mutants were obtained that exhibited defects in processing of 5.8S rRNA, with a ladder of 3' extended forms. Once the gene was cloned, it was designated RRP4 (Ribosomal RNA Processing defective 4). Endogenous Rrp4 was purified from yeast and assayed, and erroneously concluded to be a 3' to 5' exoribonuclease because it exhibited such activity *in vitro*. Through glycerol gradient ultracentrifugation, Rrp4 was found to be part of a larger 300-400 kilodalton (kDa) complex; other components of this complex were identified by mass spectrometry of the peak fractions, which led to the discovery of Rrp41, Rrp42, Rrp43, and Rrp44, all of which recapitulated the *rrp4* ts phenotype upon genetic depletion⁶. Because of its homology to bacterial RNase R, and activity of the recombinant protein *in vitro*, Rrp44 was ascribed as the processive 3' to 5' exoribonuclease in the exosome. Rrp6 remained undiscovered as a component of the exosome for two years, as its distributive activity

was erroneously attributed to the core subunits. Roy Parker's lab discovered Rrp41 and Mtr3 around the same time, and noted their roles in cytoplasmic mRNA decay, and homology to bacterial RNase PH⁹³, which later facilitated the discovery of Rrp45 and Rrp46 (Ref. 3). Improvements in the protocol for purification of endogenous exosomes also facilitated the discovery of the final constituents of the exosome – Rrp40, Csl4 and Rrp6 (Ref. 3).

Since its initial discovery as a player in ribosomal RNA biogenesis, the exosome has been found to also play essential roles in other types of RNA decay, quality control, and maturation. Messenger RNAs can be deadenylated, decapped and degraded either 5'→3' via the exoribonuclease Xrn1 (Ref. 92), or 3'→5' by the cytoplasmic exosome^{2,93}. In addition to normal mRNA turnover, the exosome functions in rapid decay of CUTs, or cryptic unstable transcripts^{57,94}, transcripts endonucleolytically cleaved by the RNA Induced Silencing Complex⁹⁵, RNAi-induced heterochromatin spreading at centromeres⁹⁶, microRNA processing⁹⁷ and in targeting activation-induced cytidine deaminase for optimal class switch recombination^{98,99}. Quality control functions for the RNA exosome include degradation of misfolded RNAs, including tRNAs, rRNAs, snRNAs, snoRNAs, and pre-mRNAs^{3,55}, and degradation of aberrant mRNAs that feed into nonsense-mediated decay, nonstop decay, and no-go decay^{100,101}.

Global architecture of the eukaryotic exosome core

The structure of the human nine-subunit exosome core (Exo9) revealed a pseudo-hexameric six-component ring composed of the RNase PH-like proteins Rrp41, Rrp45, Rrp42, Rrp43, Mtr3 and Rrp46 that is capped by a three-component ring formed by the S1/KH-domain proteins Csl4, Rrp4 and Rrp40¹⁷ (Figure 3). This structure

revealed overall architectural similarities to bacterial PNPase²⁰⁻²² and archaeal exosomes^{12,16} including a prominent central channel. In the human exosome structure, Rrp4 bridges Rrp41 and Rrp42, Rrp40 bridges Rrp45 and Rrp46, and Csl4 contacts Mtr3 and to lesser extent Rrp43. While archaeal exosomes form stable and catalytically active six-subunit RNase PH subunit rings, eukaryotic exosomes require at least one cap protein to form stable complexes in vitro. The general architecture and subunit composition of the human Exo9 core is likely conserved across eukaryotic phylogeny based on sequence analysis and conservation of individual subunits in organisms ranging from budding yeast to man¹⁷. Furthermore, some human exosome core subunits can complement deletion of the corresponding yeast genes^{23,24}.

RNase PH-like domains comprise a PH-like ring in eukaryotic exosomes

RNase PH domains are comprised of a $\beta\alpha\beta\alpha$ fold and are conserved in RNase PH, and PNPase in prokaryotes, archaeal exosomes, and eukaryotic exosomes (Figure 3). Exosome subunits with structural homology to RNase PH are thus referred to as “PH-like” proteins and include Rrp41, Rrp42, Rrp43, Rrp45, Rrp46, and Mtr3. The 6 component PH-like ring in eukaryotes consists of three distinct heterodimer pairs that are arranged in a head to tail configuration. Although eukaryotic organisms have diverged to encode these subunits in six distinct genes, Rrp41, Mtr3 and Rrp46 share higher sequence and structural similarity to archaeal Rrp41 or PNPase RNase PH 2-like proteins while Rrp42, Rrp43 and Rrp45 share greater similarity to archaeal Rrp42 or PNPase RNase PH 1-like proteins. In eukaryotes, Rrp41 pairs with Rrp45; Rrp43 pairs with Rrp46; Mtr3 pairs with Rrp42 (Figure 4).

The majority of amino acid side chains that form the phosphorolytic active site and RNA binding surfaces in bacterial PNPase and the archaeal exosome are not conserved in eukaryotic exosomes; however, amino acid side chains that comprise one potential RNA binding surface are conserved in the Rrp41-Rrp45 heterodimer interface (Figure 3). The location of this putative RNA binding site was evident in sequence alignments and by location of a tungstate ion in crystals of the human exosome core¹⁷. Furthermore, point mutations that disrupt this anion binding site (Rrp41 R95E/R96E and Rrp45 K62E/S63D) attenuate RNA decay activity of cytoplasmic exosomes (Exo9 core plus Rrp44) in vitro [25]. However, the functional consequences of mutating these residues, and their effects on Rrp6-exosome activities (Exo10⁶ and Exo11^{44/6}) were unknown, and will be discussed in this dissertation.

S1 and KH domains cap the PH-like ring

Rrp4, Rrp40, and Csl4 form a ring and cap the PH-like ring of the eukaryotic exosome core. Each of these subunits contain an N-terminal domain (NTD) that makes extensive contacts to their respective RNase PH-like 2 binding partner, tethering the cap proteins onto the PH-like ring¹⁷ (Figure 4). The Rrp4 NTD interacts with Rrp41; the Rrp40 NTD binds to Rrp46; the Csl4 NTD contacts Mtr3. Rrp4 and Rrp40 include two putative RNA binding domains, KH type I and S1 while Csl4 contains an S1 domain and C-terminal zinc ribbon fold. KH type I domains²⁶ feature a $\beta 1$ - $\alpha 1$ - $\alpha 2$ - $\beta 2$ - $\beta 3$ - $\alpha 3$ secondary structure topology and tertiary structure that consists of three beta-strands that form a sheet and pack against three alpha helices. Single stranded RNA typically binds KH type I domains via surfaces formed by residues within helix $\alpha 1$, a conserved GXXG motif between helices $\alpha 1$ and $\alpha 2$, helix $\alpha 2$, the variable loop between strands $\beta 2$ and $\beta 3$, and

residues within strand $\beta 2$ (Ref. 27). However, this motif is not conserved in eukaryotic Rrp4 and Rrp40; instead, a unique and conserved GXNG motif is found between strands $\beta 7$ and $\beta 8$. The GXNG motif is buried at the interface between the S1 and KH domains, and unless RNA binding induces a dramatic conformational change to expose the GXNG motif, this surface likely contributes to the structural stability of the protein rather than to RNA binding.

S1 domains²⁸ contain an OB (Oligonucleotide/oligosaccharide Binding) fold with a five-stranded β -sheet coiled to form a closed β -barrel²⁹. OB domains generally bind nucleic acid through surfaces composed of positively charged and hydrophobic residues on the solvent exposed β -sheet³⁰. Rrp40 exhibits the typical β -barrel, with long loops between $\beta 3$ and $\beta 4$ that project into the central channel^{17,31}. A comparably long loop between $\beta 3$ and $\beta 4$ is also present in Rrp4; however, both of these regions are disordered in the structure of the human exosome. These loops project toward the central channel and contain several basic residues that are highly conserved throughout eukaryotes and thus may be responsible for binding or guiding RNA into the central channel.

The zinc ribbon domain of Csl4 contains a 3-stranded β -sheet and is structurally related to archaeal Csl4; however, the four cysteine residues that coordinate Zn^{2+} in archaea are not conserved in eukaryotes nor is Zn^{2+} coordinated in human Csl4. While this domain is not essential *in vivo*, its deletion results in conditional defects in nonsense-mediated decay in budding yeast³². Furthermore, while Csl4 is essential *in vivo*, budding yeast strains expressing Csl4 truncations that lack either the NTD or S1 domain are still viable. These data are perhaps consistent with the observation that Csl4 is not stably associated with exosomes reconstituted *in vitro*³³. In contrast, each of the Rrp4 and Rrp40 NTD, S1, and KH domains are essential in budding yeast³².

The arrangement of the cap subunits on the PH-like six-subunit ring in the human exosome positions conserved and positively charged putative RNA binding S1 domain surfaces towards the central channel while the NTDs and KH domains are located on the periphery of the complex (Figure 5). While RNA binding cannot be detected for Rrp40 alone³¹, reconstituted exosomes lacking one cap subunit exhibit weaker RNase protection patterns compared to a complete Exo9 core³³. Alignment of multiple crystal structures of the archaeal exosome from *S. solfataricus* indicates that the cap proteins, specifically Rrp4, sometimes deviate from the three-fold symmetry observed in other crystal structures, suggesting limited conformational flexibility^{13, 34}. Furthermore, Csl4 and Rrp40, and not the PH-like subunits, display increased flexibility when the crystal structure of the human exosome core is compared to a 14 Å cryo-electron microscopy reconstruction of reconstituted Exo10 from budding yeast^{17, 33}. The significance of this structural flexibility in the context of RNA coordination and association of additional protein factors with Exo9 will be further discussed in subsequent chapters.

Rrp44, a hydrolytic endoribonuclease and processive exoribonuclease

Rrp44 includes five domains, an N-terminal PIlus-forming N-terminus (PIN) domain that contains an active site capable of endoribonuclease activity³⁵ and is responsible for tethering Rrp44 to the Exo core (see below); two cold-shock domains (CSD1 and CSD2); a central ribonuclease domain (RNB) that catalyzes processive 3' to 5' exoribonuclease activity; and a C-terminal S1 domain (Figure 6). Rrp44 is structurally and mechanistically related to bacterial RNase II and RNase R³⁷.

Humans and other metazoan eukaryotes encode three homologs of budding yeast Rrp44, including Dis3 and Dis3L, which are localized to the nucleus and

cytoplasm, respectively^{7,36}. The third paralog, Dis3L2, lacks a PIN domain and thus does not associate with the exosome, but rather has been implicated in decay of oligouridylated species, including mRNAs and microRNAs^{38,39}. Its mutation is associated with Perlman syndrome⁴⁰. A recent crystal structure reveals that Dis3L2 degrades RNA through the path utilized by bacterial RNase II, which is described in detail below⁴¹. Human Dis3 is most similar to yeast Rrp44, and budding yeast strains depleted of Rrp44 can be partially rescued by human Dis3, but not Dis3L⁷. Dis3 and Dis3L associate with exosomes in vivo as evidenced by their ability to pull down other exosome core subunits as well as Mtr4 in lysate from human cells^{7,36}.

A crystal structure of budding yeast Rrp44 lacking the PIN domain but bound to RNA⁴² revealed many overall similarities to RNase II in its apo- and RNA-bound states⁴³ (Figure 6) including conservation of CSD1, CSD2, RNB and S1 domains. Comparison of the structures reveals that Rrp44 and RNase II RNB active sites make similar contacts to the four ribonucleotides upstream of the 3' OH. Based on structural similarities within their active sites, it is likely that Rrp44 employs the same two metal ion catalytic mechanism as RNase II to hydrolyze RNA 3' to 5', resulting in the release of 5' nucleotide monophosphates¹⁹. One of two catalytic magnesium ions is visible in the Rrp44 structure and is coordinated by Asp543 and Asp552. Although the second magnesium is not detected in the Rrp44-RNA structure, it is likely to be coordinated by Asp551 and Asp549. In fact, mutation of Asp551 to Asn retains RNA binding, but leads to loss of exoribonuclease activity in vitro, and a slow growth phenotype in vivo¹⁸.

Several basic residues within the RNB domain line the active site and contact RNA via contacts to the RNA backbone. An exception is Tyr595, which participates in base stacking interactions with the 3' most nucleotide, while bases 1-5 stack with each other⁴². The prominence of protein contacts to the RNA backbone and absence of base

specific interactions are consistent with the enzyme's lack of sequence specificity; however, several direct or water-mediated hydrogen bonds between protein residues and the 2' hydroxyl groups of nucleotides 2, 3, 4, 6, and 8 impart specificity in recognition of ssRNA rather than ssDNA as Rrp44 binds ssRNA 50-fold better than ssDNA⁴². Rrp44 can degrade duplex RNAs with 3' single stranded overhangs as short as 4 nucleotides, but is most efficient when overhangs of at least 10 nucleotides⁴², similar to bacterial RNase R⁴⁴. The requirement of a 3' single stranded overhang is consistent with the structures insofar as the channel to the RNB active site is only large enough to accommodate single-stranded RNA.

Many similarities are shared between Rrp44 and RNase II; nevertheless, differences are readily apparent with respect to how they engage RNA via the CSDs and S1 domain. In RNase II, RNA threads through a channel formed by the CSDs and S1 domain into the RNB active site. In addition to contacts to the 3' end via the RNB domain, CSD2 and the S1 domain make additional contacts to single stranded RNA that contribute to the enzyme's processive activity⁴³. In contrast, the Rrp44-RNA complex shows the 5' end of RNA in a path perpendicular to that observed in RNase II in a channel formed at the interface between the RNB domain and CSD1 which is 15 Å closer to the RNB domain compared to RNase II, and more recently, Dis3L2 (Ref. 41). Analysis of the electrostatic surfaces of RNase II, Dis3L2, and yeast Rrp44 reveal that the route of ingress to RNase II and Dis3L2 is highly basic, while the same surface is acidic in yeast Rrp44. Conversely, the path ingressing RNA takes to the Rrp44 active site is basic, while the same regions in RNase II and Dis3L2 are more acidic and less solvent accessible (Figure 7). The distinct mode of RNA binding by RNase II and Dis3L2 explains their processive activities while the rationale for the unique path observed for Rrp44 is less clear. This alternative route may allow for additional modes of RNA ingress

to facilitate decay of structurally diverse sets of RNAs, accommodating substrates exiting the central channel of the eukaryotic exosome core, or directly accessing the Rrp44 active site from the solvent. It is interesting to note that the S1/KH ring and CSDs/S1 ring share overall architectural similarities, particularly with respect to their positions over an extended channel in the Rrp44 RNB domain and the exosome PH-like ring, invoking a role for the S1/KH domain ring of the eukaryotic Exo9 core analogous to the CSDs and S1 domains in RNase II and Dis3L2 with respect to ssRNA binding.

The structure of the yeast Rrp44 PIN domain was revealed in a crystal structure of full-length Rrp44 bound to Rrp41 and Rrp45 (ref. 25) (Figure 6). The PIN domain consists of a central twisted five-stranded β sheet flanked by α helices and is similar to the overall fold observed in other RNase H family members^{45,46}. PIN domains that catalyze nuclease activity include four conserved acidic residues that coordinate two divalent cations to cleave nucleic acid via a similar mechanism involving two-metal-ion catalysis⁴⁷⁻⁵⁰. The endoribonucleolytic active site of the Rrp44 PIN domain from budding yeast consists of Asp91, Glu120, Asp171, Asp198 (Figure 6).

Rrp44 endoribonuclease activity is dependent on the integrity of the PIN active site and can be observed *in vitro* in the presence of millimolar concentrations of manganese; however, an active site point mutation (D171N) that abolishes endonuclease activity *in vitro* does not display a growth defect *in vivo*³⁵. While *RRP44* is essential, a point mutation in the RNB domain that disrupts exoribonuclease activity (D551N) is viable although it exhibits a severe growth phenotype¹⁸. These observations make the biological function of the endoribonuclease activity unclear, but it is important to note that a combination of mutations (D551N/D171N) that simultaneously disrupt exoribonuclease and endoribonuclease activities results in synthetic lethality^{32,35}. The four acidic residues are conserved in human Dis3 but not in Dis3L as it only retains 2 of

the 4 acidic residues. Consistent with this observation, only Dis3 appears catalytically competent for endoribonucleolytic function⁷. In addition to its catalytic activities, the PIN domain interacts directly with Rrp41/Rrp45 heterodimer as exemplified in the structure of Rrp44 in complex with Rrp41 and Rrp45 (Figure 6). While the endoribonuclease activity is not essential, deletion of the PIN domain is lethal in budding yeast suggests that contacts to Rrp41/Rrp45 and presumably the exosome core are essential for growth³².

Rrp44 and the 10-component exosome

Models of the eukaryotic 10 component cytoplasmic exosome Exo10⁴⁴ have been proposed based on the x-ray structure of the human nine-component exosome core¹⁷, the crystal structure of the budding yeast Rrp41-Rrp45-Rrp44 trimer²⁵ (Figure 6), and negative stain and cryo-EM structures of apo budding yeast Rrp44-bound to the core exosome (Exo10⁴⁴)^{33,51}. These models reveal that Rrp44 is anchored to the bottom of exosome core through extensive interactions between the PIN domain of Rrp44 and Rrp41/Rrp45 in addition to contacts between the Rrp44 CSD1 and Rrp43. More recently, a crystal structure of Exo10^{44/6CTD} bound to RNA was solved⁵². How RNA engages the activities of Rrp44 when Rrp44 is associated with the exosome core, how the Exo9 core modulates Rrp44 endo- and exoribonuclease activities, and the importance of the central channel for exosome function *in vivo* and *in vitro* will be discussed extensively throughout this dissertation.

Rrp6, a eukaryotic exosome subunit with distributive hydrolytic activities

Rrp6 is associated with the nuclear exosome (Exo11^{44/6}) in budding yeast and humans, although recent evidence suggests the existence of a nucleolar exosome in human cells consisting of Rrp6 and the Exo9 core which I denote Exo10⁶ (Ref. 7). Rrp6 is the only non-essential subunit of the exosome; however budding and fission yeast strains lacking Rrp6 exhibit a temperature sensitive growth phenotype and accumulate many nuclear RNA precursors^{53,54}. Rrp6 is involved in 3' end processing of snRNAs, snoRNAs^{54,55}, pre-rRNAs⁵⁶, destruction of aberrant nuclear RNAs, and the degradation of cryptic unstable transcripts that result from bidirectional transcription^{57, 58}. In fission yeast, Rrp6 and the nuclear exosome cooperate with the RITS complex to induce constitutive heterochromatin spreading at centromeres^{59,60} and to silence meiotic genes in vegetative cells^{61,62}. Evidence for exosome-independent functions of Rrp6 have been reported in budding yeast, but these findings are restricted to nuclear RNAs^{63,64}. In other species, including trypanosomes⁶⁵, *Drosophila*⁵, and humans^{7,66}, Rrp6 has been detected in the cytoplasm, although the biological implications of these findings have not been fully characterized. Furthermore, in *S. cerevisiae*, combining *rrp6Δ* with *rrp44exo*- results in synthetic lethality and combining *rrp6Δ* with *rrp44endo*- results in a synthetic growth defect³⁵.

Rrp6 is composed of a PMC2NT domain, a N-terminal domain (NTD), a DEDD-Y exoribonuclease domain (EXO), a helicase and RNase D carboxy terminal (HRDC) domain, and a C-terminal domain (CTD). The PMC2NT domain is required for interaction with its nuclear cofactor, Rrp47 and this interaction is essential for both Rrp6 and Rrp47 stabilization *in vivo*^{67,68}. The exoribonuclease domain of Rrp6 is related to RNase D and members of the DEDD-Y nuclease family that are so named for four conserved acidic residues, DEDD, and a conserved tyrosine that coordinate two metals

to catalyze distributive, hydrolytic 3' to 5' exoribonuclease activity via a two metal ion mechanism⁶⁹. HRDC domains are posited to bind nucleic acid; however it remains unclear if this is its function in Rrp6 although deletion of the HRDC leads to severely diminished catalytic activity in human Rrp6 (Ref. 70). The CTD contains two putative nuclear localization sequences that are not necessary for interaction with the exosome⁶³. A structure of the PMC2NT domain of Rrp6 bound to Rrp47 and a N-terminal helix of Mtr4 was recently published⁷¹, illustrating the PMC2NT domain as a helical bundle. Structural and biochemical information regarding the CTD will be extensively discussed in this dissertation.

Crystal structures of Rrp6 fragments that include the NTD, EXO, and HRDC domains were determined from budding yeast⁶⁹ and human⁷⁰ (Figure 8). The NTD wraps around the EXO domain and forms a platform with a linker that connects the EXO and HRDC domains. The EXO core shares the α/β fold observed in the Klenow fragment of DNA Polymerase I from *E. coli*⁷² as well as conserved DEDD residues in the EXO domain that are required for coordination of the divalent metal ions for two metal ion catalysis. In Rrp6, the conserved tyrosine side chain activates a nucleophilic water molecule for cleavage of the phosphodiester. Mutating any of the conserved active site residues either abolishes or severely attenuates exoribonuclease activity *in vitro*⁷³. The human and yeast Rrp6 structures show the EXO domain and active site to be solvent-exposed, thus potentially explaining Rrp6 distributive activity as these structures lack channels that could bind or guide single-stranded RNA into the active site. The HRDC domain resembles the first HRDC domain of *E. coli* RNase D⁷⁴ and consists of five alpha helices. The HRDC confers substrate specificity, as disruption of the EXO/HRDC interface in budding yeast Rrp6 (D457A) results in deficiencies in 3' end processing of nuclear RNAs, such as snRNAs, but not in the clearance of the 5' ETS fragment of pre-

rRNA and maturation of 5.8S rRNA⁷⁵. Although Rrp6 fragments containing the NTD/EXO/HRDC domains exhibit similar catalytic activities when compared to full-length Rrp6, it is worth noting that Rrp6 fragments that include the NTD, EXO, and HRDC do not complement growth defects observed in budding yeast strains lacking *RRP6*⁶⁹.

Although the structures of the catalytic domains from budding yeast and human share many similarities throughout the EXO and HRDC domains, the human Rrp6 active site appears more solvent exposed when compared to the active site in yeast Rrp6 (Ref. 70). This structural difference is attributed to a difference in linker length between the EXO and HRDC domains – in yeast and lower eukaryotes the linker is 26 residues but in human the linker is only 10 residues long^{69,70}. The net effect of a shorter linker is a more solvent exposed human Rrp6 active site that it is able to degrade structured RNAs more efficiently than yeast Rrp6 in vitro, presumably because these larger substrates can access the human Rrp6 active site⁷⁰.

Rrp44, Rrp6 and the 11-component nuclear exosome

The 11 subunit nuclear exosome of budding yeast (Exo11^{44/6}) has genetically been the best characterized Rrp6-associated exosome complex, and includes the Exo9 core, Rrp44, and Rrp6 (Ref. 3). Although Rrp6 is not essential in budding yeast, mutation of the Rrp44 endoribonuclease site (D171N) in combination with *rrp6Δ* leads to a synthetic growth defect³⁵, and inactivation of the Rrp44 exoribonuclease site (D551N) with *rrp6Δ* results in synthetic lethality¹⁸. These data suggest overlapping functions for Rrp6 and Rrp44 activities in vivo. Insights to how the nuclear exosome differs from its cytoplasmic and nucleolar counterparts, and how Rrp6 contributes to the activities of and interacts with the exosome will be major emphases of this dissertation.

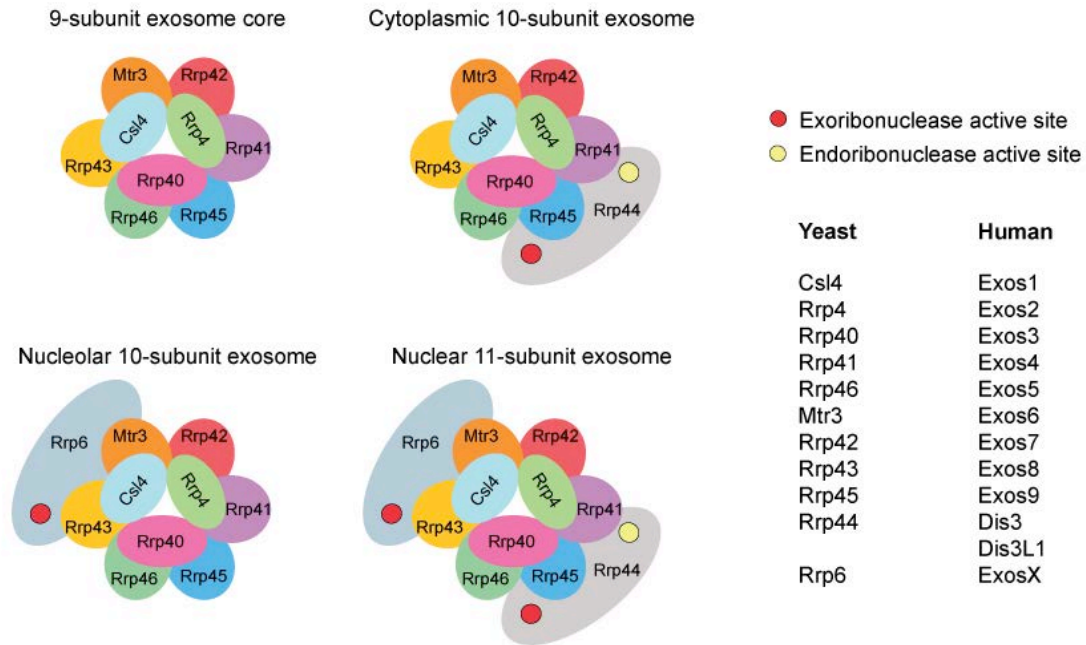


Figure 1. Schematics of eukaryotic exosomes.

Cartoon schematics depicting subunit compositions and general architecture of the nine-subunit exosome core (upper left), the cytoplasmic ten-subunit exosome (upper right), the nucleolar ten-subunit exosome (lower left) and nuclear eleven-subunit exosome (lower right). Subunits are labeled and color coded and include the PH-like ring subunits Mtr3 (orange), Rrp42 (red), Rrp41 (purple), Rrp45 (blue), Rrp46 (green) and Rrp43 (yellow); the S1/KH domain proteins Csl4 (light blue), Rrp4 (green) and Rrp40 (pink); the catalytic subunits Rrp44 (grey) and Rrp6 (grey-blue). The exoribonuclease active sites are depicted by red circles in Rrp44 and Rrp6 and the endoribonuclease active site of Rrp44 is depicted with a yellow circle. The names of subunits are indicated on the right under headings for yeast and human although human proteins are often referred to by the corresponding yeast nomenclature.

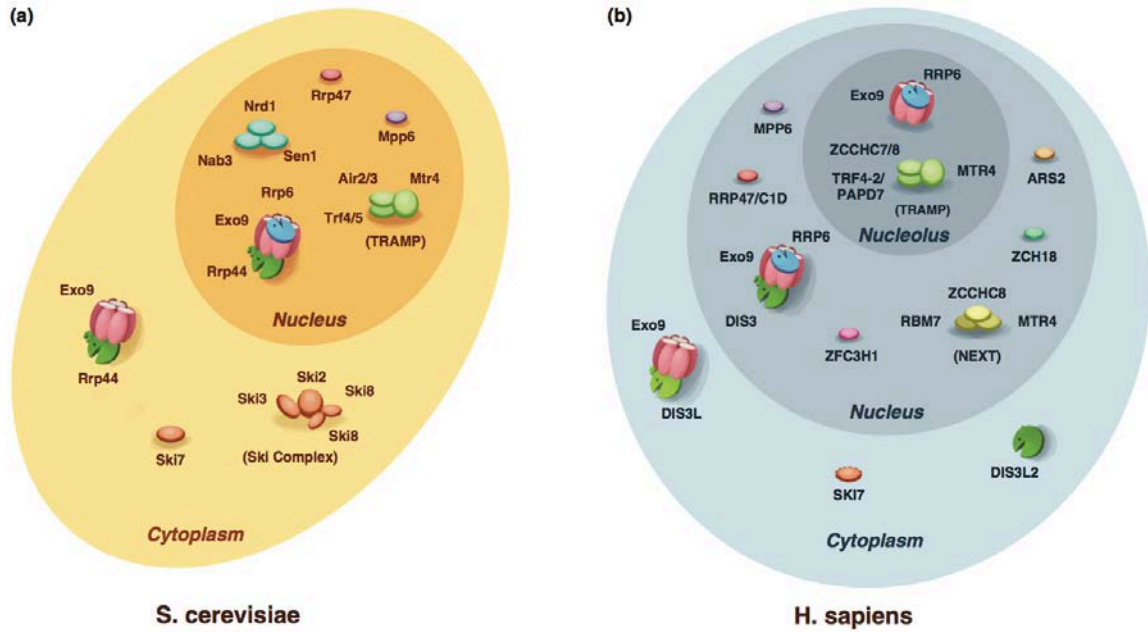


Figure 2. Exosome complexes and their various known protein cofactors

in *S. cerevisiae* (a) and *H. sapiens* (b). In addition to the cartooned exosome complexes, of particular interest in this dissertation is the nuclear cofactor, Mpp6 (Chapter 4). Figure by A. Wasmuth, from Januszyk and Lima, 2014 (Ref. 76).

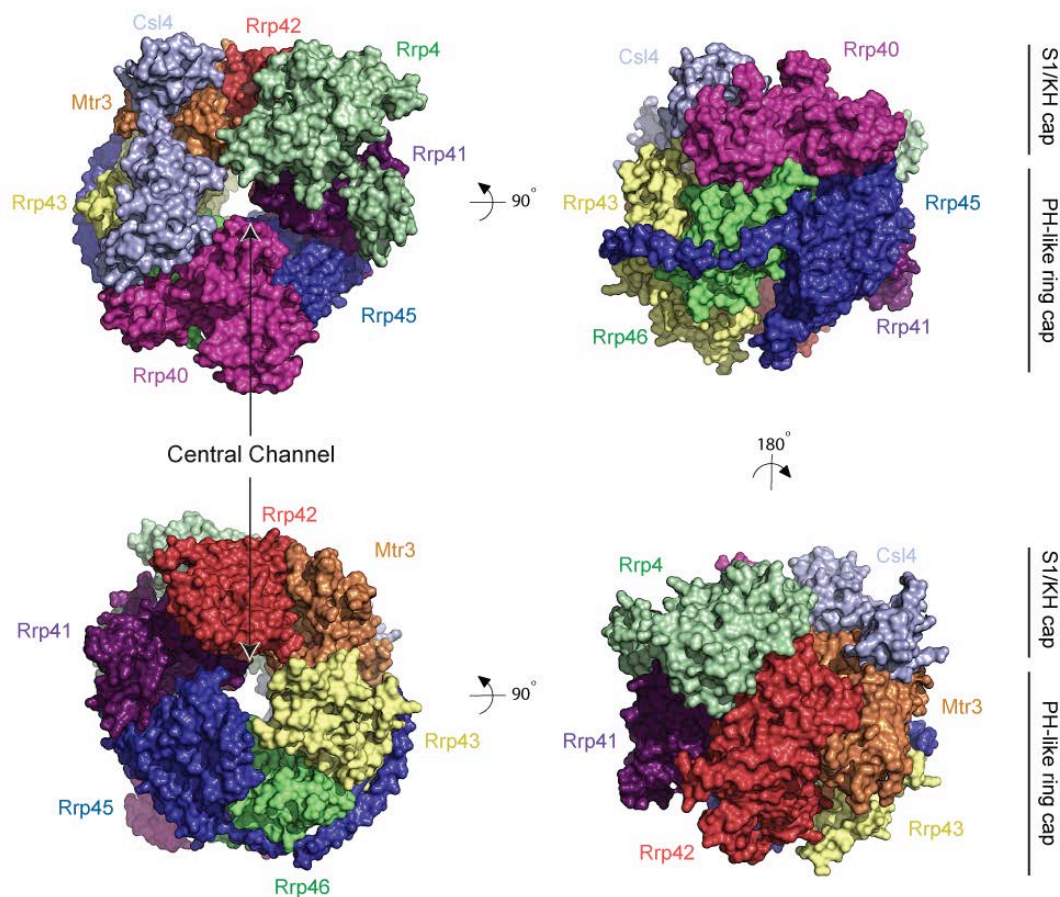


Figure 3. Structure of the human nine-subunit exosome core.

Surface representations of the human exosome core (PDB 2NN6) from the top (upper left) and bottom (lower left) in addition to two orthogonal views depicting the structure from side views to enable visualization of each exosome subunit in the complex. The subunits are labeled and color coded as in Figure 1 showing Mtr3 (orange), Rrp42 (red), Rrp41 (purple), Rrp45 (blue), Rrp46 (green) and Rrp43 (yellow); the S1/KH domain proteins Csl4 (light blue), Rrp4 (green) and Rrp40 (pink). The central channel is apparent in the left panels and indicated by a label and arrows. The positions of the S1/KH cap and PH-like ring are indicated in the right panels with lines and labels. All structure depictions generated with the program PyMol⁷⁷.

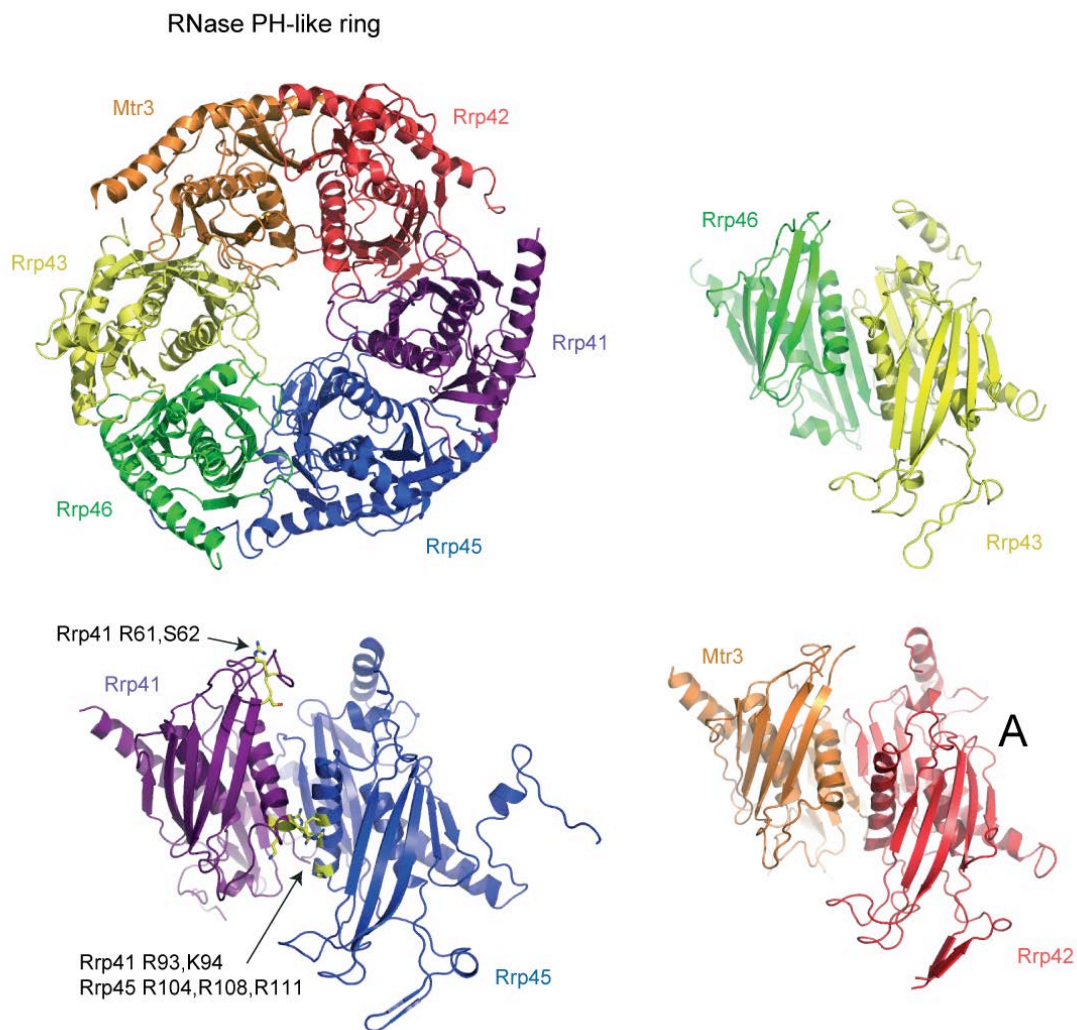


Figure 4. The human PH-like subunit ring.

Ribbon diagram of the human PH-like ring (PDB 2NN6) depicting beta strands as arrows, alpha helices as coiled ribbons and connecting elements as thin tubes (upper left). The view of the intact PH-like ring is from the 'top' as presented in Figure 1 and Figure 3 with subunits labeled and color coded with Mtr3, Rrp42, Rrp41, Rrp45, Rrp46, and Rrp43. The Rrp41/Rrp45 heterodimer is shown lower left in a side view as if the viewer were inside the central channel looking outward. Amino acid side chains implicated in RNA binding interactions labeled and side chains colored yellow for Rrp41 Arg61, Ser62, Arg93 and Lys94 and Rrp45 Arg104, Arg108 and Arg111.

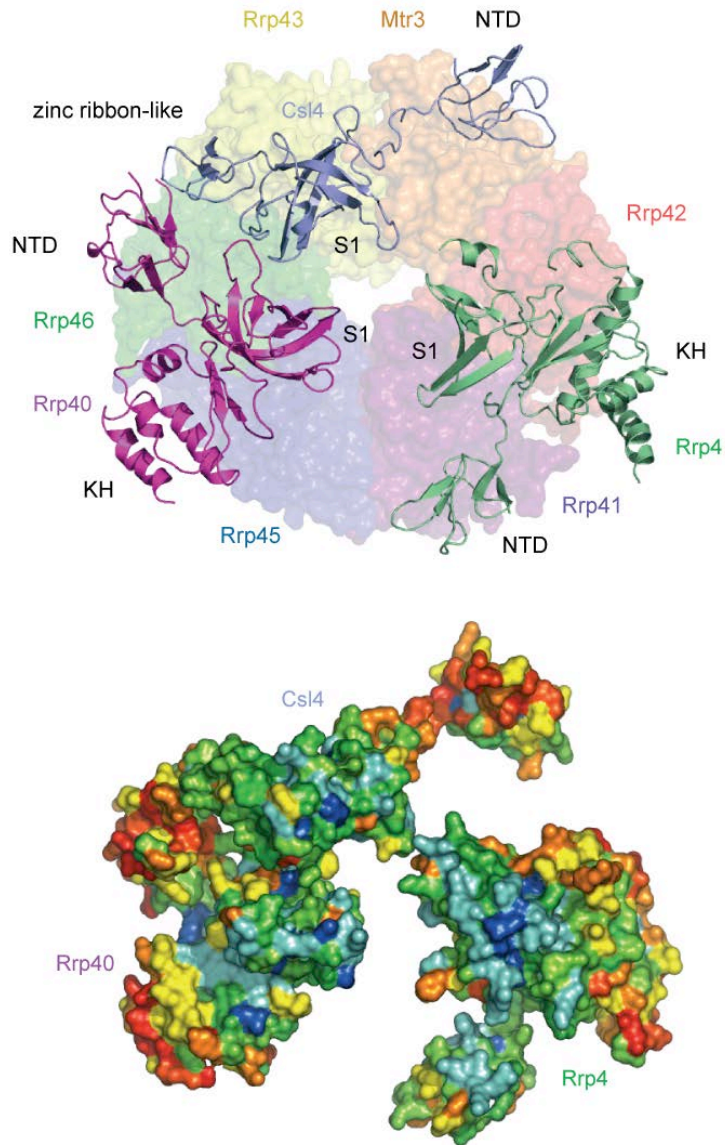


Figure 5. The human S1/KH protein ring.

Ribbon diagram of the human S1/KH proteins on top of a transparent surface representation of the PH-like ring shown from the 'top' with subunits labeled and color coded as in previous Figures with Csl4 (light blue), Rrp4 (green) and Rrp40 (pink) (top). The N-terminal (NTD), S1, KH and zinc ribbon-like domains are labeled. Note that the S1 domains from each S1/KH protein face the central channel. The bottom panel depicts just the S1/KH proteins in surface representation in the same orientation as in the top panel indicating sequence conservation colored from red (variable) to blue (conserved)

as calculated by ConSurf⁷⁸ from manually assembled sequence alignments¹⁷. Note that the most conserved surfaces are located on the S1 domains that face the central channel.

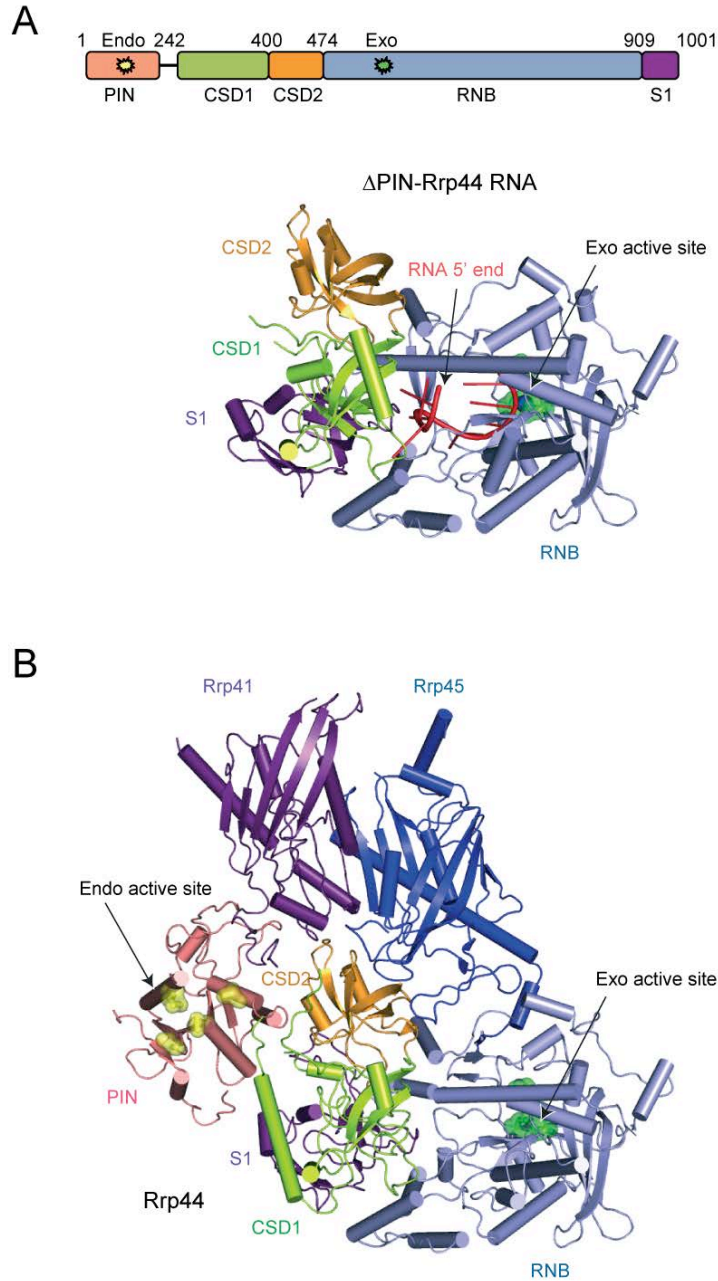


Figure 6. The endo- and exoribonuclease Rrp44.

A) Schematic representation of the Rrp44 polypeptide indicating the PIN, CSD1, CSD2, RNB and S1 domains with labels and color coded pink, green, orange, blue and purple, respectively. Amino acid numbering is for *Saccharomyces cerevisiae* Rrp44. Below the schematic is the structure of yeast Rrp44 bound to RNA (PDB 2VNU) in cartoon ribbon representation with beta strands as arrows, loops as ribbons and helices as solid tubes.

The domains are labeled and color coded as in the schematic. The exoribonuclease active site is indicated by a label and arrow with key residues colored green in stick and surface representation. RNA is shown as a red ribbon with bases indicated as sticks with the 5' end labeled and indicated by an arrow; the 3' end is buried in the exoribonuclease active site. B) Structure of full-length yeast Rrp44 in complex with yeast Rrp41 and Rrp45 (PDB 2WP8) in cartoon ribbon representation color coded as in the top panel with the PIN domain in pink. The endoribonuclease active site is labeled and indicated by an arrow with key residues colored yellow in stick and surface representation.

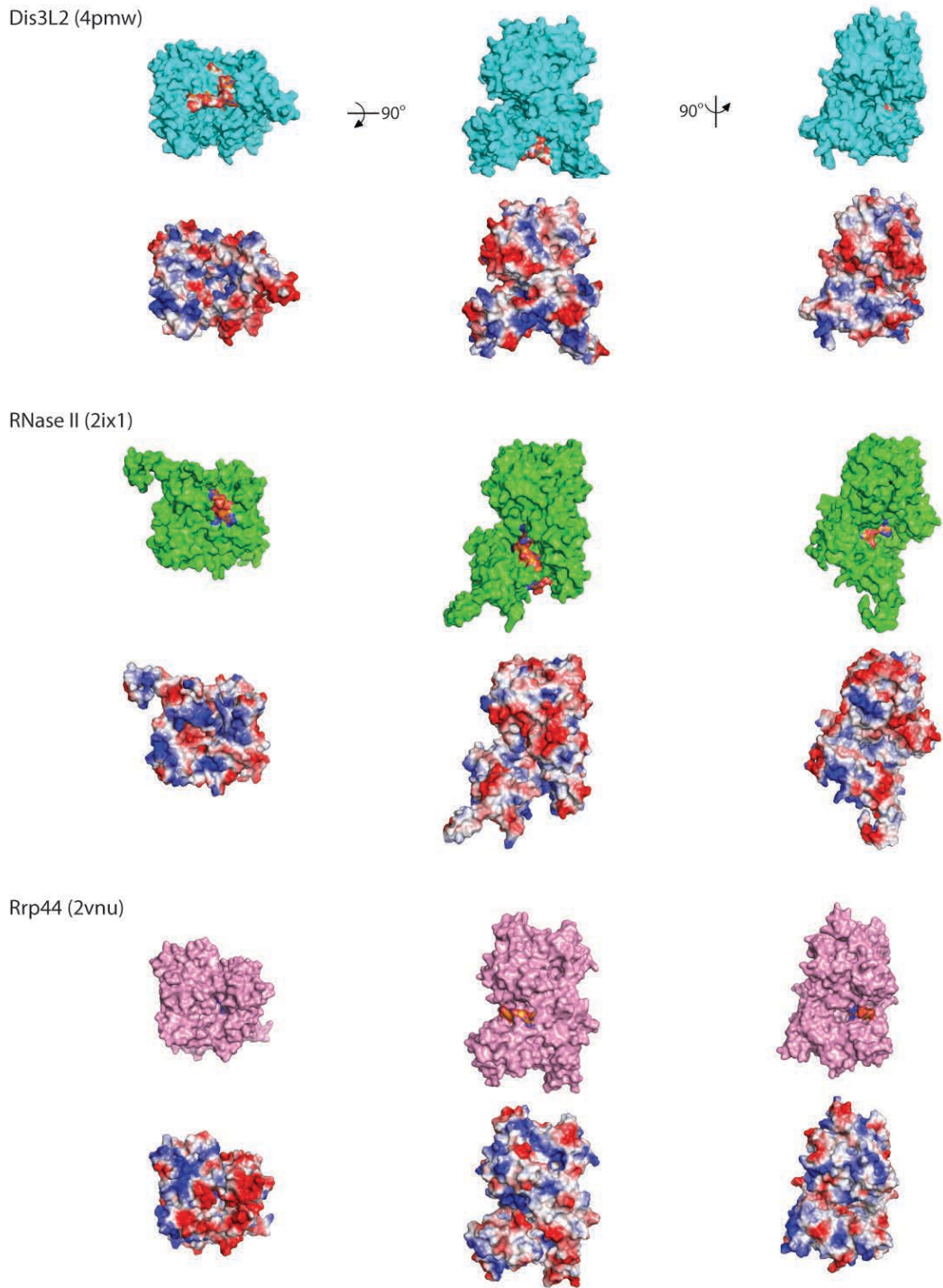


Figure 7. Structural comparison of RNA paths in murine Dis3L2, bacterial RNase II, and yeast Rrp44.

Surface representations and corresponding electrostatics for these 3 homologs. Dis3L2 (PDB: 4pmw) in cyan; RNase II (PDB: 2ix1) in green; Rrp44 (PDB: 2vnu) in pink. RNA ingress in Dis3L2 follows a similar route as RNase II, and has similar electrostatic surfaces and architecture. Ingressing RNA takes an alternative, and more electrostatically favored route to the RNB in Rrp44; this same path is utilized in Rrp44-associated exosomes engaged with RNA⁵², which will be discussed extensively in this dissertation.

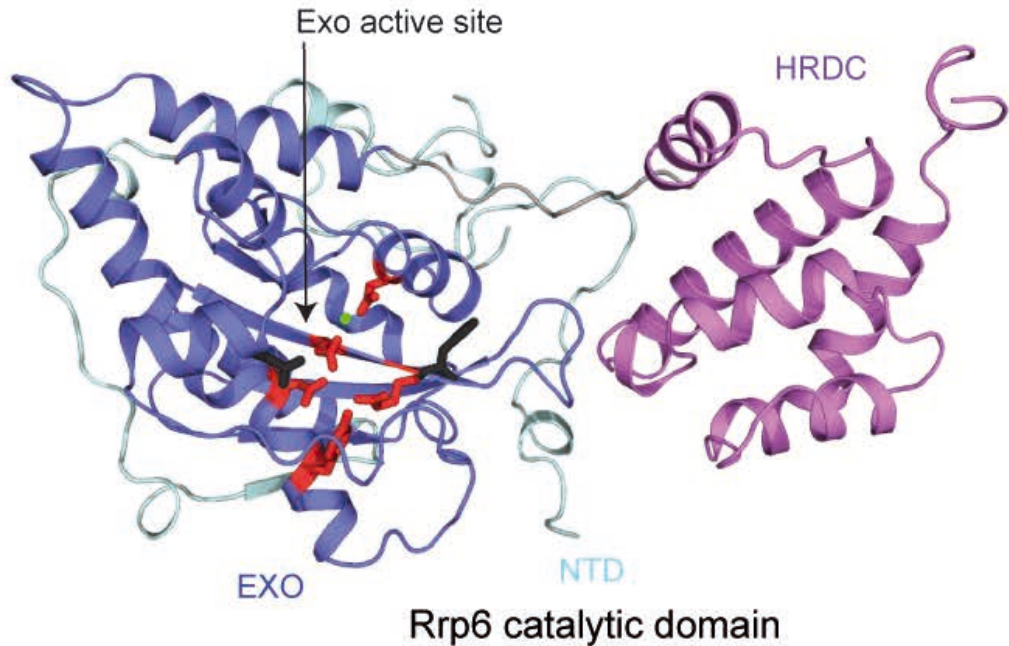
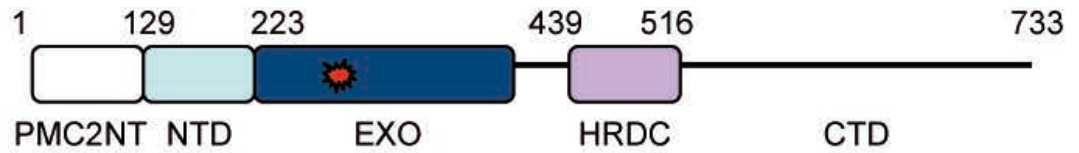


Figure 8. The exoribonuclease Rrp6.

Schematic of the Rrp6 polypeptide indicating the PMC2NT (white), NTD (light blue), EXO (dark blue), HRDC (purple) and C-terminal (CTD; black line) domains. Domains are labeled with the exoribonuclease active site colored red. Amino acid numbering is for yeast Rrp6. Lower panel depicts a cartoon ribbon representation of the human Rrp6 catalytic domain structure with alpha helices in cartoon ribbon, loops as thin ribbons and beta strands as arrows (PDB 3SAF). Domains are colored and labeled as in the schematic with the linker between the EXO and HRDC domain in grey. The EXO active site is labeled and indicated with an arrow with key side chains colored red and shown in stick representation; the magnesium ion is shown as a small green sphere.

concentration of 2% and 0.05 mM isopropyl- β -D-thiogalactoside (IPTG), and grown at 18°C overnight. The only other exception was full-length Rrp6, which required growth in a 10 liter fermenter, and a 3 hour induction at 30°C for expression⁸⁰.

Cells were resuspended in high salt buffer (350 mM) and lysed by sonication as described⁷⁹. After high speed centrifugation to pellet the insoluble material, the supernatant was loaded on a nickel-NTA column (Qiagen) and allowed to flow by gravity. After washing with 350 mM NaCl, 20 mM Tris pH 8.0, 1mM BME, and 20 mM imidazole, the column was further washed with 350 mM NaCl, 50 mM KCl, 20 mM Tris pH 8.0, 1 mM BME, 2 mM ATP, 10 mM MgSO₄ to displace chaperone impurities. Protein was eluted with 350 mM NaCl, 20 mM Tris pH 8.0, 1mM BME, and 250 mM imidazole and then purified by size exclusion chromatography. Most subunits were purified on the Superdex 200 (GE) with the exception of Smt3-Csl4 and Smt3-Rrp40, which were purified on a Superdex 75 (GE). Wild type and mutant subunits eluted at the same volumes on gel filtration. Rrp44 proteins harboring mutation in the exoribonuclease active site (D551N and D171N/D551N) were further purified by anion-exchange chromatography (MonoQ 10/10, GE) to remove nucleic acid. After elution from Ni-NTA, Smt3-Mpp6 was purified on a heparin column to remove nucleic acid, cleaved with Ulp1 overnight, and re-run on gel filtration (Superdex 75). After elution from Ni-NTA, His₆-GST-Rrp6 CTD was purified by size exclusion chromatography (Superdex 200 gave better separation than Superdex 75), and run on a final heparin column to remove contaminating nucleic acid and to separate degradation products. Prior to reconstitutions, only Smt3-Mpp6, Smt3-Rrp6, Smt3-Rrp44, and Smt3-Rrp42/Mtr3 were subjected to overnight cleavage by the SUMO protease Ulp1 (Ref. 79) and another step of purification by gel filtration to remove the 6x histidine Smt3 tags; Smt3-Rrp42/Mtr3 was Ulp1 cleaved prior to formation of Exo9 as inclusion of this tag interferes with reconstitution. At this stage, subunits were concentrated to 6 to 12 mg/mL and stored at

-80°C. For reconstitution, Exo9 subunits were mixed together as Smt3 fusions, incubated on ice for 30 minutes, followed by addition of Ulp1 for another 30 minutes prior to overnight dialysis in 100 mM NaCl, 20 mM Tris pH8.0, 10 mM DTT. Size exclusion runs (Superdex 200) of reconstituted exosomes were performed in 100 mM NaCl, 20 mM Tris pH8, 5 mM DTT. After purification, exosomes were concentrated to 12 to 14 mg/mL and stored at -80°C in a final buffer of 100 mM NaCl, 20 mM Tris pH 8.0, 0.1 mM MgCl₂, 1 mM TCEP.

Ribonuclease Assays

RNA oligonucleotides were synthesized with a 5' fluorescein as described previously^{17,70} and purchased from Invitrogen, IDT, or Dharmacon. The 49 nucleotide poly(A) and AU-rich RNA oligonucleotides have the sequences AAA A and AAU UAU UUA UUA UUU AUU UAU UAU UUA UUU AUU UAU UAU UUA UUU AUU A, respectively. Cold RNAs used in this study included AU-rich RNAs of 10, 17, 21, 24, 28, 32, 36 and 49 nts with sequence AUU AUU UAU U; AUU AUU UAU UUA UUA UU; AUU AUU UAU UUA UUA UUU AUU; AUU AUU UAU UUA UUA UUA UUU AUU; AUU AUU UAU UUA UUA UUA UAU UUU AUU UAU U; AUU AUU UAU UUA UUA UUU AUA UUU UAU UUA UU; AUU AUU UAU UUA UUA AUU AUU UAU AUU UUA UUU AUU; AAU UAU UUA UUA UUU AUU UAU UAU UUA UUU AUU A.

Unless otherwise noted in text and figure legends, exoribonuclease assays were performed under multiple turnover conditions. For mix-in experiments (Figure 34e) 2-fold molar excess of Rrp6 protein was incubated with Exo10^{Rrp44} on ice for 1 hour prior to initiating RNA decay by addition of RNA. Exoribonuclease assays were conducted using in 50 mM KCl, 20 mM Tris-HCl (pH8.0), 10 mM DTT, 0.5 mM MgCl₂, and 1U/ μ L RNase inhibitor (NEB) (1 nM enzyme and 10 nM RNA). At indicated times, 10 μ L aliquots were removed and quenched in 2X TBE-urea loading dye and flash-frozen in N_{2(l)}. Samples were analyzed by denaturing PAGE using 15% TBE-urea polyacrylamide gels (Invitrogen) and gels imaged using a Fuji FLA-5000 scanner. For Exo11 complexes, Rrp44 and Rrp6 activities were quantified separately. Rrp44 exoribonuclease activity was quantified by integrating the signal from the final 4-5 nt RNA product using MultiGauge v2.02 (Fujifilm). For experiments in Chapter 1, the fraction of full-length RNA degraded at a given time was calculated and values obtained from triplicate experiments

were plotted using Prism 5.0 and fit to a one-phase decay curve. Initial rates were calculated from data obtained within the linear range. Rrp6 activity was quantified by dividing the median length of the RNA intermediates at a given time by the full-length (49nt) RNA substrate to determine the fraction of RNA remaining. Data from triplicate experiments were analyzed using Prism 5.0 and fit to a one-phase decay curve. Initial rates were calculated from data obtained within the linear range.

Endoribonuclease assays utilized variants of Rrp44 and Rrp6 that contained mutations in their respective active sites (Rrp44-D551N and Rrp6-D238N). Endoribonuclease assays were carried out in the same reaction buffer used for exoribonuclease activity except that $MnCl_2$ was added to initiate the assays. Proteins (10 nM) were pre-incubated with 10 nM RNA at 30°C for 5 minutes and reactions were initiated by addition of 3 mM $MnCl_2$. Endonuclease assays conducted using unlabeled RNAs was scaled to 100 nM enzyme and 100 nM RNA to facilitate detection of reaction intermediates by Sybr Gold staining (Invitrogen). Samples were analyzed by denaturing PAGE using 15% TBE-urea polyacrylamide gels (Invitrogen) and gels imaged using a Fuji FLA-5000 scanner. Rrp44 endoribonuclease activity was quantified by integrating the signal of full-length (49 nt) RNA remaining at each time point using MultiGauge v2.02 (Fujifilm), and calculating the fraction of full-length RNA lost per minute. Initial rates were calculated from data obtained within the linear range and plotted using Prism 5.0.

UV-RNA crosslinking

700 nM of exosome subunits or complexes with mutations in the exoribonuclease active site were incubated on ice for 20 minutes with 50 nM of a 36 nt 5' fluorescein AU-rich RNA in a 70 μ L reaction volume. The binding reaction buffer consisted of 50 mM KCl, 20 mM Tris (pH 8.0), 10 mM DTT, 0.5 mM MgCl₂. Samples were then placed in a UV-Stratalinker (Stratagene) and subjected to 400,000 or 700,000 μ J of short-wave UV radiation (254 nm). 15 μ L aliquots were taken, added to 4X LDS loading buffer, and separated by SDS-PAGE on a 4-12% Bis-Tris gel (Invitrogen). RNA-protein adducts were visualized immediately with a fluoroimager (FITC filter); protein integrity was assessed after initial imaging by staining with Sypro Ruby (Invitrogen) and visualized with a fluoroimager (LPB filter).

For steady state UV-RNA crosslinking to 4-thiouridine (4-thioU) bearing RNAs, 500 nM of exosome complexes with mutations in the exoribonuclease active sites (D238N for Rrp6, D551N for Rrp44) were incubated for 20 minutes on ice with 50 nM 36 nt 5' fluorescein RNAs with a single internal 4-thioU (Thermo Scientific) in a 70 μ L reaction volume. Binding buffer includes 50 mM KCl, 20 mM Tris pH 8.0, 10 mM DTT, 0.5 mM MgCl₂. Crosslinking was performed by subjecting the RNA-exosome mixture to long-range UV (365 nm) for 15 minutes in the dark using a 4W handheld lamp. For the time course described in Figure 31D, 350 nM of exosome was incubated with 150 nM of RNA, and the binding reactions allowed to proceed for indicated times before initiating crosslinking for 10 minutes. 15 μ L was quenched with LDS loading buffer, and the crosslinked products were separated by SDS-PAGE (Invitrogen) and visualized with a Fuji FLA-5000 scanner (FITC filter). 4-thioU RNA included the following sequences, each of which contained a 5'-Fluorescein: 5'-FI-AAU UAU 4thioUUA UUA UUU AUU UAU UAU UUA UUU AUU UAA; 5'-FI-AAU UAU UUA UUA UU4thioU AUU UAU UAU

UUA UUU AUU UAA; 5'-FI-AAU UAU UUA UUA UUU AUU UAU UAU UUA UU4thioU
 AUU UAA; 5'-FI-AAA AAA 4thioUAA AAA AAA AAA AAA AAA AAA AAA AAA AAA; 5'-
 FI-AAA AAA AAA AAA AA4thioU AAA AAA AAA AAA AAA AAA AAA; 5'-FI-AAA AAA
 AAA AAA AAA AAA AAA AAA AAA AA4thioU AAA AAA.

Fluorescence polarization

For experiments described in Chapter 1, 200 nM 5' fluorescein labeled AU-rich
 36 nt or polyA 37 nt RNA was incubated on ice with increasing concentrations (0 – 6000
 nM) of proteins or complexes that harbored indicated mutations in the ribonuclease
 active sites (Rrp44 or Rrp6) or central channel (Rrp41 and Rrp45) for 20 minutes in a 20
 μ L reaction volume. Binding buffer consisted of 50 mM KCl, 20 mM Tris (pH8.0), 10 mM
 DTT, 0.5 mM MgCl₂, and 0.1% NP-40. Fluorescence polarization (mP) was measured at
 23°C with a SpectraMax M5 (Molecular Devices), with λ_{ex} 495 nm and λ_{em} 525 nm.
 Subsequent mP values were converted to anisotropy (mA). Using data from triplicate
 experiments, a model for receptor depletion was employed to calculate apparent K_d
 values and to plot binding curves with Prism, GraphPad Software. The receptor
 depletion model is

$$A = A_f + (A_b - A_f) \times \frac{(L + K_d + R) - \sqrt{(-L - K_d - R)^2 - 4L_T R_T}}{2L_T}$$

where A is the measured anisotropy, A_b is the anisotropy at 100% saturation, A_f is the
 anisotropy of the free RNA ligand, L is the fixed concentration of the RNA ligand, R is
 protein concentration.

The same procedure was following for experiments presented in Chapters 3 and 4
 except 50 nM RNA was used rather than 200 nM.

Yeast strains and complementation by plasmid shuffle

Heterozygous *S. cerevisiae* diploid strains, *RRP41/rrp41Δ* and *RRP45/rrp45Δ* were obtained from Open Biosystems, and are derivative of the parental strain BY4743. Strains were transformed with a *CEN URA3* (pRS416) plasmid bearing wild-type *RRP41* or *RRP45* and their respective endogenous 5' and 3' UTRs. Haploids were generated using standard sporulation protocols and the resulting haploid strains were transformed with *CEN LEU2* (pRS415) plasmids encoding WT or mutant alleles which included *rrp41-K62E/S63D/R94E/R95E*, *rrp41-R106N/R113N*, and loop insertion mutants *rrp41-S*, *rrp41-M*, *rrp41-L*, *rrp45-S*, *rrp45-M* and *rrp45-L*. Strains bearing pRS416 and pRS415 plasmids were selected after transformation by plating on minimal media (SD-Leu-Ura). Loss of the respective *CEN URA3* plasmid was selected for by plating on SD-Leu that contained 5-fluoroorotic acid (5-FOA). Growth was monitored at 23°C, 30°C, and 37°C over a period of 10 days.

The *rrp41Δrrp45Δ* strain was constructed by mating *MATα*, *his3Δ1*, *leu2Δ0*, *ura3Δ0*, *met15Δ0*, *rrp41Δ::KAN [RRP41, URA3]* to *MATa*, *his3Δ1*, *leu2Δ0*, *ura3Δ0*, *met15Δ0*, *rrp45Δ::KAN [RRP45, URA3]*. Diploids were sporulated and haploid spores selected based on their ability to grow on agar media containing G418, SD-Ura, and their inability to grow on media containing 5-FOA. The absence of both endogenous *RRP41* and *RRP45* was confirmed by analyzing genomic DNA (Harju et al., 2004) and genotyping by PCR to validate the presence of the kanMX cassette in both *RRP41* and *RRP45* loci by amplifying regions bridging the 5' UTR and the kanMX cassette. This strain was subsequently transformed with *CEN LEU2* (pRS415) plasmids encoding WT or mutant *rrp41* alleles and *CEN HIS3* (pRS413) plasmids encoding WT or mutant *rrp45* alleles. Transformants carrying pRS416-*RRP41*, pRS416-*RRP45*, pRS415-*RRP41* or pRS415-*rrp41* and pRS413-*RRP45* or pRS413-*rrp45* were selected by plating on SD-

Leu-His-Ura. Loss of the *CEN URA3* plasmids were selected by plating on media containing 5-FOA and lacking leucine and histidine. Growth was monitored at 23°C, 30°C, and 37°C over a period of 10 days.

The *rrp6Δ* strain in the W303 background was a gift from Michael Rosbash⁸¹. Haploid strains were transformed with a *CEN URA3* (pRS416) plasmid bearing wild-type *RRP6*, Rrp6 lasso or EAR deletions, or vector alone under its endogenous 5' and 3' UTRs. Strains bearing pRS416 plasmids were selected after transformation by plating on minimal media (SD-Ura). Loss of the respective *CEN URA3* plasmid was selected for by plating on SD+5-FOA. Growth was monitored at 23°C, 30°C, and 37°C over a period of 10 days. No readily discernable phenotype was apparent at 23°C so further growth experiments were conducted at 30°C and 37°C.

To introduce Rrp44-TAP into the *rrp41Δrrp45Δ* strains for purification of exosomes by tandem affinity purification, genomic DNA was isolated from the Rrp44-TAP tagged strain (Open Biosystems). The Rrp44-TAP cassette and endogenous 5' and 3' UTRs were PCR amplified and cloned into a *CEN URA* (pRS416) plasmid. Constructs were verified by sequencing and transformed into *rrp41Δrrp45Δ* strains carrying either Rrp41WT/Rrp45WT or Rrp41Med/Rrp45Sm covering plasmids. Transformants were selected on SD-Leu-His-Ura. 12L of culture were grown at 25°C in SD-Leu-His-Ura until A_{600} 1.5. Cells were harvested and processed using methods described⁸². Extracts were placed over IgG sepharose (GE Healthcare), eluted by cleavage with TEV protease (homemade), and purified over calmodulin affinity resin (Agilent Technologies). To detect exosome subunits by Western blot, polyclonal antibodies were raised against Rrp41, Rrp45, and Rrp6 (Pocono Rabbit Farms) and used to detect levels of Rrp41, Rrp45, and Rrp6. Anti-calmodulin binding protein epitope tag antibody (Millipore) was used to detect Rrp44-CBP.

RNA analysis by qPCR

Yeast strains were grown in YPD at 30°C until A_{600} 0.8. 100 mL cultures were collected by centrifugation and total RNA extracted using the hot acid phenol method⁸³. 1 µg total RNA was treated with DNase for 2 hours at 37°C before reverse-transcription (RT) using Superscript III First-Strand synthesis system, following manufacturer's instructions (Invitrogen). For reverse-transcription (RT) reactions, oligonucleotides complementary to the RNA target were used for cDNA synthesis (Primer 1 in Table 2), unless otherwise noted. PCR reactions were performed in triplicate and prepared in a 50 µL reaction volume, with 2X Sybr Green 2X PCR Master Mix (Applied Biosystems), and 2 µL of the RT reaction used as a template for PCR amplification using Primers 1 and 2, the exception being ITS2-1, which used 1 µL of the RT reaction as a template. Data were acquired using ABI Prism 7500 Real-Time PCR System (Applied Biosystems). scR1 mRNA was used for normalization. Target levels were calculated using the $2^{-\Delta\Delta CT}$ method⁸⁴ and are represented as fold enrichment over wild-type.

Crystallization and structure determination

Exo10^{6exo-} samples were mixed with polyA₂₄ RNA (Invitrogen) in a 1:1.1 molar ratio and incubated on ice for 1 hour prior to crystallization. Crystals grew at 18°C by vapor diffusion in either sitting (Greiner Bio One, Crystalquick) or hanging (Hampton Research, VDX) drop formats, in 7-11% PEG3350, 100 mM MES pH 6.7, 4-15% MPD, typically taking 3 to 5 days to appear. Crystals were harvested within 2 weeks. For cryoprotection, well solution was replaced with crystallization buffer augmented with 25-30% MPD and crystals were incubated for three days before harvesting; one day before harvest, trays were transferred to 4°C. A light polarizer was used to exclude multiple crystals and to identify crystals with single regions, which were broken off and flash frozen in liquid nitrogen for data collection. X-ray diffraction data were collected at the Advanced Photon Source 24-ID-E and 24-ID-C beam lines, and the National Synchrotron Light Source X29 beam line. Data were processed using HKL2000⁸⁵ and the structure solved by molecular replacement using Phaser⁸⁶ and coordinates of human apo Exo9 (PDB: 2NN6) and yeast Rrp6^{CAT} (PDB: 2HBL) as search models followed by docking yeast Exo10^{Rrp44+6Cterm} (PDB: 4IFD). The structure was determined by molecular replacement (Table 8). The structure is refined to R/R_{free} values of 0.223/0.262 with good stereochemistry. The final model includes six nucleotides of the polyA 24mer, and two phosphate ions that likely represent the RNA backbone (Figure 23), and 2751 of the 3156 amino acids present in the crystal.

The asymmetric unit contains one complex. Iterative rounds of refinement were accomplished using Phenix⁸⁷. RNA and side chains were manually built using O⁸⁸ and Coot⁸⁹. The model was initially refined using secondary structure restraints in conjunction with positional refinement followed by individual B-factor refinement. Secondary structure restraints were released and a final round of positional and B-factor

refinement was performed followed by refinement of TLS parameters which resulted in a further decrease in R and R_{free} values. Figures depicting the structure were prepared with Pymol⁷⁷. Surface conservation was calculated using ConSurf⁷⁸. Electrostatics were calculated using either Pymol or APBS⁹⁰ - see figure legends for details. Structure quality was assessed using MolProbity⁹¹.

Similar methods as those described above were used for crystallization and structure determination of Exo11^{6exo-/Mpp6} and Exo12^{44exo-/6exo-/Mpp6}, both complexes bound to RNA. Exo11^{6exo-/Mpp6} was grown in 11% PEG3350, 200 mM ammonium nitrate, 2% MPD. For cryoprotection, Exo11^{6exo-/Mpp6} was first dehydrated to 25% PEG3350 in mother liquor with additional 7% increments of PEG3350, and supplemented with 10% ethylene glycol prior to flash freezing. Exo12^{44exo-/6exo-/Mpp6} was crystallized in 11-13% PEG3350, either MES pH6.5 or NaCitrate pH6.0 as the buffer, and 175-200 mM ammonium sulfate. Cryoprotection was achieved in mother liquor augmented with 21% glycerol, introduced in three steps of 7% increments. Further details of crystallization conditions and structure determination are described in text in Chapter 4.

CHAPTER 1

Exo- and endoribonucleolytic activities of yeast cytoplasmic and nuclear RNA exosomes are dependent on the non-catalytic core and central channel

1.1 Introduction

While *RRP44* is essential, a point mutation in the RNB domain that disrupts exoribonuclease activity (D551N) is viable although it exhibits a severe growth phenotype¹⁸. A point mutation that disrupts endoribonuclease activity (D171N) has no discernable phenotype but a double mutant disrupting both RNB and PIN activities fails to support growth^{32,35}.

The nuclear exosome includes Rrp6, Rrp44 and Exo9. Rrp6 is a distributive 3'→5' exoribonuclease and contains an N-terminal domain important for binding to Rrp47 and the TRAMP complex^{63,64,67,71,104}, a central exoribonucleolytic domain and a C-terminal HRDC domain^{69,70}. *RRP6* is not essential, but *rrp6Δ* phenotypes include slow growth and buildup of 3' extended forms of 5.8S rRNA, snRNAs and snoRNAs^{54,56}. Furthermore, combining *rrp6Δ* with *rrp44exo-* results in synthetic lethality and combining *rrp6Δ* with *rrp44endo-* results in a synthetic growth defect³⁵.

The function of the eukaryotic Exo9 core in regulating the RNA decay activities of the exosome has been a subject of interest given that each of its nine subunits are essential for viability although devoid of catalytic activity^{17,18}. Analysis of the human exosome structure and comparison to bacterial and archaeal counterparts revealed the presence of conserved residues in the central channel that could contribute to interaction with RNA substrates¹⁷. Furthermore, co-incubation of Rrp44 with Exo9 harboring channel-facing charge reversal point mutations diminished Rrp44 exoribonuclease

activity in vitro²⁵ and electron microscopy showed density at the entry and exit points of the channel in RNA bound complexes of Exo9 and Rrp44 (Ref. 33). Although these data are highly suggestive that Exo9 functions to regulate Rrp44 exoribonuclease activities, the contribution of the RNA exosome core and central channel to each RNase activity of the exosome or for function in vivo remains unclear.

I report here that Exo9 modulates Rrp6 exoribonuclease, Rrp44 exoribonuclease and endoribonuclease activities and that mutations designed to physically occlude the PH-like ring and central channel inhibit exosome activities in vitro and fail to support the essential functions of the RNA exosome in vivo. My data invokes an RNA path that passes through the S1/KH and PH-like rings to Rrp44, one that partially overlaps with a path used by RNA to reach Rrp6 that entails the S1/KH cap and upper portions of PH-like ring. I show that Rrp6 stimulates Rrp44 activities independent of Rrp6 catalytic activity and that Rrp6 is potentially inhibited by a mutation in the Rrp44 exoribonuclease active site. Taken together, these data suggest that the RNA exosome core coordinates RNA binding to regulate substrate access to the endo- and exoribonuclease activities of the RNA exosome.

1.2 The exosome core modulates Rrp44 and Rrp6 activities in ten-subunit exosomes

The contributions of Exo9 to Rrp44 and Rrp6 RNase activities were analyzed by reconstituting 34 distinct exosomes and comparing their ability to bind and degrade RNA (Table 3). Exosome reconstitutions used recombinant proteins as described^{17,80} with notable exceptions including removal of N-terminal hexa-histidine tags from Csl4, Rrp4, Rrp40, Rrp42, Rrp46 and Rrp41. I isolated a ten-subunit complex containing Rrp44 and Exo9 (Exo10⁴⁴), a ten-subunit complex containing Rrp6 and Exo9 (Exo10⁶), and an eleven-subunit complex containing Exo9, Rrp44 and Rrp6 (Exo11^{44/6}) (Figure 9A).

Although Exo10⁶ has not been reported in yeast, recent work suggests its presence in nucleoli of human cells⁷. Exo10⁶ and Exo11^{44/6} solubility was increased by removing 128 N-terminal residues of Rrp6 (N Δ ₁₂₈Rrp6) that are not required for association with exosomes^{63,73}. Differences in catalytic activity are not observed in vitro when comparing exosomes containing N Δ ₁₂₈Rrp6 or Rrp6 (Figure 9B).

Ribonuclease activities of Rrp44, Rrp6 and reconstituted exosomes were assayed using synthetic 5'-fluorescein labeled 49 nucleotide RNAs as models for cytoplasmic (AU-rich) and nuclear (polyA) substrates of the RNA exosome. Products were detected by monitoring fluorescein fluorescence as described^{17,80}. AU-rich and polyA RNA are single stranded and small enough to penetrate the central channel; however biophysical data suggest that AU-rich RNA is highly unstructured and readily deformable while polyA RNA forms helical domains with base-stacking interactions that make it more rigid and less deformable^{105,106}. RNase activities were assayed under multiple turnover conditions (10-fold substrate excess) to facilitate initial rate measurements, as rates were too fast to measure using single turnover conditions for AU-rich RNA. It is important to note that degradation patterns for polyA RNA were similar using single (enzyme excess) or multiple turnover conditions (Figure 9C). Apparent dissociation constants (K_d) for RNA binding to catalytically dead versions of Rrp6 and Rrp44 (exo-) in free and exosome-associated states were derived using fluorescence polarization.

Comparative analysis of Rrp44 exoribonuclease activity shows Exo10⁴⁴ is 8-fold and 42-fold less active than free Rrp44 on AU-rich and polyA RNA, respectively (Figure 10A, Table 4). These results are consistent with trends observed previously^{17,25}. Exo10^{44exo-} binds AU-rich RNA 3-fold weaker than free Rrp44^{exo-} and more than 30-fold weaker for polyA RNA although binding can not be saturated for Exo10^{44exo-} with polyA

RNA indicating a $K_d > 10 \mu\text{M}$ (Figures 10A, 10B; Table 5; Figure 11). Thus, the magnitude of defects for RNA binding with Exo10^{44exo-} mirror catalytic deficiencies observed for Exo10⁴⁴ RNase activity when compared to Rrp44.

Endoribonuclease activity of free Rrp44 has been shown to be dependent on manganese and is most readily observed when Rrp44 exoribonuclease activity is disrupted in Rrp44^{exo-} (Ref. 35) while inactivating mutations in both exoribonuclease and endoribonuclease active sites (Rrp44^{exo-/endo-}) result in no ribonuclease activity (Figure 12A). Products of free Rrp44^{exo-} endoribonuclease activity differ dramatically in length and distribution when compared to those generated by Exo10^{44exo-} (Figures 10C, 10D). While free Rrp44^{exo-} generates a distributive pattern of 5' labeled RNA intermediates (from 5 nt to 49 nt) at the earliest time points for AU-rich and polyA RNAs, Exo10^{44exo-} generates intermediates with the AU-rich RNA with apparent 3' to 5' directionality because longer 5' labeled products appear before shorter products and intermediates accumulate around 23-26 nt prior to complete degradation (Figure 10C). Patterns are similar using unlabeled RNA and are consistent with distributive endoribonuclease activities for Rrp44^{exo-} and 3' to 5' directionality for Exo10^{44exo-} (Figure 12C). Endonuclease activity of Rrp44 is attenuated upon association with the Exo9 core. For polyA, the initial rate of substrate degradation, as measured by loss of the 49 nt substrate over time, is diminished 13-fold in Exo10^{44exo-} compared to Rrp44^{exo-} (Figure 10D; Figure 12B; Table 6).

Comparing Rrp6 and Exo10⁶ activities reveals similar initial rates as determined by measuring the decrease in median RNA intermediate lengths over time (Table 7); however, Exo10⁶ and Rrp6 products differ with respect to their pattern and distribution (Figure 13). Rrp6 generates RNA products that range in size between 49 nt and 20 nt as early as 0.5 minutes while Exo10⁶ produces intermediates that cluster closer together for

both AU-rich and polyA RNA substrates (Figures 13A, 13B; Figure 12D). Rrp6^{exo-} and Exo10^{6exo-} bind AU-rich RNA with similar affinities (23 nM and 19 nM, respectively), but Rrp6^{exo-} binds polyA RNA 13-fold better than Exo10^{6exo-} (121 nM and 1619 nM, respectively) (Figure 13B; Table 5). Taken together, RNase and binding data for Rrp44, Rrp6, Exo10⁴⁴ and Exo10⁶ suggest that the non-catalytic Exo9 core modulates Rrp44 and Rrp6 exoribonuclease and Rrp44 endoribonuclease activities, especially for polyA, and that defects in RNase activity can be explained in large part by a diminished capacity to bind RNA.

1.3 Rrp6 and Rrp44 activities in the eleven-subunit exosome

Rrp6 and Rrp44 activities were assessed next in the context of the eleven-subunit exosome (Exo11^{44/6}). The presence of Rrp44 does not noticeably alter Rrp6 activities (Figure 13), but Rrp6 confers a 7-fold or 43-fold increase in Rrp44 exoribonuclease activity compared to Exo10⁴⁴ using AU-rich or polyA RNA, respectively (Figures 10A, 10B). This is not due to Rrp6 generating additional RNA substrates for Rrp44 as Rrp6^{exo-} is also able to stimulate Rrp44 in Exo11^{44/6}. In agreement with these biochemical trends, the K_d for polyA RNA is the lowest when all eleven components are present in Exo11^{44/6} (Figure 10B).

The initial rates of RNA decay and intermediate patterns generated by endonuclease activity in Exo11^{44exo-/6exo-} are similar to Exo10^{44exo-}; however, degradation products are reduced to smaller sizes more quickly for the AU-rich RNA for Exo11^{44exo-/6exo-} (Figure 10C). The stimulatory effect of having Rrp6 in the complex is more evident for polyA RNA when comparing initial rates and products as Exo11^{44exo-/6exo-} is 28-fold more active than Exo10^{44exo-} (Figure 10D). Furthermore, the distributive pattern of intermediates generated by Rrp44^{exo-} with polyA RNA is compressed in reactions with

Exo11^{44exo-/6exo-}, more closely resembling the pattern and accumulation of 23-26 nt intermediates generated by Exo10^{44exo-} and Exo11^{44exo-/6exo-} with AU-rich RNA. These data suggest that Rrp6 stimulates both Rrp44 endo- and exoribonuclease activities within the context of Exo11^{44/6}.

Differences are not detected for Rrp6 activity in Exo11^{44/6} when compared to Exo10⁶ but it is noteworthy that Rrp6 is inhibited 100-fold in Exo11^{44exo-/6} (Figure 13). This suggests that RNA binding to Rrp44^{exo-} in Exo11^{44exo-/6} precludes Rrp6 from accessing RNA despite a 10-fold excess of RNA substrate in these reactions. These data also suggest that apparent K_d values for Exo11^{44exo-/6exo-} (23 nM for AU-rich and 103 nM for polyA) report on RNA binding to Rrp44 rather than Rrp6 (Table 5). Why does Rrp44 outcompete Rrp6 for binding? I believe this is likely due to differences in catalytic mechanism between Rrp44, a processive enzyme that binds and holds onto the substrate until it is completely degraded, and Rrp6, a distributive enzyme that catalyzes successive rounds of degradation and product release during decay. Data presented thus far suggests that Exo9 modulates RNA binding and RNase activities of both Rrp6 and Rrp44, albeit to differing extents. Furthermore, exosome-associated activities of Rrp6 and Rrp44 appear interdependent because Rrp6 confers a gain of function on Rrp44 activities and Rrp44^{exo-} severely inhibits Rrp6 activity in Exo11^{44exo-/6}.

1.4 RNA-protein interactions in exosomes containing Rrp6 and Rrp44

To identify exosome subunits that contact RNA I employed UV cross-linking in reactions containing Rrp6^{exo-} or Rrp44^{exo-} and their respective complexes with Exo9. It is worth noting that appearance of UV cross-linked species only suggests and by no means proves that interactions are on pathway to a productive substrate/enzyme complex. UV cross-linking efficiency was enhanced by using AU-rich RNA, and protein-RNA adducts were resolved by SDS-PAGE. The identities of core subunits were determined by reconstituting exosomes containing unique combinations of N-terminal hexa-histidine tagged subunits to generate tag-dependent mobility shifts of RNA-protein adducts upon UV-crosslinking (Figure 14).

Very weak cross-linking is observed for Exo9 (Figure 15), consistent with fluorescence polarization data (Figure 11) and RNase foot-printing²⁵ that fail to detect a specific RNA bound complex. In contrast, UV cross-linking produces several protein-RNA adducts unique to Exo10^{44exo-}, Exo10^{6exo-} and Exo11^{44exo-/6exo-} (Figure 15). Specifically, adducts are observed to Rrp44^{exo-}, the S1/KH cap proteins (Csl4, Rrp4, and Rrp40) and half of the six PH-like proteins (Rrp43, Rrp45, and Rrp41) using Exo10^{44exo-}. Adducts are observed to Rrp6^{exo-} and more weakly to the S1/KH cap proteins and to lesser extent Rrp41 using Exo10^{6exo-}. Cross-linking patterns of Exo11^{44exo-/6exo-} are similar to Exo10^{44exo-}, namely adducts are observed to Rrp44^{exo-} and the respective Exo9 subunits with only minimal cross-linking to Rrp6^{exo-}. The observation that Rrp44^{exo-} inhibits RNA cross-linking to Rrp6^{exo-} in Exo11^{44exo-/6exo-} and Rrp6 catalytic activity in Exo11^{44exo-/6}, suggests that RNA, when bound to Rrp44^{exo-}, blocks a path used by RNA to engage Rrp6 in respective Exo11^{44/6} complexes. Because UV cross-linking to the S1/KH-proteins is observed in Exo10^{44exo-}, Exo10^{6exo-} and Exo11^{44exo-/6exo-}, and since UV

cross-linking to the RNase PH-like proteins is only observed in Exo10^{44exo-} and Exo11^{44exo-/6exo-}. I posit that RNA enters a channel formed by the S1/KH cap proteins on its way to Rrp6 or Rrp44 and that RNA passes through or by the RNase PH-like ring to engage Rrp44.

1.5 The exosome central channel is essential in vivo

Previous in vitro studies indicated that Rrp44 exoribonuclease activity was compromised when Rrp44 was incubated in the presence of exosome cores that contained channel-lining charge-swap mutations in the PH-like protein Rrp41 (Ref. 25). Consistent with earlier complementation assays that incorporated three channel-lining point mutations¹⁸, I observe no growth phenotype for charge-swap point mutations in Rrp41 in vivo (Figure 16A). If the central channel plays an important role in exosome function one might expect phenotypes such as growth defects and aberrant RNA processing as observed in strains lacking *RRP6* or in strains harboring a mutation in the Rrp44 exoribonuclease active site^{18,32,103}. These apparent discrepancies suggest that interior channel surfaces are not important, that RNA can bypass the central channel to engage Rrp44 or Rrp6, or that mutations on the channel surface are not sufficient to physically occlude the channel in vivo.

To physically and electrostatically occlude the channel that is formed by the PH-like ring I constructed insertions based on the structure of human Exo9 (Ref. 17) in two loops that project into the channel. Insertions include acidic side chains and range between 2 (EL), 7 (ELGESEG) and 11 (ELGESEGESEG) amino acid residues. I refer to these insertions as Small [S], Medium [M], and Large [L] and rough calculations suggest they could project into the channel by 3.5 Å, 9 Å and 15 Å, respectively. Given the dimensions of the RNA exosome central channel and position of the loops I posit that

the flexible, extended loops in Rrp41 and Rrp45 would pose steric impediments to RNAs entering near the top and middle of the PH-like ring, respectively (Figure 17A).

The *rrp41* or *rrp45* alleles containing S, M, or L insertions were assessed in complementation assays in *S. cerevisiae* using *rrp41Δ*, *rrp45Δ*, and *rrp41Δrrp45Δ* strains (Figure 17B). While S and M insertions had little impact on growth in isogenic *rrp41Δ* and *rrp45Δ* strains, L insertions in *rrp41* or *rrp45* (*rrp41-L* or *rrp45-L*) resulted in a severe temperature sensitive growth defect or lethality, respectively (Figure 16B). In the *rrp41Δrrp45Δ* strain, *rrp41-S/rrp45-M* exhibited a slight growth defect at 37°C, while *rrp41-M/rrp45-S* grew slowly at 30°C and 37°C. Although individual *rrp41-M* and *rrp45-M* mutants had no discernable growth phenotype in *rrp41Δrrp45Δ*, combining these alleles resulted in synthetic lethality at all temperatures tested. TAP-purification of Rrp44 from the viable *rrp41-M/rrp45-S* strain confirms that channel occluded exosomes remain associated in vivo (Figure 16C). These results suggest that mutations predicted to physically occlude the central channel fail to support the essential functions of the RNA exosome in vivo.

1.6 Channel occluding mutations inhibit Rrp44 and Rrp6 activities in vitro

Our data suggest that Exo9 modulates Rrp44 and Rrp6 RNase activities, and binding and cross-linking data suggest that RNAs interact with and potentially pass through the S1/KH-protein ring to access Rrp6 and through the S1/KH-protein and PH-like ring to access Rrp44. To test this model I combined medium length insertions (Rrp41-M/Rrp45-M) to reconstitute Exo11^{44/6/channel-} because this combination failed to complement the essential functions of the exosome in vivo (Figure 16B). Exo11^{44/6/channel-} behaves similarly in vitro to Exo11^{44/6} during reconstitution and purification suggesting that loop insertions do not interfere with exosome assembly (Figure 16D).

Rrp44 exoribonuclease activity on AU-rich and polyA RNA is inhibited 45-fold and 100-fold, respectively, by channel occlusion in Exo11^{44/6/channel-} relative to WT Exo11^{44/6} (Rrp41-WT/Rrp45-WT) (Figures 18A, 18B; Figure 19A). This effect is independent of Rrp6, as I observe similar trends in Exo10⁴⁴ (Figure 19B). Occluding the channel also diminishes Rrp44 endonuclease activities in Exo11^{44exo-/6exo-/channel-} by 20-fold on polyA in comparison to Exo11^{44exo-/6exo-} (Figures 18A, 18B), a defect that is further exacerbated using exosomes reconstituted with large insertions in both Rrp41 and Rrp45 (Figure 19D).

If the central channel is used to guide RNA to Rrp44 then channel occlusion in the PH-like ring should impair RNA binding and UV cross-linking and this is exactly what is observed. Binding assays confirm that Exo10^{44exo-/channel-} is >100-fold less able to interact with AU-rich RNA (Figure 18A) while binding to polyA RNA is further weakened to nearly undetectable levels compared to Exo10^{44exo-} (Figure 18B; Figure 11). Consistent with binding data, UV cross-linking patterns to Exo9 are weakened further when its channel is occluded and RNA adducts to Rrp44^{exo-} and Exo9 are greatly

diminished in Exo10^{44exo-/channel-} relative to Exo10^{44exo-} although some cross-linking to Rrp41 and Rrp44^{exo-} is still observed (Figure 18C).

Channel occlusion in the PH-like ring was not predicted to impact Rrp6 to the same degree as Rrp44 because strong cross-linking was not observed to PH-like ring subunits in Exo10^{6exo-}; however I observe that PH-ring channel occlusion attenuates Rrp6 activity in Exo11^{44/6/channel-}, particularly with the polyA RNA, resulting in a relatively modest 5-fold reduction in initial rate relative to Exo11^{44/6} (Figure 18B). Perhaps more interesting is that PH-ring channel occlusion prevents Rrp6 from stimulating Rrp44 activities in Exo11^{44/6} and partially alleviates Rrp6 inhibition by Rrp44^{exo-} as evidenced by comparing activities of Exo11^{44exo-/6}, Exo11^{44exo-/6/channel-} and Exo11^{44/6/channel-} (Figure 18A; Figure 19A). Similar changes in activities were observed for Exo10^{6/channel-} (Figure 19B).

Consistent with inhibition of Rrp6 RNase activities in Exo10^{6/channel-}, Exo10^{6exo-/channel-} binds AU-rich and polyA RNAs 10- and 40-fold less well, respectively, compared to Exo10^{6exo-} (Figures 18A, 18B) and exhibits slightly diminished cross-linking patterns to the S1/KH cap proteins, Rrp41 and Rrp6^{exo-} (Figure 18C). Similarly, channel occlusion in Exo11^{44exo-/6exo-/channel-} attenuates binding to AU-rich and polyA RNA by 20- and 50-fold, respectively, relative to Exo11^{44exo-/6exo-} (Figure 18A). While cross-linking is diminished to PH-like ring subunits and Rrp44^{exo-} (Figure 18C) it is interesting that cross-linking is enhanced to Rrp6^{exo-} in Exo11^{44exo-/6exo-/channel-} compared to Exo11^{44exo-/6exo-}. Because PH-like ring channel occlusion inhibits RNA from gaining access to Rrp44 and partially alleviates inhibition of Rrp6 activity in exosomes containing Rrp44^{exo-}, this cross-linking pattern is consistent with PH-like ring channel occlusion diverting RNA to Rrp6. This also suggests that RNA binding to Exo11^{44exo-/6exo-/channel-} reports on RNA interactions with the S1/KH-proteins and Rrp6^{exo-} because apparent K_d values are similar to those measured for Exo10^{6exo-/channel-} (Table 5).

If RNA passes by or through the S1/KH cap and PH-like rings to engage Rrp44, and by or through the S1/KH cap and top portion of the PH-like ring to bind Rrp6, I might expect that a larger insertion at the top of the PH-ring would impact Rrp6 more than a large insertion in the middle of the PH-ring. As predicted, Rrp6 activity is diminished 4-fold further in an Exo11^{44/6/channel-} variant that contains a large insertion near the top of the channel (Rrp41-L) compared to one where a large insertion is placed in the middle (Rrp45-L) (Figure 20A). Furthermore, UV cross-linking patterns between RNA, the S1/KH cap proteins and Rrp6 is enhanced slightly in Exo10^{6exo-} complexes containing a large insertion in the middle of the channel, rather than the top (Figure 21A). Importantly, Rrp44 activity is similarly inhibited independent of insertion placement (Figure 20A).

To test this model by other means I took advantage of the observation that Rrp6 is potentially inhibited (100-fold) in Exo11 complexes containing Rrp44^{exo-} when a 49 nt AU-rich RNA is used (Figure 13A). The human Exo9 channel extends 125 Å and is long enough to accommodate approximately 30 nts of single stranded RNA if extended (~4 Å per base; Figure 17A). Based on a model of Rrp44 bound to Rrp41/Rrp45 (Ref. 25) and the observation that at least 9 nts are required for binding to Rrp44^{exo-} (Ref. 42), I posit that Rrp6 is inhibited when a 49 nt RNA substrate is bound to Exo11^{44exo-/6} because the RNA is long enough to span the entirety of the channel through the S1/KH and PH-like rings thereby competing with the portion of the S1/KH ring channel that is required by Rrp6. If true, competing 23-30 nt single-stranded RNAs should bind Rrp44^{exo-} (9 nt) and engage the PH-like ring (14-23 nt). Because these RNAs are too short to reach the S1/KH ring channel, they should mimic PH-like ring channel occlusion in Exo11^{44exo-/6} and alleviate inhibition of Rrp6 (Figure 17A). I tested this by incubating Exo11^{44exo-/6} and Exo11^{44exo-/6/channel-} with unlabeled AU-rich RNAs of 10, 17, 21, 24, 28, 32, 36, and 49 nts and then challenged these mixtures with 5' labeled 49 nt AU-rich RNA. Indeed, Rrp6

inhibition is alleviated in *Exo11^{44exo-/6}* in a manner dependent on RNA length – 17 and 21 nt RNAs partially restore Rrp6 activity while 24 and 28 nt RNAs mimic PH-like ring channel occlusion by loop insertions. Further increase in RNA length beyond 32 nt recapitulates Rrp6 inhibition (Figure 20B). This effect is mediated by RNA binding to Rrp44^{exo-} and the PH-like ring central channel because competing RNAs have no discernable effect on Rrp6 activity when assayed with *Exo11^{44exo-/6/channel-}* (Figure 20B). It is worth noting that inhibition is only partially alleviated by the 10 nt RNA, an RNA too short to simultaneously bind Rrp44^{exo-} and engage the PH-like ring channel.

1.7 Functional consequences of channel occlusion in vivo

The data presented thus far suggest that the central channel mediates RNA decay because channel occluding mutations inhibit RNA binding and RNase activities in vitro and fail to complement the essential functions of the exosome in vivo. To test if partial occlusion of the central channel alters exosome functions in viable strains containing *rrp41-S/rrp45-M* and *rrp41-M/rrp45-S*, I analyzed the abundance of several RNA substrates previously identified as exosome substrates by quantitative PCR and compared them to strains containing *RRP41-WT/RRP45-WT* or lacking *RRP6*. RNA targets included a pre-ribosomal RNA, ITS2-1 (Ref. 56), the U4 snRNA^{54,55}, and several CUTs, including NEL025C⁵⁸, CUT638, and CUT273 (Ref. 107). I also analyzed the open reading frames (ORFs) APM2 and YLR356W that are located adjacent to CUT638 and CUT273, respectively (Ref. 107).

Defects could be observed for many of the substrates in *rrp41-S/rrp45-M* and *rrp41-M/rrp45-S* when compared to WT (Figure 22). The *rrp41-M/rrp45-S* strain exhibits similar deficiencies in early pre-rRNA processing and reduced levels of ITS2-1, corresponding to the 27SA₂ pre-rRNA, as observed in *rrp6Δ* and reported in previous

studies⁵⁶. While *rrp6Δ* exhibits greater defects for all but CUT638, strains including channel occlusions accumulate a 3' extended form of the U4 snRNA (3-fold), and the CUTs NEL025C (3-fold), CUT638 (5-fold) and CUT273 (4-fold) when compared to WT.

1.8 Conclusion

The results presented here underscore the importance of the Exo9 core and central channel in RNA processing and decay because Exo9 modulates the endo- and exoribonuclease activities of Rrp44 and Rrp6 because mutations that occlude the PH-ring channel inhibit Rrp44 and Rrp6 RNase activities in vitro and fail to complement essential functions of the exosome in vivo. My data suggest that RNA passes through a channel formed by the S1/KH cap and PH-like ring to reach Rrp44 because PH-like ring channel occlusion inhibits Rrp44 RNase activities, weakens binding and UV cross-linking and alleviates Rrp44^{exo-} mediated inhibition of Rrp6 with RNAs longer than 32 nt (Figures 21B, 21C). This latter observation, along with RNA binding and UV cross-linking, supports the hypothesis that RNA passes through the S1/KH ring to access Rrp6. How RNA exits the upper portion of the S1/KH channel to access Rrp6 remains unknown, but four channels that are large enough to accommodate single stranded RNA exist below the S1/KH cap and above the PH-like ring in the human Exo9 structure (Figure 17A).

Another unresolved issue is how the exosome core selects a path for RNA to Rrp6 or Rrp44 although it appears stochastic based on the two substrates used in this study, as both Rrp6 and Rrp44 activities are evident in Exo11^{44/6} (Figure 10). Once through the S1/KH and PH-like rings RNA can be directed to either the Rrp44 endoribonuclease or exoribonuclease site because unlike Rrp6, which is potently inhibited by Rrp44^{exo-}, Rrp44 endoribonuclease activity is clearly evident in exosomes containing Rrp44^{exo-}. These in vitro data are perhaps consistent with the genetic interplay

reported between endo- and exoribonuclease active sites in vivo^{32,35,103,108}. Details regarding how a particular RNA is directed down a distinct path to one or more of the three RNase activities of the nuclear exosome will remain a focus of investigation for some time.

Our studies may shed some light on genetic and functional analysis of exosome activities in strains harboring *rrp44-D551N* (*exo-*) or in strains lacking *RRP6*. The near lethal growth phenotype observed for strains harboring *rrp44-D551N* and shared RNA processing defects in *rrp44-D551N* (*exo-*) and *rrp6Δ* indicated partially overlapping functions for Rrp6 and Rrp44 in vivo¹⁸. My data suggest that strains harboring *rrp44-D551N* may also experience a partial loss of Rrp6 function because Exo11^{44exo-/6} inhibits Rrp6 activity by 100-fold over Exo11^{44/6}. With respect to Rrp6, phenotypes observed in *rrp6Δ* strains could be due in part to partial loss of Rrp44 activities since I observe that Rrp6 can stimulate Rrp44 activities in vitro, especially for polyA RNA. In support of this hypothesis, strains harboring *rrp6-D238A* (*exo-*) grow better than *rrp6Δ* and accumulate less nucleolar polyA(+) than *rrp6Δ* (Ref. 73).

Rrp44 activities are severely compromised by channel occlusion and Rrp6 is potentially inhibited by RNA bound Rrp44^{exo-} in Exo11^{44exo-/6}. These observations suggest that each active site is sequestered from solvent when associated with the exosome core. The structural basis for this remains unclear because Exo10⁴⁴ models derived from human Exo9 and *S. cerevisiae* Rrp44-Rrp41-Rrp45 structures show Rrp44 *exo-* and endoribonuclease active sites to be solvent exposed^{17,51,25}. Sequestration of catalytic activities within a chamber is a regulatory mechanism and organization shared among other RNA and protein degrading complexes as noted previously¹⁰² and my data suggest that the exosome core functions in this regard to modulate or limit access to all three identified RNase activities of the RNA exosome.

No structural models exist yet for Exo11^{44/6}, but the observation that Rrp6 can stimulate RNA binding and Rrp44 activities in Exo11^{44/6} is particularly intriguing as evidenced by the 40-fold activation in polyA degradation when comparing Exo10⁴⁴ and Exo11^{44/6}. As noted earlier, single stranded polyA differs from the AU-rich substrate because it has secondary structure that makes it more rigid compared to the more flexible AU-rich RNA. As such, I posit that polyA is more susceptible to exclusion from the central channel because it is less able to navigate through steric impediments, including those presented by loop insertions. Furthermore, my data suggest that polyA is restricted from binding and entering the central channel in Exo10⁴⁴, an effect that is alleviated by Rrp6 in Exo11^{44/6}. This suggests that Rrp6 serves to gate the channel, activate unwinding of the polyA structure and/or activate Rrp44 through some other mechanism. These features are particularly attractive as they provide opportunities to regulate the activities of the exosome through direct targeting of RNA to the central channel or by gating the channel with other RNA or RNA-protein complexes.

Insert	Vector
His ₆ -Smt3-Csl4	pRSF-Duet1
His ₆ -Smt3-Rrp4	pRSF-Duet1
His ₆ -Smt3-Rrp40	pRSF-Duet1
His ₆ -Smt3-Rrp41/Rrp45	pRSF-Duet1
His ₆ -Smt3-Rrp42/Mtr3	pRSF-Duet1
His ₆ -Smt3-Rrp46/Rrp43	pRSF-Duet1
His ₆ -Smt3-Rrp44	pSMT3-TOPO
His ₆ -Smt3-NΔ ₁₂₈ Rrp6	pSMT3-TOPO
His ₆ -Smt3-Rrp44-D551N	pSMT3-TOPO
His ₆ -Smt3-Rrp44-D551N/D171N	pSMT3-TOPO
His ₆ -Smt3-NΔ ₁₂₈ Rrp6-D238N	pSMT3-TOPO
His ₆ -Smt3-Rrp41-M/Rrp45-M	pRSF-Duet1
His ₆ -Smt3-Rrp41-L/Rrp45	pRSF-Duet1
His ₆ -Smt3-Rrp41/Rrp45-L	pRSF-Duet1

Table 1. *E. coli* expression constructs used in Chapter 1.

Cloning and expression of above constructs described in Methods and Material.

Oligo	Sequence	Reference
** scR1-1	5'-GGCAACCGTCTTTCCTCCGTCGTAAATTTGT-3'	This study
scR1-2	5'-ATCCCGGCCGCCTCCATCAC-3'	Kufel <i>et al.</i> , 2000
U4-1	5'-AAAGAATGAATATCGGTAATG-3'	Allmang <i>et al.</i> , 1999
U4-2	5'-ATCCTTATGCACGGAAATACG-3'	This study
ITS2-1	5'-AGATTAGCCGCAGTTGG-3'	Allmang <i>et al.</i> , 2000
ITS2-2	5'-AGCGTCATTTCTTCTCA-3'	This study
** NEL025C-1	5'-CGCAGAGTTCTTACCAAACG-3'	Wyers <i>et al.</i> , 2005
NEL025C-2	5'-GCAAAGATCTGTATGAAAGG-3'	Wyers <i>et al.</i> , 2005
CUT638-1	5'-TTCAAGGACTACGAAACCACAT-3'	Xu <i>et al.</i> , 2009
CUT638-2	5'-CCGGACGTCTATATCGCTAA-3'	Xu <i>et al.</i> , 2009
CUT273-1	5'-TTCTGTATCCCTAAATAACTCCCTTA-3'	Xu <i>et al.</i> , 2009
CUT273-2	5'-CCTTAAATTGGTGGGCAAGAA-3'	Xu <i>et al.</i> , 2009
APM2-1	5'-GCAGAAAGTCTCTCTTCAAATGT-3'	Xu <i>et al.</i> , 2009
APM2-2	5'-GTCGTCAAGCCTTTTTATCCT-3'	Xu <i>et al.</i> , 2009
YLR356W-1	5'-GCCGAAAAAGCTCACACAAAA-3'	Xu <i>et al.</i> , 2009
YLR356W-2	5'-GTCTGTTGTTTAGCCATCACAA-3'	Xu <i>et al.</i> , 2009

Table 2. Oligonucleotides used for qPCR

Unless otherwise indicated, Oligonucleotide 1 used for cDNA synthesis during reverse transcription. Oligonucleotides 1 and 2 used for subsequent PCR reactions.

**Oligo dT used for cDNA synthesis. Primers 1 and 2 used for PCR.

Subunits	Reconstituted Exosomes	
	<ul style="list-style-type: none"> Exo9 Exo9^{Rrp41M/Rrp45M} 	
<ul style="list-style-type: none"> Rrp44 Rrp44^{exo-} Rrp44^{exo-/endo-} 	<ul style="list-style-type: none"> Exo10⁴⁴ Exo10^{44exo-} Exo10^{44exo-/endo} Exo10^{44/Rrp41M/Rrp45M} Exo10^{44exo-/Rrp41M/Rrp45M} Exo10^{44exo-/endo-/Rrp41M/Rrp45M} Exo10^{44/Rrp41L/Rrp45WT} Exo10^{44exo-/Rrp41L/Rrp45WT} Exo10^{44/Rrp41WT/Rrp45L} Exo10^{44exo-/Rrp41WT/Rrp45L} Exo10^{44exo-/Rrp41WT/Rrp45L} 	<ul style="list-style-type: none"> Exo11^{44/6} Exo11^{44exo-/6exo-} Exo11^{44exo-/endo/6exo-} Exo11^{44/6/Rrp41M/Rrp45M} Exo11^{44exo-/6exo-/Rrp41M/Rrp45M} Exo11^{44exo-/endo/6exo-} Exo11^{44/6/Rrp41L/Rrp45WT} Exo11^{44/6/Rrp41WT/Rrp45L} Exo11^{44/6exo-} Exo11^{6exo-/Rrp41M/Rrp45M} Exo11^{44exo-} Exo11^{44exo-/Rrp41M/Rrp45M} Exo11^{44exo-/6exo-/Rrp41L/Rrp45L}
<ul style="list-style-type: none"> Rrp6 Rrp6^{exo-} 	<ul style="list-style-type: none"> Exo10⁶ Exo10^{6exo-} Exo10^{6/Rrp41M/Rrp45M} Exo10^{6exo-/Rrp41M/Rrp45M} Exo10^{6/Rrp41L/Rrp45WT} Exo10^{6exo-/Rrp41L/Rrp45WT} Exo10^{6/Rrp41L/Rrp45WT} Exo10^{6exo-/Rrp41L/Rrp45WT} 	

Table 3. Characterized Exosome Subunits and Complexes

Exosome subunits and reconstituted complexes characterized in Chapter 1.

Representative color codes used in main text are positioned to left of subunit or complex. WT or active site mutants are indicated below the respective subunit/complex. Rrp44^{exo-} corresponds to Rrp44-D551N; Rrp44^{endo-} is Rrp44-D171N; Rrp6^{exo-} is Rrp6-D238N. Exosome complexes designated as “channel-” in the main text are reconstituted with Rrp41M/Rrp45M.

	AU-rich RNA	PolyA RNA
Rrp44	0.153 +/- 0.017	0.0122 +/- 0.0004
Exo10⁴⁴	0.020 +/- 0.007	0.000289 +/- 0.000072
Exo10^{44/41M/45M}	0.00393	--
Exo10^{44/41L/45WT}	0.00450	--
Exo10^{44/41WT/45L}	0.00239	--
Exo11^{44/6}	0.133 +/- 0.007	0.0123 +/- 0.0004
Exo11^{44/6exo-}	0.290 +/- 0.018	0.0151 +/- 0.0013
Exo11^{44/6/channel-}	0.0129 +/- 0.0119	0.000134 +/- 0.000005
Exo11^{44/6exo-/channel-}	0.00635 +/- 0.00125	0.000127 +/- 0.000034
Exo11^{44/6/41L/45WT}	0.00134 +/- 0.00042	0.000254 +/- 0.000136
Exo11^{44/6/41WT/45L}	0.000635 +/- 0.000443	0.000219 +/- 0.000029

Table 4. Initial rates for Rrp44 exoribonuclease activity

Initial rates represent accumulation of final 4-5 nt product as a fraction of total substrate (49 nt RNA) during the linear range of RNA decay:

$$\text{Initial rate} = \left(\frac{\text{Product accumulated}}{\text{Total substrate RNA}} \right) \div \text{minutes}$$

Errors indicate assays conducted in triplicate and represent ± 1 standard deviation.

Blank fields indicate that rates were not determined as products were below the limit of detection.

	AU-rich RNA	PolyA RNA
Rrp44^{exo-}	34 +/- 5	320 +/- 94
Exo10^{44exo-}	108 +/- 13	*>10,000
Exo10^{44exo-endo-}	310 +/- 70	*>10,000
Exo10^{44exo-channel-}	NB	NB
Rrp6^{exo-}	23 +/- 9	121 +/- 42
Exo10^{6exo-}	19 +/- 4	1619 +/- 336
Exo10^{6exo-channel-}	214 +/- 65	*>10,000
Exo11^{44exo-/6exo-}	23 +/- 6	103 +/- 38
Exo11^{44exo-endo-/6exo-}	17 +/- 9	272 +/- 54
Exo11^{44exo-/6exo-/channel-}	212 +/- 22	4742 +/- 1122
Exo11^{44exo-endo-/6exo-/channel-}	145 +/- 13	4663 +/- 1296
Exo9	NB	NB

Table 5. Apparent K_d values

K_d values in nM for complexes described in Chapter 1.

Assays conducted in triplicate and errors represent ± 1 standard deviation

Asterisk in front of values indicates binding could not be saturated.

NB indicates no detectable binding with fluorescence polarization.

	AU-rich RNA	PolyA RNA
Rrp44^{exo-}	0.1537 +/- 0.0384	0.0717 +/- 0.0087
Exo10^{44exo-}	0.1651 +/- 0.0362	0.0054 +/- 0.0004
Exo10^{44exo-/channel-}	0.0125 +/- 0.0014	0.0045 +/- 0.0027
Exo11^{44exo-/6exo-}	0.1106 +/- 0.0103	0.1488 +/- 0.0170
Exo11^{44exo-/6exo-/channel-}	0.0222 +/- 0.0025	0.0075 +/- 0.0051

Table 6. Initial rates for Rrp44 endoribonuclease activity

Initial rates of substrate degradation represent the fraction of full-length 49 nt RNA degraded per minute during the linear range of RNA decay:

$$\text{Initial rate} = \left(\frac{(1 - \text{fraction 49nt RNA remaining})}{\text{minutes}} \right)$$

where 1 represents the fraction of full-length 49nt RNA present at time=0 minutes.

Assays conducted in triplicate and errors represent ± 1 standard deviation.

	AU-rich RNA	PolyA RNA
Rrp6	0.547 +/- 0.021	0.0231 +/- 0.0034
Exo10⁶	0.436 +/- 0.001	0.0278 +/- 0.0033
Exo10^{6/41M/45M}	0.0975	0.00279
Exo10^{6/41L/45WT}	0.0616	0.00185
Exo10^{6/41WT/45L}	0.178	0.00789
Exo11^{44/6}	0.376 +/- 0.037	0.0290 +/- 0.0016
Exo11^{44exo-6}	0.00376 +/- 0.00102	0.00266 +/- 0.00052
Exo11^{44/6/channel-}	0.0922 +/- 0.0053	0.00583 +/- 0.00024
Exo11^{44exo-6/channel-}	0.0969 +/- 0.0029	0.00616 +/- 0.00090
Exo11^{44/6/41L/45WT}	0.0609 +/- 0.0026	0.00182 +/- 0.00011
Exo11^{44/6/41WT/45L}	0.1643 +/- 0.0048	0.00748 +/- 0.00092

Table 7. Initial rates for Rrp6 exoribonuclease activity

Initial rates represent the median RNA product length as a fraction of full-length 49 nt RNA accumulated per minute during the linear range.

$$\text{Initial rate} = \left(\frac{\text{Median Product Length}}{49 \text{ nt RNA}} \right) \div \text{minutes}$$

Errors indicate assays conducted in triplicate and represent ± 1 standard deviation.

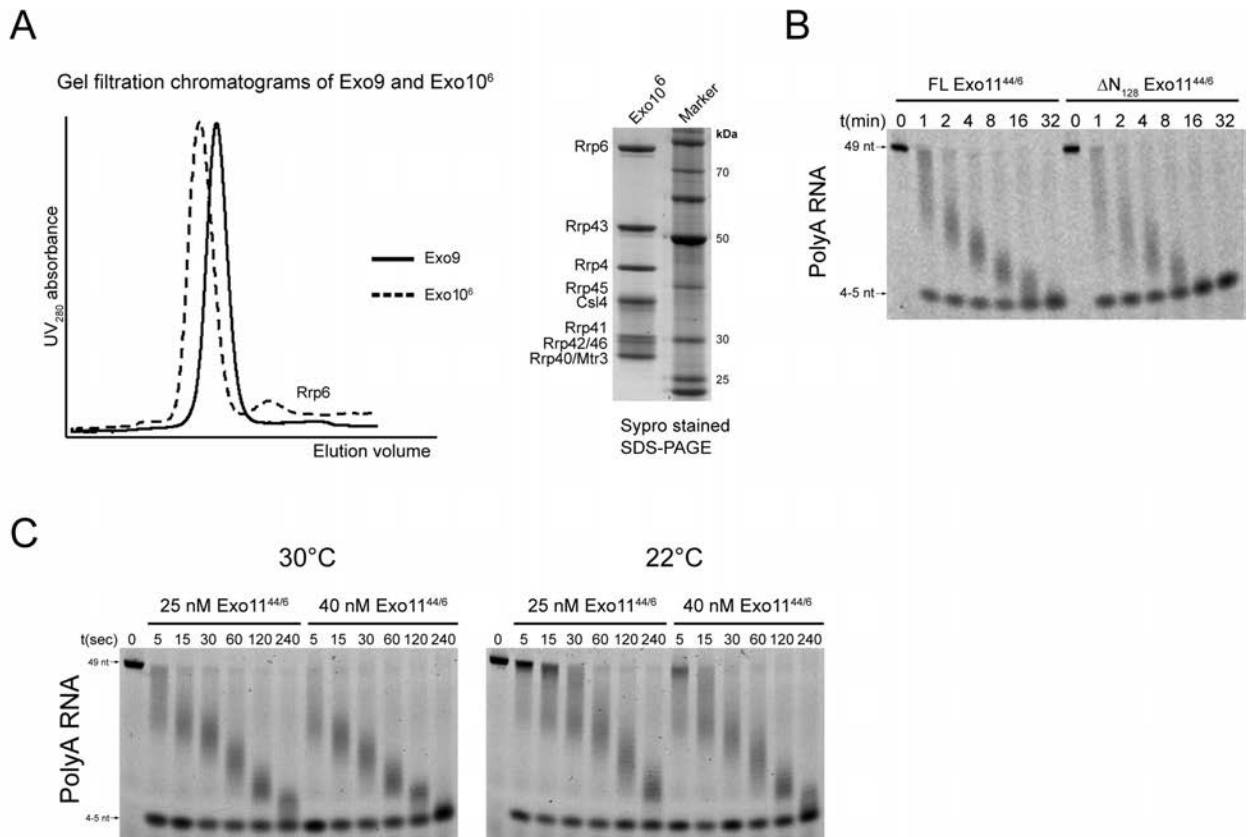


Figure 9. ΔN_{128} Rrp6 can associate with exosomes and has similar activity to full-length Rrp6.

(A) Exo10⁶, can be reconstituted as a stoichiometric particle *in vitro*. Overlay of gel-filtration traces (Superdex 200) of Exo9 (293 kDa) and Exo10⁶ (379 kDa), showing apparent size shift in Exo10⁶, indicating formation of a larger molecular weight complex (left). Sypro-stained SDS-PAGE of reconstituted Exo10⁶ after purification on Superdex 200 (right). (B) N-terminal truncation of Rrp6 does not affect its exoribonuclease activity *in vitro* in comparison to that of full-length Rrp6. RNA decay assay on 5' fluorescein PolyA RNA. (C) Single turnover conditions (enzyme excess) result in the same pattern of RNA decay as multiple turnover (substrate excess). 5nM of 5' fluorescein-labeled polyA 49 nt RNA was assayed in the presence of 25 or 40 nM Exo11^{44/6} at 30°C (left) or 22°C (right) using buffer conditions described in Methods. Reaction products were resolved by denaturing PAGE and visualized with a fluoroimager.

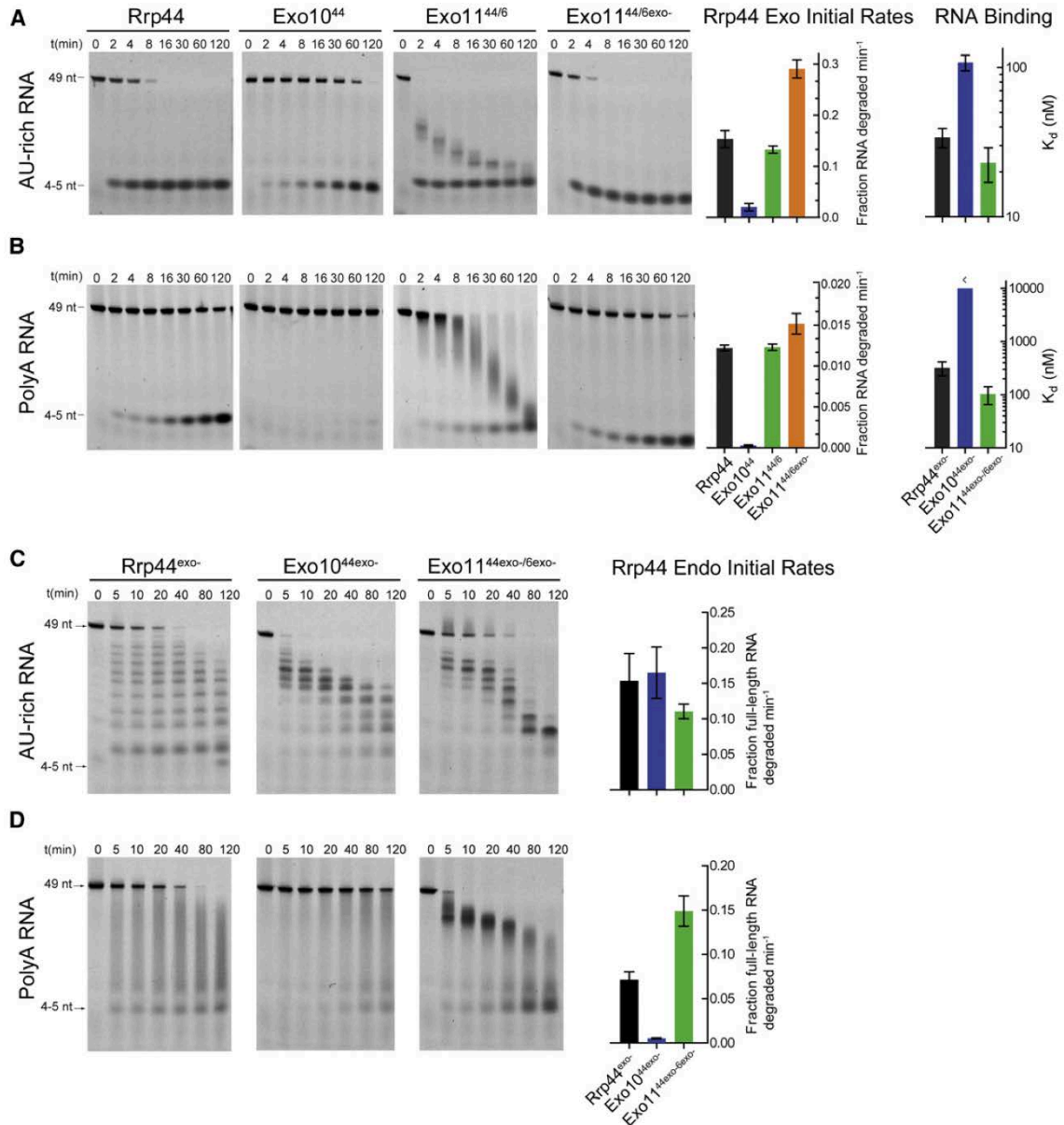
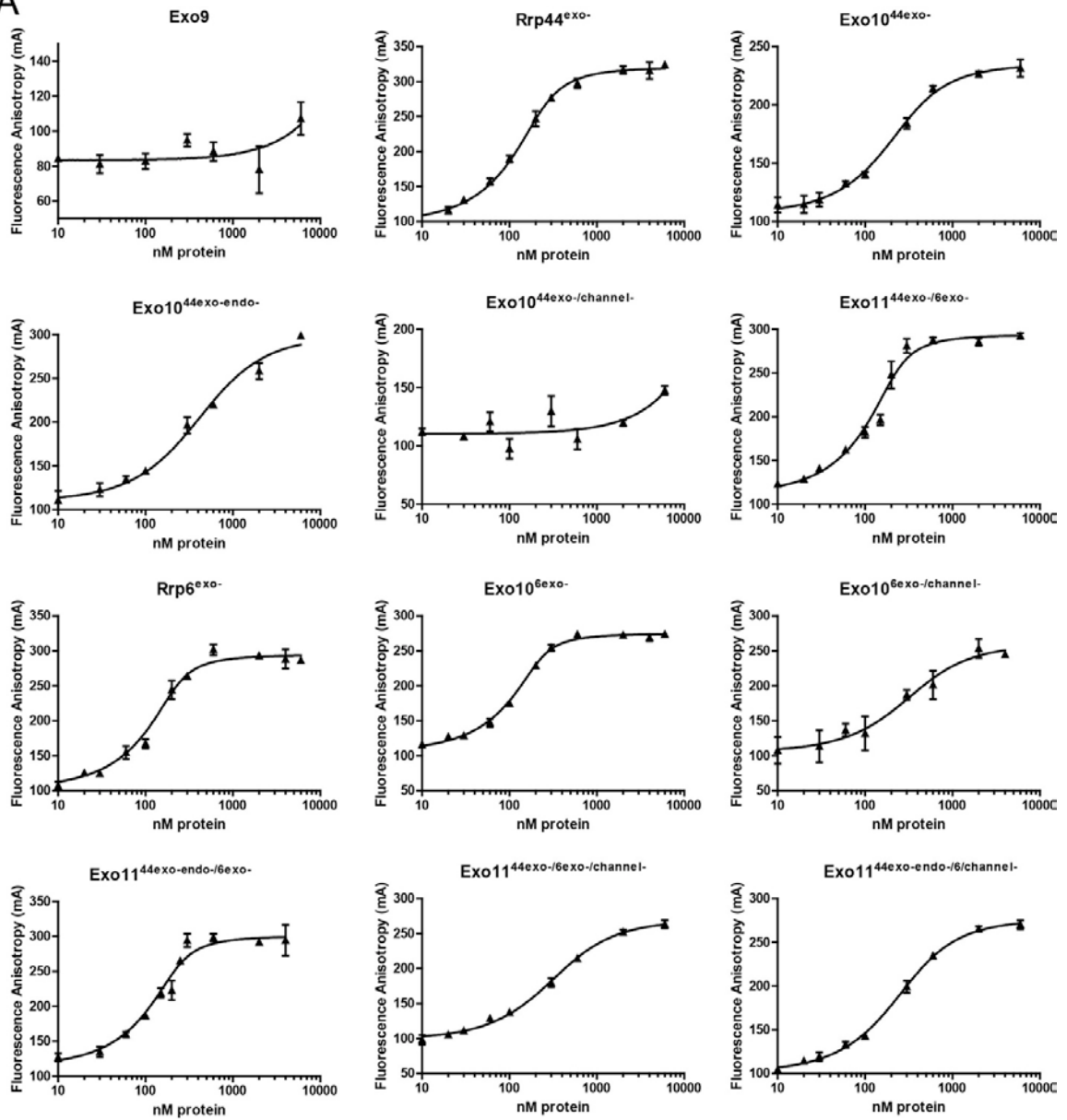


Figure 10. The Exo9 core alters exoribonuclease, endoribonuclease and RNA binding activities of Rrp44.

Association of Rrp44 with Exo9 (Exo10⁴⁴) diminishes the exoribonuclease and RNA binding activities on (A) AU-rich and (B) polyA RNAs. Rrp6 stimulates Rrp44 activity in Exo11^{44/6} independent of Rrp6 catalytic activity^{44/6}. Multiple turnover RNA decay assays performed using 5' fluorescein labeled RNAs and reaction products separated by Urea-PAGE. Representative gels and quantitation. Bar graphs depicting initial rates of Rrp44-

mediated exoribonuclease activity determined from data obtained in the linear range. Bar graphs depicting dissociation constants (K_d) were derived by fluorescence polarization of catalytically dead variants of free and Exo9 core-associated Rrp44 assayed using 5' fluorescein labeled (A) AU-rich or (B) polyA RNA. The pattern of intermediates generated by Rrp44^{exo-} changes after association with Exo9 (Exo10^{44exo-}) or Exo9 and Rrp6^{exo-} (Exo11^{44exo-/6exo-}) for (C) AU-rich and (D) polyA RNA (See Figure S3C for assays using unlabeled RNA). The distributive pattern of intermediates observed for Rrp44^{exo-} (short and long 5' labeled products accumulate simultaneously) is altered to patterns that appear to be generated 3' to 5' in Exo10^{44exo-} and Exo11^{44exo-/6exo-} for AU-rich RNA because longer 5' labeled products appear before appearance of shorter products. Exo10^{44exo-} has weaker endonuclease activity on polyA RNA but is stimulated by addition of Rrp6^{exo-} in Exo11^{44exo-/6exo-}. A stoichiometric ratio of enzymes and 5'-fluorescein RNA (10 nM) was incubated in reaction buffer in the presence of 3 mM MnCl₂ (See Methods and Materials). Error bars represent ± 1 standard deviation as calculated from three independent experiments. Bar graphs color coded according to Table 3.

A



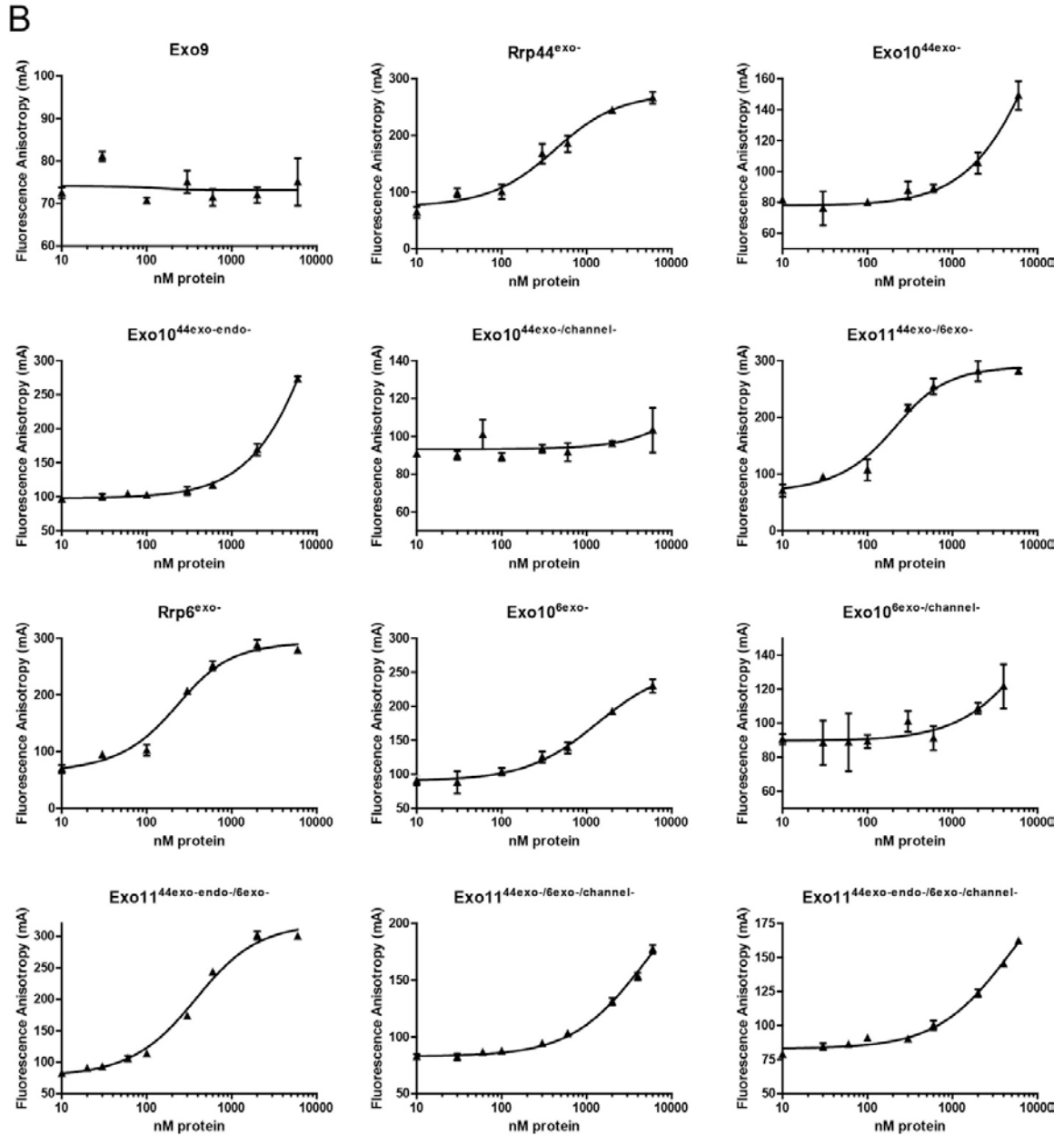


Figure 11. Experimental data used to derive apparent dissociation constants for various exosome subunits and complexes on AU-rich and PolyA RNAs.

(A) Assays on 5' fluorescein 36nt AU-rich RNA. (B) Assays on 5' fluorescein 37nt PolyA RNA. Assays conducted in triplicate. Error bars are ± 1 standard deviation. Assay conditions and data analysis are listed in Methods and Materials. Full list of apparent K_d values is found in Table 5.

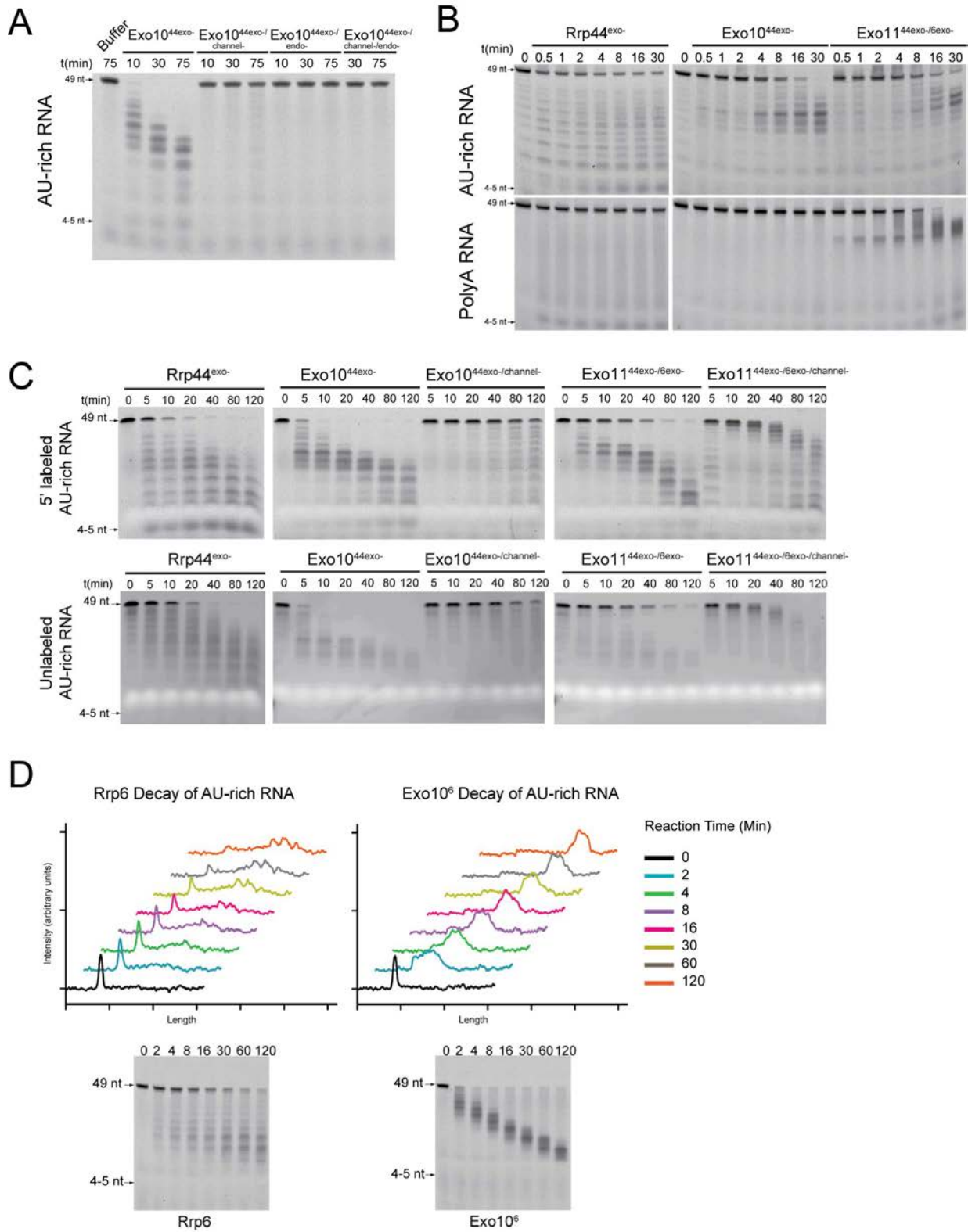


Figure 12. RNase activities associated with the exosome are modulated by the Exo9 core.

(A) Endonuclease activity is dependent on integrity of the Rrp44 PIN active site and Exo9 central channel, is modulated by association with the Exo9 core. Exo10^{exo-} displays endonuclease activity while mutating the Rrp44 PIN active site abolishes activity in Exo10^{exo-/endo-}. (B) Representative gels used to quantitate initial rates presented in Figure 1. Rrp44 endonuclease activity is stimulated by presence of Rrp6 (comparing Exo10^{44exo-} and Exo11^{44exo-/6exo-}), particularly on polyA RNA. Assays were conducted at 30°C, with 10 nM enzyme and 10 nM 5' fluorescein-labeled RNA. (C) Endoribonuclease activity of Rrp44^{exo-} displays a channel-dependent 3' to 5' directionality when associated with the exosome. RNA decay assays conducted using 100 nM 5' fluorescein labeled AU-rich 49 nt RNA, or 100 nM unlabeled AU-rich 49 nt RNA to visualize the total population of RNA intermediates. Endonuclease activity of free Rrp44^{exo-} displays differing patterns of decay on 5' labeled versus unlabeled AU-rich RNA, indicative of non-directional distributive activity. In contrast, the similar patterns obtained with 5' labeled or unlabeled RNAs suggest that the Exo9 core lends 3' to 5' directionality to Rrp44 endonuclease activity. 100 nM enzyme was used for all reactions. 5' fluorescein products detected with a fluorimeter; unlabeled RNA reaction intermediates were stained with Sybr Gold before visualization with a fluorimeter. (D) The distribution of AU-rich RNA intermediates characteristic of free Rrp6 exoribonuclease activity becomes more compact when Rrp6 associates with the Exo9 core (Exo10⁶). Representative urea-PAGE of AU-rich RNA intermediates processed by Rrp6 and Exo10⁶ (left) used to generate histogram plots (right) with ImageJ software¹⁰⁹.

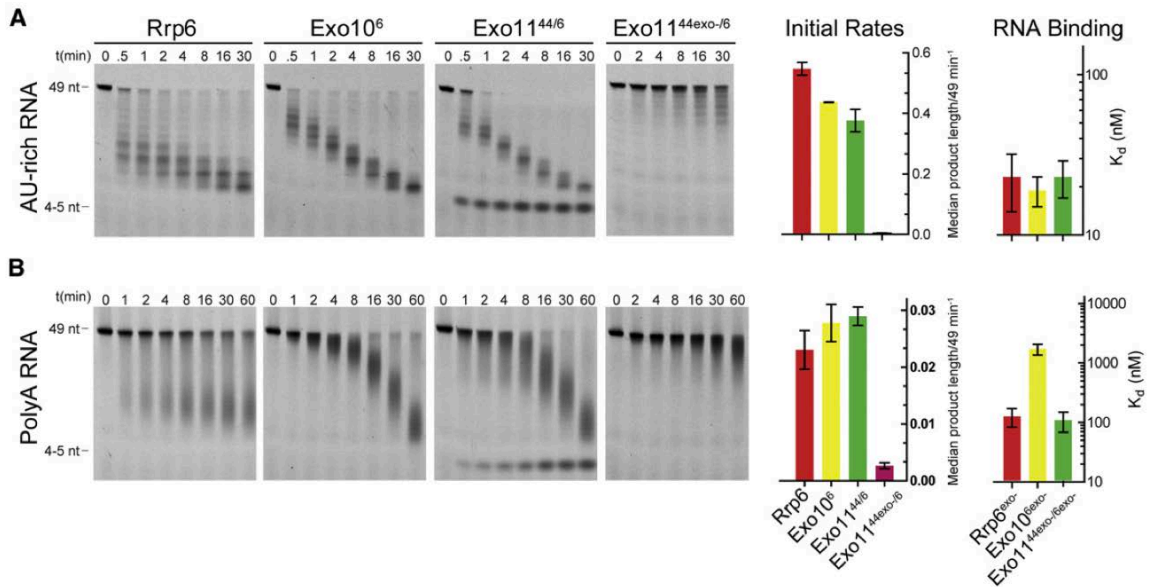


Figure 13. The Exo9 core alters Rnp6 exoribonuclease activity and RNA binding.

Association of Rnp6 with Exo9 (Exo10⁶ or Exo11^{44/6}) results in formation of a unique pattern of (A) AU-rich or (B) polyA RNA intermediates compared to Rnp6. Bar graphs representing initial rates of Rnp6-mediated exoribonuclease activity calculated by determining the median length of products generated over time and dividing the median length by substrate length (49 nt). Bar graphs depicting dissociation constants (K_d) derived by fluorescence polarization of catalytically dead variants of free and Exo9 core-associated Rnp6 using 5' fluorescein labeled (A) AU-rich or (B) polyA RNA. Error bars represent ± 1 standard deviation as calculated from three independent experiments. Bar graphs color coded according to Table 3.

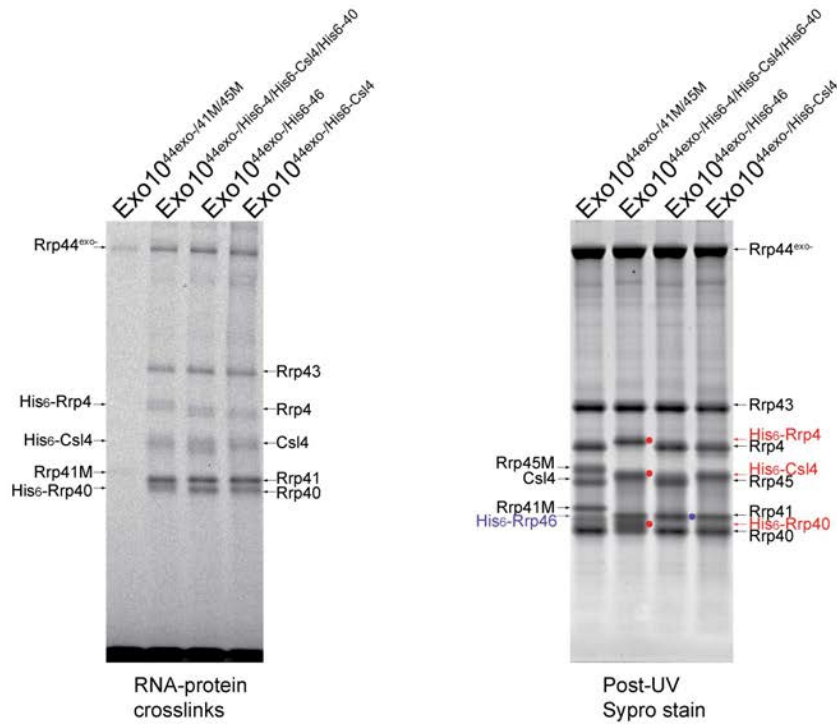
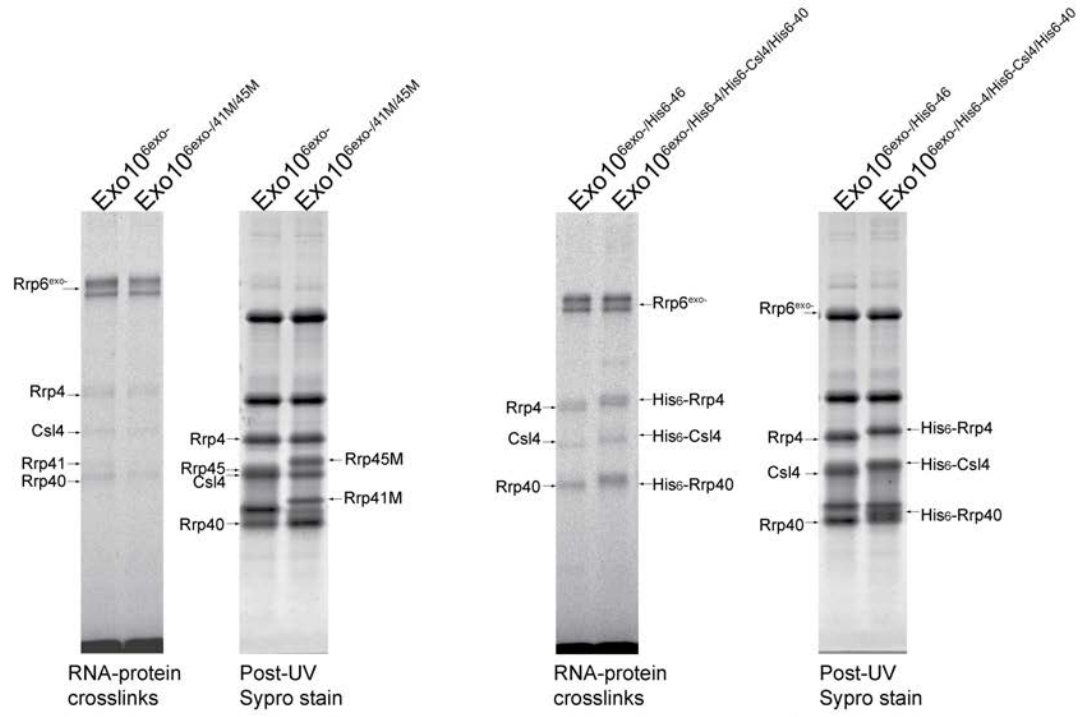


Figure 14. Exo10^{6exo-} and Exo10^{44exo-} form RNA crosslinks with the cap proteins and Rrp41 while Exo10^{44exo-} also crosslinks with the PH-like subunits in the Exo9 core.

Exosomes were reconstituted with subunits that would display a mobility shift relative to their tagless variants and analyzed by SDS-PAGE. Subunits either contained engineered loop insertions (Rrp41-M/Rrp45-M) or N-terminal His₆-tags. For Exo10^{6exo-} and Exo10^{44exo-} complexes containing His₆-Csl4, His₆-Rrp4, His₆-Rrp40, corresponding shifts in the mobilities of UV-RNA crosslinks are observed, indicating crosslinking to the tagged-subunits. Exo10^{44exo-} complexes reconstituted with Rrp41-M/Rrp45-M display a weak RNA-crosslink to Rrp41-M. Red dots indicate His₆-tagged S1/KH cap subunits; blue dots indicated the PH-like ring component, His₆-Rrp46.

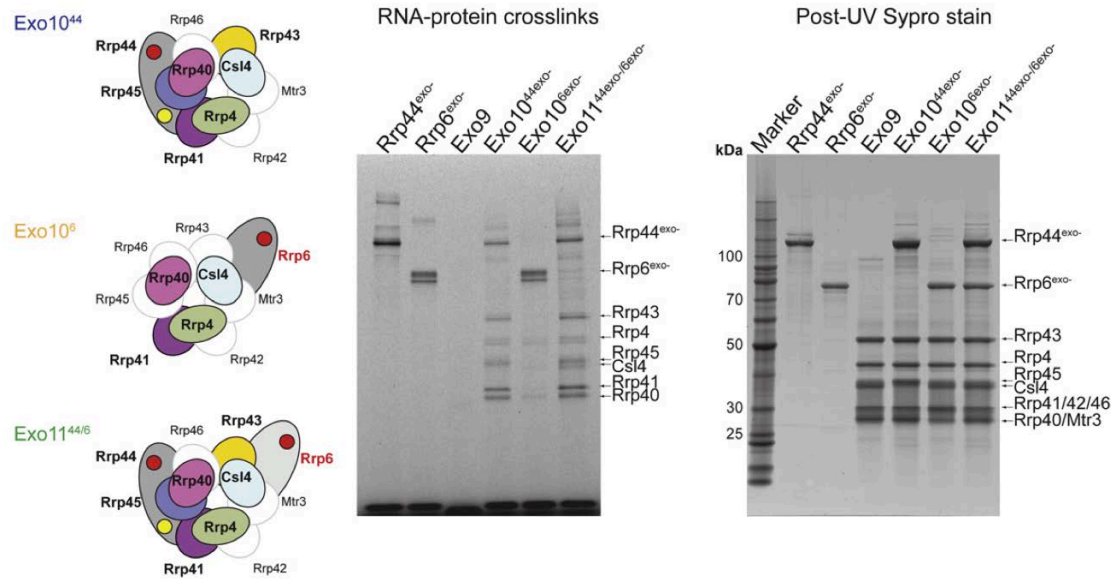


Figure 15. UV-RNA cross-linking reveals exosome-RNA contacts.

Schematics of Exo10^{44exo-} (top), Exo10^{6exo-} (middle) and Exo11^{44exo-/6exo-} (bottom) shown on left. Subunits for which no cross-linking was observed are outlined, labeled and shown in white while subunits for which RNA-protein cross-links were detected are outlined, labeled and colored. Exosome subunits and exosomes were incubated with 5' fluorescein AU-rich RNA and illuminated by UV to induce cross-linking. UV RNA-protein cross-linked products were separated by SDS-PAGE and gels were scanned to detect 5'-fluorescein RNA-protein adducts (middle), then stained with Sypro Ruby and scanned to visualize total protein (right). Subunit positions in respective gels indicated by labels and arrows. Molecular weight markers shown in left lane for the Sypro Ruby stained gel.

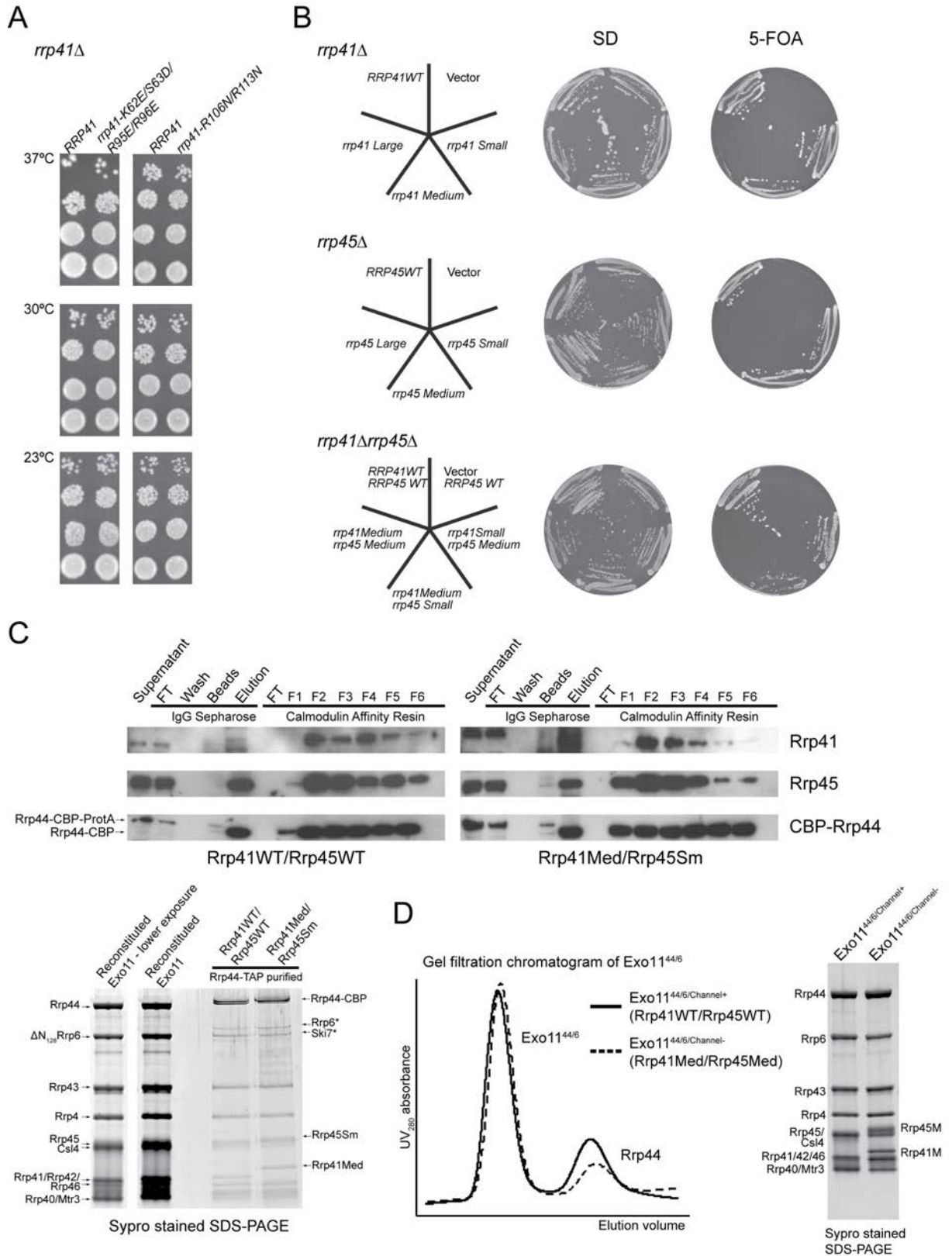


Figure 16. Channel-lining loop insertions fail to rescue the essential functions of the exosome *in vivo*, but do not interfere with exosome assembly *in vivo* or *in vitro*.

(A) Charge swap point mutations lining the exosome channel (Rrp41-K62E/S63D/R95E/R96E and Rrp41-R106N/R113N) grow similar to wild-type Rrp41 in *S. cerevisiae*. 5-FOA selected strains were spotted on YPD-agar and incubated for 3 days at 23°C, and for 2 days at 30°C and 37°C. (B) *S. cerevisiae* *rrp41Δ*, *rrp45Δ*, or *rrp41Δrrp45Δ* strains bearing Rrp41WT, Rrp45WT, or Rrp41WT/Rrp45WT plasmids, respectively, were complemented with wild-type or mutant alleles bearing various sized loop insertions and were assessed for growth at 30°C on minimal media lacking (left) or containing (right) 5-FOA. Not shown in *rrp41Δrrp45Δ* background is vector control for Rrp45/Rrp41WT, which failed to support growth on 5-FOA. (C) *S. cerevisiae* *rrp41Δrrp45Δ* strains bearing Rrp41WT/Rrp45WT, or Rrp41Med/Rrp45Sm plasmids were transformed with Rrp44-TAP plasmid and selected on 5-FOA. 12L cultures were grown in SD-Leu-His-Ura, lysed, and purified on IgG sepharose, followed by calmodulin affinity resin. Antibodies raised against Rrp41 and Rrp45, and an antibody recognizing calmodulin binding protein (CBP) were used to detect Rrp41, Rrp45, and Rrp44-CBP, respectively, by Western blot (top). Eluate from calmodulin affinity resin was resolved by SDS-PAGE, alongside reconstituted Exo11^{44/6} and stained with Sypro Ruby (bottom). (D) Channel occluded Exo11^{44/6} complexes can be reconstituted *in vitro* and behave similar to WT Exo11^{44/6} complexes. Gel-filtration overlay (Superdex 200) of Exo11^{44/6/channel+} and Exo11^{44/6/channel-} (calculated molecular weight of 493 kDa). A peak representing excess Rrp44 (114 kDa) is also present (left). Sypro Ruby-stained SDS-PAGE of reconstituted Exo11^{44/6/channel+} and Exo11^{44/6/channel-} after purification on Superdex 200 (right).

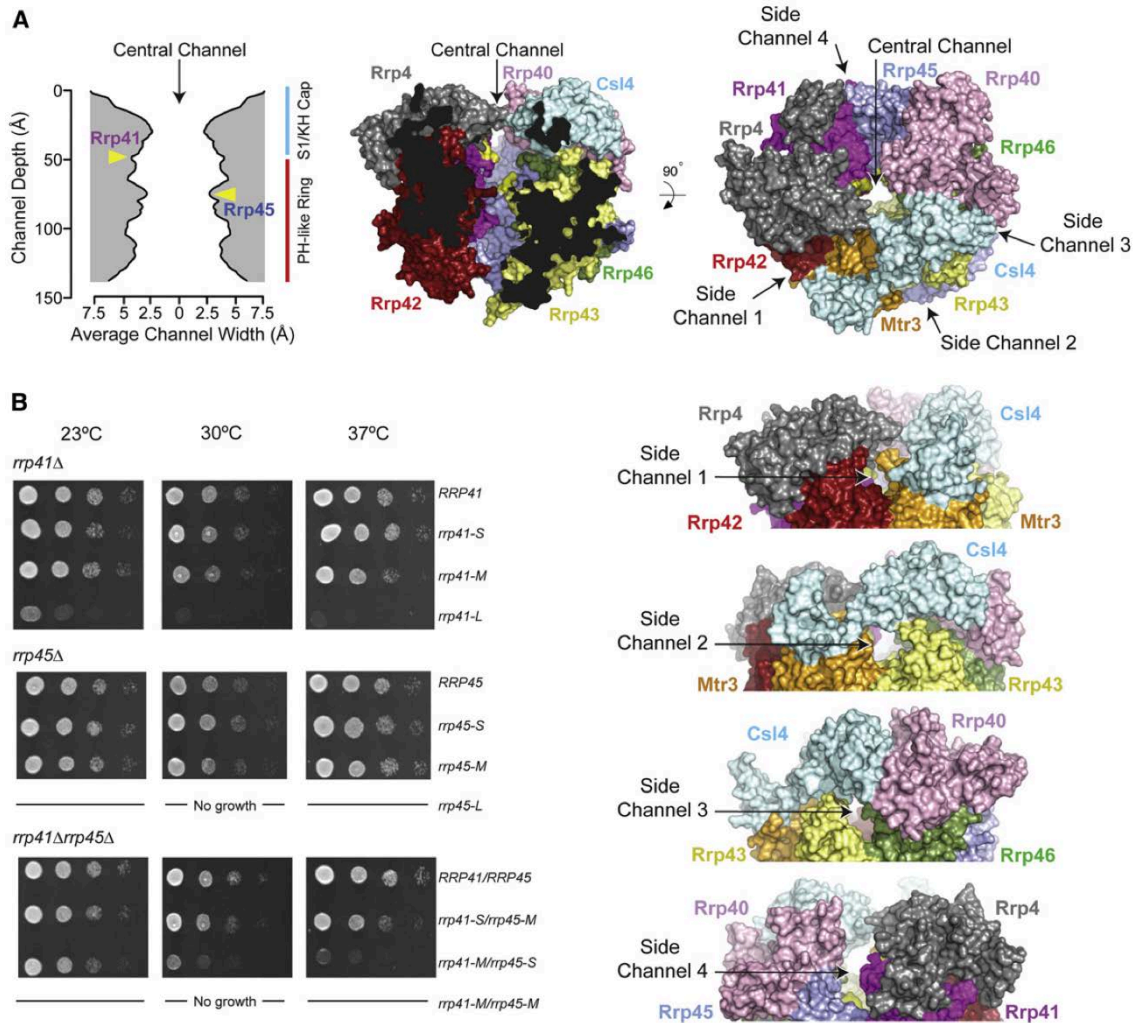


Figure 17. The exosome central channel is essential in vivo.

A) The width and dimensions of the channel (left) were calculated using the dimensional analysis program, HOLE¹¹⁰. Axes are labeled. The middle panel shows a view of the human Exo9 core (PDB 2NN6) in surface representation. The central channel is made apparent by removing Mtr3 and cutting away remaining surfaces of Csl4, Rrp43 and Rrp42. The positions of insertions in Rrp41 and Rrp45 are colored yellow in the structure and indicated by labels and yellow arrows in the graph depicting channel dimensions. Right panel depicts an orthogonal view of the Exo9 core in surface representation showing all nine subunits. A label and black arrow indicates the positions of the central

channel and four putative side channels. Subunits colored and labeled. Below this panel are four side views of the S1/KH cap and top portion of the PH-like ring highlighting four potential side channels. B) Serial 10-fold dilutions of *S. cerevisiae* *rrp41* Δ (top), *rrp45* Δ (middle) or *rrp41* Δ *rrp45* Δ (bottom) bearing *RRP41* or *RRP45* or mutant *rrp41* or *rrp45* alleles containing insertions ranging between 2 [S], 7 [M] and 11 [L] amino acids spotted on YPD agar grown at 23°C (left), 30°C (middle), and 37°C (right).

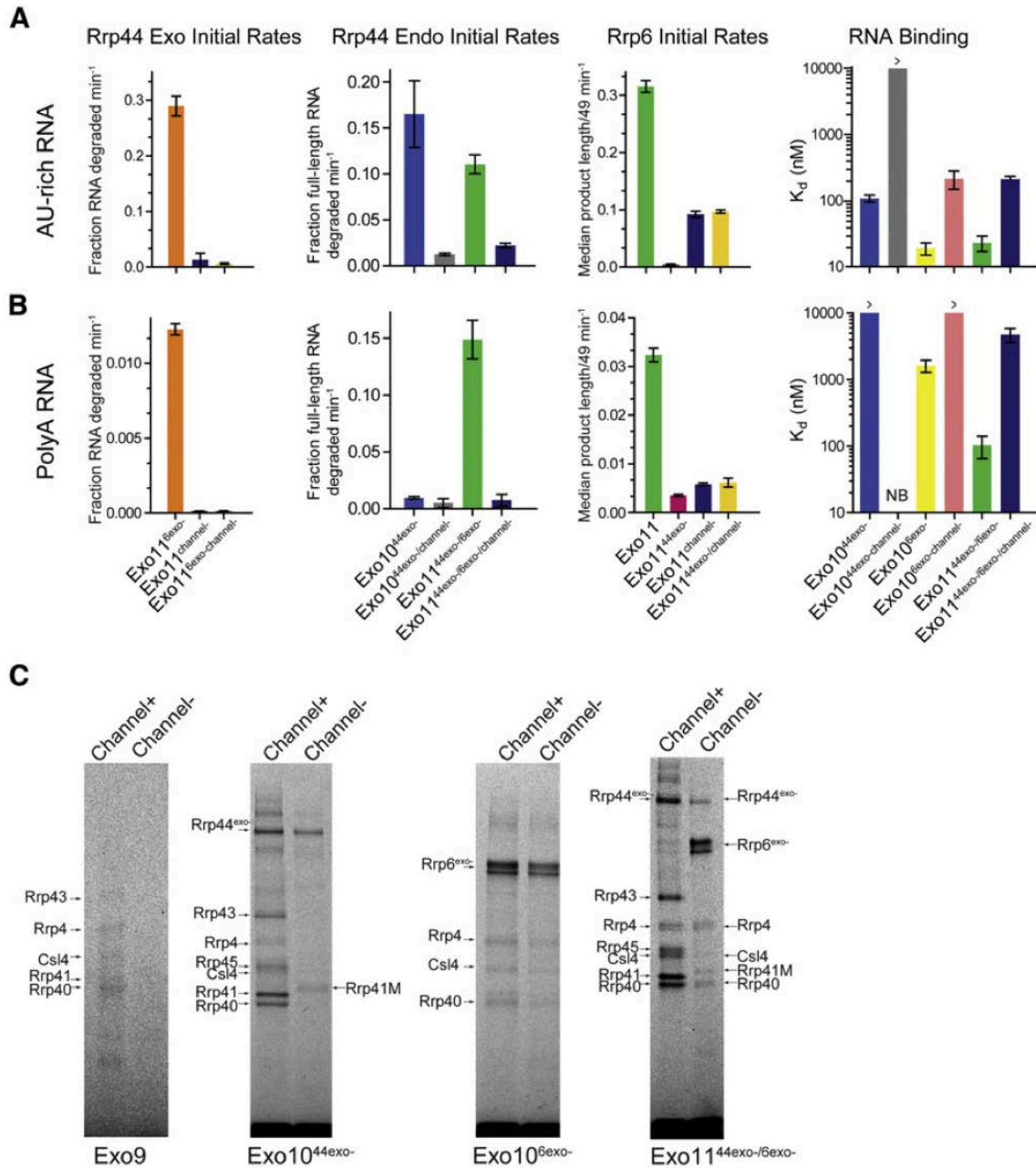


Figure 18. Channel occlusion inhibits RNA binding and RNase activities of Rrp44 and Rrp6.

Bar graphs depicting initial rates calculated for Rrp6 and Rrp44 RNase on A) AU-rich and B) polyA RNA. Occluding the central channel of Exo11^{44/6} (Exo11^{44/6}/channel⁻) with loop insertions (Rrp41-M/Rrp45-M) inhibits both Rrp44 activities while Exo11^{44exo-6}/channel⁻ diminishes Rrp6 exoribonuclease activities and alleviates Rrp6 inhibition by Rrp44^{exo-}.

Rrp44 endonuclease activities are inhibited by channel occlusion in Exo10^{44exo-} and Exo11^{44exo-/6exo-}. Assays performed in triplicate and initial rates calculated from data obtained in the linear range (Figures 19A and 19C). Bar graphs on the right depict apparent K_d values for various exosome complexes with RNA. Error bars are ± 1 standard deviation. C) Channel occlusion in Exo9 leads to diminished cross-linking (left). Panel to the right shows that channel occlusion in Exo10^{44exo-} leads to loss of most RNA-protein adducts to core subunits. Next panel shows that channel occlusion in Exo10^{6exo-} slightly weakens cross-linking to the S1/KH cap proteins and Rrp6. On the right, channel occlusion in Exo11^{44exo-/6exo-} shifts the cross-linking pattern from one involving Rrp44, the PH-like and S1/KH rings to one involving Rrp6 and the S1/KH ring. Products separated by SDS-PAGE and imaged by detecting the fluorescence of the 5' labeled AU-rich RNA. Major cross-linked species are labeled and indicated by arrows.

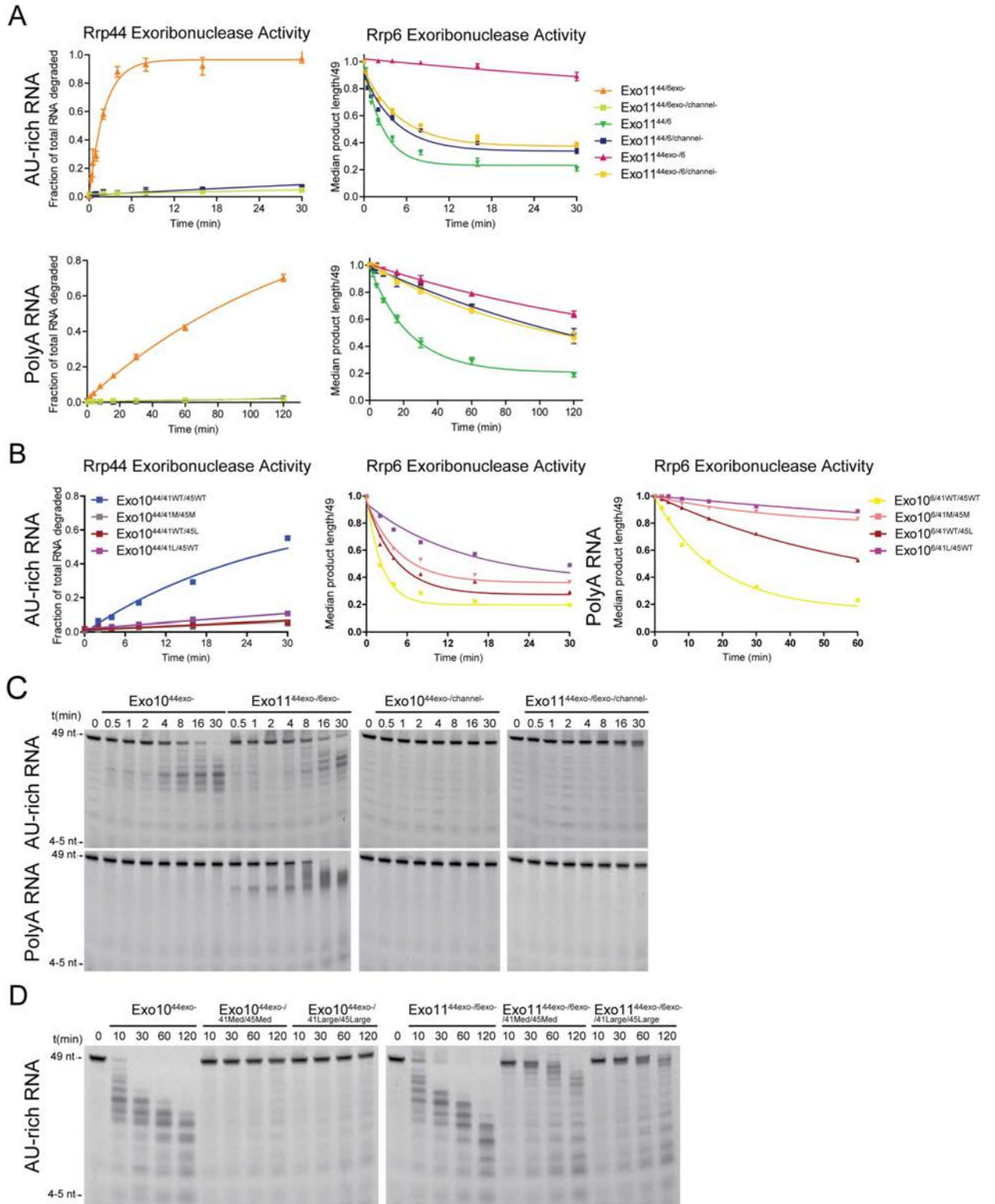


Figure 19. All three RNase activities associated with the exosome are attenuated by channel occlusion by loop insertions.

(A) Exoribonuclease assays of Exo11^{44/6} complexes used to derive initial rates of Rrp44 and Rrp6 on AU-rich and PolyA RNAs in Figures 18A and 18B, respectively. RNA decay assays were performed in triplicate under multiple turnover conditions, samples taken at indicated time points, separated on Urea-PAGE, and visualized with a fluorimager. (B) Rrp6 utilizes the top of the central channel to process RNAs while Rrp44 requires the entire channel to access and degrade RNA. Exoribonuclease assays of Exo10⁴⁴ and Exo10⁶ complexes bearing large loop insertions placed towards the top of the channel (Rrp41Large/Rrp45WT), towards the middle (Rrp41WT/Rrp45Large), or medium loop insertions engineered onto both subunits (Rrp41Medium/Rrp45Medium). Loop insertion placement equally blocks Rrp44 activity in Exo10⁴⁴ complexes, while loop insertions located towards the top of the channel (Rrp41Large/Rrp45WT) impair Rrp6 activity more than those placed towards the middle (Rrp41WT/Rrp45Large). Representative decay assays were performed on the same day with 5'-fluorescein labeled AU-rich and PolyA RNAs. (C) Rrp44 endonuclease activity is dependent on the integrity of the central channel. Representative gels used to derive initial rates of Rrp44 endonuclease activity shown in Figure 18. (D) Exo11^{44exo-/6exo-} complexes bearing large loop insertions (Rrp41Large/Rrp45) are less able to degrade 5' fluorescein labeled AU-rich RNA than complexes with smaller loop insertions (Rrp41Medium/Rrp45Medium).

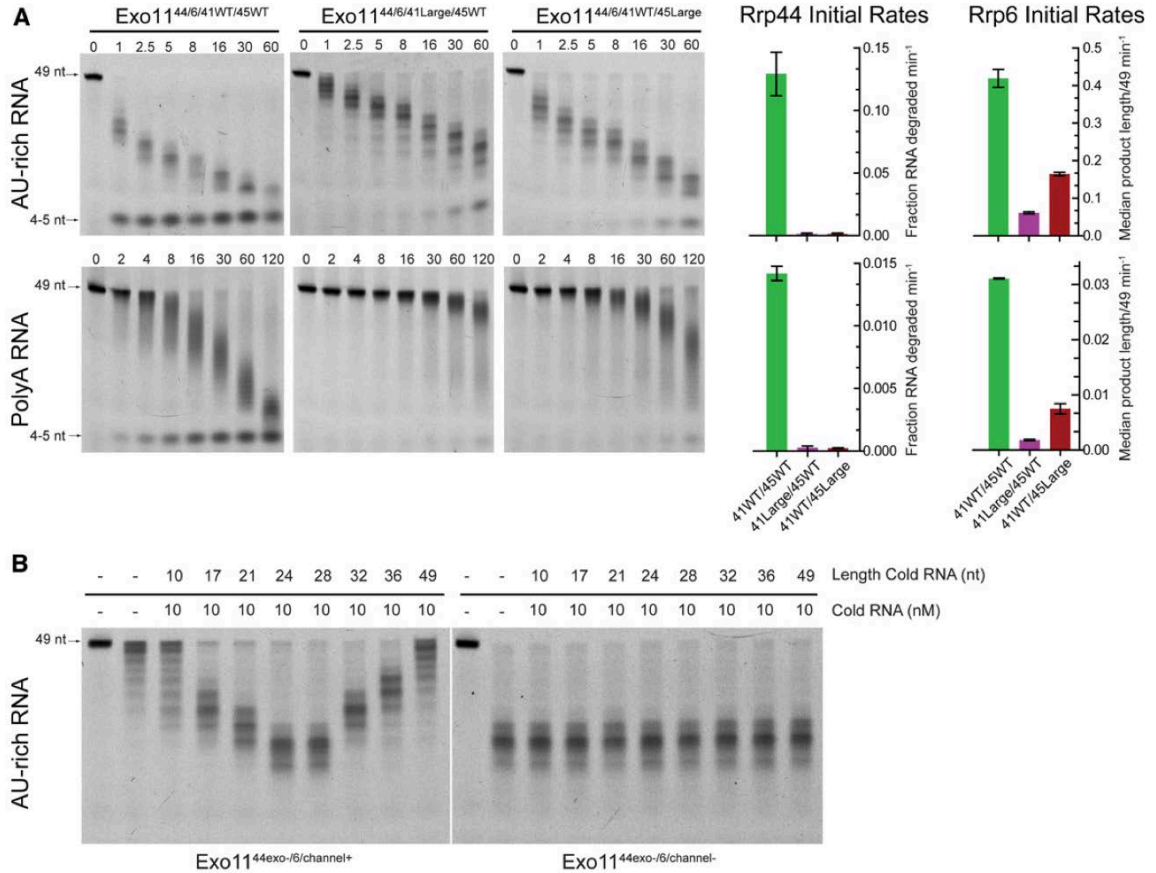


Figure 20. Rrp6 is more dependent on the upper portion of the channel to access RNA.

A) RNA decay assays using AU-rich or polyA RNA for WT exosomes and exosomes reconstituted with large loop insertions at the top (41Large) or middle (45Large) of the channel. Bar graphs on right indicate initial rates of decay mediated by Rrp44 or Rrp6. Rrp44 activity is inhibited by insertions at either position while the insertion at the top of the channel (Exo11^{44/6} 41Large/45WT) impedes Rrp6 activity more than insertion in the middle (Exo11^{44/6} 41WT/45Large). Decay assays performed in triplicate. Error bars are \pm 1 standard deviation. B) Inhibition of Rrp6 activity in Exo11^{44exo-/6} by 49 nt AU-rich RNA is alleviated by short competing RNAs that mimic channel occlusion in the PH-like ring. End point assay (15 minutes) of reactions containing 10 nM unlabeled AU-rich RNAs

(10, 17, 21, 24, 28, 32, 36, 49 nts) that were pre-incubated with 1 nM Exo11^{44exo-/6} or Exo11^{44exo-/6/channel-}. Reactions were then challenged with 10 nM 49 nt 5-fluorescein AU-rich RNA and reaction intermediates detected by denaturing PAGE. Reactions containing unlabeled 24 or 28 nt mimic channel occlusion and alleviate Rrp6 inhibition in Exo11^{44exo-/6} to similar levels observed in Exo11^{44exo-/6/channel-}.

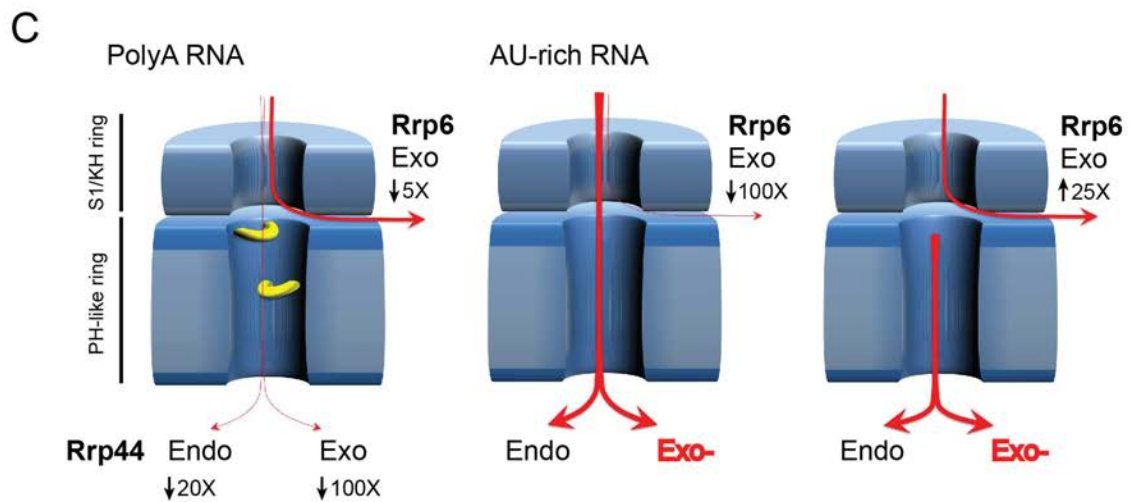
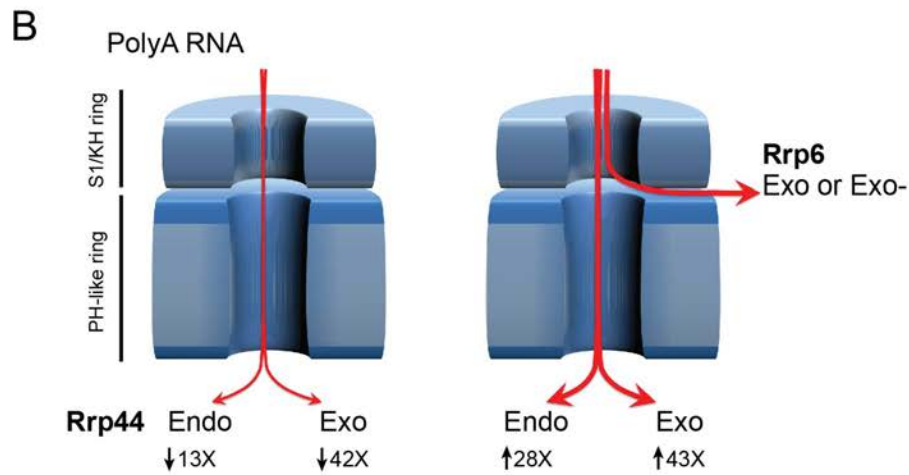
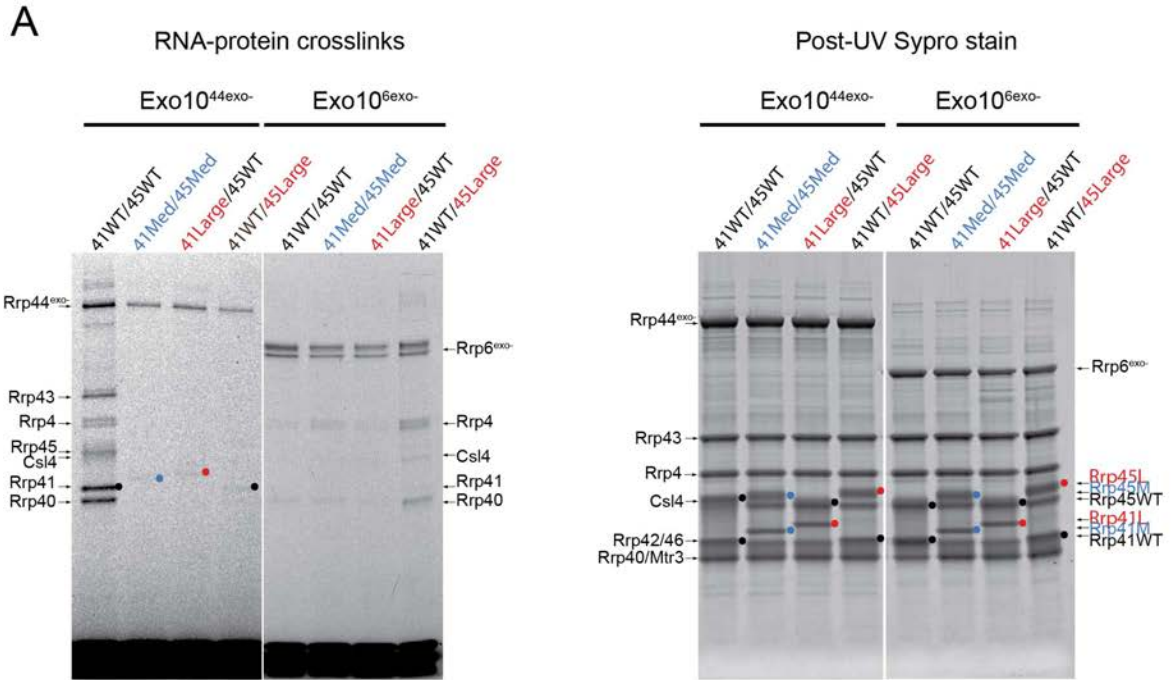


Figure 21. Loop insertions placed towards the bottom of the channel (Exo10^{6exo-} Rrp41WT/Rrp45L) enhance UV-RNA crosslinks in Exo10^{6exo-}, while insertions placed towards the top of the channel (Exo10^{6exo-} Rrp41L/Rrp45WT) attenuate UV-RNA crosslinks relative to channel open complexes.

(A) Patterns of UV-RNA crosslinks in Exo10^{44exo-} complexes do not vary with location of loop insertion placement, and RNA-protein crosslinks to core subunits and Rrp44^{exo-} are equally attenuated. Products of 5' fluorescein AU-rich RNA crosslinked to Exo10^{6exo-} and Exo10^{44exo-} by UV light were resolved by SDS-PAGE and visualized with a fluorimager (left); protein products were later stained with Sypro Ruby (right). Blue dots indicate medium insertions; red indicates large insertions; black represent WT subunits (no insertions). (B) Model of Exo9 and central channel modulation of Rrp44 and Rrp6 exo- and endonuclease activities. Association of Rrp44 with Exo9 attenuates Rrp44 endoribonuclease activity 13-fold and exoribonuclease activity 42-fold on polyA RNA, relative to free Rrp44 (left). Presence of Rrp6 in Exo11^{44/6} stimulates both Rrp44 activities 28-fold and 43-fold on polyA RNA (right). (C) Extended loops within the PH-like ring of the central channel block Rrp44 exonuclease activity 100-fold and endonuclease activity 20-fold, while attenuating Rrp6 activity 5-fold on polyA RNA (left). 49 nt AU-rich RNA bound by Rrp44^{exo-} in Exo11^{44exo-/6} extends through the entirety of the PH-like and S1/KH rings, inhibiting Rrp6 activity on AU-rich RNA 100-fold (middle). AU-rich RNAs 24-28 nts engaged by Rrp44^{exo-} in Exo11^{44exo-/6} are not long enough to bind the upper S1/KH ring, resulting in reactivation of Rrp6 by 25-fold (right).

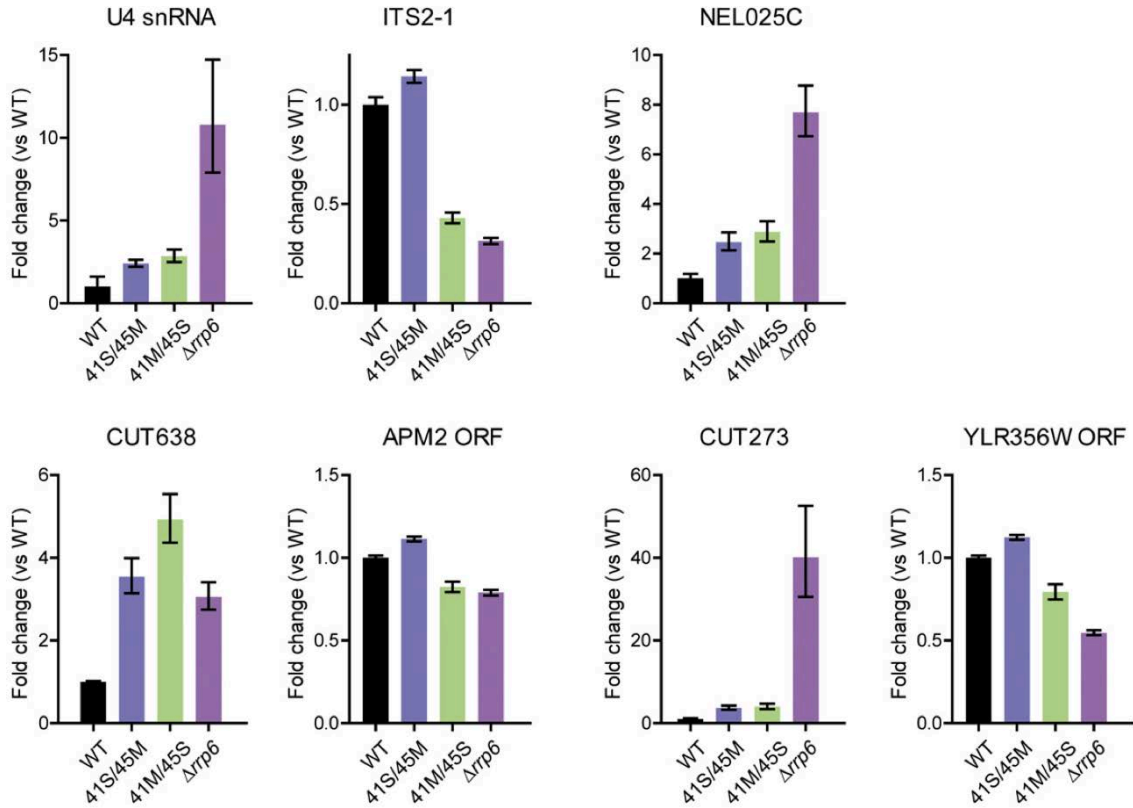


Figure 22. Channel occlusion results in aberrant RNA processing in vivo.

Previously identified substrates of the RNA exosome were analyzed by qPCR from total RNA obtained from *rrp41 Δ rrp45 Δ* strains bearing WT *RRP41/RRP45* or mutant alleles containing small/medium (*rrp41-S/rrp45-M*), and medium/small (*rrp41-M/rrp45-S*) insertions and compared to levels in an *rrp6 Δ* strain. Bar graphs show quantitation of results obtained from triplicate experiments. Error bars represent ± 1 standard deviation. Targets were normalized to *Scr1* mRNA. *APM2* and *YLR356W* ORFs serve as controls for *CUT638* and *CUT273*, respectively.

CHAPTER 2

Structure of an Rrp6-RNA Exosome Complex Bound to PolyA RNA

2.1 Introduction

The eukaryotic RNA exosome core is a large and essential nine subunit complex formed by a two-stacked ring of six RNase PH-like proteins on the bottom and three S1/KH domain “cap” proteins on the top. Exo9 associates with two catalytic subunits, the endo- and 3' to 5' processive exoribonuclease Rrp44, and the 3' to 5' distributive exoribonuclease Rrp6 (Ref. 111). In *Saccharomyces cerevisiae*, the cytoplasmic exosome includes Exo9 and Rrp44 (Exo10^{Rrp44}), the nuclear exosome contains Exo9, Rrp44 and Rrp6 (Exo11^{Rrp44/Rrp6})⁶, and a nucleolar exosome including Exo9 and Rrp6 (Exo10^{Rrp6}) has been posited in *Homo sapiens*⁷. It is thought that each exosome complex may be uniquely equipped to target different RNA substrates, in conjunction with protein cofactors, to catalyze RNA turnover, quality control, or processing within the context of their respective cellular compartments¹¹².

Rrp6 is a member of the RNase D family of exoribonucleases¹¹³, and is proposed to hydrolyze RNA via two metal ion catalysis^{47,114,115}. Its domain structure includes a N-terminal PMC2NT domain that associates with its protein cofactor Rrp47 (ref. 67), an exoribonuclease domain (EXO), a HRDC domain, and an intrinsically unstructured C-terminal domain (CTD) that associates with the Exo9 core⁹. The EXO and HRDC domains constitute the catalytic module as illustrated in crystal structures of *S. cerevisiae* and human Rrp6 (Ref. 69,70). A crystal structure of Exo10^{Rrp44+Rrp6Cterm} bound to RNA revealed how approximately 100 Rrp6 CTD residues interact with Exo9 (Ref. 52); however, no structures yet exist for Rrp6 in complex with Exo9 or RNA.

Chapter 1 proposed a model wherein Rrp44 and Rrp6 utilize an overlapping channel within the S1/KH ring to engage RNA substrates, that Rrp6 activities are modulated by Exo9 and dependent on the integrity of the central channel, and that Rrp6 can stimulate Rrp44 in binding and degradation of single-stranded RNA in the context of the nuclear exosome¹¹⁶. To determine the structural basis for these observations, I crystallized Rrp6 with Exo9 and single-stranded polyA RNA.

2.2 Global architecture of Exo10^{Rrp6}-polyA RNA

Crystals of Exo10^{Rrp6} were obtained in the presence of a 24 nucleotide single-stranded polyA RNA that included a Rrp6 construct containing residues 128-685 that lacked exoribonuclease activity (D238N)^{73,116}, the PMC2NT domain (1-127)¹¹⁶ and its last 48 C-terminal residues. Analysis of RNA in washed crystals shows partial degradation with RNA spanning 20-24 nucleotides (nt) (Figure 23D). These crystals diffracted x-rays to 3.3 Å and the structure was determined by molecular replacement (Table 8). The final model includes six nucleotides of the polyA 24mer, and two phosphate ions that likely represent the RNA backbone (Figure 23A-C).

The structure shows Rrp6 positioned atop the Exo9 S1/KH ring with Exo9 subunits resembling that determined for human Exo9 (ref. 17) and yeast Exo9 (ref. 52) in Exo10^{Rrp44+Rrp6Cterm} (Figure 24A,B). The polyA RNA is coordinated within the S1/KH ring with residues from the Rrp6 active site contacting the RNA 3' end (Figure 24C). The N-terminus of my Rrp6 construct (Met128) is in a location that would place the N-terminal PMC2NT domain of Rrp6 over the Exo9 central channel in an ideal position to interact with cofactors such as Rrp47 that presumably facilitate recruitment of substrates to the RNA exosome (Figure 24A). The Rrp6 EXO domain is wedged between and contacts both Rrp4 and Rrp40. While the Rrp6 HRDC domain is proximal to Rrp4, no direct

contacts are apparent in the structure. Consistent with previous results⁵², the Rrp6 CTD wraps around the N-terminal domain (NTD) of Csl4 and engages in interactions with the PH-like subunit, Rrp43, before reemerging near the top of the Exo9 core between the C-terminal domain of Csl4 and the NTD of Rrp40 (Figure 24A; Figure 25A,B). CTD residues 629-684 and eight residues (517-524) that link the Rrp6 HRDC domain and CTD were not observed in electron density.

The NTD of Rrp4 and the S1 domains of Rrp4 and Rrp40 comprise the interaction surface with the Rrp6 EXO domain burying approximately 2230 Å² of surface area in the complex. The interfaces between Rrp6 and the Rrp4 NTD (Region 2) and S1 domain (Region 3) form the primary contact interface (1750 Å²) while interactions with the Rrp40 S1 domain and a portion of the Rrp4 S1 domain encompass a region proximal to the RNA binding site (Region 1), surfaces that are highly conserved across evolution (Figure 26A,B). Rrp6 surfaces are less well conserved compared to Rrp4 or Rrp40, but it is notable that they are better conserved in comparison to the Rrp6 CTD, which is important for interaction with the exosome core (See below)⁵². Alignment of exosome-associated Rrp6 to the yeast Rrp6 catalytic module (EXO-HRDC) reveals few differences with the exception that residues 424-432 alter conformation, reorganizing from a loop and short hairpin in free Rrp6, to a α -helix that is proximal to a disordered loop between residues 145 and 158 from the Rrp4 S1 domain (Figure 25C). Residues 424-432 link the Rrp6 EXO and HRDC domains, are highly conserved, and were previously thought to comprise a protein interaction module⁶⁹. While extensive, the interactions between the catalytic module and Exo9 are not sufficient for Rrp6 association with the exosome. Analytical gel filtration studies show the CTD of Rrp6 is necessary and sufficient for exosome association and thus likely facilitate interactions between Exo9 and the Rrp6 catalytic modules (Figure 27).

The structure of Exo10^{Rrp6} bound to polyA RNA reveals how an RNase D family member interacts with RNA (Figure 26C). The Rrp6 catalytic domain and active site bind A₂₁A₂₂A₂₃A₂₄ with the 2'-OH and 3'-OH of the terminal A₂₄ coordinated through two main chain hydrogen bonds to the backbone amide and carbonyl oxygen of His241 and the Glu240 side chain carboxylate in a manner similar to that observed for AMP within the Rrp6 catalytic domain⁶⁹. An additional contact is observed to A₂₄ between the N7 adenine position and Gln345 side chain amide. The scissile phosphate of A₂₄ and A₂₃ is coordinated by a single magnesium ion that bridges the phosphate and the side chain carboxylate of Asn238 (Asp in the wild-type enzyme) based on positive electron density. In addition, a hydrogen bond is observed between the scissile phosphate and invariant side chain hydroxyl of Tyr361, a residue that was mutated to alanine in the yeast AMP-Rrp6 complex (Figure 28A,C). Consistent with the two-metal ion reaction mechanism¹¹⁵, two metal ions are coordinated by conserved side chain carboxylates in the yeast Rrp6-AMP complex in an ideal position to contact the scissile phosphate based on superposition of the RNA in my complex with AMP in the Rrp6-AMP complex (Figure 28C,D). Several contacts between the metal ions and RNA are missing in my structure due to the D238N substitution as this residue bridges both metal ions in the Rrp6-AMP active site.

The remaining contacts to the polyA RNA are notable as they reveal several non-specific interactions that are consistent with the ability of Rrp6 to degrade RNA of any sequence. The A₂₃ 2'-OH is within hydrogen bonding distance of the side chain carboxylate of Asp296 while the A₂₃ phosphate is in hydrogen bonding distance of the Leu328 backbone amide. The A₂₃ base is situated over the A₂₄ base with additional van der Waals contacts provided by side chains of Trp299, Met295 and Phe294. Phe294 is positioned between the A₂₃ and A₂₂ bases, presumably disrupting base stacking

interactions. The A₂₂ base and ribose are cradled by van der Waals contacts to Phe294, Gly292, His291 and Tyr315 while its phosphate is within hydrogen bonding distance with the backbone amide of His291. Lys319, His326 and Tyr315 contribute the remaining contacts to the A₂₁ base although none appear to interrogate the identity of the base. Consistent with the importance of the aforementioned interactions, sixteen of eighteen residues observed in direct contact to the RNA or metal cofactors are conserved in human Rrp6 (Figure 28A,B)^{69,70}.

2.3 RNA passes through the S1/KH ring to reach the Rrp6 active site

Four of the six nucleotides of polyA 24mer RNA observed in electron density (5'-A₁₉A₂₀A₂₁A₂₂A₂₃A₂₄-3') are coordinated by Rrp6 placing the 5' end (A₁₉) proximal to conserved, basic side chains from Rrp4 residues Lys122 and Arg123, while Rrp40 Lys108 points toward A₂₄ and Arg110 is proximal to the phosphate of A₂₁ and ribose of A₂₀ (Figure 29A). Additional densities, modeled as PO_{4a} and PO_{4b} with spacing consistent with the RNA phosphate backbone, are observed within the S1/KH ring nearest to Arg150 and proximal to Arg145 and Arg202 of Csl4 (Figure 23A-C). Each of the residues noted in Csl4, Rrp4 and Rrp40 are highly conserved in other family members¹⁷. No additional density consistent with RNA is observed within the PH-like ring.

Based on biochemical data I previously suggested that Rrp6 and Rrp44 utilized a shared portion of the central channel to engage their RNA substrates¹³. Alignment of Exo10^{Rrp6} with Exo10^{Rrp44+Rrp6Cterm} shows that the RNA molecules overlap within the S1/KH central channel (Figure 29A,B). Yet, a striking feature of Exo10^{Rrp6} is that RNA passes through the S1/KH ring in the reverse direction from that observed in Exo10^{Rrp44+Rrp6Cterm} (Ref. 52). Although a subset of side chains emanating from the S1/KH

cap proteins contact RNA, none make contacts that would enforce directionality. Because no additional density is apparent within the central channel in the Exo10^{Rrp6} complex, I sought to determine the relative importance of the S1/KH ring and PH-like ring in directing RNA to Rrp6 as was observed, albeit in the opposite direction, for RNA interactions within Exo10^{Rrp44+Rrp6Cterm}.

Yeast Exo10^{Rrp6} and Exo11^{Rrp44/Rrp6} complexes were reconstituted with Csl4 and Rrp40 that contained amino acid substitutions for Arg145, Arg150, Arg202; and Lys107, Lys108, and Arg110, respectively. Indeed, mutations in the S1/KH cap proteins severely diminish Rrp6 and Rrp44 mediated degradation of polyA RNA (Figure 29C) or AU-rich RNA (Figure 30A) in both Exo10^{Rrp6} and Exo11^{Rrp44/Rrp6} complexes. In contrast, insertion of a large loop in Rrp45 that is predicted to occlude the PH-like ring channel well below the S1/KH ring¹¹⁶ did not impair Rrp6 activities in Exo10^{Rrp6} or Exo11^{Rrp44/Rrp6}. Consistent with the RNA bound Exo10^{Rrp44+6Cterm} structure, the Rrp45 loop insertion inhibits Rrp44 activity.

To further delineate the role played by Exo9 in directing RNA to Rrp6 and Rrp44 I reconstituted catalytically dead yeast exosome complexes comprising Exo10^{Rrp6}, Exo10^{Rrp44} and Exo11^{Rrp44/Rrp6} and subjected them to long wavelength UV crosslinking in the presence of 36nt polyA or AU-rich RNA bearing single 4-thiouridine substitutions in positions 6, 21, and 29 from the 3' end in addition to a fluorescein molecule linked to the 5' end (Figure 31A; Figure 32A,B). 4-thiouridine substitutions do not impair the decay activities of the exosome complexes (Figure 32C). In the respective 4-thiouridine positions from the 3' end, the AU-rich RNA crosslinks to Rrp44, followed by the PH-like ring, and finally to the S1/KH cap in Exo10^{Rrp44} and Exo11^{Rrp44/Rrp6}, entirely consistent with previous biochemical studies and the RNA path observed in the Exo10^{Rrp44+Rrp6Cterm} crystal structure^{25,52,116,117}. Consistent with previous biochemical data showing that Rrp6

was important for Exo10^{Rrp44} binding to polyA RNA (Chapter 1)¹¹⁶, crosslinks were only observed to Rrp44 in Exo10^{Rrp44}; however, addition of Rrp6 in Exo11^{Rrp44/Rrp6} results in crosslinks that progressed from Rrp44 through the PH-like ring to the S1/KH ring and Rrp6 as the 4-thiouridine probe was moved 3' to 5'.

Consistent with the Exo10^{Rrp6} polyA RNA structure, crosslinks are observed to Rrp6 and Rrp4 when 4-thiouridine is placed 6 nts from the 3' end. Although there is no obvious structural impediment to prevent RNA from entering the PH-like ring, both polyA and AU-rich RNA crosslinked products are only observed to Rrp4, Csl4 and Rrp40 when the 4-thiouridine is positioned 21 or 29 nts from the 3' end (Figure 31C; Figure 32). This pattern contrasts with crosslinking patterns observed for Exo10^{Rrp44} and Exo11^{Rrp44/Rrp6} wherein crosslinks are observed to the PH-like ring subunits when 4-thiouridine is placed at positions predicted to crosslink to the PH-like ring.

The data described thus far are consistent with a model in which distinct but overlapping paths guide RNA to Rrp6 or to Rrp44 (Figure 31D). So how is a path selected? It appears that path selection is stochastic in vitro because both Rrp6 and Rrp44 degradation products can be observed under conditions of limiting enzyme (Figure 29C) or limiting substrate (Figure 31C). Unlike the distributive mechanism utilized by Rrp6 that binds and releases substrates repeatedly, Rrp44 is a processive enzyme that binds and holds onto its substrates until completely degraded. As such, UV crosslinking patterns under steady state reflect the most stable interaction with Rrp44 even when Rrp6 is present (Figure 32A), a pattern that can be reversed in complexes containing PH-like ring channel occlusions (Chapter 1)¹¹⁶. A time course was conducted under conditions of slight enzyme excess to observe stochastic sampling of the two paths via UV crosslinking (Figure 31C). As predicted based on the distributive and processive mechanisms of Rrp6 and Rrp44, respectively, crosslinked products are

observed to Rrp44, Rrp6 and the S1/KH ring proteins at the earliest time points and this pattern is lost once most of the RNA finds its way into the active site of Rrp44.

Structural analysis of the Exo10^{Rrp6} polyA complex suggests at least four potential paths into the S1/KH ring and Rrp6 (Figure 31E; Figure 33A) although paths 1 and 2 appear most likely with respect to electrostatics and conservation. Importantly, these paths are available in Exo11^{Rrp44/Rrp6} as they do not involve surfaces from the PH-like ring or Rrp44. Because Rrp6 sits atop the S1/KH ring I next modeled Rrp6 onto the Exo10^{Rrp44} RNA complex to determine if a path to Rrp44 was still available (Figure 31D; Figure 33B). As can be observed, the central channel is still visible proximal to the proposed 5' end of a single stranded RNA substrate suggesting those paths to Rrp6 and Rrp44 are available in Exo11^{Rrp44/Rrp6}.

2.4 The central channel widens in Exo10^{Rrp6}

I previously reported that Rrp6 enhanced the ability of Rrp44 to bind or degrade RNA by 100- and 43-fold, respectively, an observation that was especially evident for polyA RNA (Chapter 1)¹¹⁶. This phenomenon is also evident in crosslinking experiments (Figure 31A). These observations suggest that Rrp6 enables RNA penetration into the PH-like ring and central channel. To query differences in Exo10^{Rrp6} that might account for this activity, I compared structures of Exo10^{Rrp6} and Exo10^{Rrp44+Rrp6Cterm}.

The global architecture of the PH-like ring does not exhibit large differences (Figure 34D); in contrast, the Exo9 channel widens in Exo10^{Rrp6} principally through movement of Rrp4, Rrp40 and Csl4 away from the central channel (Figure 34A,B). RNA binds between the Rrp4 and Rrp40 S1 domains (Figure 29A,B) and in Exo10^{Rrp6} the gap between Rrp4 and Rrp40 S1 domains increases by ~4 Å resulting in widening of the channel throughout the S1/KH ring as calculated by HOLE¹¹⁰ (Figure 34C). Although

Exo10^{Rrp6} and Exo10^{Rrp44+Rrp6CTerm} are already bound to RNA in these structures, the increase in channel width could account for the stimulatory effects of Rrp6 on Rrp44 activities, especially since no direct physical interaction exists between Rrp44 and Rrp6. While it remains unclear how Rrp6 exerts this change or if an apo Exo10^{Rrp44} structure differs from its RNA bound configuration, the Rrp6 EXO domain is positioned between the S1 domains of Rrp4 and Rrp40 (Figure 26A), and this position could push Rrp4 and Rrp40 outward to widen the S1/KH ring central channel.

Rrp44 exoribonuclease activity was assayed using single-stranded polyA RNA in reactions containing Exo10^{Rrp44} and different Rrp6^{exo-} constructs lacking the PMC2NT domain to identify Rrp6 domains required for Rrp44 stimulation. Addition of Rrp6^{exo-} in trans stimulates Rrp44 activity to levels comparable to reconstituted Exo11^{Rrp44/Rrp6exo-} (Figure 34E). In contrast, adding the Rrp6 CTD or catalytic module, alone or together, fails to stimulate Rrp44 activity. Given that the Rrp6 CTD is necessary and sufficient for Exo9 interaction, it would appear that intact Rrp6 is necessary to stimulate Rrp44 activity in Exo11^{Rrp44/Rrp6exo-} because the Rrp6 CTD is required to bring the Rrp6 catalytic module in proximity to the S1/KH ring which elicits channel widening through its interaction with Rrp4 and Rrp40. Further experiments and structures will be required to determine if channel widening is a regulated feature of Exo11^{Rrp44/Rrp6} or if additional cytoplasmic factors elicit channel widening of Exo10^{Rrp44}.

2.5 Conclusions

The structure of Exo10^{Rrp6} shows Rrp6 positioned above the Exo9 S1/KH ring and central channel with RNA spanning the S1/KH ring and Rrp6 active site. Analogous to Rrp44 and its PIN domain, which is necessary and sufficient to bind the exosome core, Rrp6 is tethered to Exo9 by its CTD, which is also necessary and sufficient for exosome core interaction. As such, I deem it highly likely that the catalytic domains of Rrp44 and Rrp6 may adopt a variety of conformations that differ from those observed in the Exo10^{Rrp6} and Exo10^{Rrp44+Rrp6CTerm} complexes, and that this feature could enable interactions between the RNA exosome and a variety of RNA substrates or cofactors.

It is notable that Rrp6 activities are altered when associated with Exo9 (Chapter 1). I believe these differences can be attributed to Rrp4, Rrp40 and Csl4 residues that provide additional contacts to the RNA within the S1/KH ring as mutation of these residues decreases Rrp6 activities when associated with Exo9 (Figure 29C). Analogous to Rrp44, Rrp6 becomes dependent on the integrity of the central channel when associated with the Exo9 core, an observation that is remarkable given that Rrp44 and Rrp6 active sites are somewhat exposed to solvent in both Exo10^{Rrp6} and Exo10^{Rrp44+Rrp6CTerm} complexes, perhaps consistent with a recent report that shorter RNAs are directed to the Rrp44 active site via a channel-independent “direct access” route¹¹⁸.

That a similar segment of the central channel is used to engage RNA in opposing directions suggests that 3' to 5' directionality is not imparted by the Exo9 core but by the exoribonuclease active site in either Rrp6 or Rrp44. Distinct but overlapping paths to Rrp6 and Rrp44 could serve as a point of regulation by committing the exosome to distributive trimming or processive degradation depending on how a particular RNA substrate is delivered to the exosome. Another advantage of this model is that once a path is selected, the exosome is unable to interact with another substrate until

completing the task at hand because the paths overlap. Although path selection is stochastic in vitro (Figure 31D), cofactors of the nuclear exosome include Mpp6 (ref. 119), Rrp47 (ref. 67), and TRAMP (ref. 120) and these factors may impart directionality to bias selection of a particular path, or may hold RNA substrates proximal to the exosome to enable multiple encounters to facilitate transitions between editing, processing or degradation activities of the exosome.

Rrp6 interaction with the Exo9 core stimulates Rrp44 activities, perhaps through widening of the S1/KH ring, thus enabling RNA ingress through the PH-like ring toward the Rrp44 active site. Channel gating mechanisms as a point of regulation have been described in many other systems including, but not limited to, the proteasome¹²¹⁻¹²⁵. While many other degradation complexes place their catalytic activities in a protected compartment accessed by gating a substrate responsive channel, the RNA exosome appears inside out, with its catalytic subunits located on the periphery of the exosome core and central channel. While the functional relevance of this architecture is not entirely clear, it is evident that the exosome core and central channel modulate the activities of its catalytic subunits by requiring RNA to pass through distinct elements of the channel before being processed or degraded.

Exo10 ^{Rrp6} /polyA	
Data collection	
Space group	P2 ₁ 2 ₁ 2
Cell dimensions	
<i>a, b, c</i> (Å)	193.3, 200.1, 97.4
α, β, γ (°)	90.0, 90.0, 90.0
Resolution (Å)	50-3.3 (3.42-3.3) *
<i>R</i> _{merge}	6.1 (65.3)
<i>I</i> / σ <i>I</i>	15.5 (1.4)
Completeness (%)	97.7 (96.9)
Redundancy	5.2 (3.1)
Refinement	
Resolution (Å)	50-3.3
No. reflections	56332
<i>R</i> _{work} / <i>R</i> _{free}	22.7/26.5
No. atoms	21595
Protein	21450
Ligand/ion	145
Water	0
B-factors	
Protein	125
Ligand/ion	156
Water	n/a
R.m.s deviations	
Bond lengths (Å)	0.002
Bond angles (°)	0.47
One crystal was used.	
*Highest resolution shell is shown in parenthesis.	

Table 8. Data collection and refinement statistics for Exo10⁶

* Statistics calculated using Phenix⁸⁷; highest shell statistics indicated in parentheses,

† Calculated with the program Molprobit⁹¹

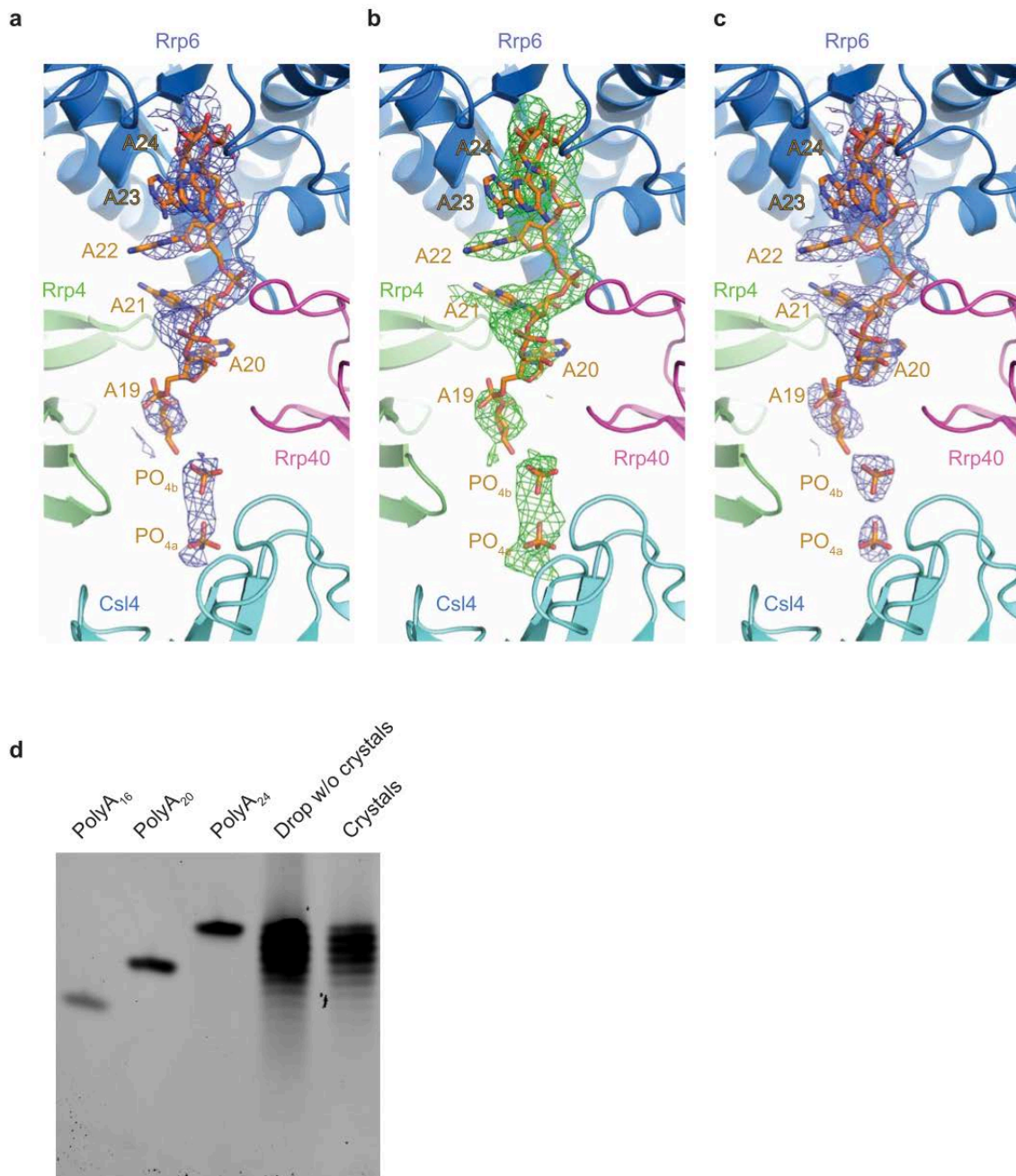


Figure 23. View highlighting electron densities covering RNA bound to Rrp6, Rrp4, Rrp40 and Csl4 within the Exo10^{Rrp6}-polyA structure.

(A) Simulated annealing 2fo-fc omit map contoured at 1.0 σ .

(B) Simulated annealing fo-fc omit map contoured at 2.0 σ .

(C) Final 2fo-fc omit map contoured at 1.0σ . RNA and phosphate oxygen, nitrogen, carbon and phosphate atoms are colored red, blue, orange and deep orange, respectively. Electron density maps shown as wire mesh colored blue for 2fo-fc maps and green for the fo-fc map. Rrp6, Rrp40, Rrp4 and Csl4 are labeled and shown in cartoon representation in teal, magenta, green and light blue, respectively.

(D) 20 to 24 nucleotides of polyA RNA are present in crystals of Exo10^{Rrp6}. Crystals of Exo10^{Rrp6} bound to polyA₂₄ RNA were first washed by two rounds of transfer to 1 μ L well solution, then dissolved in water and TBE-urea sample buffer, and analyzed by 15% TBE-urea PAGE. A drop without crystals was run as a control. RNA was stained by Sybr Gold.

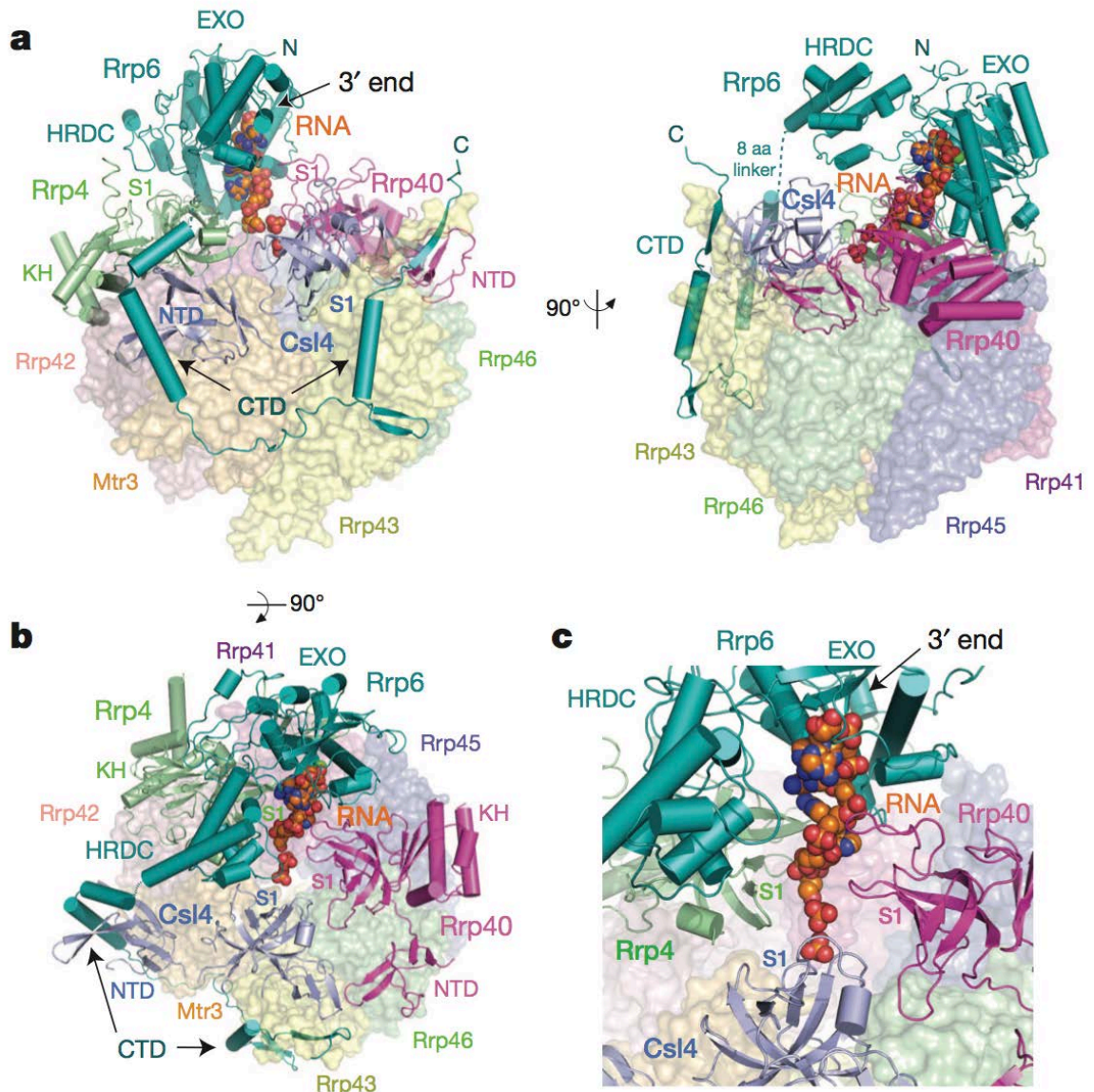


Figure 24. Overall structure of a RNA bound Rrp6 exosome.

A,B,C, Cartoon and surface representation of *S. cerevisiae* Exo10^{Rrp6} bound to polyA RNA showing views from the **(A)** sides and **(B)** top, and **(C)** close-up view with RNA engaged by the Rrp6 exoribonuclease (EXO) domain and S1 domains of Rrp40, Rrp4, and Csl4. The RNase PH-like ring is depicted as transparent surfaces, the S1/KH ring and Rrp6 as cartoons, and RNA as spheres. The Rrp6 catalytic module sits above the S1/KH ring and engages the RNA at its 3' end.

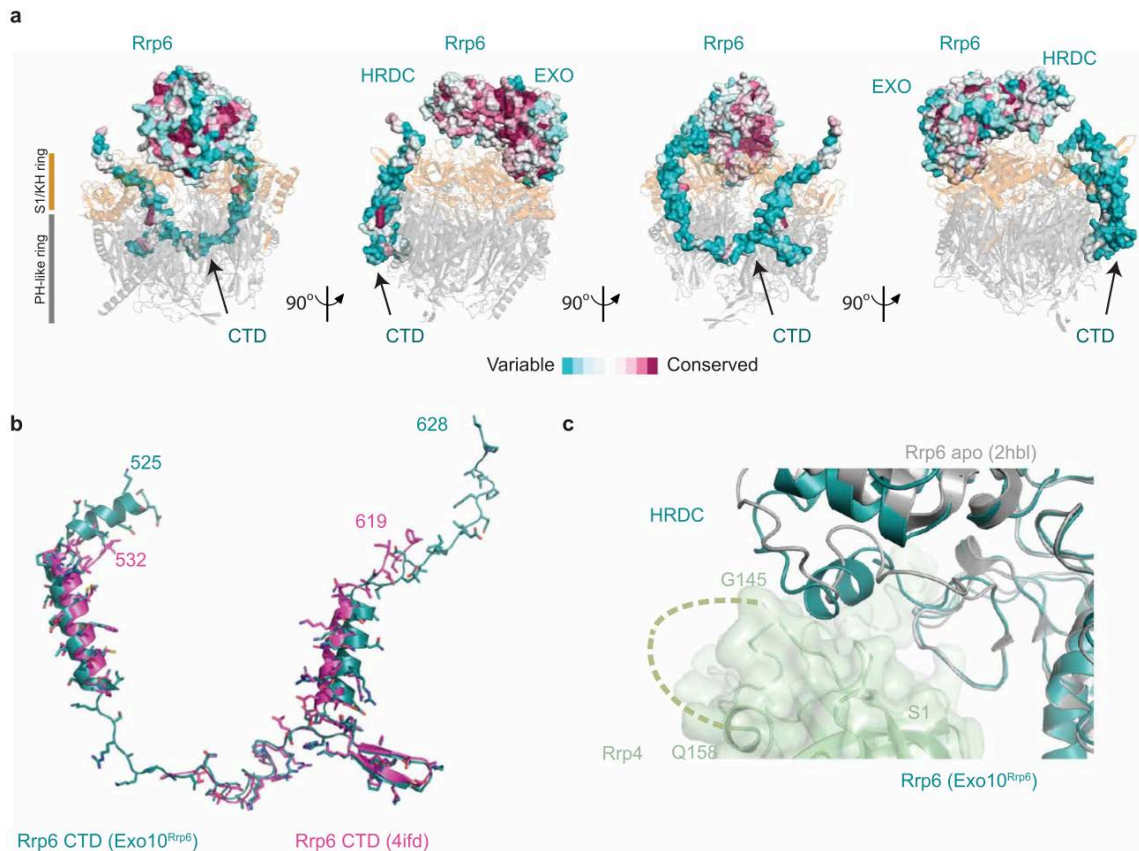


Figure 25. Rrp6 features within Exo10^{Rrp6}

(A) The primary sequence of the catalytic module of Rrp6 (EXO and HRDC) is highly conserved, whereas sequence conservation within the CTD varies. Rrp6 in Exo10^{Rrp6} is represented as a surface, and colored according to sequence conservation as calculated by ConSurf⁷⁸, colored from red (highly conserved) to blue (variable). The Exo9 core is depicted as a transparent cartoon, with the S1/KH ring in orange, and the PH-like ring in grey.

(B) Superposed structures of the Rrp6 CTD from Exo10^{Rrp6} (residues 525-628; teal) and Exo10^{Rrp44+Rrp6Cterm} (residues 532-557, 565-619; magenta; PDB 4IFD) reveal overall similarity between for residues within the respective models.

(C) The conserved linker between the EXO and HRDC domain of Rrp6 adopts an α -helix when associated with the exosome core. Superposition of the Rrp6 catalytic domains

from the structures of Exo10^{Rrp6} and Rrp6-AMP (PDB: 2HBL) shows residues Pro424 to Asn433 rearrange from a loop in the AMP-bound structure to a helix that is adjacent to a conserved albeit disordered loop in the S1 domain of Rrp4. Rrp6 is represented as cartoons, with Rrp6 from the Exo10^{Rrp6} structure in teal, and the Rrp6-AMP structure in grey. Rrp4 is in light green and depicted as a cartoon with a transparent surface, with the S1 loop representing residues Gly145 to Gln158 shown as a dashed line.

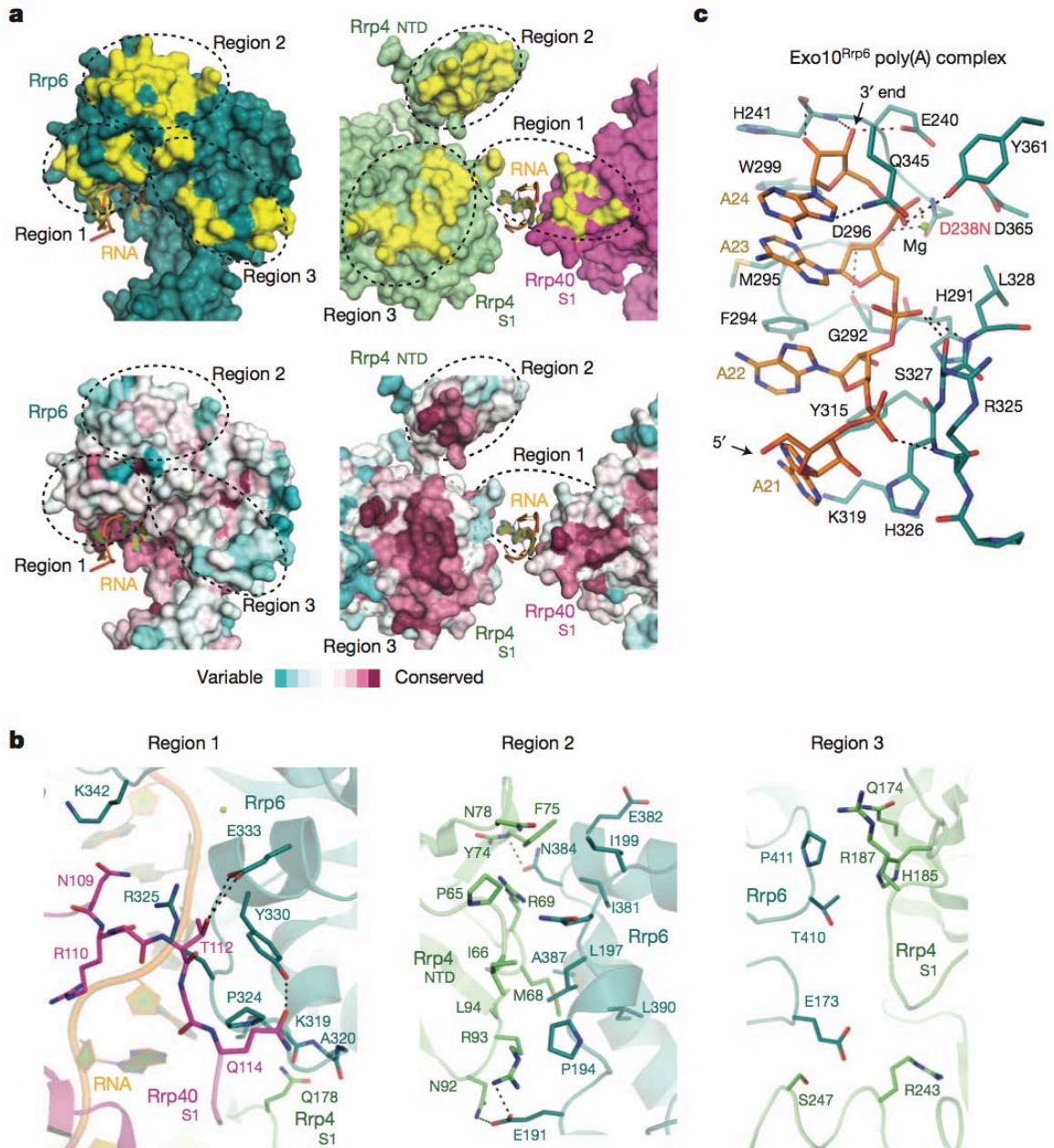


Figure 26. Rrp6 contacts with the S1/KH ring and RNA.

(A,B) The Rrp6 EXO domain interacts with the S1/KH proteins, Rrp4 and Rrp40, spanning three regions, indicated as yellow surfaces (A) and in atomic detail (B). A. Regions of interaction between Rrp6 and Rrp4/Rrp40 are depicted as an open book representation (160°), with Rrp6 in teal (left) and Rrp4 in pale green and Rrp40 in magenta (right). Below, surfaces are colored by sequence conservation from red

(conserved) to blue (variable). **B.** Atomic contacts between Rrp6 and the Rrp4 and Rrp40 are depicted as sticks. **C.** Zoom-in of atomic contacts between RNA and residues within the Rrp6 active site in Exo10^{Rrp6}-RNA. Rrp6 residues are depicted as sticks and colored teal; RNA is orange; magnesium as a green sphere and labeled. A catalytic aspartate, N238, is mutated (D238N) and labeled in red. Potential hydrogen bonds are depicted as dashed lines.

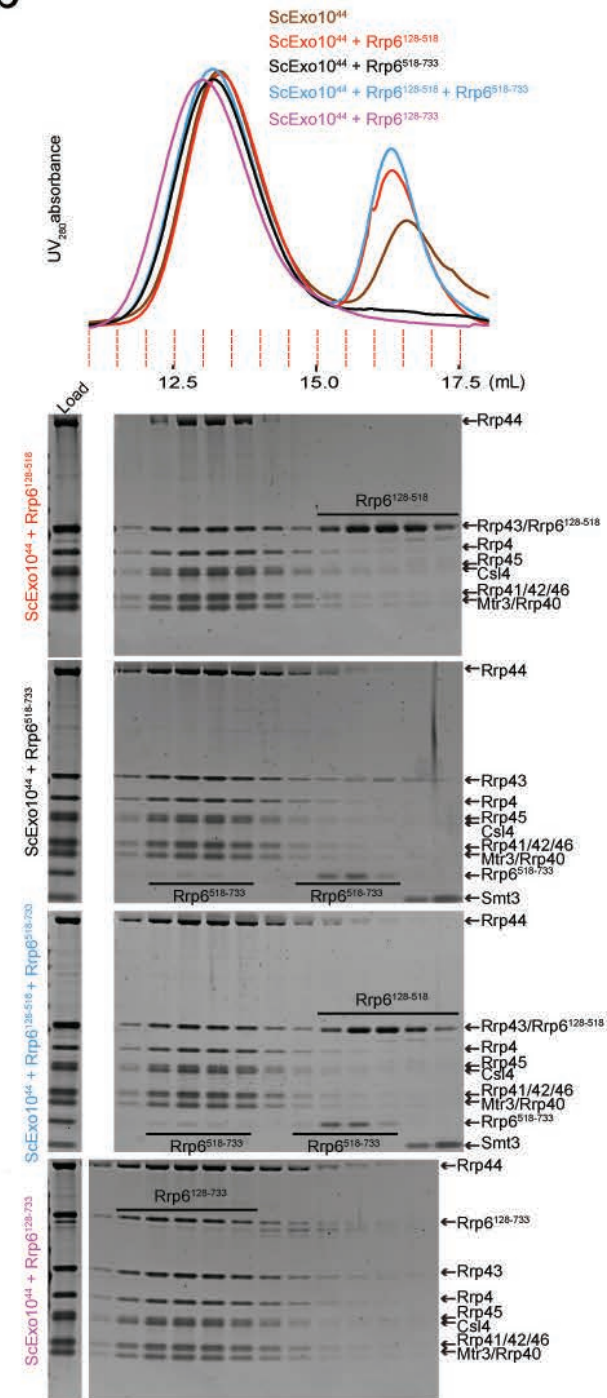
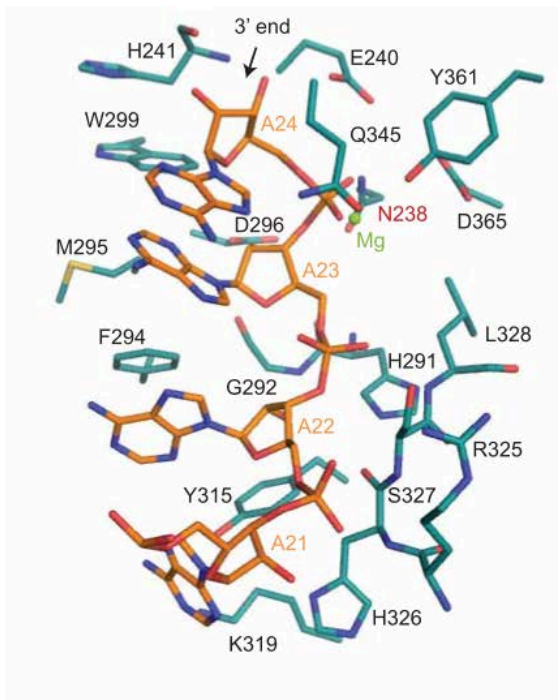
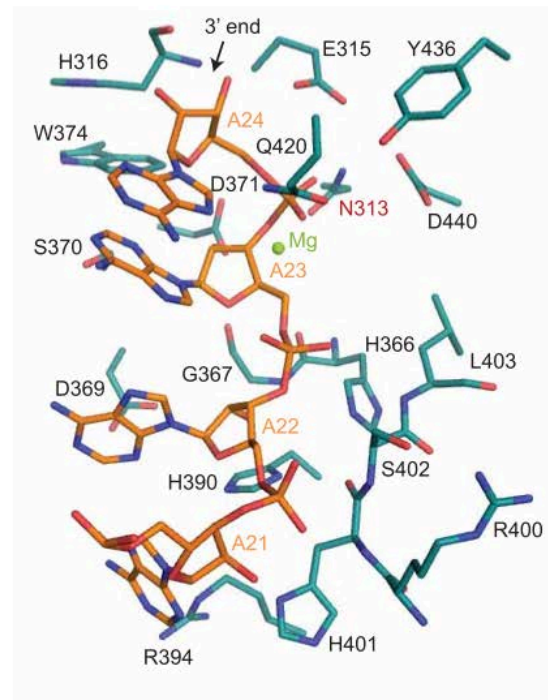
a**b**

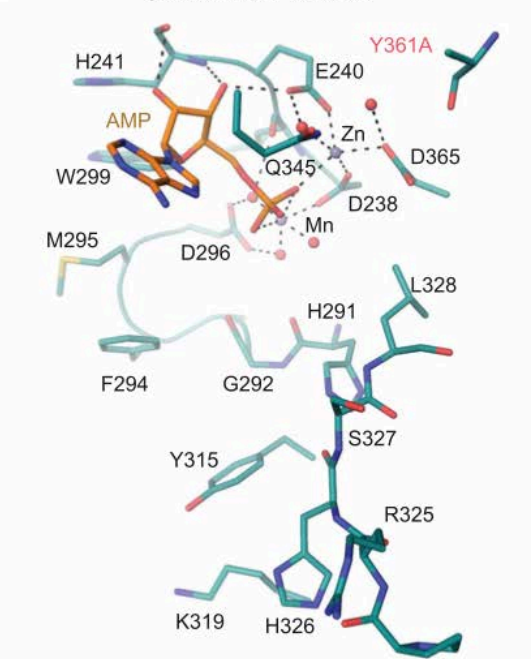
Figure 27. The Rrp6 CTD is required for interaction with yeast Exo9.

(A) Schematic representation of Rrp6 including from N- to C-terminus the PMC2NT, EXO, HRDC and C-terminal (CTD) domains. EXO and HRDC comprise Rrp6^{CAT}. Below are lines representing individual elements used in gel filtration analysis in **(B)** along with amino acid numbering specific for *S. cerevisiae* (Sc) Rrp6.

(B) Interaction studies of budding yeast Rrp6 with ScExo10^{Rrp44}. Rrp6 (residues 128-733), Rrp6^{CAT} (residues 128-518), the Rrp6^{CTD} (residues 518-733), or both were incubated with Exo10^{Rrp44} for one hour on ice before analysis by size exclusion chromatography (Superose 6) in reconstitution buffer. Rrp6 and Rrp6^{CAT} were added in 1.5-fold molar excess to Exo10^{Rrp44}, while Rrp6^{CTD} was added in 3-fold molar excess. Rrp6 (residues 128-733) and Rrp6^{CTD}, but not Rrp6^{CAT}, interact with Exo10^{Rrp44}. Fractions were analyzed by SDS-PAGE and protein detected with Sypro Ruby.

a*S. cerevisiae* Rrp6 with RNA**b***H. sapiens* Rrp6 with RNA (model)**c**

yRrp6cat AMP complex

**d**

Hybrid model for Rrp6 active site

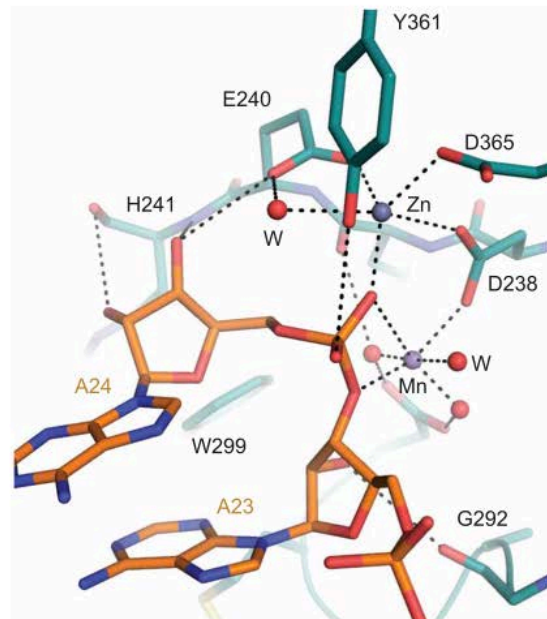


Figure 28. RNA interactions within the Rrp6 active site.

(A,B) View of RNA nucleotides 24 to 20 from the 3' end in the active site of *S. cerevisiae* Rrp6 from the structure of Exo10^{Rrp6} **(A)** and the same RNA modeled into the active site of *H. Sapiens* Rrp6 (PDB: 3SAF) based on superposing the respective EXO domains **(B)**. Residues involved in RNA contacts in the structure of yeast Exo10^{Rrp6} are shown as teal sticks in **(A)**; the corresponding residues in human are shown in **(B)**. In both structures, a catalytic aspartate is mutated to asparagine and labeled in red (N238 in yeast; N313 in human). RNA is shown as orange sticks, and magnesium ions are represented as green spheres.

(C) Structure of the yeast Rrp6 catalytic domain in complex with zinc (Zn; blue sphere) and manganese (Mn; yellow sphere) in complex with AMP (PDB 2HBL). Active site residues are depicted as in **(A,B)**. The conserved Tyr361 side chain was mutated to alanine in this structure (labeled Y361A in red).

(D) Model of the Rrp6 active site constructed by superposing the 3' nucleotide in the Exo10^{Rrp6} polyA structure to the AMP ligand from PDB 2HBL. Amino acid side chains are labeled and putative interactions between metal ligands, active site residues and RNA are depicted by dashed lines.

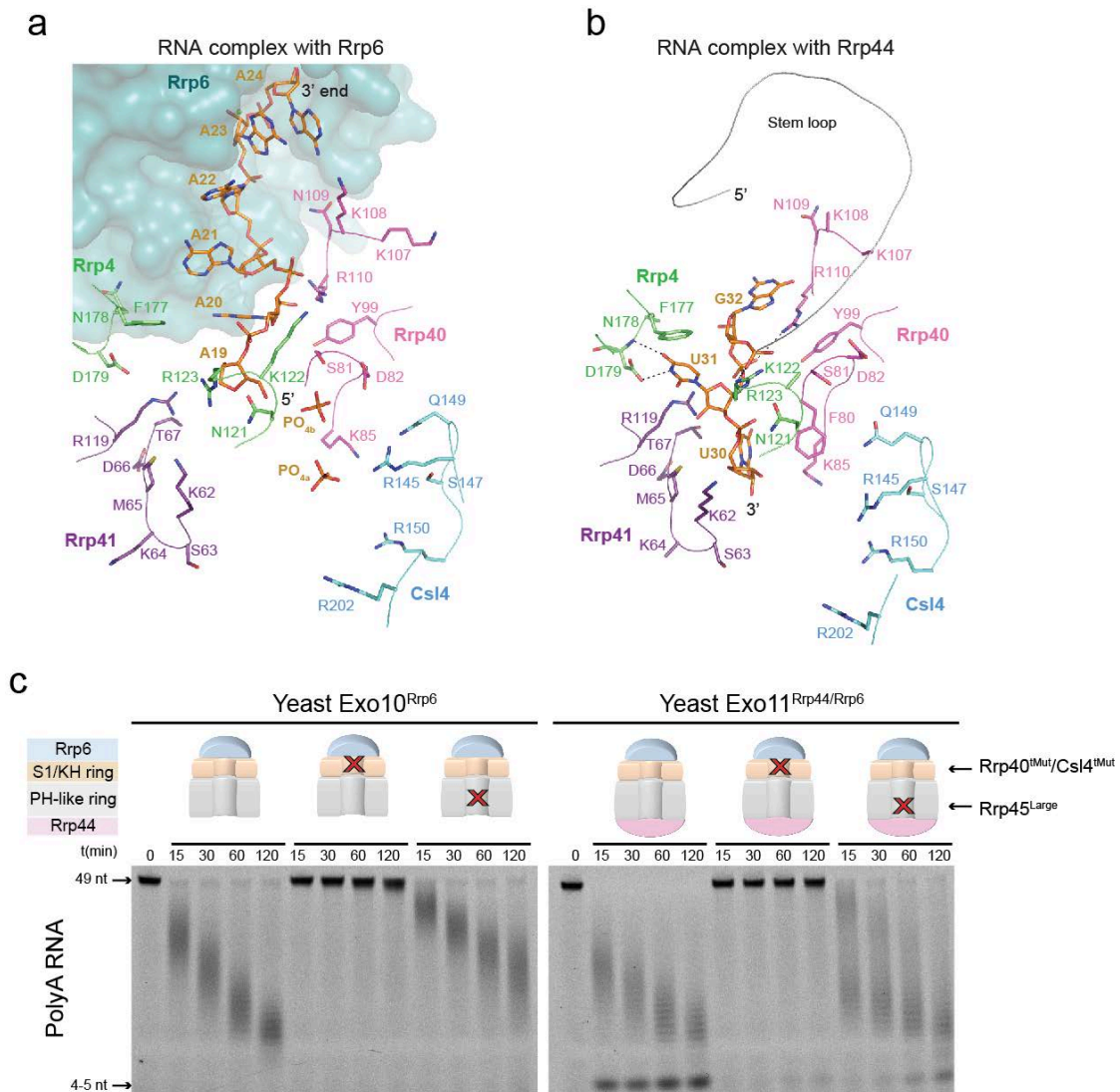


Figure 29. Rrp6 activities depend on the integrity of the S1/KH ring.

(A,B) RNA in complex with (A) Exo10^{Rrp6} and (B) Exo10^{Rrp44+Rrp6Cterm} shows partially overlapping but distinct paths for RNA within the S1/KH ring. RNA and S1/KH side chains involved in contacts in either structure are depicted as sticks, with color-coded labels adjacent to corresponding subunits. Rrp6 EXO domain (A) depicted as a surface representation, and the stem loop (B) in Exo10^{Rrp44+Rrp6Cterm} is drawn as a ribbon. (C) Mutating residues proximal to RNA in the S1/KH ring severely inhibits Rrp6 activities in yeast Exo10^{Rrp6}, and Exo11^{Rrp44/Rrp6}, while introducing a channel occluding insertion within the lower half of the PH-like ring (Rrp45-Large) does not. Rrp44 exoribonuclease

activity in Exo11^{Rrp44/Rrp6} is impaired by mutations in both S1/KH and PH-like rings. RNA decay assays performed using synthetic 5' fluorescein labeled 49 nucleotide (nt) polyA RNA with reconstituted exosomes, intermediates were resolved by denaturing PAGE. RNA decay assays were conducted at least three times for each of the samples with typical results depicted in **(C)**.

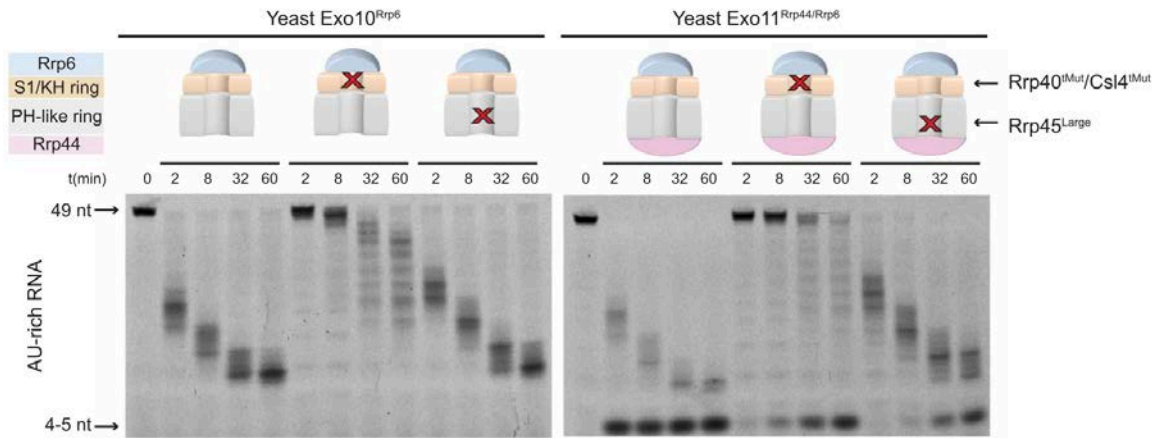


Figure 30. Central channel mutations and their impact on Rrp6 degradation of AU-rich RNA.

1 nM of reconstituted wild-type and mutant yeast Exo10^{Rrp6} and Exo11^{Rrp44/Rrp6} were incubated with 10 nM 49 nt 5' fluorescein AU-rich RNA at 30°C. Reaction intermediates were analyzed after indicated time points by denaturing PAGE and imaged with a fluoroimager. Rrp6 activity decreases in the presence of the Rrp40 K107E/K108E/R110D and Csl4 R145A/R150A/R202D mutations in both Exo10^{Rrp6} and Exo11^{Rrp44/Rrp6} while is mostly unaffected by the channel occlusion in the Rrp45^{Large} exosome. Rrp44 exoribonuclease activity is attenuated by mutations in both the S1/KH and PH-like ring in Exo11^{Rrp44/Rrp6}.

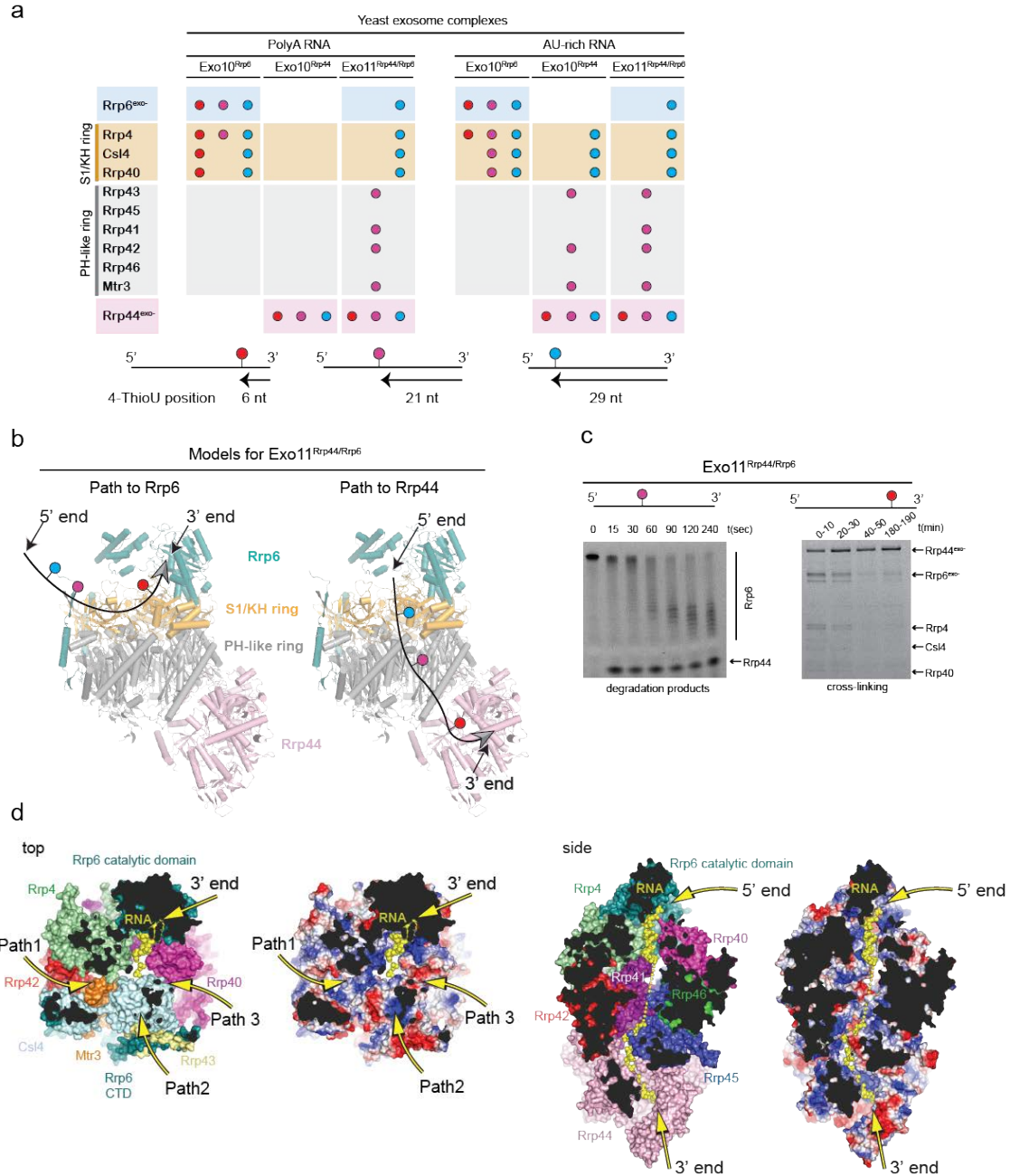


Figure 31. Distinct but overlapping RNA paths to Rrp6 and Rrp44.

(A) Schematic representation of RNA crosslinking patterns. The RNA path to Rrp6 depends on the S1/KH ring while the RNA path to Rrp44 depends on the S1/KH and PH-like ring to engage RNA. 5' fluorescein 36 nt synthetic RNAs labeled with a single 4-thiouridine at 6, 21, or 29 nts from the 3' end to enable site-specific UV crosslinking to

exosome complexes containing catalytically dead Rrp6 and/or Rrp44. Crosslinked products were resolved by SDS-PAGE (Figure 32A).

(B) Models for the RNA path to Rrp6 and Rrp44 in Exo11^{Rrp44/Rrp6}. Cartoon representation of Exo11^{Rrp44/Rrp6} made by superposing PH-like rings from Exo10^{Rrp6} and Exo10^{Rrp44+6Cterm} with the S1/KH ring colored orange, the PH-like ring colored grey, Rrp6 colored teal and Rrp44 colored pink. The RNA is depicted as an arrow with the arrowhead representing the 3' end anchored in Rrp6 (left) or Rrp44 (right). The position of 4-thioU at 6, 21 or 29 nt is depicted by red, purple or blue circles, respectively, based on observed patterns shown in **(A)**.

(C) RNA engages Rrp6 or Rrp44 in a stochastic manner in Exo11^{Rrp44/Rrp6}. (Left) RNA degradation assays under enzyme excess (5 nM 5' fluorescein 36nt 4-thioU RNA, 25 nM enzyme) indicating the presence of Rrp6 products and Rrp44 products. (Right) Time course and RNA crosslinking to 350 nM Exo11^{Rrp44exo-/Rrp6exo-} using 150 nM 5' fluorescein 36 nt polyA RNA bearing a 4-thiouridine 6 nts from the 3' end. The reaction was initiated by combining protein and RNA followed by UV crosslinking for 10 minutes. Decay and binding reactions performed at 22°C, and reaction intermediates resolved by denaturing urea PAGE and SDS-PAGE, respectively. RNA decay assays and crosslinking were conducted at least three times for each of the samples with typical results depicted.

(D) Structure of an Exo11^{Rrp44/Rrp6} model derived by superposing the PH-like ring subunits in Exo10^{Rrp6} and Exo10^{Rrp44+6Cterm}. RNA paths to the Rrp6 active site. RNA (yellow) shown as derived from the Exo10^{Rrp6} polyA complex. Top view of the complex with subunits colored as in Fig. 24 (left) next to a representation with surfaces colored according according to electrostatic potential as calculated by Pymol³⁴. Subunits that are visible are labeled in the left panel as is the RNA. Three putative paths that traverse the S1/KH ring into the Rrp6 active site denoted by yellow arrows and labels (P1, P2, P3) (See Figure 33A).

fluorimager. In comparing the His₆-tagged and tagless complexes, mobility shifts are apparent in crosslinks corresponding to the S1/KH cap proteins.

(C) 4-thioU RNAs are bona fide decay substrates for exosome complexes and catalytic subunits, Rrp6 and Rrp44. Conditions using substrate excess (10 nM RNA, 1 nM enzyme), 4-thioU polyA RNAs (left) and AU-rich RNAs (right) are comparably degraded to corresponding 36 nt RNAs lacking 4-thioU. Reactions were performed at 30°C and stopped after indicated time points and resolved by denaturing PAGE and imaged with a fluorimager. 4-thioU RNAs are color-coded as in **(A)** and **(B)**.

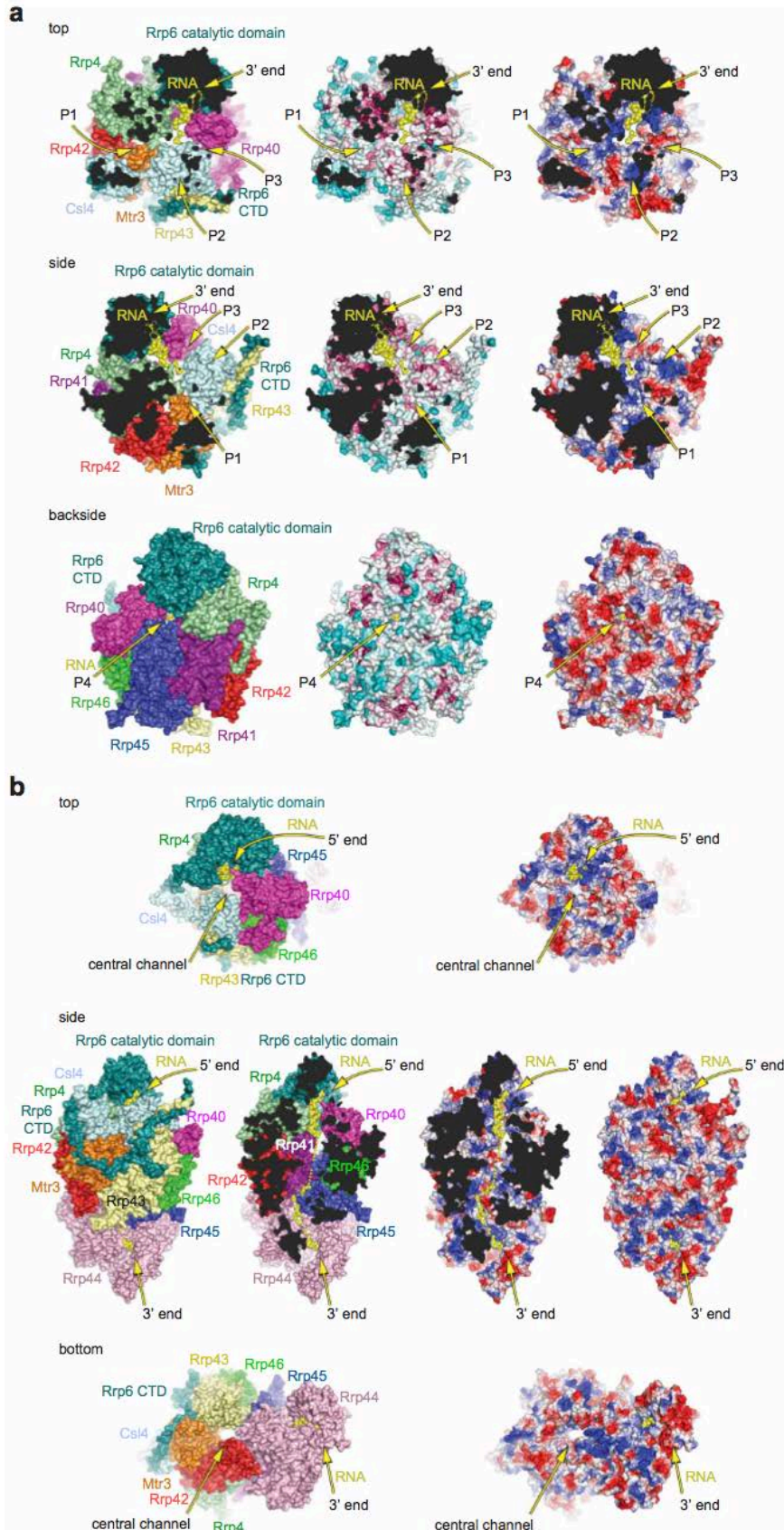


Figure 33. RNA paths to Rrp6 and Rrp44.

Structure of an Exo11^{Rrp44/Rrp6} model derived by superposing the PH-like ring subunits in Exo10^{Rrp6} and Exo10^{Rrp44+6Cterm} (PDB 4IFD).

(A) RNA paths to the Rrp6 active site. RNA (yellow) shown as derived from the Exo10^{Rrp6} polyA complex. Three views are provided from the top, side and backside of the complex with subunits colored as in Figure 24 (left), surfaces colored according to conservation as calculated by ConSurf⁷⁸ (middle) from red (highly conserved) to blue (variable), and surfaces colored according to electrostatic potential as calculated by Pymol⁷⁷ (right). Subunits that are visible are labeled in the left panel as is the RNA. Three putative paths that traverse the S1/KH ring into the Rrp6 active site are denoted by yellow arrows and labels (P1, P2, P3) in the top and side views and a fourth path (P4) under the Rrp6 catalytic domain is denoted in the backside view. Based on conservation, electrostatics and crosslinking I deem P1 or P2 as the most likely path of ingress for the incoming RNA substrate. The top and side views utilize cutaway surfaces to illustrate the putative paths and surface properties.

(B) RNA paths to the Rrp44 active site. Subunits and surfaces depicted as in **(A)** with the exception that the RNA is now derived from the structure of Exo10^{Rrp44+6Cterm} (PDB 4IFD) with the RNA edited to remove the stem loop after nucleotide 36. Top, side and bottom views are depicted with the RNA path indicated by a yellow arrow with 5' and 3' ends labeled. The position of the central channel is also labeled and indicated by a yellow arrow in the top and bottom views. The top and side views show that RNA could pass by Rrp6 to penetrate the S1/KH and PH-like ring central channel.

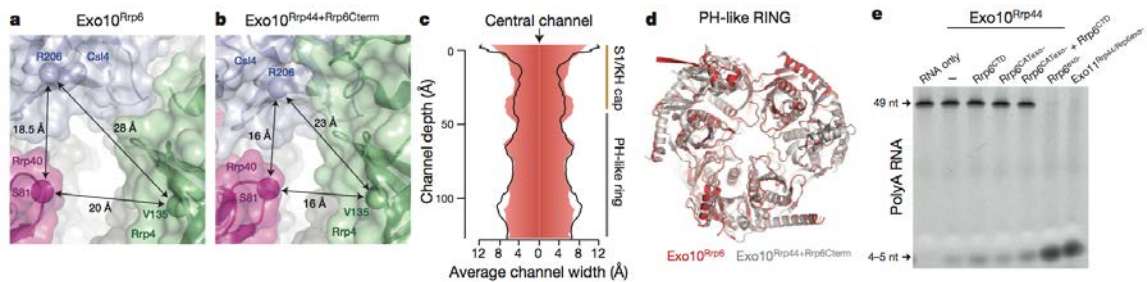


Figure 34. Widening of the S1/KH ring in Exo10^{Rrp6}.

(A,B) Left, close-up view of the central channel looking from the top of the S1/KH ring into the PH-like ring along the path of the RNA. S1/KH subunits represented as cartoons with transparent surfaces in (A) Exo10^{Rrp6} and (B) Exo10^{Rrp44+Rrp6Cterm}, with Rrp4 in green, Rrp40 in magenta, and Csl4 in light blue. Distances between labeled amino acids in each structure are indicated. **(C)** Channel dimensions in Exo10^{Rrp6} (red) and Exo10^{Rrp44+6Cterm} (black) calculated using HOLE¹¹⁰. **(D)** Superimposition of the PH-like rings does not reveal large changes between Exo10^{Rrp6} (red) and Exo10^{Rrp44+6Cterm} (grey). **(E)** Only Rrp6^{exo-} (residues 128-733), and not the Rrp6^{CTD} (518-733) or Rrp6^{CAT} (128-518), is sufficient to allow passage of polyA RNA to the Rrp44 active site in Exo11^{Rrp44/Rrp6exo-}. RNA degradation reactions with 5' fluorescein 49nt polyA were performed using Exo10^{Rrp44} alone, or in mixtures with the Rrp6^{CTD}, Rrp6^{CAT}, both, or Rrp6^{exo-}. Rrp44 reaction products resolved by denaturing PAGE. RNA decay assays were conducted at least three times for each sample with typical results depicted.

CHAPTER 3

RNA Recruitment by the RNA Exosome: Redefining the Rrp6 C-terminal Domain

3.1 Introduction

Two recent crystal structures of yeast exosomes bound to either Rrp44⁵² or Rrp6 (Ref. 126, Chapter 2) revealed how Exo9 recruits and modulates the activities of both enzymes. In the structure of the Rrp44-bound exosome (Exo10^{44/Rrp6CTD}), Rrp44 is tethered to the bottom of the Exo9 PH-like ring via its PIN domain, with the RNB domain positioned below the central channel. A fragment of Rrp6 associates with Exo9 via the N-terminal one hundred residues of its CTD (518-618) that form extensive contacts on the periphery of Exo9 between the cap protein, Csl4, and the PH-like subunit, Rrp43. In the structure of Exo10⁶, the Rrp6 CTD is in the same orientation, while the catalytic module of Rrp6 rests atop the S1/KH ring, with its EXO domain hovering above the Exo9 central channel. Despite their orientation on opposite ends of the core, both catalytic subunits' exoribonuclease active sites are sequestered from solvent, and therefore utilize the Exo9 central channel to form an extended RNA binding surface that feeds RNA into either active site, which in turn modulates the activities of all three ribonuclease activities, as has been demonstrated *in vitro* (Chapter 1, Ref. 116). While these structures provide a vital picture of the terminal snapshots of RNA decay after the RNA has been engaged by either 3' to 5' exoribonuclease, how the earlier steps occur – initial RNA encounter, and subsequent path selection through the Exo9 central channel to the Rrp6 and Rrp44 active sites, is unclear. Furthermore, the role of the C-terminal most portion of the Rrp6 CTD has remained largely unknown. I demonstrate that this region of approximately one hundred residues of Rrp6 functions as a RNA recruitment factor, which I refer to as the RNA “lasso.” In the case of free Rrp6, the lasso functions to

enhance RNA decay by presumably offering an additional binding site. In the context of the exosome, the lasso functions to first sense and subsequently recruit RNA to the exosome core, during which RNA ingresses via the S1/KH cap proteins to the central channel, and is then finally shunted to either Rrp6 for distributive trimming or to Rrp44 for processive decay.

3.2 The Rrp6 CTD is composed of two independent modules: an Exosome Associating Region (EAR), and a “lasso” region that recruits RNA

Rrp6 has been considered to be composed of four distinct regions – three intrinsically ordered domains (PMC2NT, EXO, and HRDC), and an intrinsically disordered CTD of approximately two hundred residues. Recent crystal structures of the Rrp6 exosome show ordering of the first one hundred residues of the CTD once Rrp6 associates with the exosome, whereby two alpha helices of the Rrp6 CTD form extensive contacts with Csl4, Rrp43 and Mtr3 of Exo9 (Ref. 52,126). As such, it will hereafter be referred to as the Exosome Associating Region (EAR) of Rrp6. However, the role of the remaining 100 residues of the disordered C-terminal region has remained unclear. Despite being present in the crystal, this C-terminal region of Rrp6 remained disordered in the crystal structure of the Rrp6 exosome bound to polyA RNA (Chapter 2 and unpublished data). Consistent with this observation, these residues were vulnerable to proteolysis by chymotrypsin, in the absence and presence of RNA, while the rest of the Rrp6 exosome, including the EAR, was not (Figure 35), suggesting this region does not reorder in the presence of Exo9 and/or RNA. Analysis of its amino acid sequence reveals lysine and arginine dense clusters, with an isoelectric point of 10.32. Although this region shows poor primary sequence conservation (Figure 36A), its physiochemical properties are highly conserved. Given that a disordered stretch of basic residues could

likely facilitate nucleic acid recruitment, I tested the ability of this region to bind nucleic acid. Recombinant His₆-GST-Rrp6-CTD pulled down nucleic acid from yeast lysates; treatment with RNase A, and not DNase I, resulted in loss of the precipitated nucleic acid. Indeed, binding of RNA to the Rrp6-CTD was specific as liberation of the Rrp6-CTD by TEV cleavage of the His₆-GST tag resulted in contaminating RNA in the flowthrough, and not in the His₆-GST elution (Figure 36B).

To evaluate the extent of nucleic acid binding, dissociation constants were determined for the Rrp6 CTD on single-stranded RNA and DNA by fluorescence polarization. The Rrp6 CTD bound nucleic acid tightly, with a K_d of 50 to 60 nanomolar, regardless of being offered RNA or DNA (Figure 36C). Given its inherent disorder and ability to bind nucleic acid, I redefine this region as the Rrp6 “lasso” (Figure 36D).

To determine if the lasso and the EAR are functionally distinct, exosomes were reconstituted with different varieties of Rrp6 and evaluated for complex formation via size exclusion chromatography. Consistent with previous studies^{116,126}, Rrp6 containing both the EAR and lasso reconstitutes stoichiometrically with Exo9; Rrp6 containing the EAR but lacking the lasso similarly associates with Exo9; however, Rrp6 lacking the EAR but containing the lasso no longer associates with Exo9 (Figure 36E). Taken together, these results suggest two distinct modalities within the C-terminal two hundred residues of Rrp6.

I next assayed the effects of disrupting the EAR and lasso regions on Rrp6 exoribonuclease activity. All constructs assayed lacked the N-terminal PMC2NT domain as it has been shown previously that deletion of this region does not alter Rrp6 activity in comparison to full-length Rrp6 *in vitro* (Chapter 1, Ref. 116). Decay of a single-stranded polyA RNA was comparable when assaying activities of the Rrp6 catalytic module (EXO and HRDC domains, residues 128-516), with and without varying lengths of the EAR (residues 128-589; 128-634). Presence of half the lasso (residues 128-685) resulted in a

slight 2-fold increase in polyA RNA decay, while the intact lasso conferred a 4-6 fold gain of function (Figure 37A). Consistent with its ability to bind RNA on its own (Figure 36C), lasso-containing Rrp6 binds polyA RNA 4-fold better than lassoless Rrp6 (Figure 37B). Interestingly, Rrp6 lacking the EAR but containing the lasso appears to be even more active (EARless Rrp6), and is able to process polyA RNA over 5 times faster than the catalytic module, and binds polyA RNA 6-fold tighter than lassoless Rrp6. This result suggests that the EAR, in its disordered state, has a slight inhibitory effect on Rrp6 catalytic activity, perhaps by partially occluding the Rrp6 active site when not associated with the Exo9 core. While the lasso confers on Rrp6 the ability to degrade RNA quickly, RNA intermediates rapidly accumulate around 9-12 nucleotides in lasso-containing Rrp6, rather than the smaller 4-5 nucleotide products observed with lassoless Rrp6 constructs. This stalling is not due to enzyme instability because the same trend is observed on decay of RNAs shorter than 49 nucleotides (Figure 37C). Notably, EARless Rrp6 is not prone to as much stalling as full-length Rrp6 when provided an intact lasso, consistent with the EAR being inhibitory in the context of free Rrp6 (Figure 37A). Whether this observed difference in product length is merely an *in vitro* artifact or bears *in vivo* significance is not known. Nevertheless, it is clear that the lasso facilitates the rapid turnover of long single-stranded RNAs by free Rrp6.

3.3 The Rrp6 Lasso Promotes RNA Binding and Decay Activities of Rrp6 and Rrp44 in 10- and 11-Component Exosomes

Because the lasso alters Rrp6 activity *in vitro*, I next determined whether it has a similar effect on Rrp6 exosome activity. Three Rrp6 constructs were reconstituted and purified with recombinant Exo9: full-length lasso (128-733), partial lasso (128-685), and no lasso (128-634) and assayed for decay on AU-rich and polyA RNA. The integrity of

the lasso had a more profound effect on Rrp6-containing exosomes than on free Rrp6. On AU-rich RNA, partial and full lasso deletion resulted in a striking 6-fold and 16-fold loss of Rrp6 activity, respectively. Similar trends were observed for polyA RNA, with partial and full lasso deletions resulting in 4-fold and 16-fold attenuation of decay (Figure 38A).

Another consequence of deleting the lasso was an alteration in the distribution of RNA intermediates produced by Rrp6. RNA intermediates generated by exosomes containing an intact lasso had a smaller distribution, while the partial and lassoless exosomes produced a wider distribution (Figure 38A). This disparity may be attributed to the difference in binding affinities for RNA within the various exosomes, whereby the lasso prevents “slippage” of the RNA from the Rrp6-Exo9 interface. Indeed, lasso deletion results in up to a 20-fold loss of binding of AU-rich, and over a 15-fold loss for polyA, a conservative estimate given that polyA RNA binding could not be saturated for partial- and lassoless Exo10⁶ (Figure 38B).

Despite resulting in a tighter distribution of intermediates and a higher initial rate of Rrp6-mediated exosome decay, Rrp6 decay of RNA in lasso-containing exosomes seems to follow a biphasic mode of decay, with a rapid burst of RNA decay, followed by a slower second phase. Similar to what was observed for free Rrp6, Exo10^{6-IntactLasso} cannot efficiently degrade shorter RNAs (see Section 3.4). In contrast, partial and lassoless exosomes follow a single-phase mode of decay, in which in the latter part of the reaction, RNA is degraded more efficiently than by lasso-containing exosomes (Figure 38C).

It has been shown that the only region dispensable to visualize Rrp6-dependent stimulation of Rrp44 exoribonuclease activity in Exo11^{44/6} is its PMC2NT domain – that is, the Rrp6 catalytic module combined with the CTD are both required (Chapter 2, Figure 34). In isolation, the Rrp6 CTD (both the EAR and lasso) is not sufficient,

presumably because the Rrp6 catalytic module is needed to physically induce Exo9 central channel widening¹²⁶, thus facilitating RNA ingress to the Rrp44 active site. However, the effects of deleting the lasso while preserving the Rrp6 catalytic module and EAR on Rrp44 activities are unknown. Eleven subunit exosomes were reconstituted with varying lengths of the Rrp6 lasso – including intact lasso, partial lasso, and no lasso, in both the context of catalytically active and dead Rrp6. Rrp6 exoribonuclease activity in Exo11^{44/6} was modulated by the lasso to the same extent as in Exo10⁶ (Figure 39A, Figure 38A). As observed previously, Rrp44 is able to robustly degrade polyA RNA when the Rrp6 lasso is intact (Figure 10). However, RNA decay by Exo11 reconstituted with either Rrp6 containing a partial lasso, or a lasso delete exhibits severely inhibited Rrp44 exoribonuclease activity, down 15-fold and 30-fold, respectively (Figure 39A). This trend is independent of Rrp6 catalytic activity (Figure 39B). Despite the robust activity of Rrp44 on AU-rich RNA, the presence of the Rrp6 lasso further facilitates Rrp44 decay of this RNA, with Rrp44 in Exo11^{44/6-IntactLasso} 15-fold and 30-fold more active than partial and lassoless exosomes (Figure 39A,B). The fact that the lasso confers the same advantage to Rrp44 decay on either polyA or AU-rich RNA is consistent with the lasso's non-specificity of RNA binding (Figure 36C). Furthermore, binding of Exo11^{44exo-/6exo-} to RNA is compromised in lasso deletions, with up to a 6-fold decrease in affinity for polyA RNA (Figure 39C).

I next tested the effect of Rrp6 lasso length on Rrp44 endoribonuclease activity. It has been observed previously that the endoribonuclease activity of free Rrp44 yields a distributive, uniform banding of intermediates^{32,35}; however, Rrp44 association with Exo9 alters the endoribonuclease activity by conferring 3' to 5' directionality and an exosome “footprint” that is dependent on the integrity of the Exo9 central channel (Chapter 1, Figure 12; Ref. 116). Similar to its exoribonuclease activity, polyA RNA can only be efficiently processed by the endoribonuclease activity of Rrp44 when Rrp6 is

simultaneously present on the exosome, unlike the case with the more flexible AU-rich RNA, in which the exosome footprint is observable independent of Rrp6 association. Interestingly, while the accessibility of polyA RNA to the Rrp44 endoribonuclease active site is not dependent on Rrp6 catalytic activity, it also does not appear to rely on the integrity of the lasso (Figure 39D). Similar to what is observed for the Rrp44 exoribonuclease activity, an appreciable attenuation of Rrp44 endonuclease activity is observed with lasso deletions. However, once RNA eventually encounters the exosome, it gains access to the endoribonuclease active site of Rrp44, presumably due to widening of the central channel via the Rrp6 catalytic module (Chapter 2, Figure 34; Ref. 126) to accommodate passage of the bulkier polyA RNA to Rrp44. Consistent with this, the Rrp6 catalytic module artificially tethered to the Exo9 core by a linker to Csl4 (see section 3.6) is sufficient to confer the exosome “footprint” on polyA RNA (Figure 39E).

3.4 The Rrp6 Lasso Facilitates the Decay of Longer RNAs

Because of the biphasic nature of Rrp6 decay in Exo10^{6-IntactLasso}, I hypothesized that the lasso is important for the recruitment of longer RNAs to the exosome. Exo10⁶ exoribonuclease activity was assayed on 49, 36, 24, and 14 nucleotide RNAs in complexes containing full, partial, and no lassos. Similar to previous results, lasso-containing exosomes are able to degrade longer RNAs more efficiently than lasso mutants, being approximately 15-fold and 8-fold more active than lassoless exosomes on 49 and 36 nucleotide RNAs, respectively (Figure 40). Interestingly, lasso-containing exosomes switch to a one-phase mechanism almost identical to lasso mutants when offered the shorter RNAs (14 and 24 nucleotides). Incidentally, Exo10^{6-IntactLasso} protects approximately 24 to 28 nucleotides of RNA as determined by ribonuclease protection assays (Figure 41). It is possible that longer RNAs are preferentially degraded by

Exo10^{6-IntactLasso} because 24 to 28 nucleotides is the length required to satisfy the composite binding surface from the Rrp6 active site, through the Exo9 surface, to the Rrp6 lasso. RNAs shorter than this length no longer have the advantage of this avidity and therefore are not preferentially degraded. On the contrary, these smaller intermediates may exhibit product inhibition, contributing to the second, slower phase of decay in Exo10^{6-IntactLasso} (Figure 38C) by non-productively binding the lasso, resulting in charge neutralization of the RNA-lasso moiety, resembling Exo10^{6-Lassoless}. Consistent with this hypothesis, Exo10^{6-IntactLasso} has the lowest affinity for 14 nt RNA, and the highest for 24 nt RNA. This trend holds for Exo10^{6-IntactLasso} although binding is overall much weaker (Figure 42).

3.5 The Rrp6 Lasso Feeds RNA into the Exo9 Central Channel

Numerous studies have reported the importance of the central channel in Rrp44- and Rrp6-mediated RNA decay both *in vitro*^{25,116} and *in vivo*^{116,117,127}. Based on the structure of the Rrp6 exosome, the lasso is likely oriented above the S1/KH ring; therefore, once it has recruited RNA, the engaged RNA would then thread through the S1/KH ring en route to Rrp6 or through the entirety of the S1/KH and PH-like ring to reach Rrp44. Conversely, absence of the lasso should yield a greater dependence on the Exo9 central channel because of the disruption of RNA binding modules. To test these possibilities, I sought to determine how, if at all, lasso status impacted RNA decay in exosomes bearing mutations in the Exo9 central channel.

Decay of RNA in Exo10⁶ was first assessed in lasso-containing exosomes. Consistent with previous results (Chapter 2, Figure 29), a triple point mutation in Rrp40 within the S1/KH ring results in a minor inhibition of Rrp6 activity, while coupling the same Rrp40 mutants with three Csl4 point mutations more effectively occludes the

S1/KH ring, and results in more severe Rrp6 inhibition (Figure 43). However, exosomes with compromised lassos (either partial or full delete) are much less capable of overcoming the S1/KH channel mutations than exosomes with intact lassos. These exosomes are severely inhibited by the Rrp40 triple mutant alone, and are incapable of degrading RNA in the context of the Rrp40/Csl4 mutants.

These results suggest that both the Rrp6 lasso and the central channel are important for RNA decay; while loss of one can be compensated for by the presence of the other, loss of both sites results in severe inhibition of RNA decay by Rrp6-containing exosomes. It remains to be seen if the same trend holds for Rrp44-associated exosomes.

3.6 The Rrp6 Lasso Stimulates Rrp6 and Rrp44 Activities Independent of the EAR

To distinguish between the role of the Rrp6 EAR as a scaffold or a modulator of Rrp6 and Rrp44 activities, I engineered a variant of Rrp6 that could associate with the exosome independent of the EAR. Using the structure of Exo10⁶ as a guide, the C-terminal region of the catalytic module was fused to the N-terminus of the S1/KH subunit Csl4 via a 9 residue exogenous linker. In addition, two different lasso lengths of Rrp6 were fused onto the Csl4 C-terminus, proximal to where the Rrp6 lasso would be located in intact Rrp6 (Figure 44A). These engineered constructs, Rrp6^{CAT}-Csl4, Rrp6^{CAT}-Csl4-Lasso1, and Rrp6^{CAT}-Csl4-Lasso2 were reconstituted with Exo10^{44WT} and assayed for their ability to degrade RNA in comparison to Exo10^{44WT} and Exo11^{44WT/6WT}. Surprisingly, the lassoless fusion activated Rrp44 on AU-rich RNA, but not on polyA RNA (Figure 44B), suggesting that the widening of the Exo9 central channel by the Rrp6 catalytic module alone is not sufficient to promote Rrp44 activation by Rrp6 on polyA RNA. Rrp6 meanwhile displayed weak activity on both AU-rich and polyA RNAs. However, Rrp6

fusions bearing lassos resulted in activation of both Rrp44 and Rrp6 on AU-rich and polyA RNAs, with Exo11-Rrp6^{CAT}-Csl4-Lasso2 exhibiting activity comparable to wild-type Exo11^{44/6}, suggesting that both the Rrp6 EAR and lasso serve as distinct recruitment factors, with the EAR serving as a scaffold to recruit Rrp6 to Exo9, and the lasso recruiting RNA to the 10- and 11-subunit exosomes. To determine if these features of the lasso are conserved in higher eukaryotes, one hundred residues of the putative *H. sapiens* lasso was fused to the *S. cerevisiae* Rrp6^{CAT}-Csl4 and assayed for its ability to similarly recruit RNA. On both AU-rich and polyA RNAs, the human lasso conferred a gain-of-function to Rrp44 and Rrp6 activities, suggesting functional rather than sequence-specific conservation of the Rrp6 lasso from yeast to human.

3.7 *In vivo* Consequences of Lasso Deletion

Given that Rrp6 lasso integrity modulates all three ribonuclease activities associated with the exosome, I sought to determine the functional consequences, if any, of Rrp6 lasso deletion. A previous study found that a Rrp6 CTD deletion fully rescued the growth defect of the Rrp6 null in *S. cerevisiae* in a S288C background. Given the results presented above, this experiment was repeated in a W303 strain background with finer Rrp6 truncations because it has since become more appreciated that $\Delta rrp6$ exhibits a more measurable temperature sensitive growth defect than in the S288C^{81,128,129}. Another consideration in experimental design was that two putative nuclear localization signal (NLS) sequences have previously been identified within the Rrp6 lasso⁷⁵. Although mutation of these sequences resulted in a very slight mislocalization of Rrp6, and no observable growth phenotype or accumulation of known Rrp6 and/or exosome targets⁷⁵, I included these two NLS sequences and the flanking sequences in between (corresponding to residues 700 to 721) in my lasso deletions to

ensure that any observable phenotype was not due to Rrp6 mislocalization. Therefore, strains were complemented with plasmids bearing no Rrp6, full-length Rrp6 (1 to 733); $\Delta 635-699;722-733$ (lassoless), $\Delta 686-699;722-733$ (partial lasso); and $\Delta 519-618$ (EARless). Yeast grown in minimal media on both solid agar (Figure 45A) and liquid media (Figure 45B) exhibited a barely detectable temperature sensitive growth defect of lassoless Rrp6 at 37°C, but not at 30°C. However, growth on rich media exacerbated these differences (Figure 45A). Interestingly, EARless Rrp6 grows almost as well as wild-type Rrp6 on minimal media, but nearly phenocopies the Rrp6 deletion on rich media. Whether this is due to an exosome association defect or free Rrp6 hyperactivation is unclear at the moment. The observed growth defects are not due to protein instability of the truncations as determined by Western blot using a Rrp6-specific antibody. These results suggest that the kinetic defects of lasso compromised exosomes observed *in vitro* may have functional consequences *in vivo*, as the exosome's ability to deal with the rapid RNA turnover and maturation demands of the cell is compromised. Future experiments will examine what free and exosome associated-Rrp6 RNA targets are accumulated in EARless and lasso deletion strains, respectively, and test if growth under different conditions of stress¹³⁰ (during which RNA decay demands may increase) exacerbates growth defects in lasso deletions.

3.8 RNA Ingress in Rrp6-Containing 10- and 11-Component Exosomes

Once RNA has been recruited towards the exosome by the Rrp6 lasso, what path does it then take to Rrp6? While the structure of Exo10⁶ engaged with polyA RNA shows electron density corresponding to 8 nucleotides from the Rrp6 active site, the crystals contained 20 to 22 nucleotides of RNA (Chapter 2, Figure 23. Ref. 126), suggesting that 12 to 14 nucleotides towards the 5' end remained unresolved.

Furthermore, site-specific UV crosslinking revealed that all three S1/KH cap proteins contacted a 36-nucleotide RNA from its 3' to 5' ends in the Rrp6-exosome while PH-like ring subunits were excluded (Chapter 2, Figure 31. Ref. 126). These observations are consistent with two hypotheses regarding the route of RNA ingress to the Rrp6 active site: there are multiple routes of RNA ingress along the S1/KH ring; or one region is preferentially utilized but due to its solvent exposed nature, ingressing RNA is extremely disordered and thus its path partially stochastic. To distinguish between these two possibilities, candidate sites on the surface of Exo10⁶ were examined based on protein architecture, electrostatic surfaces and sequence conservation for a likely route of RNA ingress (Figure 33, Ref. 126). Based on these criteria, the most promising candidate was the region between Rrp4, Mtr3, Rrp42, Csl4, and the HRDC/EAR of Rrp6, as it forms a large, positively charged cleft that would be able to accommodate bulkier RNAs (Figure 46A), and its features present in the structure of human Exo9 (Ref. 17). To test if this surface was involved in Rrp6-mediated RNA decay, three point mutants were introduced: two electrostatic mutations: Csl4 R206D and Mtr3 K132E, and one to disrupt potential base-stacking interactions, Rrp4 W278A. Expression, and purification of these mutant subunits in isolation and as reconstituted Exo9 particles were comparable to their wild-type counterparts.

The ability of Exo10⁶ to degrade RNA was first assayed in the context of the triple mutant. Although decay of both AU-rich and polyA RNAs was inhibited in the Exo10⁶ mutant, the extent of inhibition varied according to RNA substrate, where the triple mutant was no longer active on polyA RNA but displayed impaired activity on AU-rich RNA (Figure 46B). Because of the striking effects of the triple mutant, I reconstituted Exo10⁶ with only two of the three assayed mutants: Mtr3 K132E and Rrp4 W278A. As expected, the double mutant was more active than the triple mutant on AU-rich RNA; nevertheless, decay of polyA RNA was still severely inhibited (Figure 46C).

To determine how the identified region, if at all, is coupled to the Rrp6 lasso, Exo10^{6/Lassoless} was reconstituted and assayed in the context of Exo9 wild-type and the triple mutant. Almost no difference in decay was observed in lassoless exosomes when this region was mutated (Figure 46D), suggesting that the Rrp4/Mtr3/Csl4 route of RNA ingress to the Rrp6 active site is selected once RNA has been recruited towards the exosome by the Rrp6 lasso.

To test the relevance of this region on Rrp44 RNA decay in the 11 subunit nuclear exosome, I reconstituted Rrp44-containing exosomes with the Exo9 triple mutant. Decay of AU-rich RNA by Exo10⁴⁴ was very mildly affected by the mutations (Figure 46B), consistent with the path of RNA observed in the Exo11^{44/6EAR} crystal structure, whereby RNA accesses Rrp44 by traversing through the entire Exo9 central channel, and therefore would not rely on this region. In the presence of Rrp6^{exo-}, however, Exo11^{44WT/6exo-} is strikingly inhibited by the triple Exo9 point mutations, on both AU-rich and especially polyA RNA (Figure 46B). Based on current structural models and the biochemical data presented here, it is likely that the path of RNA observed in Exo11^{44/6EAR} reflects a path of RNA utilized in the cytoplasmic exosome, or Exo10⁴⁴, while in Exo11, the Rrp6 catalytic module would partially occlude the Exo9 central channel, thereby requiring additional and/or alternate routes of RNA ingress to accommodate entry to both Rrp6 and Rrp44 active sites.

3.9 Conclusions

The studies presented here shed light on previously unresolved questions pertaining to initial stages of RNA decay by the exosome, specifically RNA encounter followed by ingress towards Rrp6 and Rrp44 in the context of Rrp6-containing exosomes, highlighting a substantial role for a previously unappreciated fragment of

Rrp6, its C-terminal region, or “lasso”. Using a combination of *in vitro* and *in vivo* approaches, I find that deleting this disordered region of approximately one hundred residues has severe consequences on Rrp6 activity, in and out of the exosome, and on both endo- and exoribonuclease activities of Rrp44, and that this stimulation is dependent on the integrity of the central channel. Biochemical results further suggest that both RNA recruitment by the Rrp6 lasso and the channel widening induced by the Rrp6 catalytic domain are necessary for Rrp6-mediated activation of Rrp44, particularly on polyA RNA, a substrate of the nuclear exosome, as neither alone is sufficient to activate Rrp44 exoribonuclease activity on polyA RNA.

Once RNA is bound by the lasso, it is then in proximity to a series of basic regions: the Rrp4/Mtr3/Csl4 cleft of Exo9, the positively charged surface of the Rrp6 HRDC and EXO active sites, and the Exo9 central channel. I have identified a region of RNA ingress that is implicated particularly in the decay of polyA RNA in Rrp6-containing 10- and 11-subunit exosomes, and that this path selection seems to be contingent on the integrity of the Rrp6 lasso. While decay of AU-rich RNA was also impaired, alternate regions of Exo9 may exist that can accommodate these more flexible RNAs, or the mutations tested are not sufficient to disrupt their coordination. Thus, RNA can be subsequently committed to either Rrp6 or Rrp44 active sites once engaged by the Rrp6 lasso.

No such disordered, highly basic sequence is present in prokaryotic RNase D⁷⁴, suggesting the Rrp6 lasso is a unique eukaryotic exosome-specific feature. Given its importance in recruiting and subsequently facilitating decay of larger RNAs, the Rrp6 lasso likely serves as a processivity factor to cope with the demands of the eukaryotic cell for rapid RNA turnover and processing. A basic polypeptide extension would be advantageous for recruiting RNAs because its RNA binding surface is more solvent exposed, unlike the Rrp6 and Rrp44 active sites when bound to the exosome^{52,116}.

Consistent with this hypothesis is the Rrp6 lasso's biophysical (Figure 47) and functional (Figure 44B) conservation in eukaryotes, which has remained conserved without evolutionary pressure to maintain a defined structure and primary sequence.

A number of studies exist documenting the importance of small disordered fragments in effecting changes in the functions of larger multisubunit complexes^{131,132} and RNA biogenesis factors¹³³, with an additional factor, Mpp6, to be discussed in Chapter 4. Future work will undoubtedly continue to uncover novel regulatory roles for other small, disordered regions in such complicated assemblies.

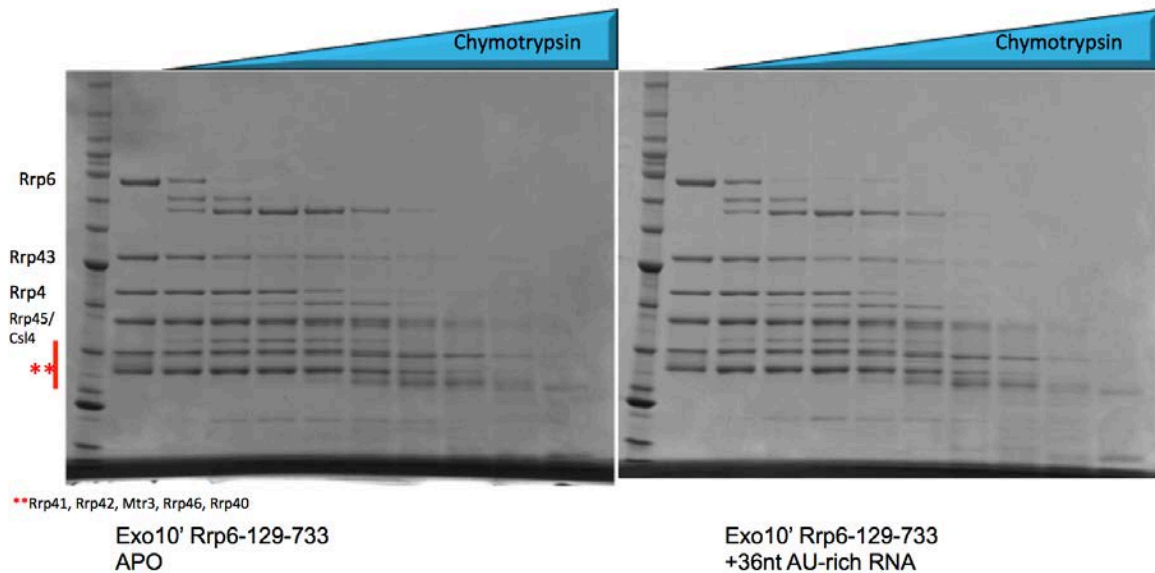


Figure 35. A 10 kilodalton region of the Rrp6 C-terminus in Exo10⁶ is vulnerable to limited proteolysis, in the absence or presence of RNA.

Fixed amounts of Exo10⁶ (8 micrograms) were treated with increasing concentrations of chymotrypsin. Reactions proceeded at room temperature for 1 hour before being quenched with LDS buffer and boiled at 95°C for 2 minutes. Products were analyzed by SDS-PAGE and stained with Coomassie. Gel on the left shows digested products of apo Exo10⁶ while gel on the right shows products of Exo10⁶^{exo-} incubated with 3 fold molar excess AU-rich 36 nt RNA for 30 minutes prior to proteolysis.

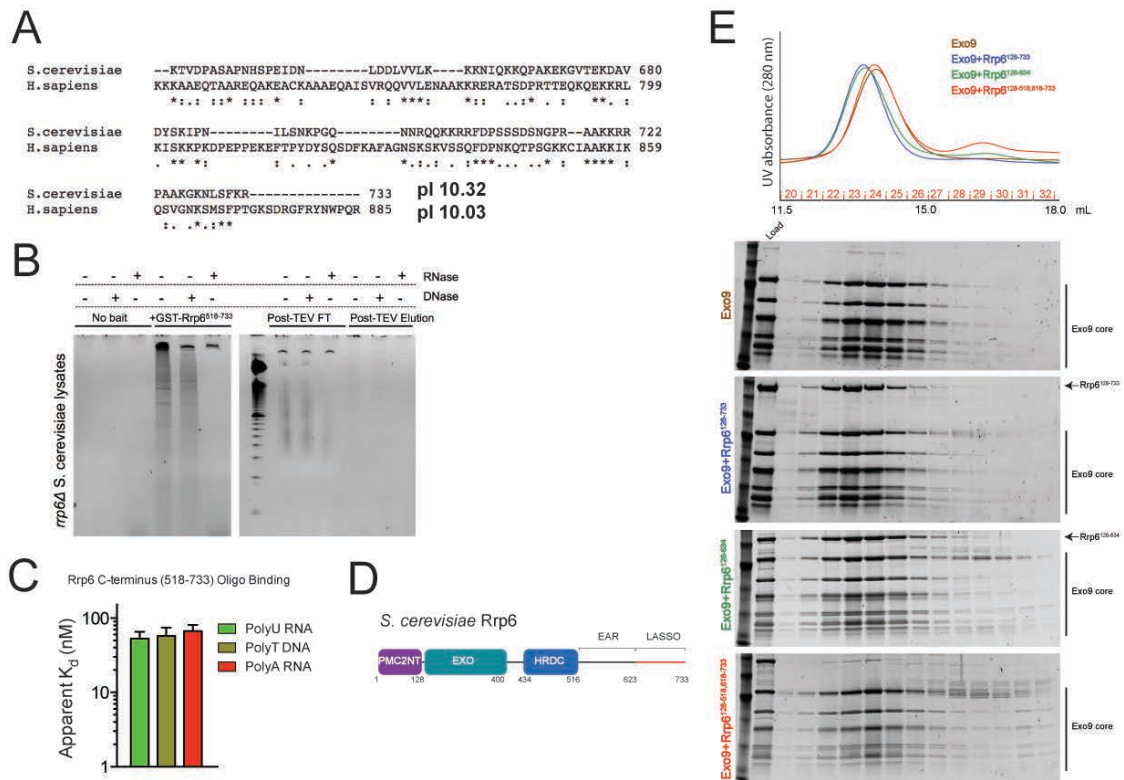


Figure 36. The Rrp6 CTD is composed of two modules – an Exosome Associating Region (EAR) and a disordered “lasso” that binds RNA.

(A) The C-terminal most 100 residues of *S. cerevisiae* Rrp6 aligns poorly with that of *H. sapiens*, but both are highly basic and share a similar pI. Alignments performed with ClustalW and pI's calculated with ExPasy ProtParam. (B) The Rrp6 CTD (EAR and lasso) preferentially binds endogenous RNA from *S. cerevisiae* lysates. Recombinant nucleic acid free His₆-GST-Rrp6 CTD or buffer was incubated with lysates derived from Δ rrp6 and immobilized on nickel-NTA resin, and eluted with imidazole. Eluates were subsequently incubated with TEV protease and reapplied on nickel-NTA to distinguish between nucleic acid bound to His₆-GST and the Rrp6 CTD. Samples were treated with DNase I, RNase A, or buffer to query the identity of bound nucleic acid, and quenched in formamide buffer and analyzed by denaturing (urea) TBE electrophoresis. Nucleic acid was stained with Sybr Gold. (C) Fluorescence polarization binding measurements of the Rrp6 CTD on 5' fluorescein-labeled 36 nt polyU and polyA RNAs, and polyT DNA. (D)

Revised domain structure of Rrp6. (E) Analytical gel filtration analyses and corresponding gels showing Exo9 alone (brown); +Rrp6 with CTD intact (blue); +Rrp6 lacking the lasso (green); +Rrp6 lacking the EAR (red). Rrp6 association with Exo9 is dependent on the Rrp6 EAR, but independent of its lasso.

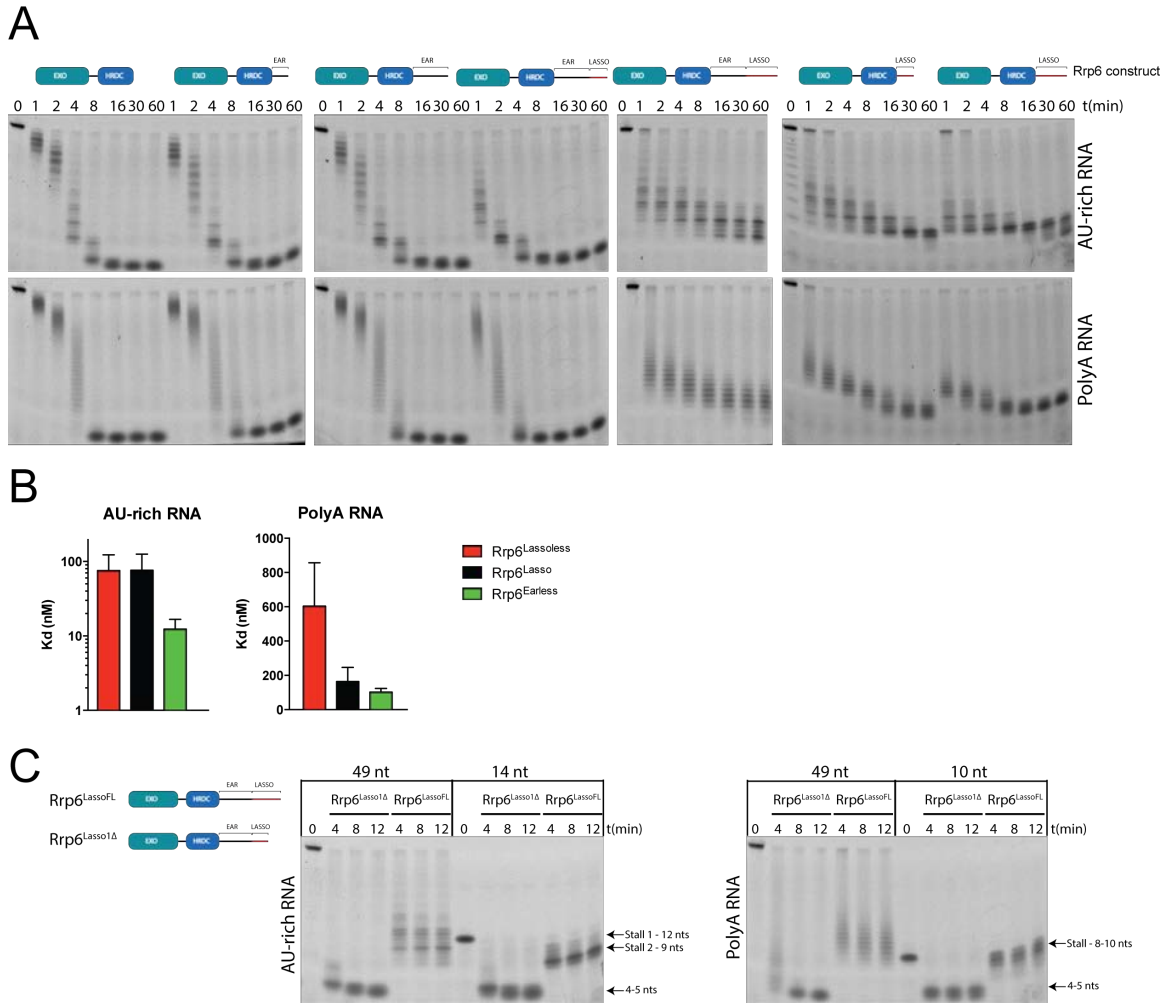


Figure 37. The Rrp6 lasso stimulates its RNA binding and ribonuclease activity, while the EAR exhibits a mild inhibitory effect.

(A) Rrp6 ribonuclease activities on AU-rich and polyA RNAs. Constructs vary from the minimal catalytic module to Rrp6 containing an intact EAR/lasso. RNA decay assays performed using 5' fluorescein labeled 49 nt AU-rich and polyA RNA. (B) Catalytically dead Rrp6 variants (D238N) were analyzed for their ability to bind 36 nt AU-rich RNA and 37 nt polyA RNA via fluorescence polarization. Results of triplicate experiments shown. (C) Larger (9-12) decay RNA intermediates accumulate in reactions with Rrp6^{IntactLasso}, whereas smaller 4-5 nt products accumulate when the lasso is truncated, regardless of the size of the initial substrate.

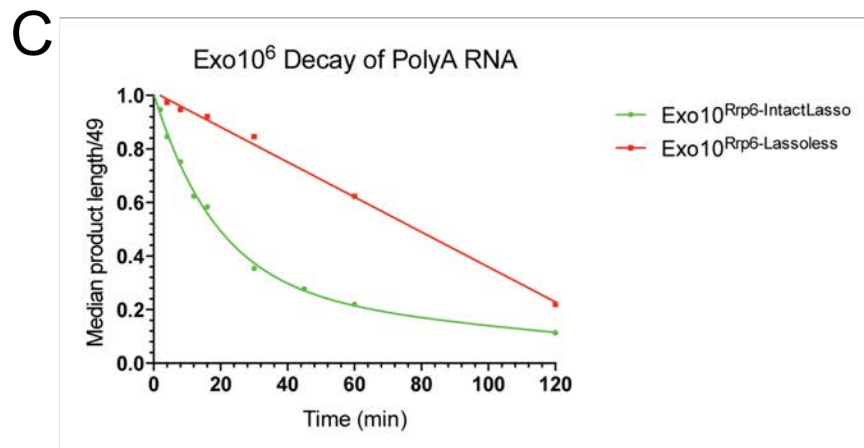
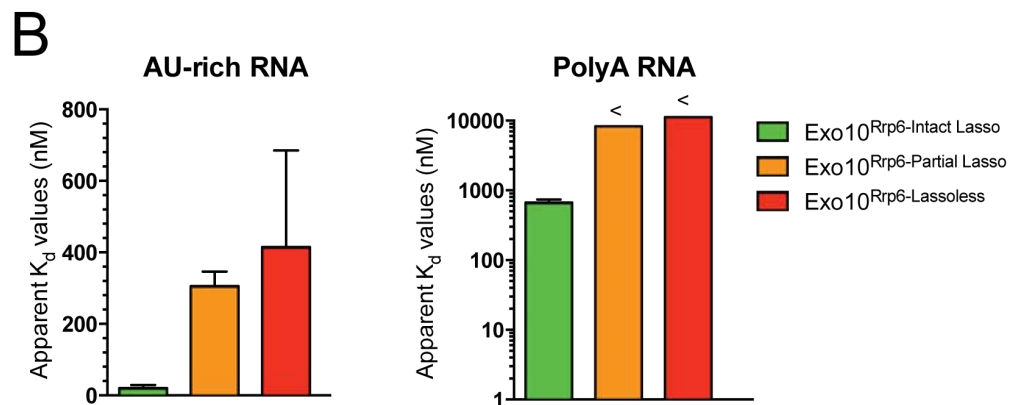
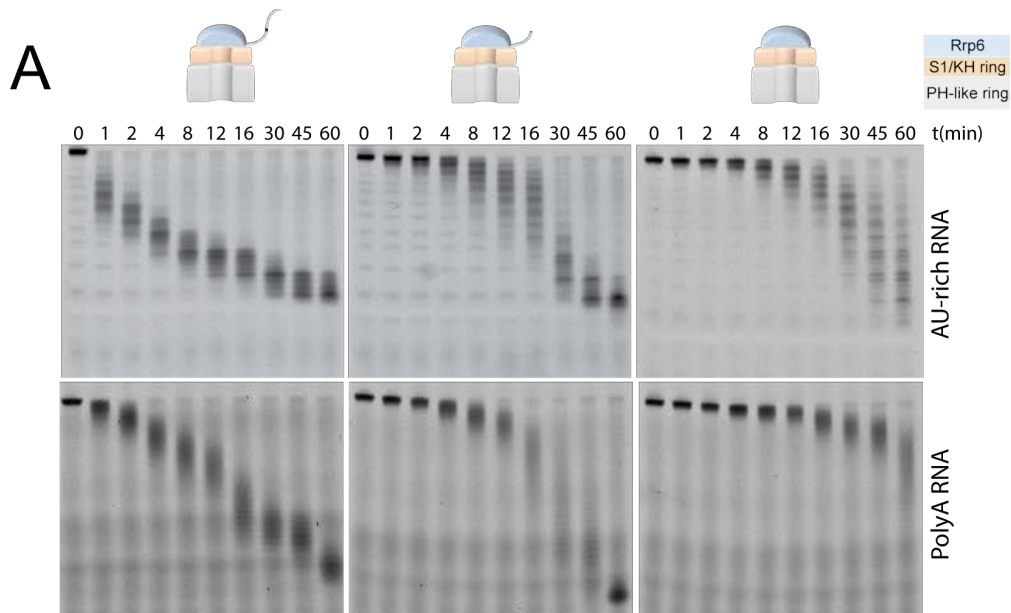


Figure 38. The Rrp6 lasso enhances RNA binding and the rate of decay in Exo10⁶.

(A) Rrp6 activity is severely attenuated when the lasso is compromised in the context of Exo10⁶. RNA decay assays performed using synthetic 5' fluorescein labeled 49

nucleotide (nt) polyA RNA with reconstituted exosomes, with intermediates resolved by denaturing PAGE. (B) Catalytically dead Rrp6 variants (D238N) of Exo10⁶ with different lasso lengths were analyzed for their ability to bind 36 nt AU-rich RNA and 37 nt polyA RNA via fluorescence polarization. Results of triplicate experiments shown. (C) Decay of 10 nM polyA RNA by 1 nM Exo10⁶, with and without the Rrp6 lasso. Exo10^{6-IntactLasso} can be modeled as two-phase decay, while Exo10^{6-Lassoless} follows a one-phase decay mechanism. Fraction of full-length substrate (49 nt) was plotted as a function of reaction time (min).

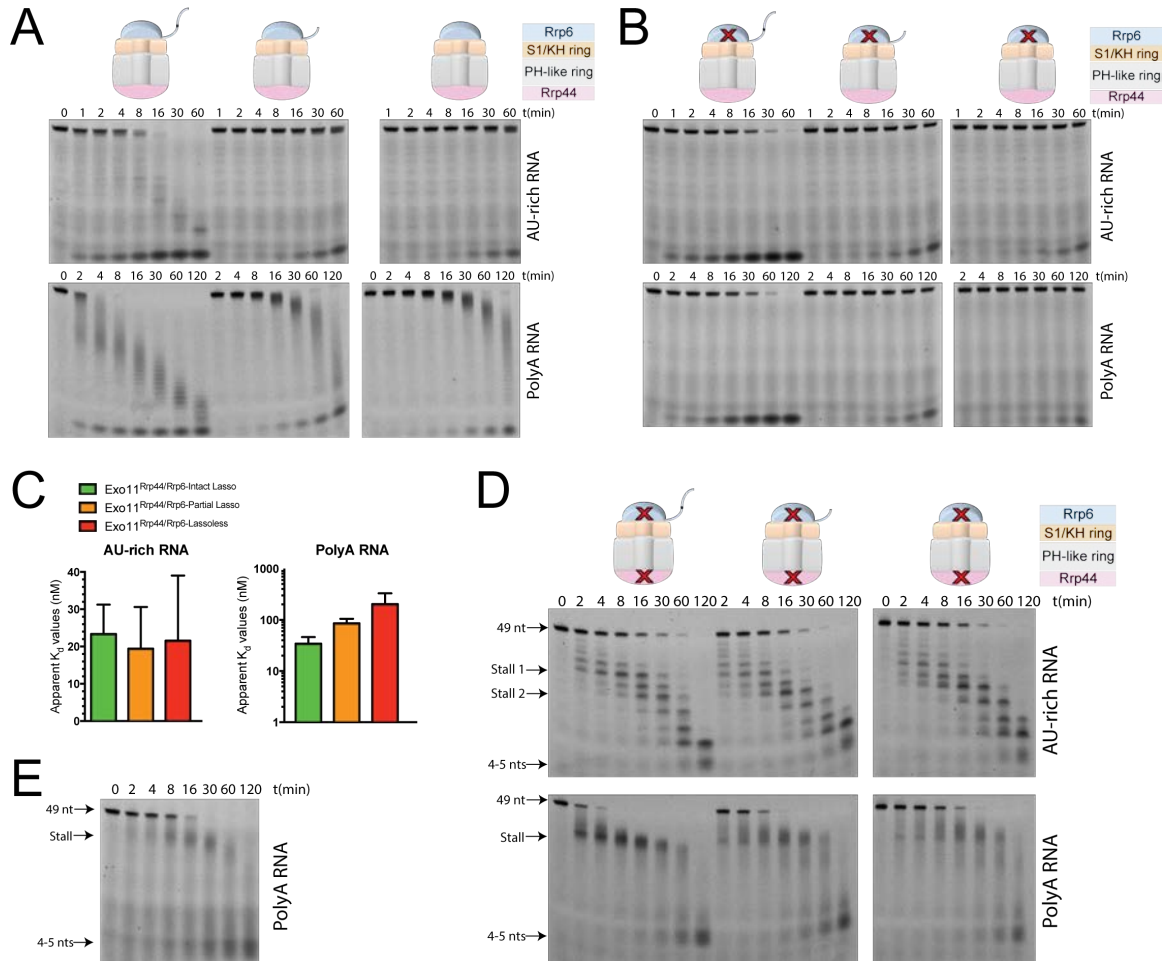


Figure 39. The Rrp6 lasso stimulates all three ribonuclease activities of the nuclear exosome, Exo11^{44/6}.

(A,B) RNA decay assays performed using 5' fluorescein labeled 49 nucleotide (nt) polyA RNA with reconstituted Exo11^{44/6} and Exo11^{44/6exo-}. AU-rich RNA was assayed at 12°C to be able to observe differences in Rrp44 activity due to lasso deletion. PolyA RNA was assayed at 30°C. (C) Binding of different lasso variants of Exo11^{44exo-/6exo-} to 5' fluorescein AU-rich 36 nt and polyA 37 nt RNAs was determined by fluorescence polarization. (D) Endonuclease activity of Rrp44 in the context of different lasso variants was assayed in Exo11^{44exo-/6exo-} for decay of AU-rich and polyA RNAs. (E) The EAR and lasso of Rrp6 are not necessary to facilitate access of polyA RNA to Rrp44 in Exo10^{44exo-/Csl4-Rrp6CAT}. See Figure 44 for details regarding this complex.

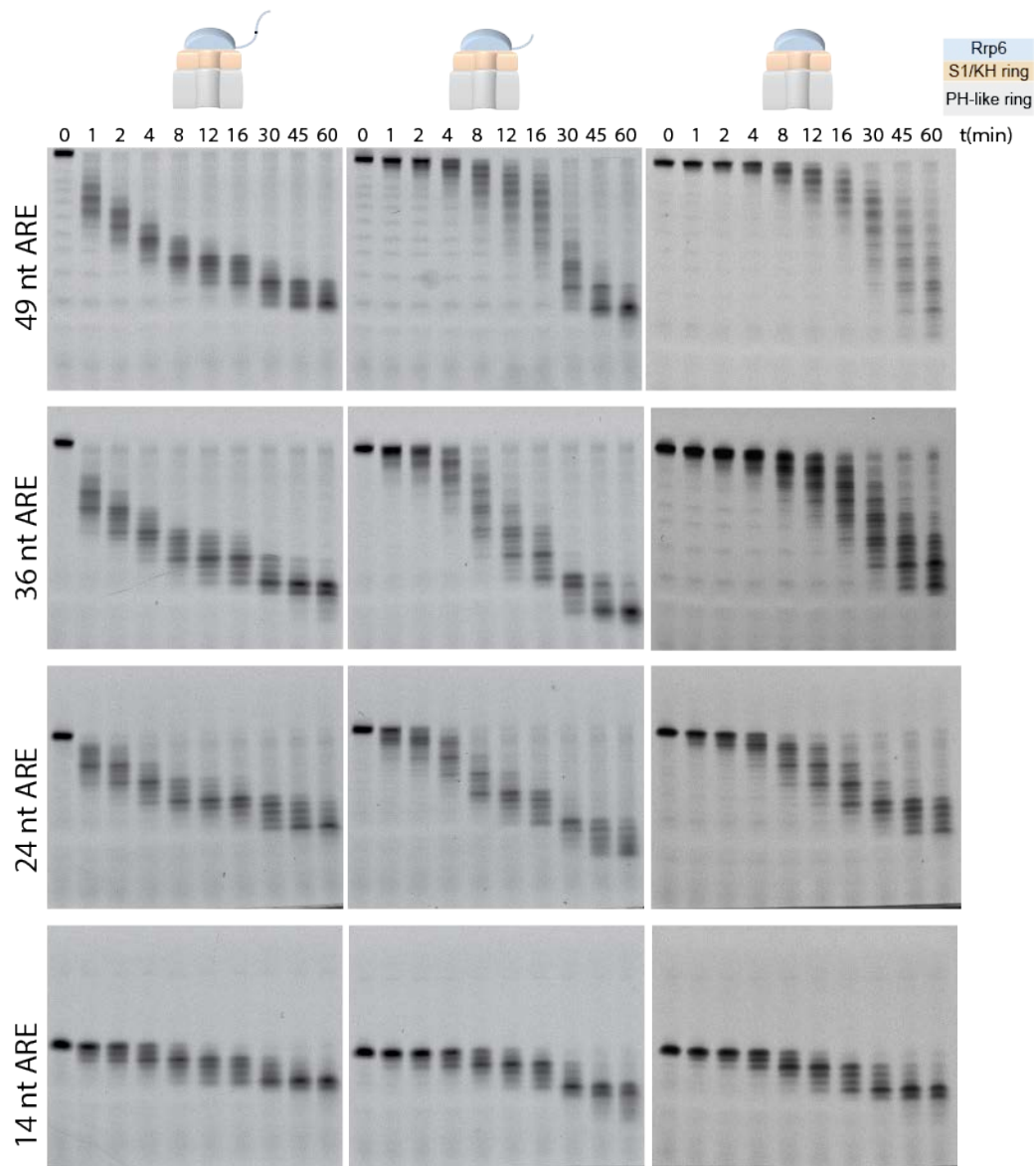


Figure 40. The Rrp6 lasso facilitates efficient decay of longer RNA.

Different lasso variants of Exo10⁶ were assayed for their activities on 5' fluorescein-labeled 49, 36, 24, and 14 nt single-stranded AU-rich RNAs. Intermediates were resolved by denaturing PAGE.

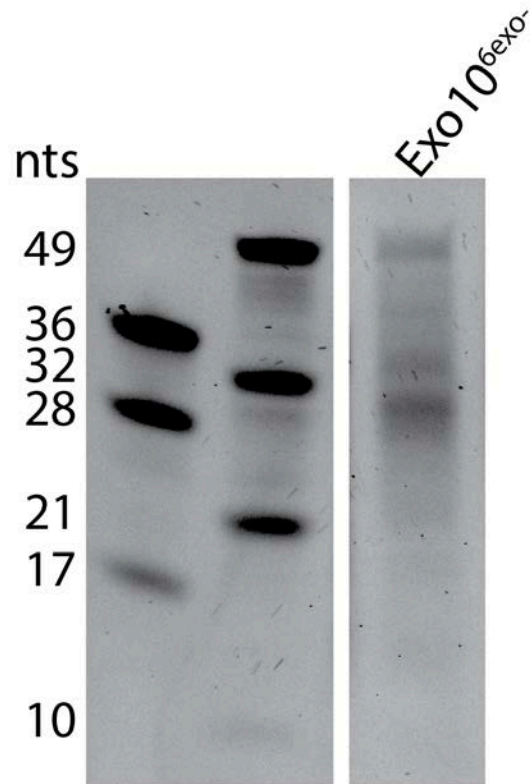


Figure 41. Ribonuclease A protection of single-stranded RNA by Exo10^{6exo-}.

Exo10^{6exo-} was incubated with unlabeled 49 nt single-stranded AU-rich RNA and subjected to ribonuclease A digestion for 3 minutes before the reaction was quenched with phenol. RNA intermediates were purified by phenol:chloroform:isoamyl alcohol extraction and ethanol precipitation and separated by denaturing PAGE, and visualized with Sybr Gold.

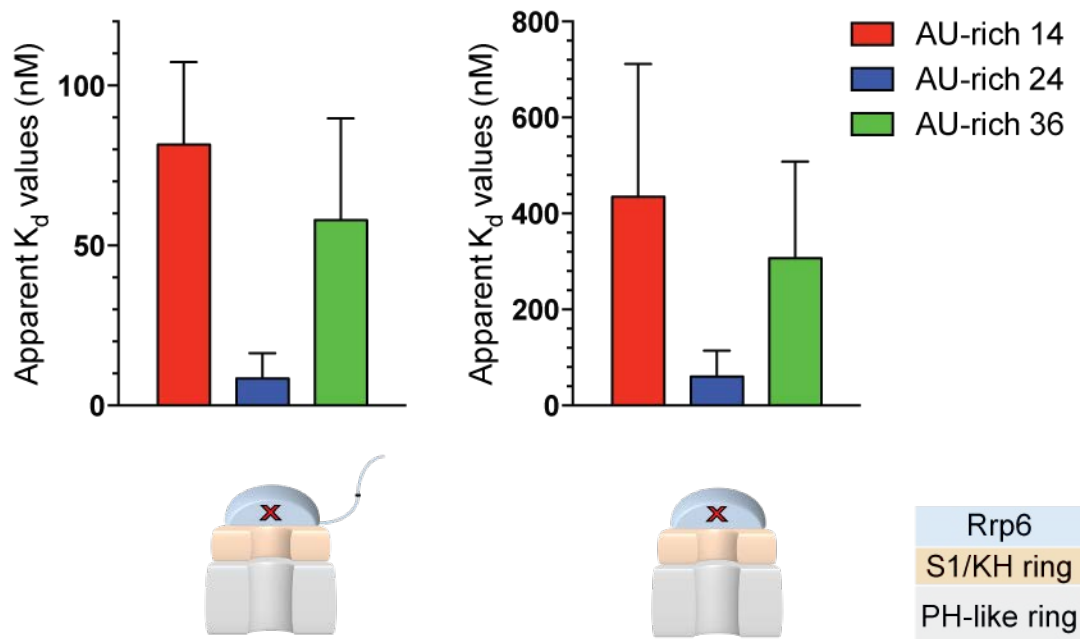


Figure 42. Exo10⁶ binding to different length RNAs.

50 nM of 5' fluorescein single-stranded AU-rich RNA of 14, 24, and 36 nts were incubated with various concentrations of catalytically dead Exo10^{6-IntactLasso} and Exo10^{6-Lassoless} and binding measure by fluorescence polarization.

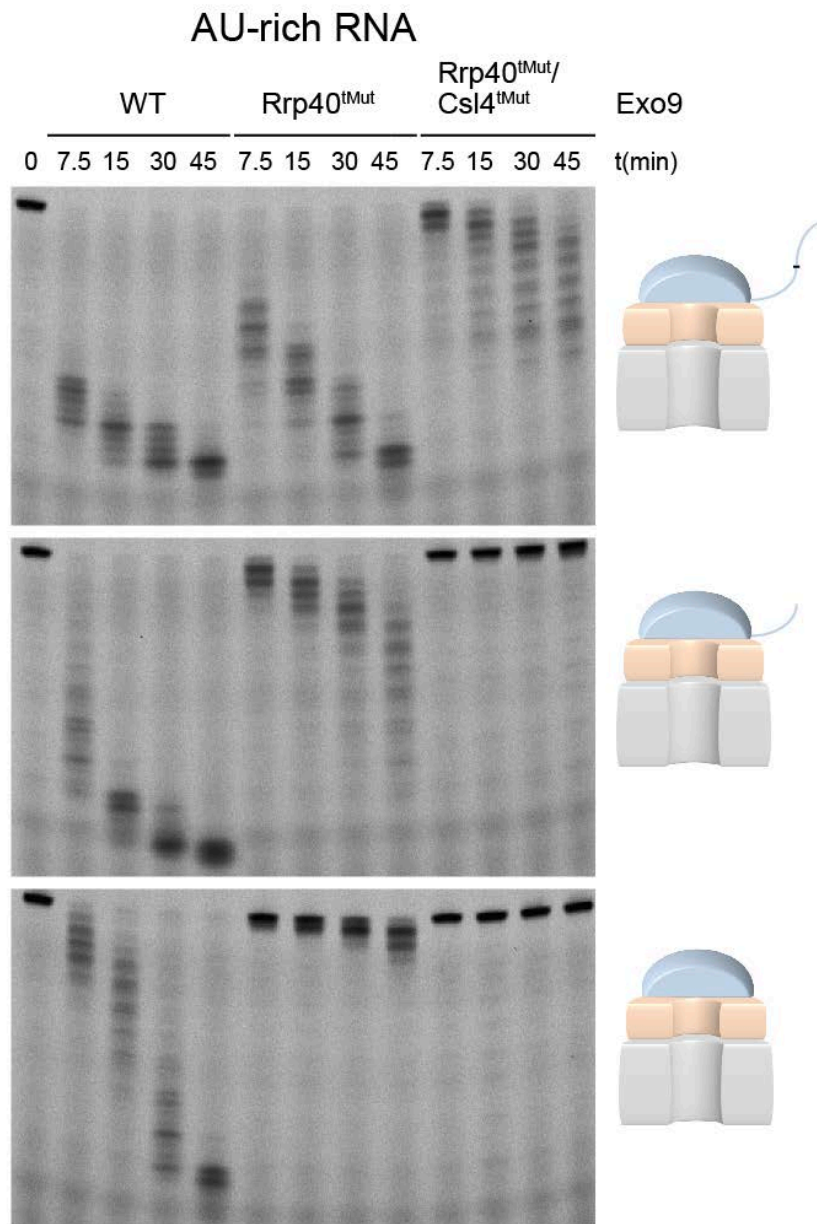


Figure 43. The Rrp6 lasso recruits RNA through the Exo9 S1/KH ring in Exo10⁶.

Exo10⁶ with different lasso lengths (intact, partial, and lassoless) with mutations within the S1/KH ring described in Chapter 2 were assayed for their activities on 5' fluorescein single-stranded 49 nt AU-rich RNA. Exo10⁶ with lasso deletions were more sensitive to mutations within the S1/KH ring. RNA intermediates were resolved by denaturing PAGE and visualized with a fluoroimager.

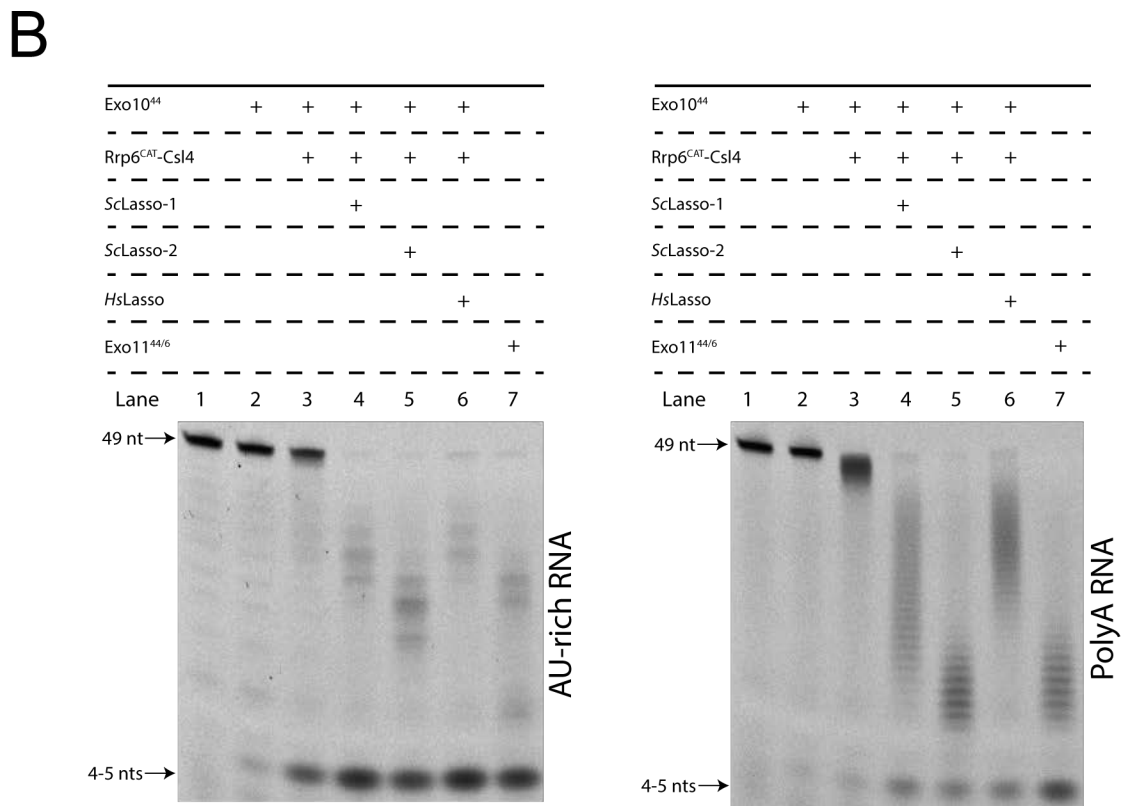
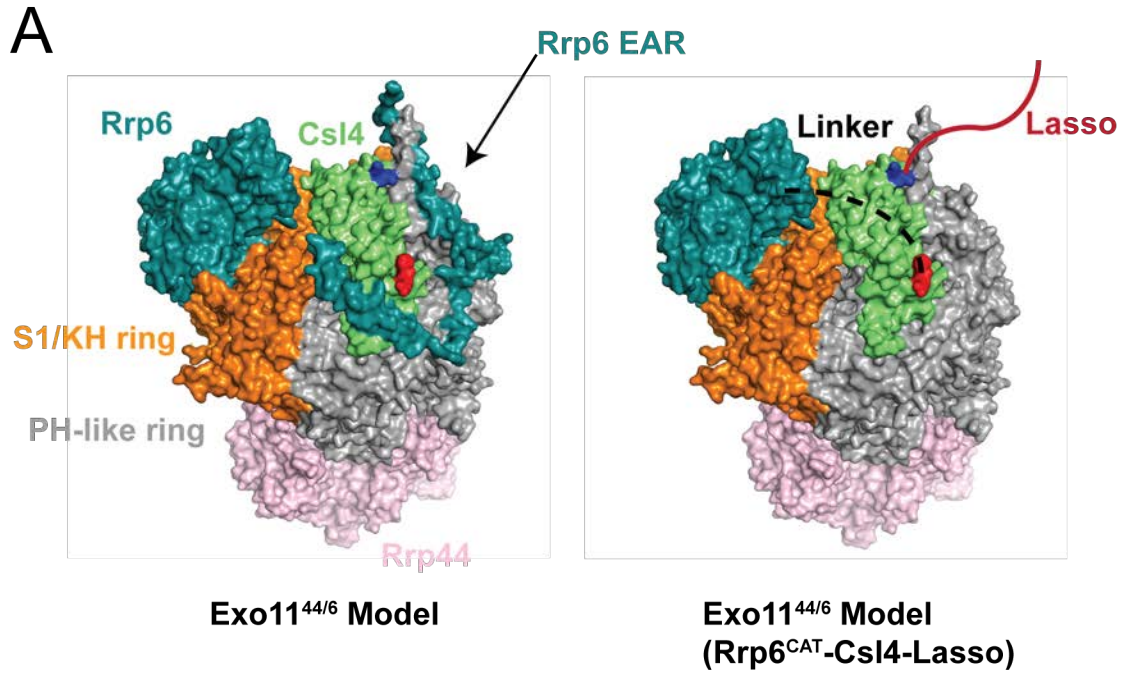


Figure 44. The Rrp6 lasso stimulates Rrp6 and Rrp44 activities independent of the EAR through a conserved mechanism.

(A) Left: Structure of Exo10⁶ (PDB: 4OO1). Right: Strategy for fusing the C-terminus of Rrp6-CAT to the N-terminus of Csl4 (red) to tether Rrp6-CAT to Exo9, bypassing the need for the Rrp6 EAR, and for appending variants of the Rrp6 lasso to the C-terminus of Csl4 (blue), proximal to where the C-terminus of the Rrp6 EAR would be. (B) Endpoint decay (60 minutes) of 5' fluorescein labeled 49 nt AU-rich RNA (left) and polyA RNA (right) by various reconstituted exosomes under multiple turnover conditions. Rrp6^{CAT-Csl4} signifies Exo10^{44WT} reconstituted with catalytically competent Rrp6^{CAT-Csl4}; ScLasso-1, ScLasso-2, and HsLasso represent the same complex, but with the C-terminus of Csl4 bearing fusions of Rrp6 lasso regions 685-733, 618-733 from *S. cerevisiae*, and 741 to 885 from *H. sapiens*, respectively.

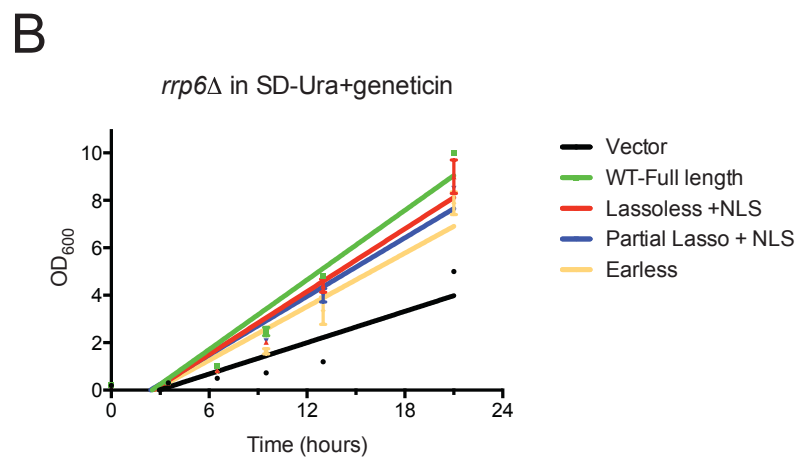
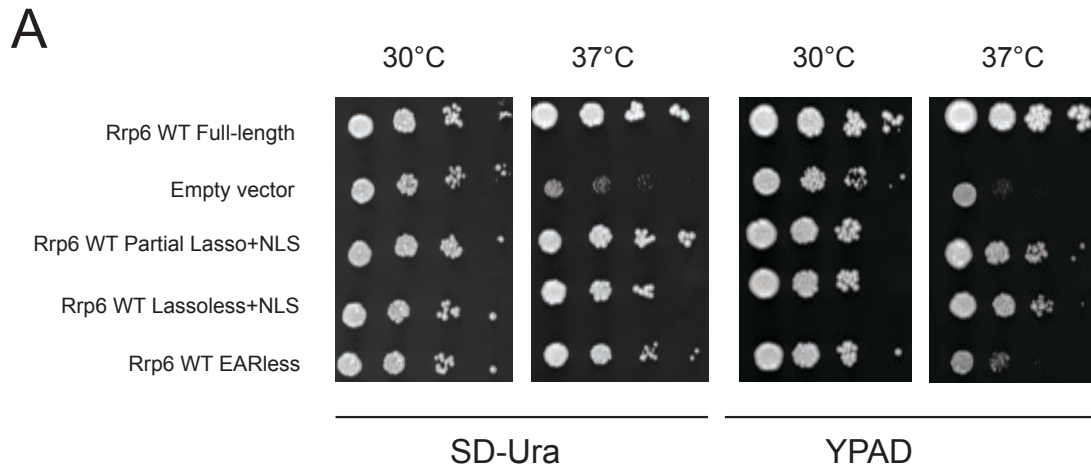


Figure 45. The importance of the Rrp6 lasso *in vivo*.

(A) Serial 10-fold dilutions of *S. cerevisiae* W303 *rrp6Δ* bearing *RRP6* or mutant *rrp6* containing lasso or EAR deletions, spotted on solid agar composed of minimal (SD-Ura, left) or rich (YPAD, right) media supplemented with 200 μg/mL geneticin and grown at 30°C and 37°C. (B) Liquid culture growths of the transformants in (A) in minimal media supplemented with 200 μg/mL geneticin and grown at 37°C.

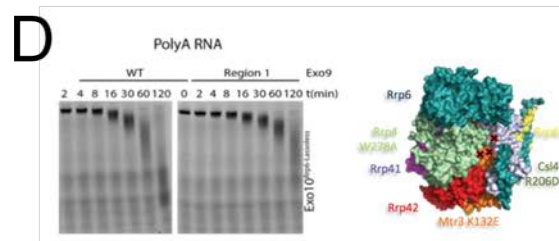
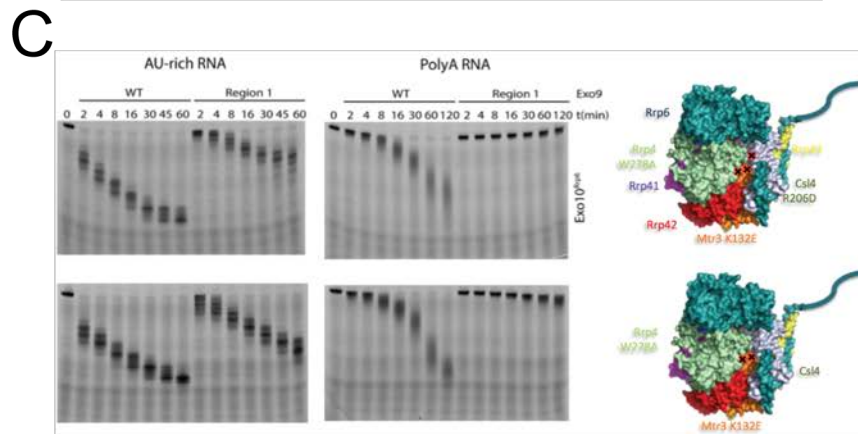
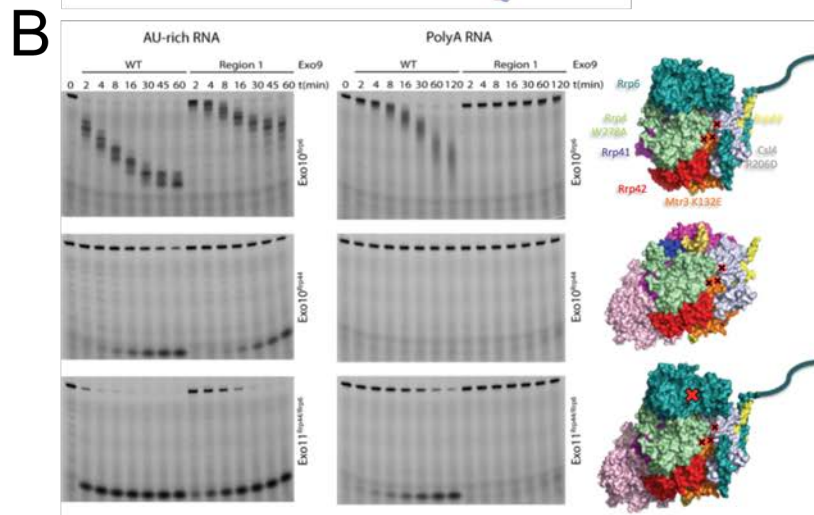
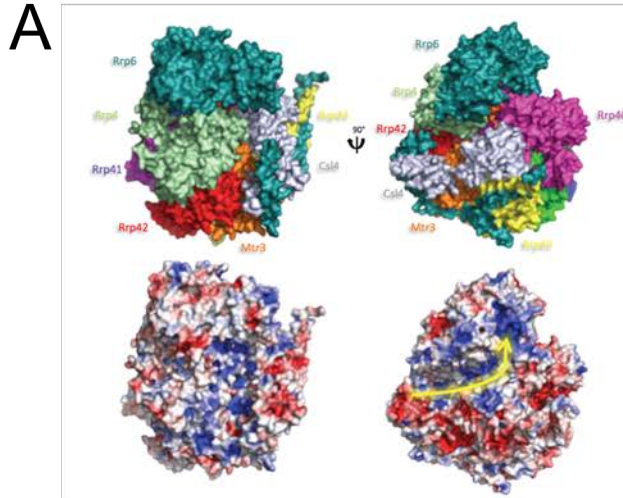


Figure 46. An identified route of RNA ingress in Exo10⁶ and Exo11^{44/6}.

(A) Based on the structure of Exo10⁶ bound to polyA RNA, potential routes of RNA ingress to Rrp6 were analyzed based on surface architecture and electrostatics of Exo9. A candidate path formed by Rrp4, Mtr3, Rrp42, and Csl4 was selected for mutational analysis. Electrostatics were calculated using APBS⁹⁰. (B) 1 nM Exo10⁶, Exo10⁴⁴, and Exo11^{44WT/6exo-} were assayed for their activities on 10 nM 5' fluorescein 49 nt AU-rich (left) and polyA RNAs (right) when three point mutations were introduced in the candidate region (Rrp4 W278A/Mtr3 K132E/Csl4 R206D). (C) A double mutant (Rrp4 W278A/Mtr3 K132E), while more active than the triple mutant, still inhibits Rrp6 exoribonuclease activity in Exo10⁶, particularly on polyA RNA. RNA intermediates were analyzed by denaturing PAGE and imaged by a fluoroimager. (D) Candidate region mutations have little effect on Exo10^{6-Lassoless} decay of polyA RNA, suggesting that the Rrp6 lasso directs RNA towards this route of ingress. 2.5 nM Exo10^{6-Lassoless} with or without mutations in the candidate region were incubated with 10 nM 5' fluorescein polyA RNA for the indicated timepoints.

CHAPTER 4

Insight to Exosome Stimulation by its Nuclear Cofactor, Mpp6

4.1 Introduction

Mpp6 is a small (21 kDa, 186 residue) nuclear protein cofactor of the eukaryotic RNA exosome. TAP-tagged Mpp6 pulled down all 11 subunits of the nuclear exosome in stoichiometric quantities, and in addition, Rrp47, Nrd1, and components of the TRAMP complex – Mtr4, Trf4, Air1 and Air2 (Ref. 119). Genetic studies in *S. cerevisiae* have shown that while Mpp6 is not essential, its deletion is synthetic lethal with the Rrp6 cofactor, Rrp47, and with Rrp6 (Ref. 68, 119). These findings have led to the notion that Mpp6 stimulates Rrp44 activity in the context of the exosome, and not Rrp6; nevertheless, no *in vitro* studies have directly shown how Mpp6 (or any protein cofactor of the exosome) modulates exosome activity, if at all. Furthermore, RNA intermediates that accumulate in the absence of Mpp6 are similar to those found in deletions of components of the TRAMP complex, suggesting overlapping functions^{119,135}. The results discussed in this final chapter will address biochemical and structural aspects of Mpp6 stimulation of exosome activity.

4.2 Mpp6 is a disordered protein that binds nucleic acid

The limited genetic and biochemical data surrounding Mpp6 focuses on its function in the context of the full-length protein. Details regarding its domain structure and insight to its molecular function have not been studied. Mpp6 is a highly basic protein, with a pI of 9.98, and has been shown to bind nucleic acid in budding yeast and in human¹³⁶, with a preference for polyU sequences¹¹⁹. Despite its conserved function,

Mpp6 only contains two small stretches of high sequence conservation, one in its N-terminal region and one in its core (Figure 48A)¹¹⁹. Based on secondary structure prediction, the former is predicted to form an alpha-helix (residues 10-22, Helix 1), while the latter is thought to be composed of a small beta-strand (109-116, Strand 2) (Figure 48B). The remainder of Mpp6 is poorly conserved, and predicted to be primarily disordered, the exception being a beta-strand (81-89, Strand 1), and a C-terminal helix (160-170, Helix 2).

To determine the molecular architecture of Mpp6, and to determine how it modulates exosome activity, if at all, recombinant Mpp6 was expressed as a Smt3-fusion in *E. coli* and subsequently purified. Analysis of pure Mpp6 by circular dichroism indeed suggests that Mpp6 is unstructured (Figure 49A). Recombinant Mpp6 was highly contaminated with nucleic acid after two chromatography steps (IMAC and size exclusion); an extra ion exchange chromatography step was necessary to separate nucleic acid from Mpp6 (either heparin or MonoS), which could be performed either before or after Smt3 cleavage with Ulp1 (Figure 49B). Nucleic acid-free Mpp6 was then tested for its ability to bind RNA *in vitro* via fluorescence polarization (Figure 49C). Similar to previous results, Mpp6 tightly bound polyU RNA, with a K_d of 168 nM, along with similar binding to the flexible AU-rich RNA (62 nM). Mpp6 was also able to bind polyA RNA in my assay, albeit to a lesser extent, with a K_d of 1.379 μM. This finding is consistent with polyA RNA being a substrate of the nuclear exosome.

4.3 Mpp6 primarily stimulates Rrp6 in an Exo9-dependent manner

Mpp6 was mixed with Exo9 in molar excess and assayed for interaction via gel filtration. Full-length Mpp6 runs on SDS-PAGE around the same molecular weight as the smallest exosome core subunits, Rrp46, Rrp40, and Mtr3 so a C-terminal truncation of

Mpp6 (1-156) was used early on to unambiguously confirm association with Exo9. Consistent with recent results published⁷¹, Exo9 is sufficient for Mpp6 association (Figure 50). In contrast, Mpp6 failed to associate with either of the catalytic subunits, Rrp6 or Rrp44.

To test the effect of Mpp6 on exosome activity, Mpp6 was mixed with exosomes reconstituted with Rrp6, Rrp44, or both. The presence of Mpp6 on Exo10⁶ resulted in a modest 2-fold gain-of-function in degradation of flexible AU-rich RNA, but a more substantial 8- to 10-fold activation on more rigid polyA RNA (Figure 51A). The magnitude of Rrp6 stimulation on decay of both RNAs was the same in the context of Exo11^{44/6}, with even a slight decrease in Rrp44 exoribonuclease activity (Figure 51B). The endoribonuclease activity of Rrp44 in Exo11^{44exo-/6exo-} was also unaffected by Mpp6 (Figure 52A). Similarly, Mpp6 diverts short wave UV-induced RNA crosslinks from Rrp44 to Rrp6 in Exo11^{44exo-endo-/6exo-} (Figure 51C). Interestingly, Mpp6 can stimulate Rrp44 exoribonuclease activity in the nuclear exosome if Rrp44 is the only catalytically active site - Exo11^{44/6exo-} exhibits approximately a 2.5-fold gain-of-function on polyA RNA (Figure 52B). No greater advantage towards decay of AU-rich RNA is observed when Mpp6 is present.

It has been well established that Rrp47 is a Rrp6 protein cofactor that binds to and stimulates Rrp6 by interacting with its N-terminus, thus resulting in its stabilization *in vivo*^{67,68}. Because a population of exosome independent Rrp6 exists in *S. cerevisiae*⁶³, Rrp47 association and function is not limited to the exosome, unlike the case with Mpp6. To evaluate if Mpp6 and Rrp47 confer different effects on nuclear exosome activity, which would be consistent with the synthetic lethality observed *in vivo*, Mpp6, Rrp47, or both were mixed with Exo11^{44/6} reconstituted with full-length Rrp6, as Rrp47 requires the N-terminal PMC2NT domain for association^{67,71}. Decay was monitored on single-stranded polyA RNA and on unmodified tRNA_{iMet}, a known substrate for the nuclear

exosome¹³⁷. Both Mpp6 and Rrp47 added in isolation resulted in the same magnitude of stimulation specifically for Rrp6 – approximately 8-fold for polyA RNA, and 4-fold for tRNA_{iMet} – and none for Rrp44; no advantage in decay was evident when both cofactors were mixed together on either RNA (Figure 53A,B). These results do not explain the observed synthetic lethality between Rrp47 and Mpp6 – it is possible that distinct RNA classes are preferentially degraded by one cofactor versus the other; that knocking out Rrp47 and Mpp6 results in the crippling of Rrp6 activity, both in and out of the exosome; or that Mpp6 and Rrp47 are both involved in recruitment of other protein factors. It was recently demonstrated that Rrp47 recruits Mtr4, the RNA helicase in TRAMP, to Rrp6 (Ref. 71). It remains to be seen how, if at all, Mpp6 contributes to this interaction.

Although it does not associate with Mpp6 *in vivo*, the cytoplasmic exosome, Exo10⁴⁴, was assayed for RNA decay in the presence of Mpp6. No activation of Exo10⁴⁴ was observed on polyA RNA; however, Mpp6 resulted in a modest 2.5-fold gain-of-function of Rrp44 activity on AU-rich RNA (Figure 54A). Finally, Mpp6 was mixed with Rrp44 (Figure 54B) and Rrp6 (Figure 54C) in isolation. Consistent with the gel filtration results discussed above, Mpp6 failed to alter the activities of the catalytic subunits outside of the exosome. Taken together, these findings suggest that Mpp6 is primarily a nuclear exosome Rrp6 cofactor, because it preferentially stimulates Rrp6 activity in an exosome-dependent fashion in the context of the model RNA substrates discussed.

4.4 Mpp6 facilitates decay of both PolyA and PolyU RNAs

The explanation for the more substantial effect of Mpp6-stimulated decay of polyA rather than AU-rich RNA cannot simply be distilled to preferential decay of structured versus unstructured RNAs because Mpp6 similarly stimulates Exo10⁶ and Exo11^{44/6} 8-fold on polyU RNA (Figure 55), which like AU-rich RNA, is unstructured. The

significance of these findings is unclear because oligouridylation, a 3' posttranscriptional tag associated with RNA decay by the exosome and other exoribonucleases¹³⁸⁻¹⁴⁰, has not been described in budding yeast. Because this process has been characterized in fission yeast and mammals, it is possible that the findings presented here may extend to orthologous species equipped with oligouridylation machinery. Indeed, Rrp44 demonstrates robust activity on Exo11^{44/6}, almost entirely excluding Rrp6 from accessing polyU RNA (although this bias is less in the presence of Mpp6), consistent with studies of Dis3 and Dis3L2 in mammals and fission yeast^{38,39,41}.

4.5 RNA ingresses through the S1/KH ring to Rrp6 in Exo10⁶ in the presence of Mpp6

To determine if Mpp6 stimulates Rrp6 activity primarily through the Exo9 central channel, exosomes bearing mutations within the PH-like and S1/KH rings were assayed in the presence and absence of Mpp6. Rrp6 exosomes were used because the presence or absence of catalytically active Rrp44 did not affect the magnitude of Mpp6-dependent stimulation of Rrp6. Exo10⁶ bearing a large insertion in the lower half of the PH-like ring (Rrp41-WT/Rrp45-Large) was previously reported to be 3.5-fold less active than channel open exosomes on polyA RNA. Addition of Mpp6 relieved the PH-like ring channel inhibition, and was as active as channel open Exo10⁶ with Mpp6 (Figure 56A). Introduction of two medium-sized insertions within the PH-like ring (Rrp41-Medium/Rrp45-Medium) inhibits Rrp6 activity to a greater extent, approximately 10-fold¹¹⁶. Therefore, Mpp6 Exo10^{6exo-} with and without these channel occlusions were reconstituted for binding studies by fluorescence polarization (Figure 56B). Reliable measurements could not be determined for Exo10^{6/channel-} (binding greater than 10 μ M); however, Exo10^{6/Mpp6/channel-} bound polyA RNA with a Kd of 207 nM, 3.8 fold tighter than Exo10^{6/channel+} (782 nM), but 2.3 times weaker than Exo10^{6/Mpp6/channel+} (92 nM). Although

impaired in its ability to bind and degrade RNA in comparison to its channel open counterpart, Exo10⁶^{Mpp6/channel-} may be more active than wild-type Exo10⁶ because RNA no longer relies as heavily on the PH-like ring RNA binding site to reach Rrp6 when Mpp6 contributes an additional, non-exclusive RNA surface, or because a route distinct from that observed in the Rrp6-exosome crystal structure is utilized in a Mpp6-associated exosome. To test this possibility, Exo10⁶ bearing mutations in the S1/KH ring (Chapter 2, Figure 29) and lining the Exo9 central channel were assayed with and without Mpp6. Consistent with previous observations, these mutations resulted in the inability to degrade polyA RNA. Unlike the described mutations in the PH-like ring, the presence of Mpp6 activated Exo10⁶, but exhibited approximately a 4-fold defect in decay relative to wild-type Exo10⁶ (Figure 56C). On AU-rich RNA, mutation of RNA binding sites in the S1/KH ring resulted in attenuated activity, with a loss of the “bundling” of intermediates characteristic of Rrp6-exosome decay, with a wider distribution of intermediates similar to that observed in free Rrp6, perhaps due to a higher off rate with a compromised central channel. Interestingly, Mpp6, although 2-fold less active than wild-type Exo10⁶, restores the exosome-specific pattern of intermediates. While these results do not differentiate between the possibilities of a second channel independent route taken by RNA in the presence of Mpp6 or an activating conformational change induced in Exo9 and/or Rrp6 upon Mpp6 association, they nevertheless highlight the relevance of the RNA path to Rrp6 observed in the Exo10⁶ crystal structure for Mpp6-stimulated RNA decay.

Further evidence for the Mpp6 exosome utilizing a similar mode of RNA ingress as described in previous biochemical and structural studies (i.e. through the S1/KH ring) was provided through long-wave UV crosslinking of RNAs containing single 4-thiouridine substitutions at various positions from the 3' end (Chapter 2) (Figure 57A) Besides the appearance of a small molecular weight crosslink likely corresponding to

Mpp6 in Exo10^{6/Mpp6}, and potentially one to two extra slightly larger crosslinks to 4thiouridine 6 nt from the 3' end, patterns of crosslinks were identical between Exo10⁶ and Exo10^{6/Mpp6} for polyA 4thiouridine RNAs. However, overall intensities of crosslinks were greater for Exo10^{6/Mpp6}, which is consistent with the biochemical results discussed above.

Additionally, the protection pattern of single-stranded 49 nucleotide AU-rich RNA by catalytically dead Rrp6 exosomes with or without Mpp6 was probed by ribonuclease A. Rrp44 containing exosomes were evaluated first, as their protection patterns have been published previously²⁵. Exo10^{44exo-} protected RNA fragments between 32 to 33 nucleotides, consistent with previous results (Figure 57B). Consistent with RNA being bound primarily by Rrp44 in Exo11^{44/6} (Chapter 2, Figure 31), the protection pattern of 32 to 33 nucleotides did not change in Exo11^{44exo-/6exo-}. However, the extent of protection is greater, with a larger population of RNA bound, consistent with measured binding affinities due to the Rrp6-dependent activation of Rrp44 (Chapter 1, Figure 10). Due to its distributive nature and more solvent exposed RNA binding paths (Chapter 1, Figure 13; Chapter 2, Figure 24), Exo10^{6exo-} exhibited much weaker protection than that of Rrp44-containing exosomes. Nevertheless, protection was observed for fragments ranging from 28 to 30 nucleotides. Mpp6 did not alter the length or distribution of RNA protected, but did improve the extent of protection, consistent with its enhancement of RNA binding in Exo10⁶.

Exo11^{44exo-/6WT} in the presence of RNAs 36 nt and longer was found to be one of the most potent, albeit indirect, inhibitors of Rrp6 activity I have characterized *in vitro* (Chapter 1)¹¹⁶. Rrp44^{exo-} preferentially binds RNA by its 3' end, while the free 5' end of the RNA sterically and electrostatically occludes other RNA molecules from approaching Rrp6, resulting in approximately a 100-fold decrease in Rrp6 activity. To test if Mpp6 can bypass this inhibitory effect of Rrp44^{exo-} and shunt RNA elsewhere to gain access to

Rrp6, Exo11^{44exo-/6WT} was assayed on polyA RNA in the absence and presence of Mpp6. Mpp6 alleviated some of the inhibition by Rrp44^{exo-} (Figure 57C), but the bundling of intermediates characteristic of Rrp6 decay in Exo10⁶ was lost, suggesting that the exosome/Mpp6 RNA binding surface is compromised by the free 5' end of the bound RNA. This result provides further evidence that RNA ingress towards Rrp6 in Exo11^{44/6} is consistent in the presence or absence of Mpp6. It also suggests that while Mpp6 appears to commit a larger population of RNA to distributive trimming by Rrp6, RNA binding by Rrp44 remains substantially strong, such that the population of RNA engaging Rrp44 persists long enough to continually block new RNAs from accessing the Rrp6 active site.

4.6 Identification of a minimal region of Mpp6 sufficient for exosome binding and stimulation

Mpp6-induced activation of the Rrp6 exosome may occur because of the following non-mutually exclusive possibilities: the disordered, basic stretches of Mpp6 may serve as an electrostatic trap to recruit RNA towards the exosome; or Mpp6 binding may induce conformational changes in the exosome, and potentially Rrp6, that are more favorable for RNA ingress and decay. To determine the regions of Mpp6 necessary for exosome stimulation, truncations from the N- and C-terminal ends of Mpp6 were cloned, expressed, purified, and assayed for both stimulation of Exo10⁶ exoribonuclease activity and exosome association. Because of its apparent lack of secondary structure in isolation, truncations were made in fine increments of approximately 10 to 20 residues, in the event that these regions of Mpp6 become ordered upon exosome association (Figure 58A). In addition to the full-length construct (1-186), truncations were made to disrupt the conserved Helix 1 (23-186); to disrupt or preserve the two beta-strands in the

Mpp6 core 91-186 (Δ Strand1), 81-120 (Strand 1&2 only), 81-186 (Strand 1&2 with intact C-terminus), 23-120 (Strand 1&2 with mostly intact N-terminus^{**}); to truncate at (1-156) or disrupt (1-165) Helix 2; and to target interspersing loop regions (44-186), (59-186), (1-174). In addition, full-length Mpp6 from *Kluyveromyces lactis* (*K. lactis*) was cloned, expressed, purified and assayed to determine if orthologous Mpp6 from the same family, *Saccharomycetaceae*, maintains similar properties as that from *S. cerevisiae*. *K. lactis* Mpp6 is 176 amino acids long, has a basic pI of 9.8, and is predicted to have similar secondary structure elements as *S. cerevisiae*.

Except for 91-186 (Δ Strand1) and *K. lactis* Mpp6, all of the constructs stably associated with the exosome (Figure 58A) and stimulated Exo10⁶ decay of polyA RNA to the same extent (Figure 58B). Therefore, Strands 1 & 2 compose the minimal exosome binding region (residues 81-120), with all other regions dispensable for exosome activation. Deletion of Helix 1 did not affect Mpp6 association with the exosome or its ability to stimulate Exo10⁶. It is possible that it is conserved from yeast to man for recruitment of other protein components of the exosome, for instance the TRAMP complex. Surprisingly, Δ Strand1 did not stimulate Exo10⁶ at all, while *K. lactis* Mpp6 stimulated approximately 3-fold, suggesting partial association with Exo10⁶, despite only 25% sequence similarity within the minimal exosome binding region of Mpp6.

Similarly, four of the Mpp6 constructs were compared for their ability to bind polyA 24 RNA via fluorescence polarization: full-length, the minimal region (81-120), Δ N half (81-186), and Δ C half (23-120). Only Δ N half Mpp6 bound RNA with substantially weaker affinity, with the Mpp6 minimal construct capable of binding RNA with a similar affinity as the full-length protein (Figure 58C). These results suggest that the model of Mpp6 serving as an electrostatic trap composed of highly basic, disordered regions that

^{**} Construct 1-120 could not be stably expressed.

recruit distal RNA molecules, similar to the Rrp6 lasso (Chapter 3), is unlikely and that the latter scenario is more probable.

4.7 Crystallization of Mpp6 Exosomes

To determine how Mpp6 stimulates exosome activity, I sought to crystallize a Mpp6 bound exosome. Crystals of RNA-bound Exo10^{6exo-/Mpp6} were readily obtained in various conditions; however, because of the inherent flexibility of Mpp6, and due to its stimulatory effect on Rrp6 and therefore potential residual ribonuclease activity over time, it was extremely challenging to obtain well-diffracting crystals.

After performing sparse-matrix screens at various temperatures and finding initial crystal hits, all of the following combinations and pre-crystallization treatments were exhausted to improve crystals of Exo10^{6exo-/Mpp6}: all Mpp6 constructs described above; selenomethionine-incorporated Mpp6 for placement of Mpp6 via calculated anomalous signal from selenomethionine¹⁴¹; partial, intact, and lasso-deleted flavors of Rrp6 exosomes; Exo9 PH-like ring channel occluded exosomes to maximize RNA occupancy towards a potential Mpp6/Rrp6 route of ingress; single-stranded RNAs of various lengths, sequences, preparations, and molar ratios to exosome; in drop limited proteolysis using papain, subtilisin, chymotrypsin and trypsin to facilitate improved crystal contacts by removal of disordered regions that may poison crystal contacts¹⁴²; chemical additives through rational candidate and unbiased approaches¹⁴³; and seeding¹⁴⁴. Extensive post-crystallization treatments were also explored with varied success, including dehydration, cryoprotection under oil, mixed cyroprotectants using the “confusion principle,” data collection at room temperature in a humidity controlled device (HC1 and NE-CAT, Advanced Photon Source), and glutaraldehyde crosslinking¹⁴⁵. After two years of screening over 800 crystals ranging in size from 30 micrometers to 1

millimeter, derived from various initial hits, all crystals obtained of Mpp6-Exo10⁶ were the same crystal form – rod-shaped crystals that contained P32 symmetry, with 3 exosome in the asymmetric unit (ASU). Certain additives exacerbated crystal growth problems – for example, ethylene glycol, which was necessary to increase crystal size, tended to produce overlapping, multiple crystals that appeared by eye to arise from a single nucleation; certain truncations of Mpp6 resulted in crystals with high mosaicity and twinning fractions. All crystals were mosaic; coupled with the large unit cell (269 to 286; 269 to 286; 125 to 128 angstroms for a, b, and c, respectively, depending on post-crystallization treatment), finding crystals with well-separated reflections was a concern. Another challenge was the diffraction limit of this crystal form, presumably from poor crystal contacts and the intrinsic disorder of Mpp6. This is reflected in the fact that the vast majority of crystals could not diffract beyond 5.5 to 6 angstroms, a common dropoff point in intensities for protein crystals, and that any crystal that diffracted beyond 5.5 angstroms was consistently anisotropic to varying degrees. Nevertheless, most obtained datasets were of good enough quality for molecular replacement and their structures determined using Exo10⁶ as a search model. The best diffracting crystal to date of Exo10⁶_{exo-/Mpp6} contains polyA24 at a 1:3 molar ratio (at least 3-fold molar excess RNA:exosome was required to obtain any crystals); contains full-length Mpp6 and Rrp6 with a partial lasso (128-685); required 6 months to grow (final size of ~300 micrometers in the longest direction) in 2% MPD, 200 mM ammonium nitrate, 13% PEG3350; but required dehydration to 25% with PEG3350 supplemented with 10% ethylene glycol for cryoprotection. Despite mild anisotropy in the smallest dimension, it diffracted to 4.5 angstroms overall, and contains 3 exosomes in its asymmetric unit (Figure 59A), with variable density potentially corresponding to Mpp6 in each exosome related by non-crystallographic symmetry (NCS). Placing two generic beta-strands into this density in two of the three NCS copies further improved maps.

Another approach to obtain crystals of Mpp6 exosomes was to crystallize Exo12^{44exo-endo-/6exo-/Mpp6} with both Rrp44 and Rrp6 active sites immobilized by a dual 3' ended single-stranded RNA synthesized via click chemistry¹⁴⁶. Discussion of the methodology used and characterization of this reagent will not be expanded upon because the author of this document did not directly synthesize this RNA, but briefly, in the presence of Cu⁺², two single-stranded RNAs are “clicked” together via their 5' ends if one contains an alkyl group and the other an azide group, and the resulting RNA purified by HPLC.

The 3'-3' RNA was mixed with Exo11^{44exo-endo-/6exo-} reconstituted with minimal Mpp6 (82-120) at a 1.1:1 molar ratio and screened by sparse matrix crystallization screens. Crystals only grew at 4°C, and appeared in the screens after one week, and by one month, grew to their full size of 150 to 200 micrometers. These crystals do not suffer from as much disorder and mosaicity issues of the Exo10⁶+Mpp6 crystals, as they have stronger crystal contacts. They are consistently anisotropic, however, and range in severity. A single crystal diffracted to 3.6 angstroms, with one molecule in the ASU and P212121 symmetry. The structure was determined by molecular replacement using Exo10⁶ and the Rrp44-Rrp41-Rrp45 trimer as search models.

4.8 A Diversion about a Divergent RNA Path to Rrp44

It is apparent in the model that 3'-3' RNA is not spanning the entire central channel from Rrp6 to Rrp44 active as predicted during its conception and design; in contrast, it bridges two symmetry-related exosomes, with RNA bypassing the Exo9 channel and emerging from the “direct access” route of Rrp44 (Ref. 118) from one 3' end and angling into the Rrp6 active site via its other 3' end (Figure 59B). Within the EXO domain of Rrp6, a number of conserved residues within loop regions coordinate the RNA

from its active site towards where the N-terminal PMC2NT domain would be, including Lys131, Tyr244, Arg245, Tyr344, Arg350, Tyr432, which form part of a conserved, basic patch (Figure 60A). The RNA is then directed towards two distinct Rrp44 molecules from different symmetry mates (Figure 60B). As RNA does not appear to take this route in the Exo10⁶+Mpp6 structure, it remains to be seen if this RNA path represents that of the Rrp47-Rrp6-associated exosome; an exosome-independent path (Rrp6-Rrp47 heterodimer); or is an artifact of crystal packing.

Rrp44 is swung out, similar to the “apo” conformation observed by cryo-electron microscopy¹¹⁸, unlike the familiar swung in conformation visualized by crystallography and cryo-EM that represents Rrp44 engaged with RNA traversing the entire Exo9 central channel (Figure 61A). It is not clear if this conformation represents a productive complex, and if so, when and why this path to Rrp44 is utilized. It is interesting to note that despite the dramatic pivoting required of Rrp44 to swing “in” and “out,” the RNA path adopted is always that described in the crystal structure of free Rrp44 bound to RNA, rather than that of bacterial RNase II or mammalian Dis3L2 (Figure 8).

The swung out conformation likely represents that observed in UV-induced crosslinking experiments of channel occluded Exo10⁴⁴, whereby RNA-protein crosslinks are observed only to Rrp44 and not to exosome core subunits; and in the endoribonuclease assays of Exo10⁴⁴, in which polyA RNA is degraded in a pattern consistent with free Rrp44 and lacks the exosome-specific “footprint” of endoribonuclease decay, consistent with Exo10⁴⁴ being virtually incapable of binding and degrading this RNA (Chapter 1, Figures 10,12). It has been postulated that that this route may be used for processing of structured RNAs, or RNAs too short to reach Rrp44 via Exo9 central channel, which would not benefit from the large, composite RNA binding interface¹¹⁸ If this is true, then short RNAs should be processed through the Rrp44 direct access route, and longer RNAs diverted from a through-channel path to

direct access in the presence of a channel occlusion. Exo10^{44/channel+} and Exo10^{44/channel-} were assayed for activities on single-stranded 49, 36, 24, and 14 nt AU-rich RNA (Figure 61B). As previously reported, PH-like ring channel occlusions inhibit Rrp44 activity in Exo10⁴⁴; the difference in levels of inhibition between channel open and occluded exosomes becomes less apparent the smaller the RNA, with virtually no difference in decay on a 14 nt RNA, one too short to span the Exo9 central channel to Rrp44 (Figure 57B, Ref. 25). Nevertheless, the population of RNA processed by the direct access route is vanishingly small in comparison to the through channel route, with no enhancement of RNA degradation via direct access in the presence of channel occlusions. Furthermore, this assay performed on channel open and occluded Exo11^{44/6} resulted in the diversion of RNAs too short and those impeded by channel occlusions regardless of length to Rrp6, rather than to the Rrp44 direct access route. Although the *in vitro* results presented here do not support a substantial role for this newly identified path, the possibilities of its biological relevance in processing specific RNAs of a defined structure and sequence, or its propensity for regulation by an as-of-yet discovered post-translational modification cannot be discounted.

Further details regarding the Mpp6-independent features of this structural model will not be discussed because another independent researcher in my laboratory is currently characterizing the significance of the conformational switch of Rrp44 at atomic resolution (2.9 angstroms) based on a similar crystal form. Subsequent discussion will be limited to the notable differences between the Mpp6-bound and apo models of Exo10⁶ and Exo11^{44exo-endo-/6exo-}.

4.9 Mpp6 Associates with the S1/KH ring Subunit, Rrp40

In both structures of Mpp6-bound exosomes, mostly contiguous unmodeled density appears in the same regions: spanning across the KH domain of Rrp40, and then wedging between its S1 and N-terminal domains (NTD) (Figure 62A). Because the structure of Exo12^{44exo-endo-/6exo-/Mpp6} contains the minimal fragment of Mpp6 (Strands 1&2) necessary to enhance exosome activity, it can be inferred that the unaccounted for density observed in the same region of Exo11^{6/Mpp6} corresponds to this minimal Mpp6 fragment. Even at low resolution the density is consistent with two beta strands connected by a disordered loop, in accordance with the secondary structure prediction for this region. Nevertheless, either more work is needed to improve the pre-existing maps, or higher quality data will need to be obtained to attempt to assign the register of Mpp6. Furthermore, the NTD of Rrp40 is poorly ordered and may undergo structural rearrangement, a possibility given that NMR studies have shown that the NTD is disordered in the absence of exosome association³¹. Therefore, this region of the model, and any conclusions drawn about Mpp6 association, need to be cautiously interpreted at this stage. Despite this caveat, the S1 and KH domains of Rrp40 are ordered and thus these observed binding surfaces may be tentatively discussed.

The minimal region of Mpp6 that crystallized is highly basic, with a pI of 10.11. Electrostatics calculations of Rrp40 reveal large acidic patches corresponding to where the modeled Mpp6 beta strands associate (Figure 62B). Based on secondary structure prediction, a disordered region of approximately 16 to 18 residues connects the two beta strands. Weaker, positive density is observed between the modeled beta strands in the higher resolution model of Exo12^{44exo-endo-/6exo-/Mpp6}, likely corresponding to this loop (Figure 62C – FEM density). The surface of Rrp40 is similarly negative in this region. Furthermore, the Mpp6 binding surface of Rrp40 is highly conserved (Figure 62B). Interestingly, the only other region of Rrp40 that is as conserved is the portion of the S1

domain responsible for coordinating RNA along the Exo9 central channel, and the scaffolding interactions that lock the PH-like ring subunits Rrp46 and Rrp45 together. Despite the high conservation, the Rrp40-Mpp6 interface is expansive, thus utilizes all three domains of Rrp40 as a binding platform for Mpp6. Consistent with this, two point mutations in Rrp40 predicted to partially impede Mpp6 interaction, K183A/E185A, were not sufficient to alter either Mpp6 association with the exosome or stimulation of polyA decay by Exo10⁶ (Figure 63A). Meanwhile, exosomes lacking Rrp40 altogether could not associate with Mpp6, nor did Rrp6 exosome activity undergo Mpp6-dependent stimulation (Figure 63B). Although Mpp6 appears to interact primarily with Rrp40 based on the two structural models, Rrp40 is not sufficient for Mpp6 interaction as assayed by gel filtration chromatography, either in its full-length or minimal form (Figure 63C). This is likely because the NTD of the Rrp40 subunit is disordered and known to undergo structural rearrangement to beta-hairpins upon exosome binding; this conformational change may be necessary for Mpp6 interaction, or other surfaces of the Exo9 may be required for stable Mpp6 association.

So how does Mpp6 stimulate exosome activity? Alignment of Exo12<sup>44exo-endo-/6exo-
/Mpp6</sup> with Exo11^{44exo-endo-/6exo-} by the PH-like ring reveals conformational changes in the Rrp6 catalytic module (CAT). Specifically, the Rrp6 CAT appears more “open” in the presence of Mpp6, and is peeled away from the Exo9 central channel, facilitating greater RNA access to the S1/KH ring. This conformation is likely to be due to Mpp6 rather than an artifact of crystal packing or the non-canonical RNA route via the Rrp6 EXO domain (Figure 64A) because it is similarly present in all three NCS copies of Exo11^{6exo-/Mpp6} in comparison to Exo10^{6exo-} (Figure 64B). However, no significant changes in Exo9 are apparent, including channel widening of the S1/KH ring (Figure 64C, Figure 34). Additionally, the catalytic module of Rrp44 is further swung out; however, at this stage of

analysis, it is likely that this conformational change is due to differences in crystal packing in the Mpp6-bound and apo exosomes.

The observed conformational rotation of Rrp6 CAT in Mpp6 associated exosomes may be due to the destabilization of the molecular contacts bridging loops within the S1 domain of Rrp40 to a helix in the Rrp6 EXO domain (Figure 65A). For instance, in Exo11^{44exo-endo-/6exo-}, Arg325 of Rrp6 hydrogen bonds to the backbones of Pro111 and Arg110 in Rrp40; Tyr330 contacts Gln114; Glu333 hydrogen bonds to Thr112; and Gln345 interacts with Asn109. However, all contacts except for a hydrogen bond between Arg325 of Rrp6 and the backbone of Arg110 in Rrp40 are lost in Exo12^{44exo-endo-/6exo-/Mpp6}. Except for Gln345 of Rrp6 to Asn109 of Rrp40, all of the aforementioned contacts are observed in Exo10^{6exo-} (Figure 65B)¹²⁶; conversely, no contacts are preserved in Exo11^{6exo-/Mpp6}. While the current structural model does not coherently describe how, if at all, Mpp6 exerts this effect, it is possible that satisfying the acidic patch of Rrp40 with the set of basic contacts contributed by Mpp6 may distally weaken the interaction between the S1 domain Rrp40 and the Rrp6 catalytic domain, thus making the Rrp6 catalytic module, and its RNA binding surfaces, more accessible to ingressing RNA.

Given the stimulatory effect of Mpp6 on Exo10⁶ activity, its binding surface on Rrp40, and the more open configuration of the Rrp6 CAT, Exo10⁶ bearing mutations in the Rrp4/Mtr3/Rrp42/Csl4 cleft described in Chapter 3 (Region 1) were assayed in the presence of Mpp6 because two point mutations (Mtr3 K132E and Rrp4 W278A) are sufficient to nearly ablate Exo10⁶ decay of polyA RNA *in vitro* (Figure 46), despite being orthogonal to the Mpp6 binding surface (Region 2). Addition of Mpp6 was sufficient to overcome the RNA decay defect introduced by the Region 1 mutations; Exo10^{6/Region1Mut/Mpp6} was more active than Exo10⁶, but still less active than Exo10^{6/Mpp6} (Figure 66). It remains to be seen if Mpp6 enhances RNA ingress through Region 2 by

binding RNA directly, or if it alleviates the dependency of Exo10⁶ on Region 1 by indirectly making Rrp6 CAT more accessible to approaching RNAs. Finer UV-crosslinking experiments using RNAs with single 4-thiouridine substitutions every two nucleotides to compare RNA crosslinks between Exo10⁶ and Exo10^{6/Mpp6}, with and without Region 1 mutants, will help distinguish between these possibilities.

4.10 Cooperativity between the Rrp6 Lasso and Mpp6

Another observation from electron density maps of all Mpp6-associated exosomes crystallized is that the Rrp6 CTD/Rrp43 NTD beta-hairpin interaction^{52,126} appears to take a turn towards the C-terminal zinc ribbon domain of Csl4 and the NTD of Rrp40, rather than being directed upwards and towards the solvent as observed in the structure of Exo10⁶ (Figure 67A,B). This latter positioning of the Rrp6 CTD/Rrp43 NTD was crucial for formation of crystal contacts. Interestingly, crystals of Exo11^{6exo-/Mpp6} were not readily attainable in this crystallization condition, despite the accessibility of the Mpp6 binding surface of Rrp40. Nevertheless, crystals stochastically formed in one crystallization drop out of hundreds only in the presence of the minimal Mpp6 construct. Although these few crystals could not diffract beyond 5.6 angstroms, it was evident that their crystal packing diverged from Exo10⁶ (monoclinic P1211 rather than orthorhombic P22121, with two copies in the ASU rather than one) and that the Rrp6 CTD/Rrp43 NTD was no longer involved in crystal contacts. Rather, unmodeled density consistent with interactions with Csl4 and Rrp40 is visible (Figure 67C).

To test the significance of this potential interaction, Exo10⁶ reconstituted with either full-length, partial or lassoless Rrp6 was assayed for decay of polyA RNA in the presence and absence of the minimal Mpp6 construct (Figure 68A). As observed previously, lasso intact Exo10⁶ is stimulated at least 10-fold by Mpp6; however, either

partial or complete loss of the Rrp6 lasso attenuates the magnitude of Mpp6-mediated stimulation of polyA decay by Exo10⁶ to less than 2-fold, suggesting a potential cooperativity mechanism between the Rrp6 lasso and Mpp6. To test this possibility, Exo10⁴⁴ was assayed with either the Rrp6 CTD (EAR plus full lasso), Mpp6, or both because Rrp44 is known to be inactive on polyA RNA in the absence of intact Rrp6 (Figure 34). As previously observed, the Rrp6 CTD alone was marginally capable of activating Exo10⁴⁴, while Mpp6 alone had no effect (Figure 68B). However, the combination of both the Rrp6 CTD and Mpp6 significantly activated Exo10⁴⁴, to levels indistinguishable from exosomes reconstituted with intact Rrp6 (Figure 68C). This intriguing result suggests that Mpp6, in conjunction with the Rrp6 CTD, somehow bypasses the necessity for Rrp6 CAT-induced activation of Rrp44 in the nuclear exosome.

4.11 Conclusions

In summary, the experiments discussed here suggest that Mpp6 associates with Exo9, binding primarily to the S1/KH subunit, Rrp40. Mpp6 preferentially stimulates Rrp6 in the context of the exosome, utilizing RNA binding surfaces within the upper region of the Exo9 central channel, that are primarily Region 1 independent. The greatest effects of Mpp6-mediated stimulation are observed for polyA RNA, which is degraded 8 to 10-fold more efficiently by Rrp6 exosomes in the presence of Mpp6, while AU-rich RNA is modestly stimulated approximately 2-fold. As a result, the differences in Exo10⁶ rates of decay for polyA and AU-rich RNAs described in Chapter 1 are virtually non-existent. Thus, the presence of this small nuclear cofactor facilitates efficient decay of a nuclear substrate, polyA RNA. This stimulation is also coupled to the Rrp6 lasso (Figure 69). Furthermore, Mpp6 can induce Rrp44 stimulation on polyA RNA in the presence of

catalytically compromised Rrp6 with an intact CTD. Higher resolution structures and more quantitative biochemical experiments will elucidate the precise nature of this cooperativity. Finally, a minimal region consisting of two to three conserved beta-strands is sufficient to bind Exo9 and stimulate the exosome as efficiently as full-length Mpp6. The structure of this 4.5 kDa peptide bound to RNA-engaged Exo10⁶ and Exo11^{44/6} reveals a potential basis for Mpp6 stimulation of Rrp6 activity, as networks of hydrogen bonds to Rrp40 are lost, resulting in a minor displacement of Rrp6 CAT that facilitates access to an RNA binding surfaces involving Mpp6, the S1/KH ring, and the Rrp6 lasso and its active site.

Although it is not clear if an Rrp6 CTD-Mpp6 interaction (if it directly exists) can induce a gating mechanism to Rrp44, similar to that of the Rrp6 CAT observed in Exo10⁶, it would be interesting to determine if these two modules interact genetically. Specifically, would deletion of Mpp6 in the lassoless strains described in Chapter 3 result in an exacerbated growth phenotype, or synthetic lethality, as is known for $\Delta rrp6\Delta mpp6$ (Ref. 119)? Furthermore, what is the significance of the highly conserved N-terminal helix of Mpp6, particularly in a protein that is otherwise poorly conserved? Would the minimal fragment of Mpp6 that is sufficient for exosome association and stimulation *in vitro* complement the growth defect of $\Delta mpp6$ *in vivo*, or are the N- and C-terminal halves of Mpp6 performing as of yet undiscovered functions in recruitment of nuclear protein cofactors/complexes, or providing additional layers of regulation to exosome function?

Figure 48. Mpp6 is a small, positively charged and disordered protein with poor sequence conservation.

(A) Two small stretches of Mpp6 are highly conserved throughout eukaryotes (Sequence analysis and panel from *Milligan et. al, 2008, Ref.119*). (B) Mpp6 is mainly disordered, but features two helices in its N- and C-terminal ends, and two to three beta strands within its core. Black arrows signify where N- and C-terminal truncations were made (see section 4.6). Secondary structure prediction performed with Jpred¹⁴⁷.

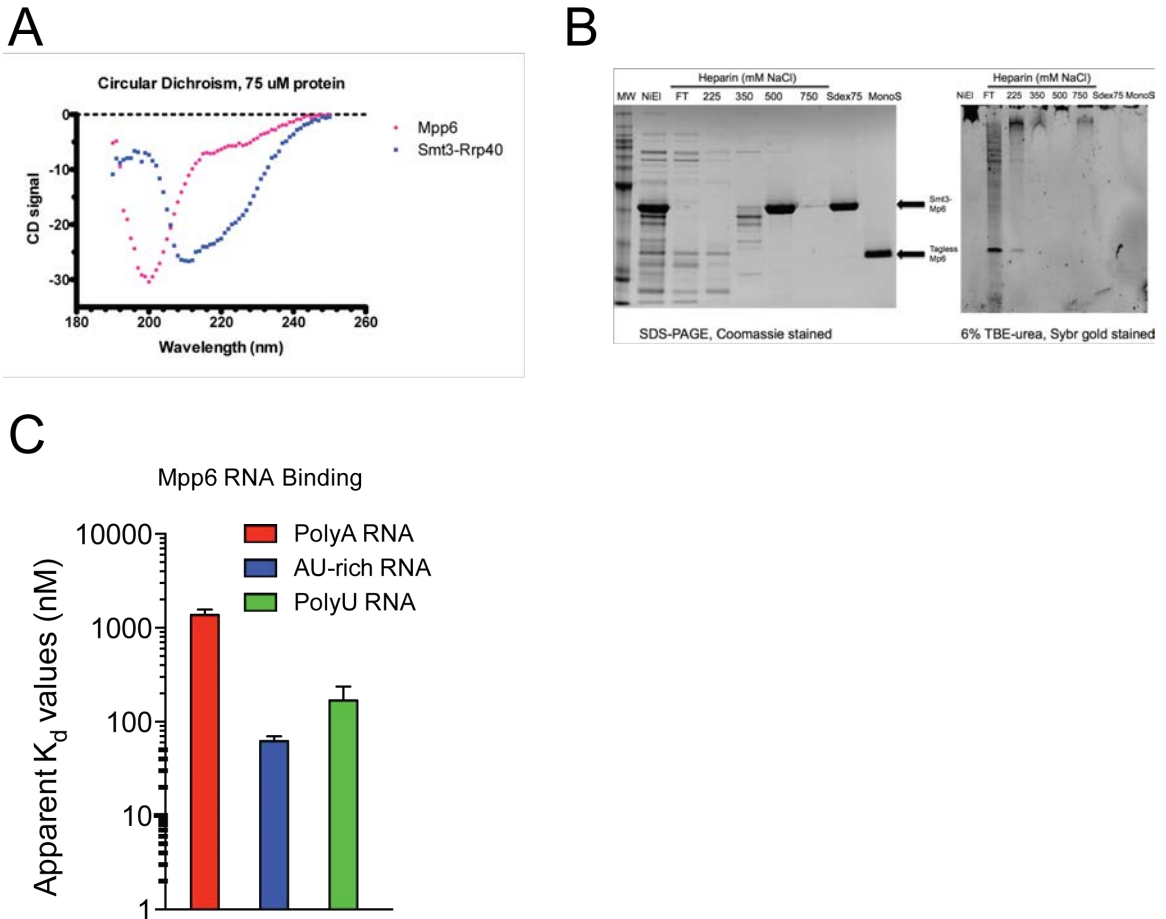


Figure 49. Mpp6 is a disordered protein that binds RNA.

(A) Circular dichroism spectra comparing Mpp6 (pink) to Smt3-Rrp40 (blue). Data collected for Mpp6 is consistent with random coil, while Smt3-Rrp40 suggests presence of secondary structure, including alpha-helices and beta-sheets. Spectra collected at room temperature. (B) Recombinant Smt3-Mpp6 copurifies with nucleic acid from *E. coli* that can be removed by cation exchange chromatography. (C) Recombinant tagless Mpp6 binds 36 nt AU-rich and polyU RNAs with nanomolar affinities, and is also competent to bind 37 nt polyA RNA, as assayed by fluorescence polarization using 5'fluorescein single-stranded RNAs.

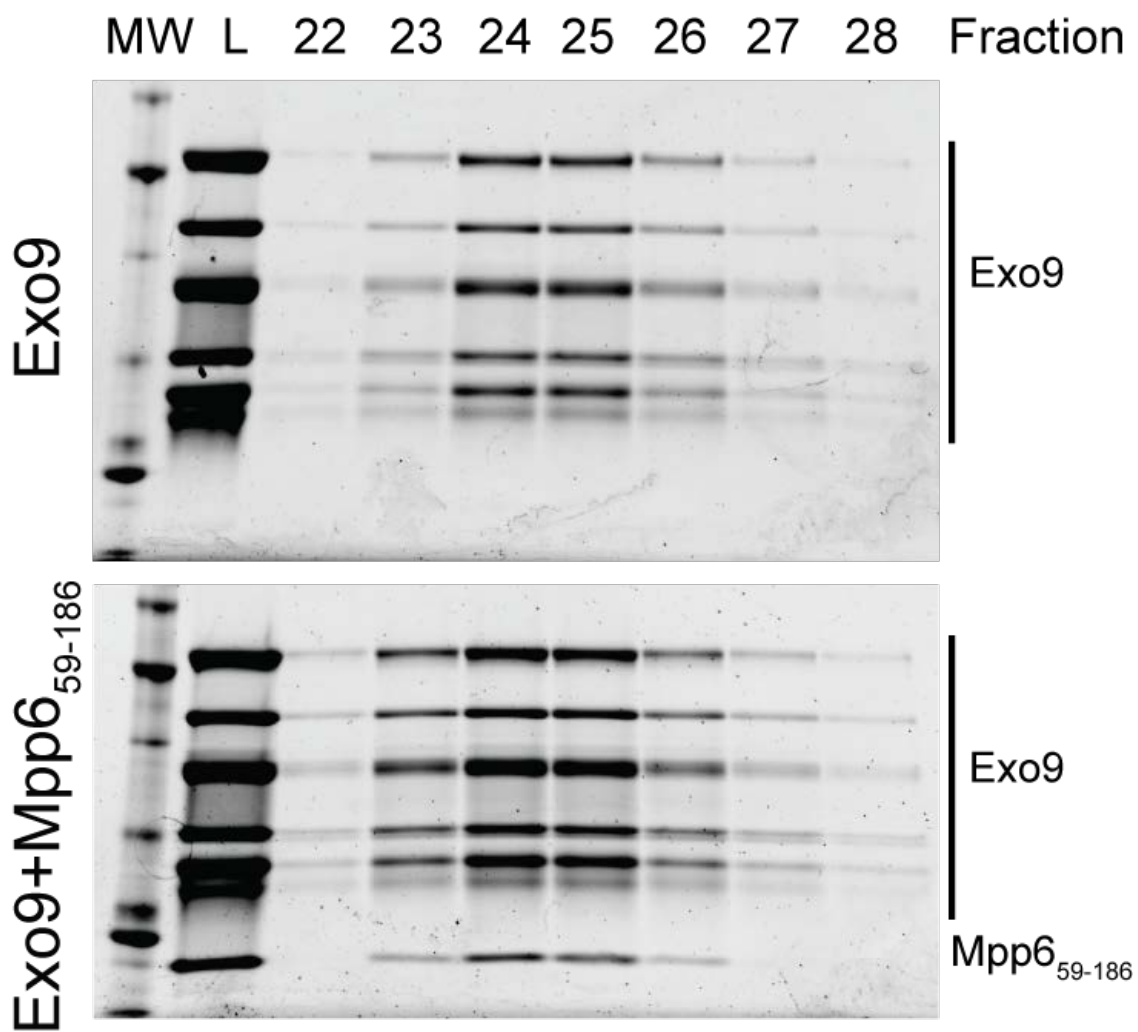


Figure 50. Exo9 is sufficient for Mpp6 association.

Mpp6₅₉₋₁₈₆ was mixed with Exo9 in a 3:1 molar ratio and run on analytical gel filtration (Superose 6). Pooled fractions were analyzed by SDS-PAGE and stained with Sybr Gold.

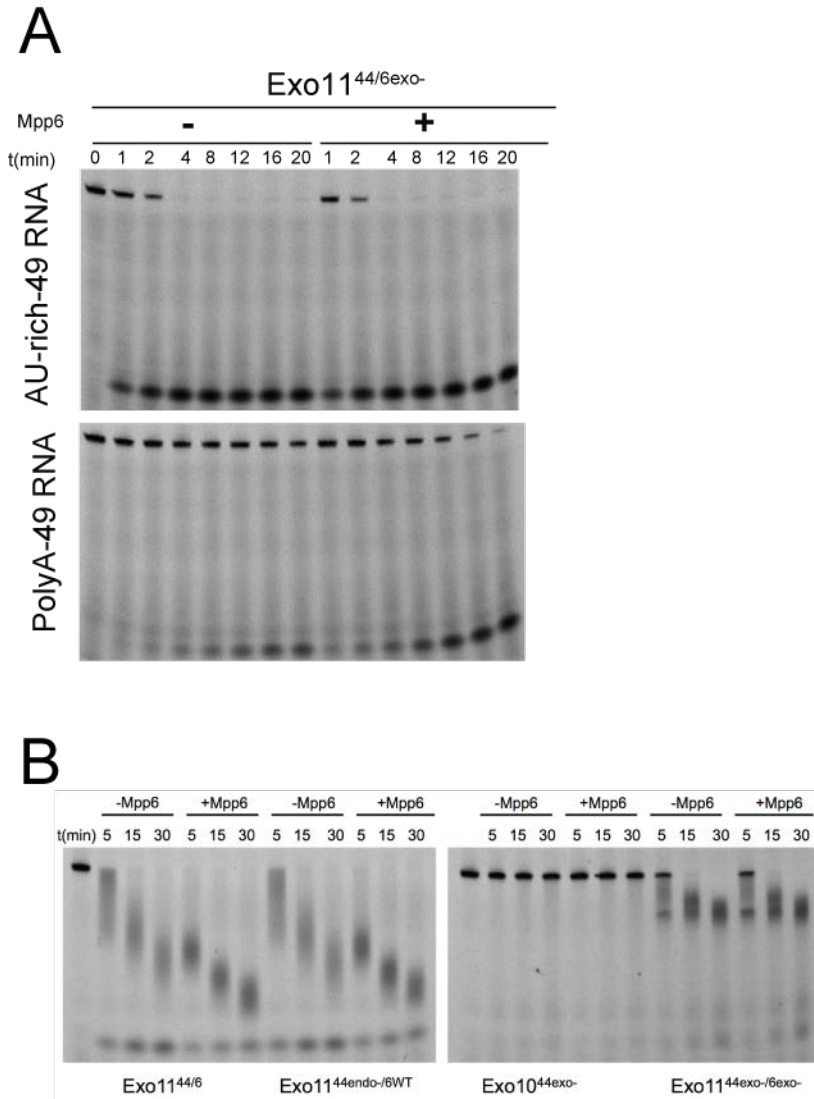


Figure 52. Mpp6 effect on Rrp44 decay in Exo11^{44/6}.

Mpp6 can stimulate the Rrp44 exoribonuclease, (A) but not the endoribonuclease, (B) activity in Exo11^{44/6} if it is the only catalytically competent active site. (A) and (B, left) – exoribonuclease assays of Rrp44 activity in the context of Exo11^{44/6} on single-stranded 5'fluorescein 49 nt AU-rich and polyA RNAs. In (A), catalytic inactivation of Rrp6 (D238N) facilitates the stimulation of Rrp44 activity on polyA, but not AU-rich RNA. In (B), mutation of the endonuclease active site (D171N) of Rrp44 does not alter Mpp6-stimulated decay of Exo11^{44/6} on polyA RNA. (B, left) Endonuclease activity of Exo10^{44exo-} and Exo11^{44exo-/6exo-} in the presence and absence of Mpp6 on polyA RNA.

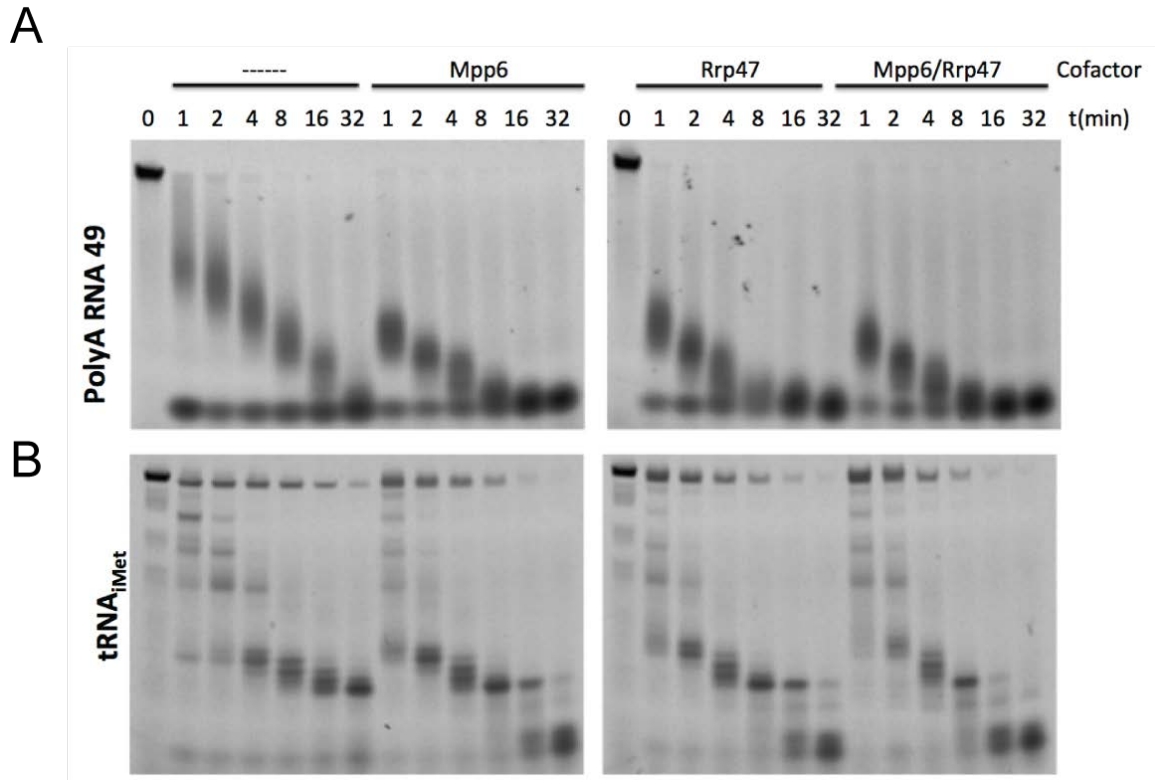


Figure 53. Mpp6 and Rrp47 similarly stimulate Rrp6 in full-length Exo11^{44/6} and do not display additive effects *in vitro*.

5 nM full-length Exo11^{44/6} was assayed with either 20 nM of 5' fluorescein labeled 49 nt polyA or 5' fluorescein labeled *in vitro* transcribed tRNA_{Met} that was refolded prior to initiation of decay. Exo11^{44/6} was incubated with 2-fold molar excess full-length Mpp6, Rrp47, or both before initiation of decay. Decay intermediates were analyzed by denaturing PAGE and visualized with a fluoroimager.

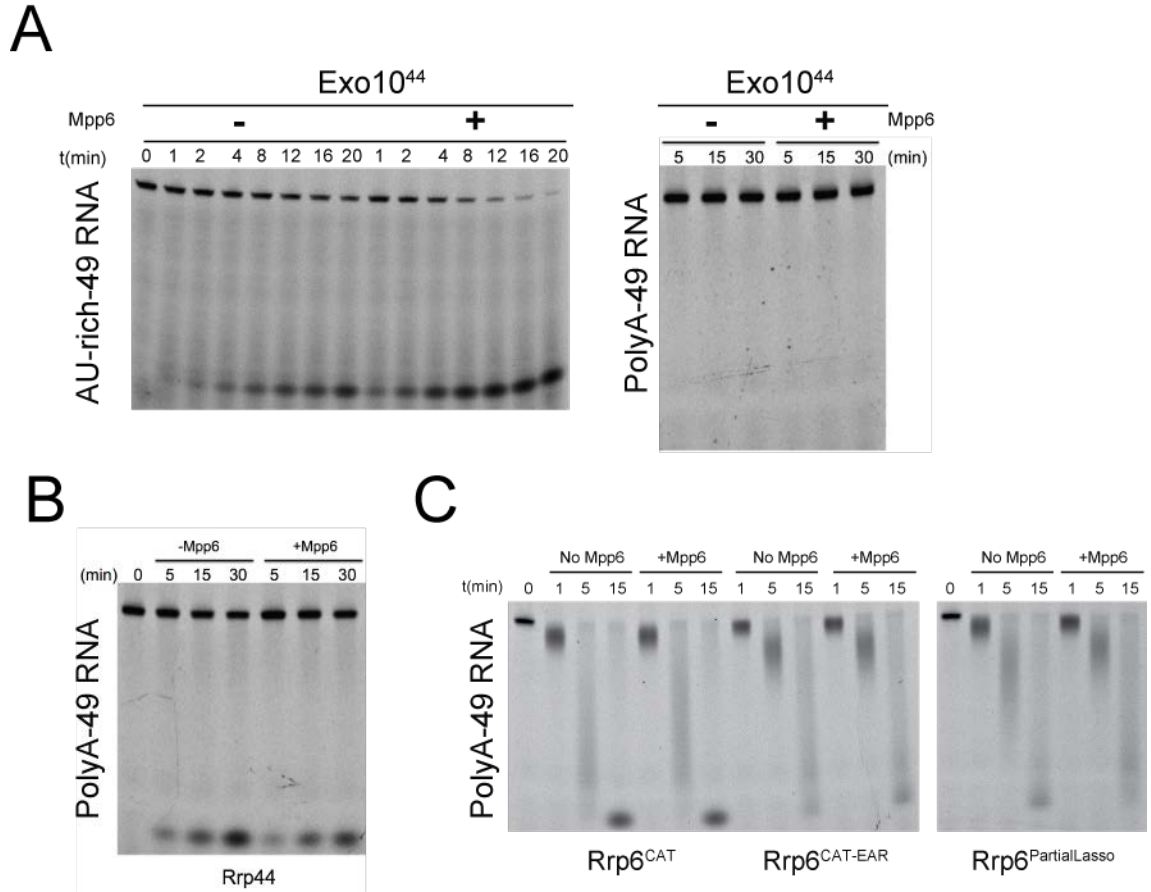


Figure 54. Mpp6 does not stimulate Rrp44 or Rrp6 outside of the exosome.

The cytoplasmic exosome, Exo10⁴⁴, can be stimulated by Mpp6 on AU-rich, but not polyA RNA, but does not alter Rrp44 or Rrp6 activities out of the exosome. Rrp44 exoribonuclease assays with AU-rich RNA (A) and polyA RNA (A, B) were assayed in (A) and out of the exosome (B), in the absence and presence of Mpp6. Rrp6 exoribonuclease activity was assayed in the presence and absence of Mpp6, using various constructs of Rrp6. RNA decay intermediates were analyzed by denaturing PAGE and visualized with a fluorimager.

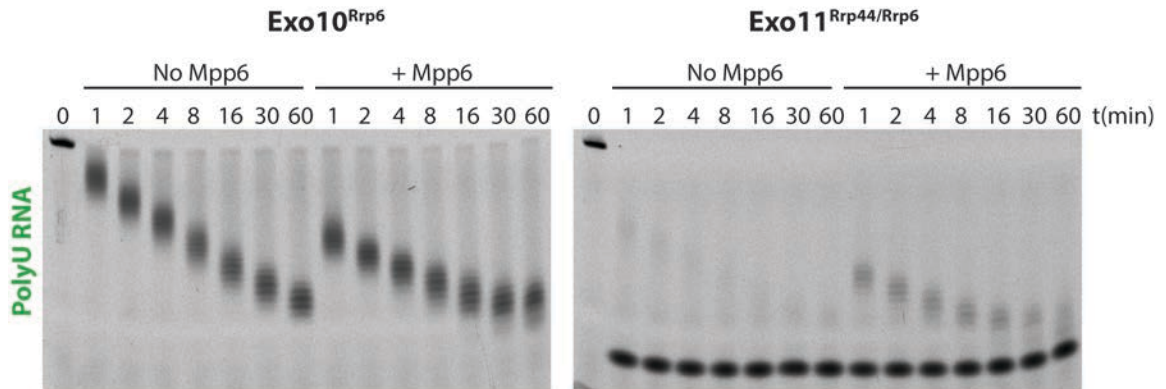


Figure 55. Mpp6 greatly stimulates Rrp6 decay of single-stranded polyU RNA.

Exoribonuclease assays of single-stranded 49 nt 5' fluorescein polyU RNA using Exo10⁶ and Exo11^{44/6} in the absence and presence of Mpp6. PolyU decay by Exo10⁶ is greatly stimulated by Mpp6 (left), and is similarly enhanced in Exo11^{44/6}. RNA intermediates were analyzed by denaturing PAGE and imaged with a fluoroi-mager.

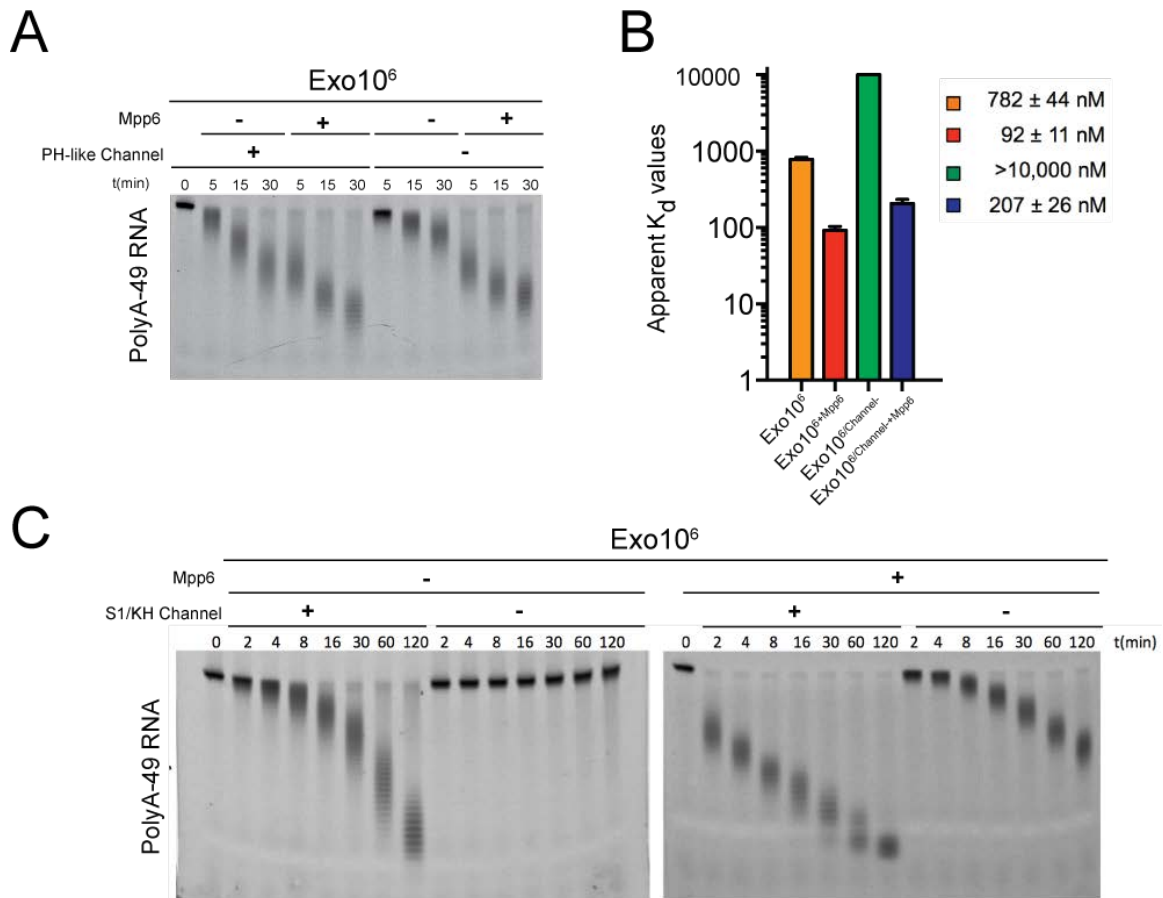


Figure 56. Effect of Exo9 channel mutations on Mpp6 stimulation.

Mpp6-associated exosomes are more affected by S1/KH ring mutations than PH-like ring channel occlusions. (A) A large insertion towards the lower half of the PH-like ring (Chapter 1) has no inhibitory effect in the presence of Mpp6. Exoribonuclease assays of Exo10⁶ in the presence and absence of Mpp6, with and without PH-like ring occlusions. (B) Binding constants in nanomolar determined for various catalytically dead channel open and occluded exosomes for 5' fluorescein single-stranded 37 nt polyA RNA. Fluorescence polarization results of triplicate experiments shown. (C) Exo10⁶ bearing mutations within Csl4 and Rrp40 lining the S1/KH ring central channel (Chapter 2) were assayed for exoribonuclease activity on polyA RNA in the absence or presence of Mpp6.

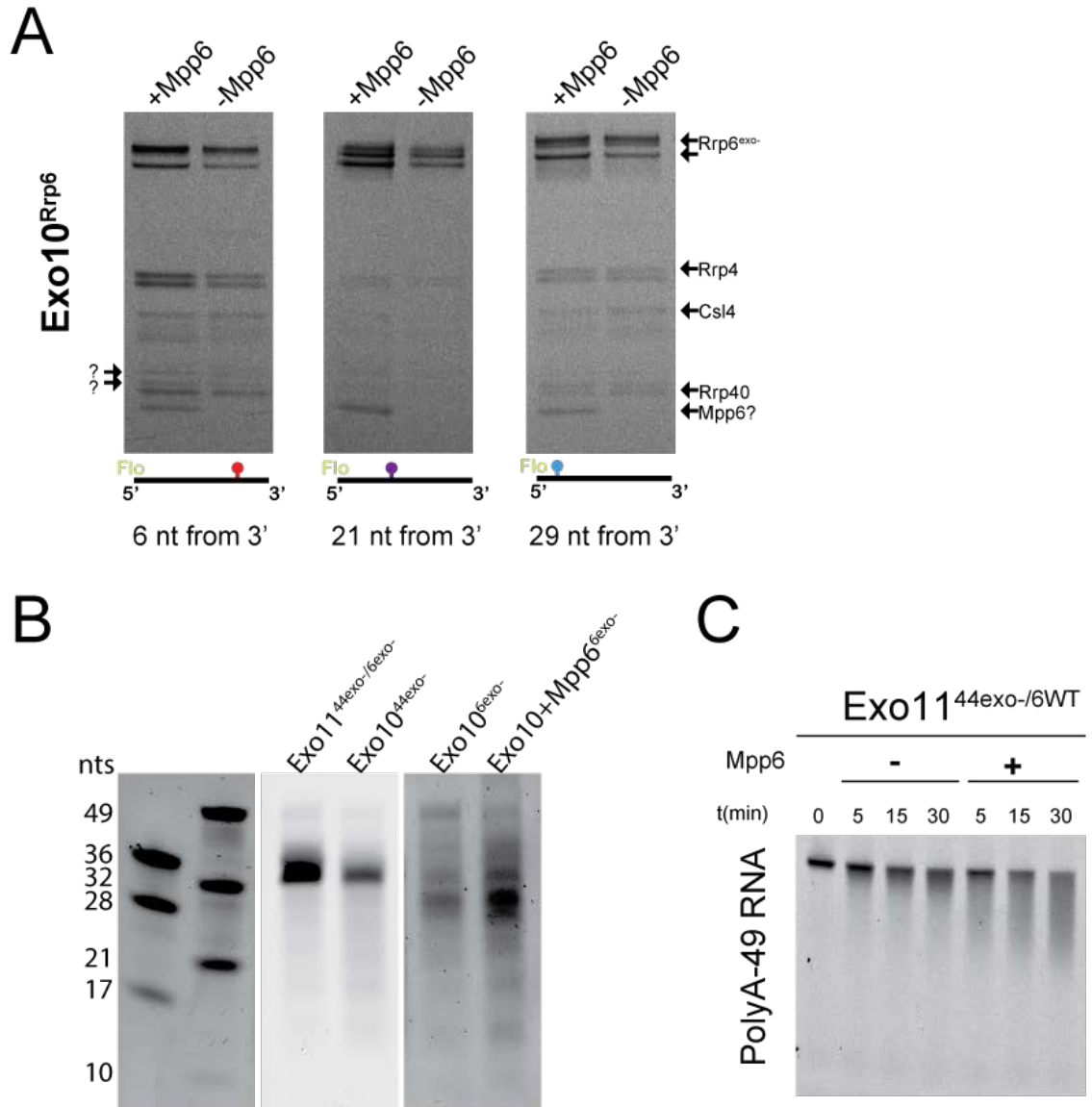
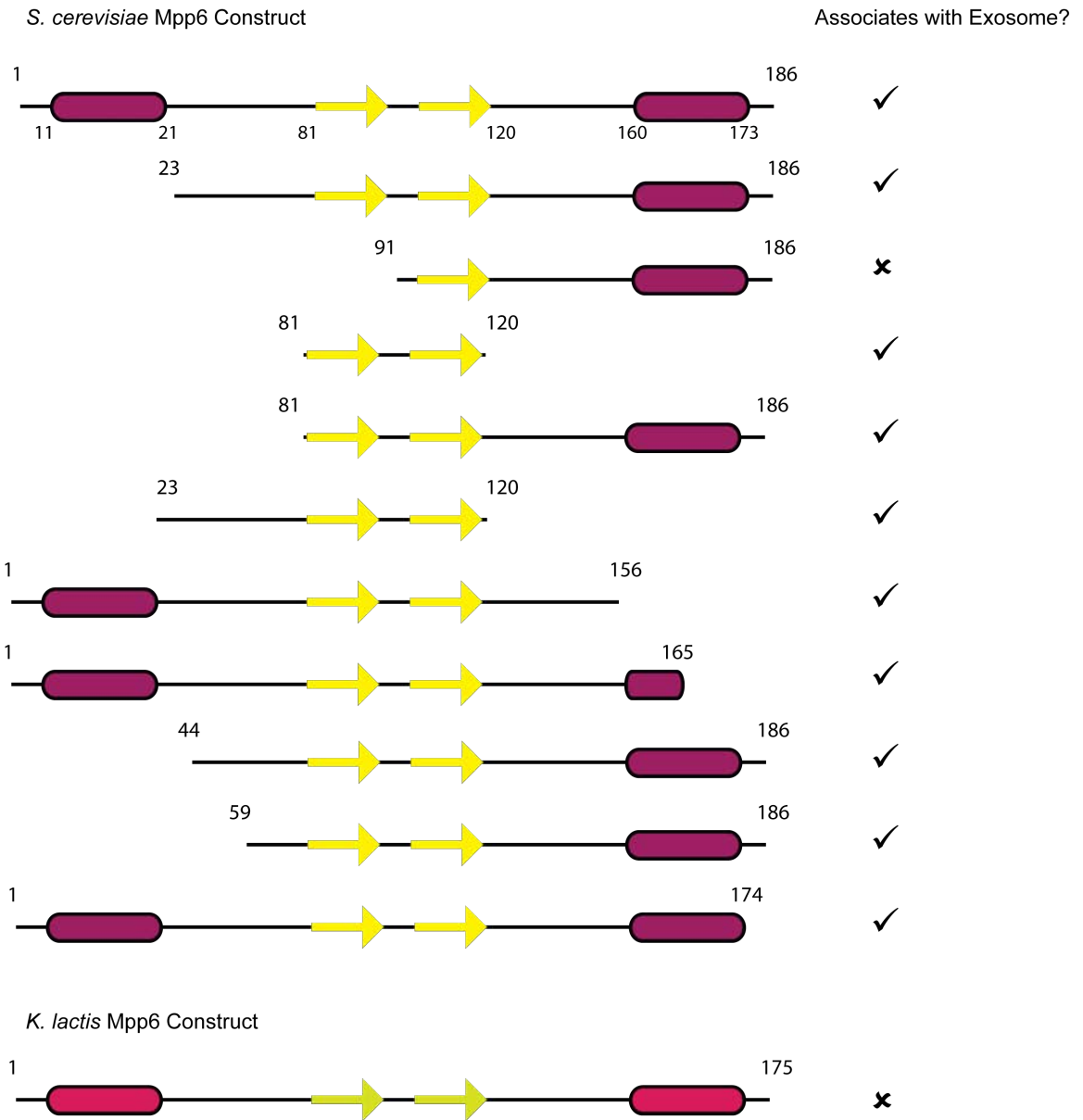


Figure 57. Mpp6 exosomes use similar surfaces as Exo10⁶ for RNA binding.

(A) Long range UV site-specific crosslinking using 5' fluorescein-labeled 4-thiouridine substituted RNAs described in Chapter 2 (Figures 31 and 32) was used to compare RNA-protein crosslinks in Exo10^{6exo-} and Exo11^{6exo-/Mpp6}. Crosslinks were separated by SDS-PAGE and visualized with a fluorimeter. (B) Ribonuclease A protection assays on unlabeled single-stranded 49 nt AU-rich RNA using catalytically dead Rrp44-, Rrp6-, and

Mpp6- containing exosomes. Protected fragments analyzed by denaturing PAGE and visualized with Sybr Gold. See Figure 41 in Chapter 3. (C) Mpp6 stimulates, albeit weakly, Rrp6 decay in Exo11^{44exo-/6WT}, suggesting use of the partially overlapping route shared by Rrp44 (see Chapters 1 and 2, Figures 10, 20, 29).

A



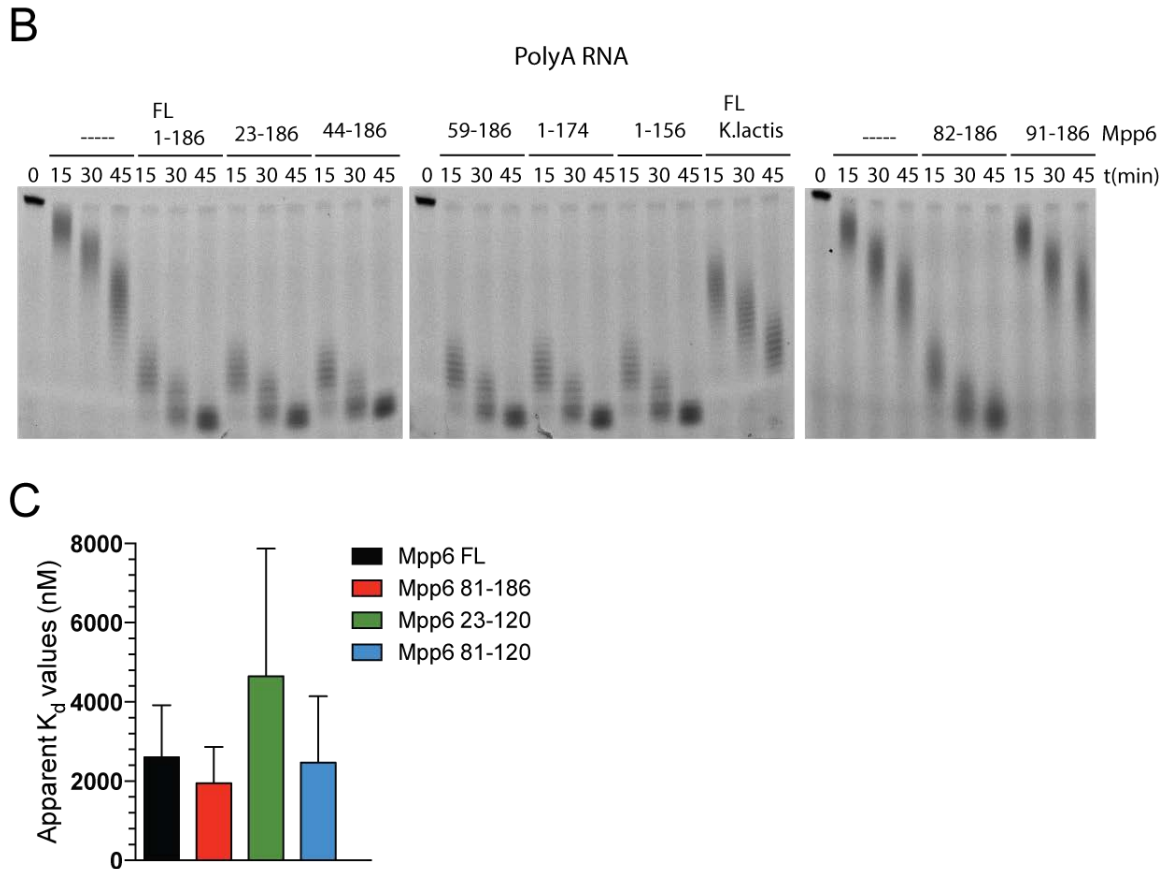


Figure 58. Domain deletion analysis of Mpp6

reveals a minimal fragment is necessary and sufficient for exosome association and stimulation. (A) Domain deletion analysis of Mpp6 and indication of whether or not the expressed and purified construct was competent to associate with the exosome as assayed by analytical gel filtration. Helices represented as purple cylinders; beta-strands as yellow arrows; disordered regions as connecting black lines. (B) Representative Mpp6-mediated stimulation assays showing exoribonuclease activity of Exo106 on 5' fluorescein 49 nt polyA RNA. Note the partial stimulation by *K. lactis* Mpp6. (C) Binding constants in nanomolar determined for various Mpp6 constructs on 5' fluorescein polyA 24 nt RNA. Constructs include full-length, the minimal construct (81-120), a N-terminal half deletion (81-186), and a C-terminal half deletion (23-186). Fluorescence polarization results from triplicate experiments shown.

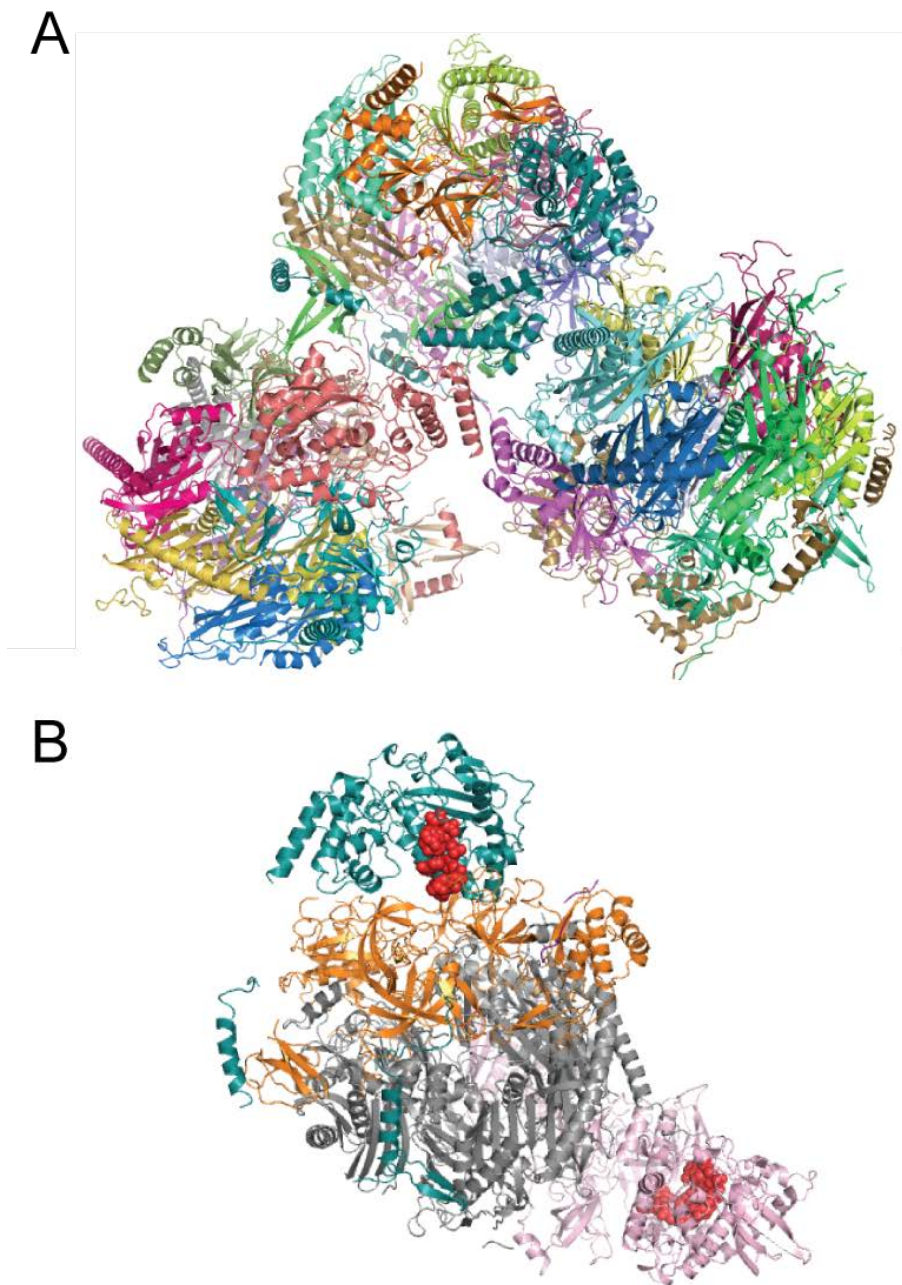


Figure 59. Global architecture of Mpp6 exosomes bound to RNA.

(A) Exo11^{6/Mpp6} bound to polyA24 RNA with three copies in the asymmetric unit (ASU).

(B) Exo12^{44/6/Mpp6} with both Rrp44 and Rrp6 active sites engaged with a 30 nt double 3' ended RNA.

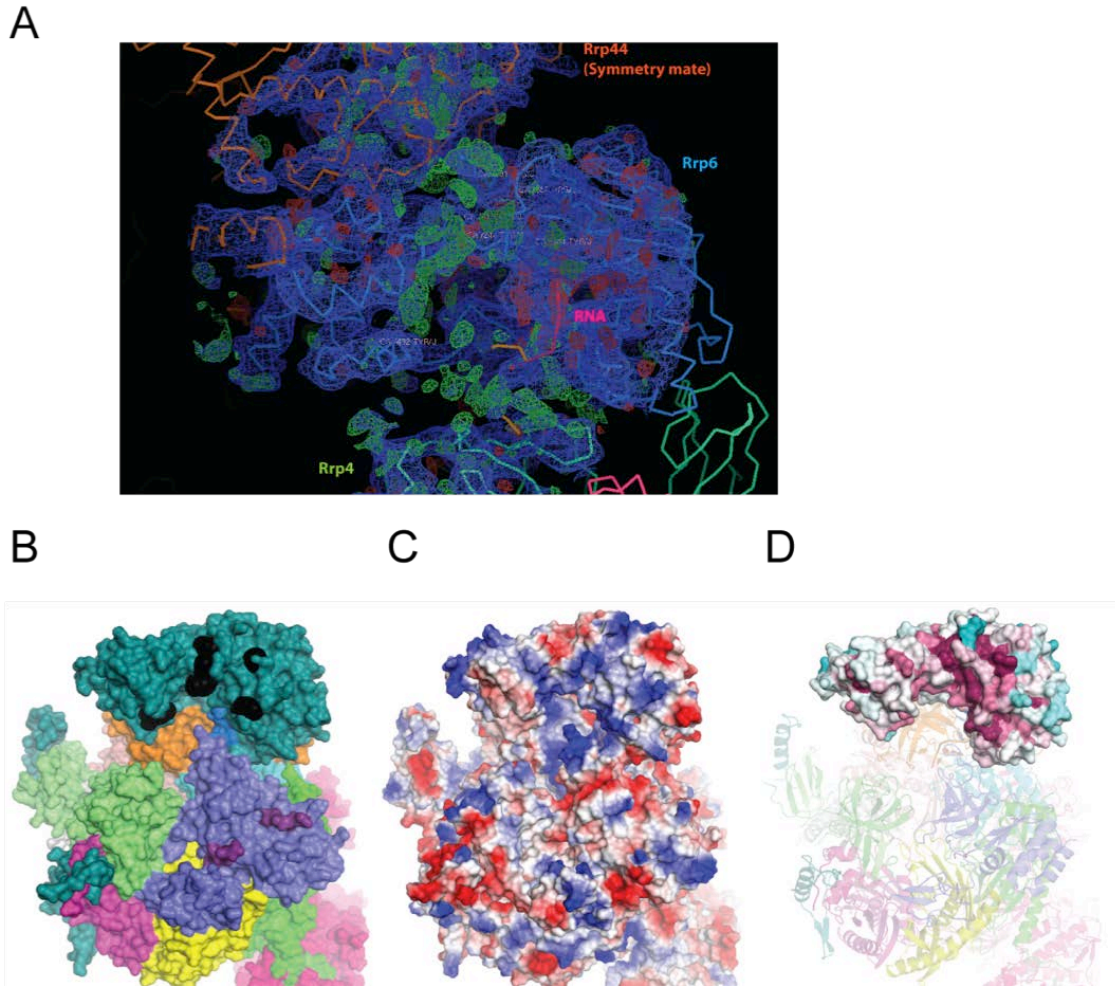
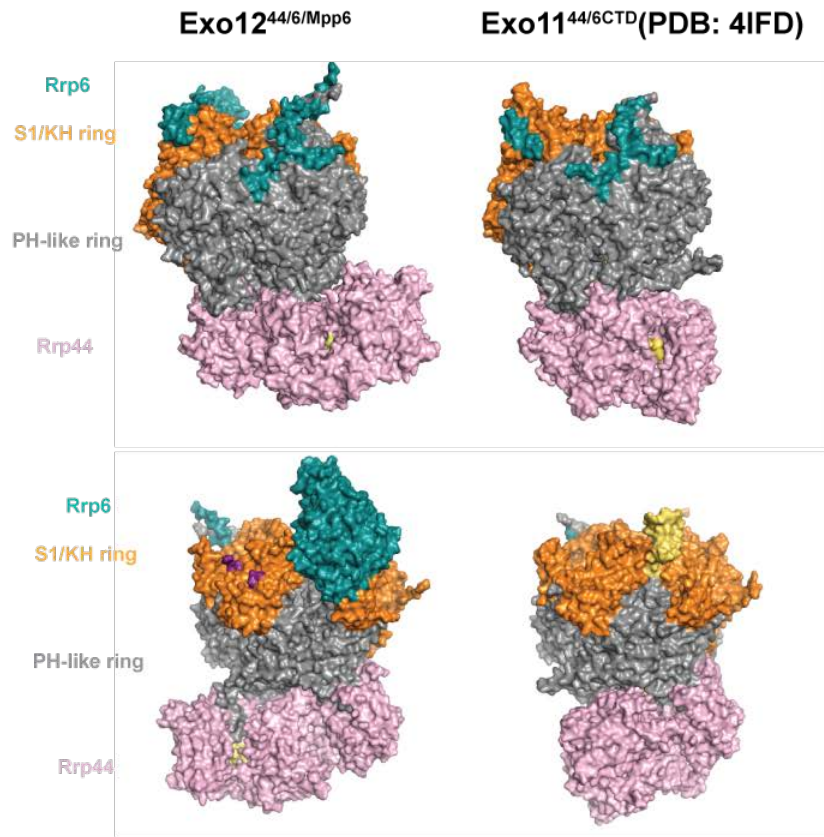


Figure 60. RNA path in Exo12^{44/6/Mpp6}.

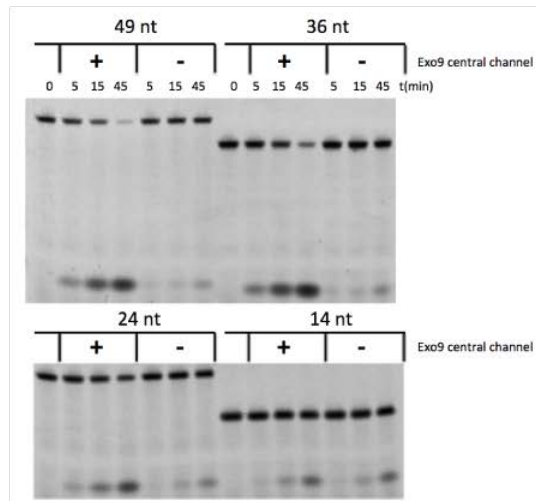
3'-3' RNA in the Exo12^{44/6/Mpp6} structure travels via a basic, conserved path through the Rrp6 EXO domain and interact with Rrp44 through crystallographic symmetry. (A) Feature enhanced map of 2Fo-Fc (1.5 RMSD) in blue, Fo-Fc in green and red (2.5 RMSD). Unmodeled density corresponding to RNA (green) is seen making approximately a 45 degree angle from the Rrp6 active site from a 3' end, and traveling along the Rrp6 EXO domain. Two Rrp44 molecules related by symmetry are shown in orange and coordinate the RNA via the RNB of one molecule and the PIN domain of the other. Residues involved in contacting the RNA are in black in (B), with electrostatics (C)

and conservation features (D) depicted. (A) prepared with Coot⁸⁹. (B,C) with Pymol⁷⁷. (D) with Consurf⁷⁸.

A



B



C

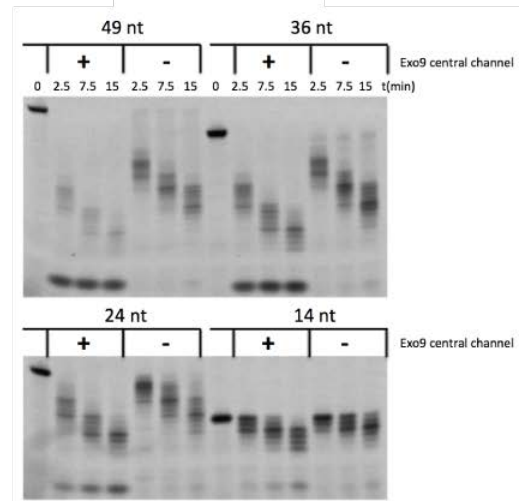
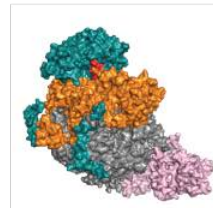


Figure 61. The “direct access” route to Rrp44 and implications for decay of small RNAs.

(A) Comparisons between the structure of Exo1244/6/Mpp6 engaged with a dual 3'-3' single-stranded RNA that does not span the central channel (left) and with Exo1144/6CTD (4IFD) bound to single-stranded RNA threading through the Exo9 central channel (right). Two different orientations are presented to appreciate the “swung out” conformation on the left versus the “swung in” Exo9 channel-engaged form on the right. Figure prepared with Pymol⁷⁷. Exoribonuclease assays of channel open and occluded Exo10⁴⁴ (B) and Exo11^{44/6} (C) on 5'-fluorescein single-stranded AU-rich RNAs of various lengths (49, 36, 24, 14 nts). 24 and 14 nts would be predicted too small to span the channel, and thus their decay is marginally affected by channel occlusions. In Exo11^{44/6}, RNA, regardless of its size, is shunted to Rrp6 when the channel is occluded.

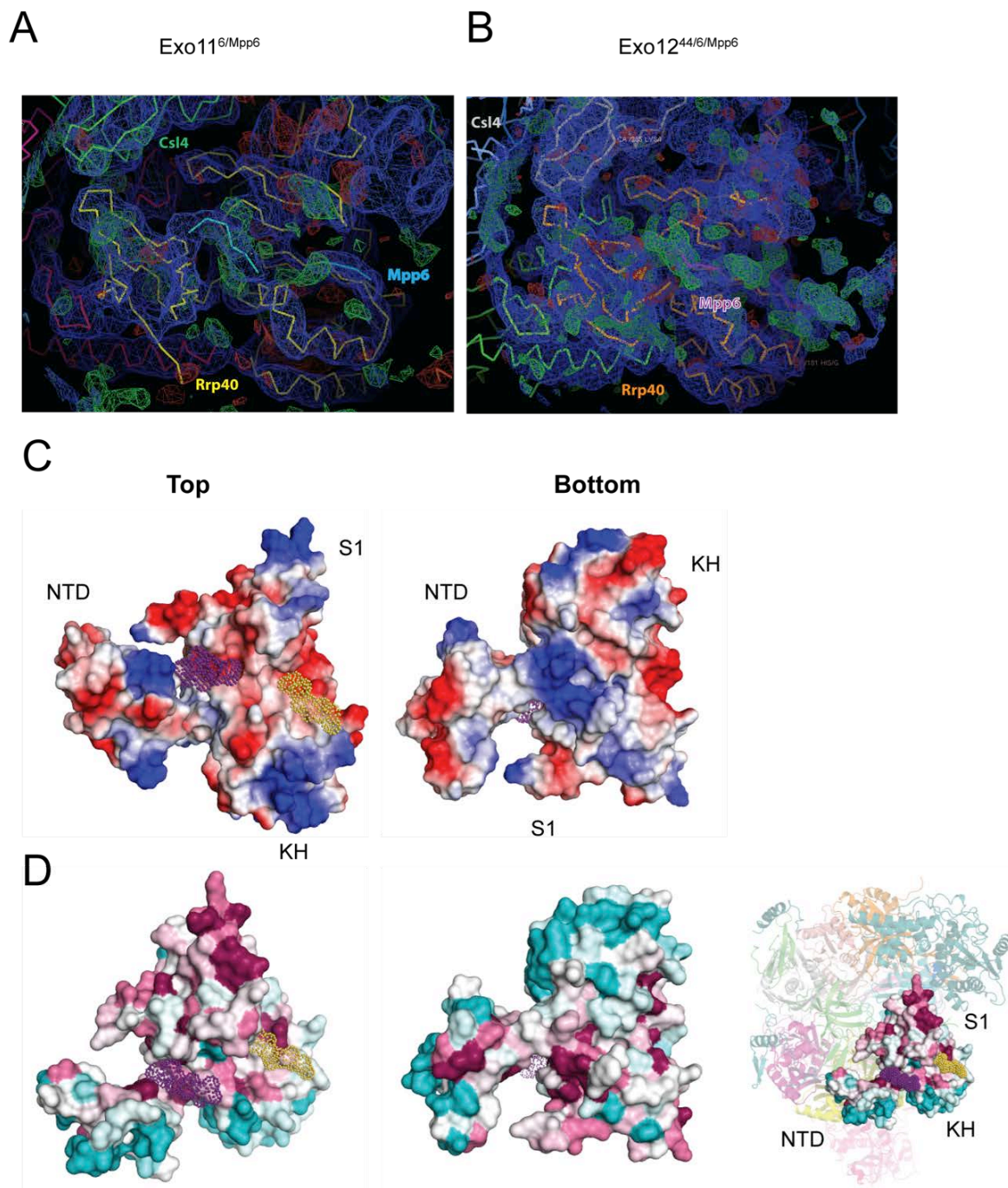


Figure 62. Density likely corresponding to Mpp6 is found primarily on acidic, conserved surfaces of Rrp40.

Feature enhanced map of 2Fo-Fc (1.5 RMSD) in blue, Fo-Fc in green and red, contoured at 2.0 RMSD for Exo11⁶/Mpp6 (A) and 2.5 RMSD for Exo12^{44/6}/Mpp6 (B) showing

unmodeled density on the surface of Rrp40 likely corresponding to Mpp6. Prepared with Coot⁸⁹. The Mpp6 binding surface of Rrp40 is acidic (C) and conserved (D). Rrp40 shown on the top (left) and bottom (right) views. Mpp6 is shown as partially transparent purple and yellow dots on the surface top surface representations of Rrp40. (C) calculated with Pymol⁷⁷. (D) calculated with ConSurf⁷⁸.

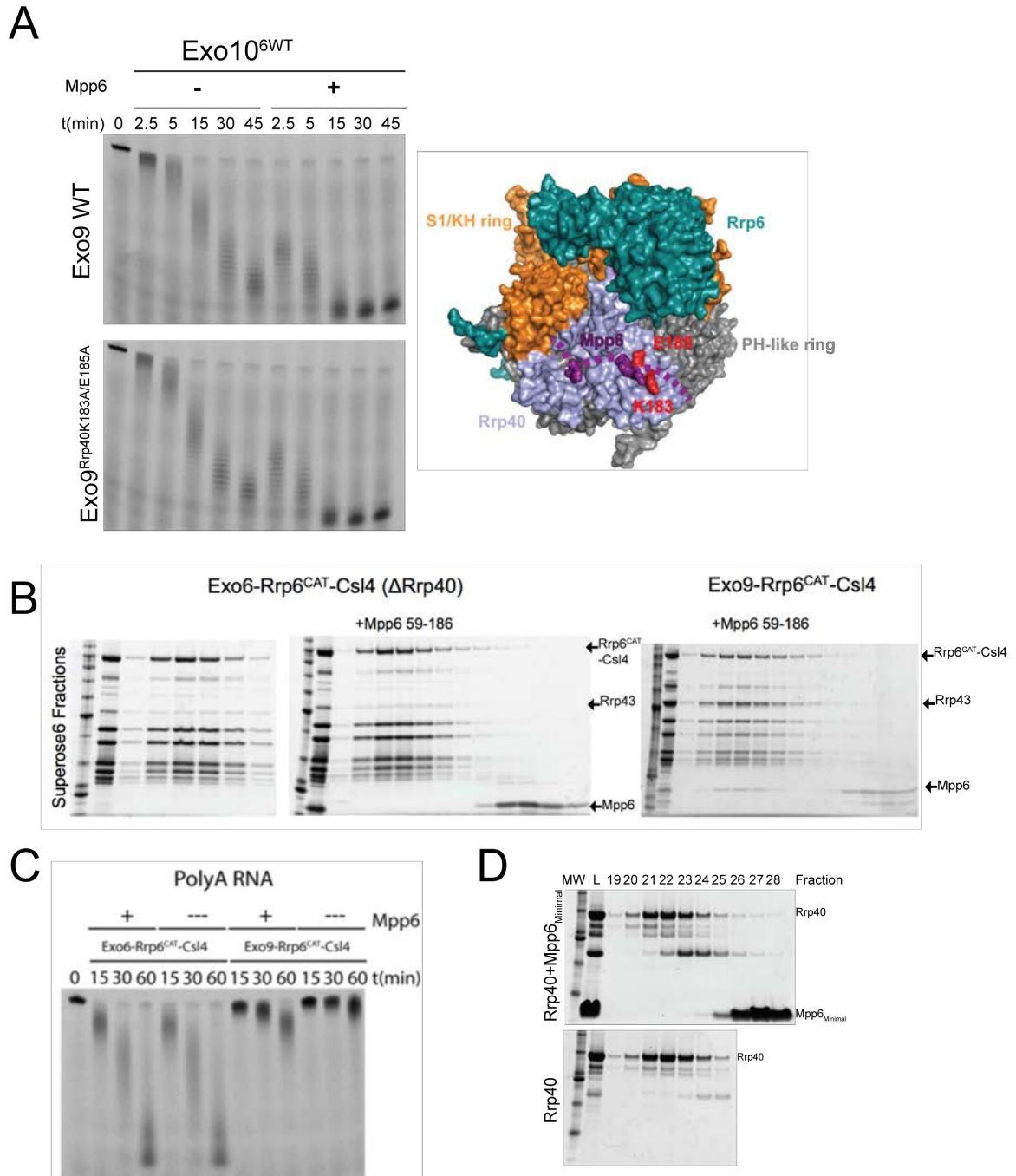


Figure 63. Mpp6 binding surface evaluation.

(A) Two point mutations (K183A/E185A) were introduced in the KH domain of Rrp40 proximal to where density likely corresponding to Mpp6 is found in structural models.

These mutations were not sufficient to interfere with binding of minimal Mpp6 (81-120) or stimulation of Exo10⁶ activity. Structure of Exo10⁶ (PDB: 4001) with Mpp6 coordinates

from Exo12^{44/6/Mpp6}. Mpp6 in purple, with dashed lines representing regions of unmodeled, weaker density. Mutations highlighted in red. (B) Because a stable Exo8^{Δ40} could not be formed on via preparative gel filtration (data not shown), Exo8^{Rrp6CAT-Csl4} was reconstituted and purified. Despite Rrp46/Rrp43 substoichiometry due to the absence of stabilizing contacts with Rrp40, the purified complex was stable upon reapplication on analytical gel filtration (Superose 6) (left) but could not associate with Mpp6 (middle), while Exo9^{Rrp6CAT-Csl4} (Rrp40 included) is competent for Mpp6 association (right). Representative fractions of chromatography peaks analyzed by SDS-PAGE and stained by Sypro Ruby. (C) Decay assays on 5' fluorescein single-stranded polyA RNA of Exo8^{Rrp6CAT-Csl4(ΔRrp40)} compared with Exo9^{Rrp6CAT-Csl4}, minus and plus added Mpp6. Rrp6 activity was stimulated by Mpp6 only when Rrp40 was present, albeit slightly. See explanation in section 4.10, Figure 68. (D) Full-length Rrp40 is not sufficient for Mpp6 association. Analytical gel filtration analysis (Superose 12) of Rrp40 and minimal Mpp6 (81-120). No observable shift of full-length Rrp40 or comigration of Mpp6 is observed, indicating lack of complex information.

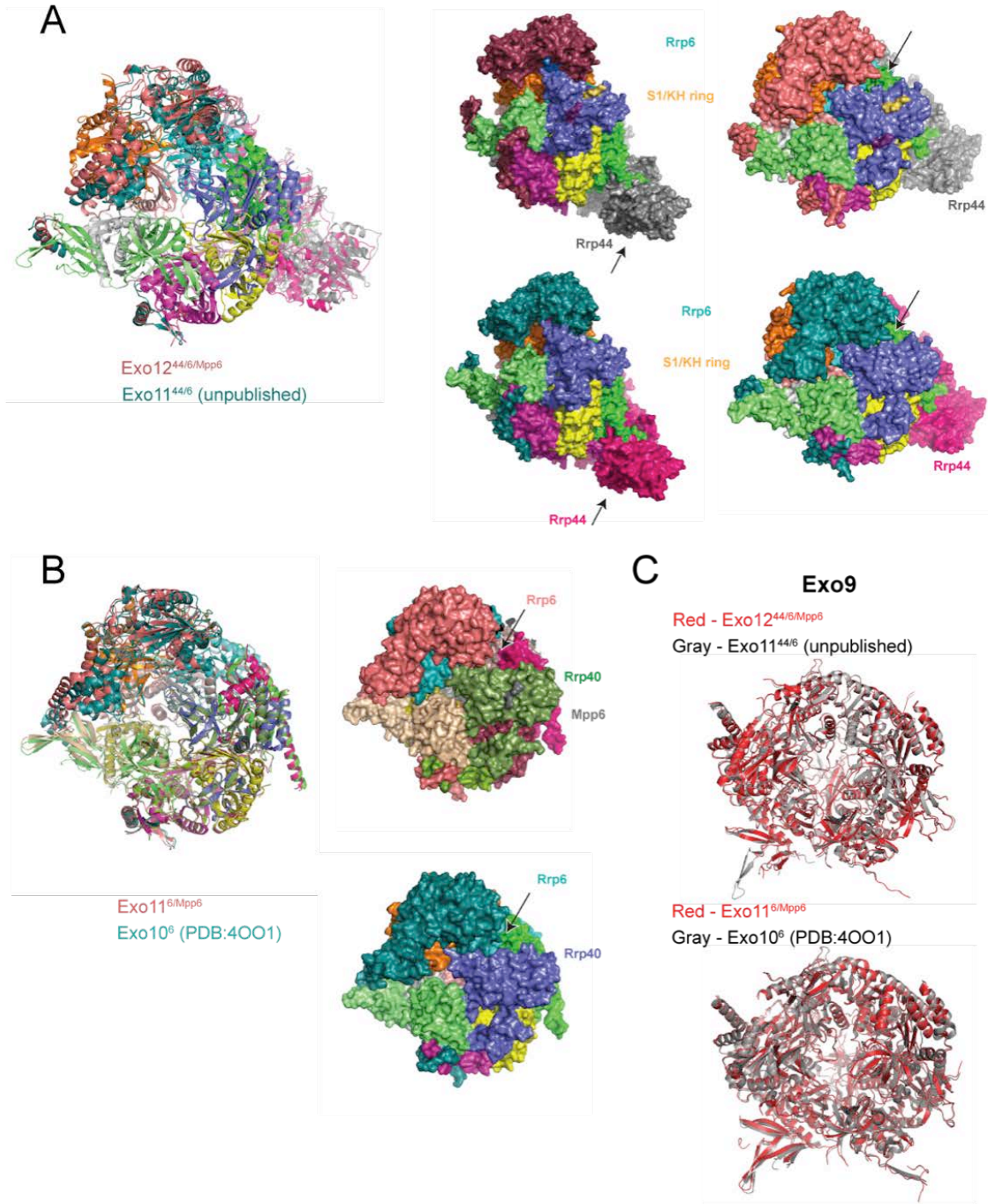


Figure 64. Mpp6 association induces the rotation of the Rrp6 catalytic module away from the Exo9 central channel.

(A,B) Left – cartoon representations of Exo12^{44/6}/Mpp6 (A) and Exo11⁶/Mpp6 (B) showing the displacement of Rrp6 CAT and the Rrp44 RNB in (A) and Rrp6 in (B) in comparison to

structures of Mpp6 apo exosomes. Right – surface representations of two different views, side and from the top, of Mpp6 bound (top) and Mpp6 apo (bottom) exosomes. Arrows point to the observed points of rotation. The indicated region between Rrp6 (red/teal) and Rrp40 (purple) is explored in finer detail in Figure 65 (C) Exo9 aligned by the PH-like ring of Mpp6-bound (red) and apo (gray) exosomes do not show any noticeable differences in Exo12^{44/6/Mpp6} and Exo11^{6/Mpp6}.

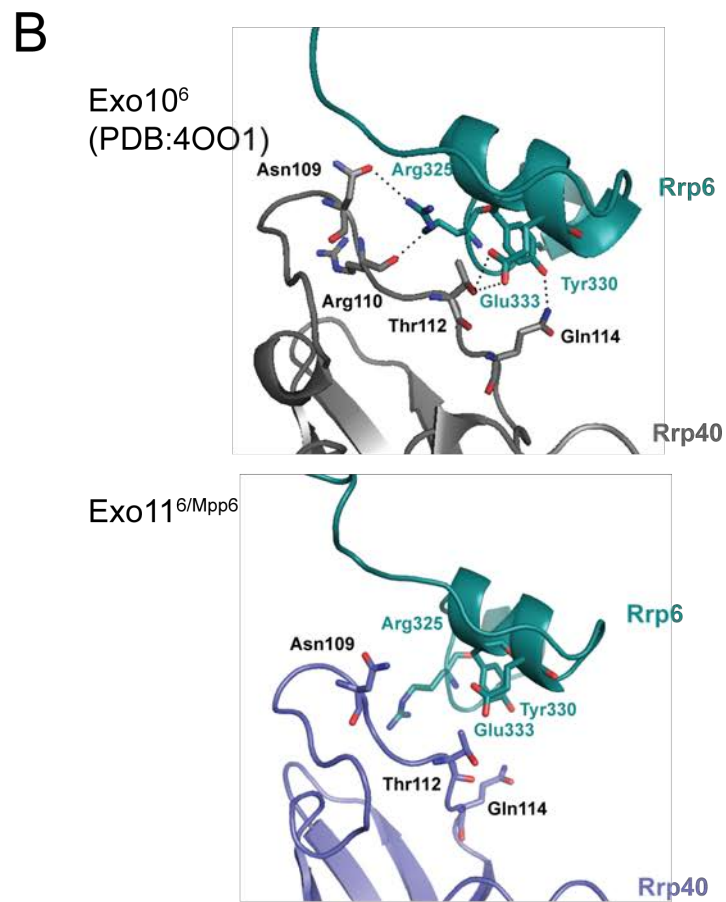
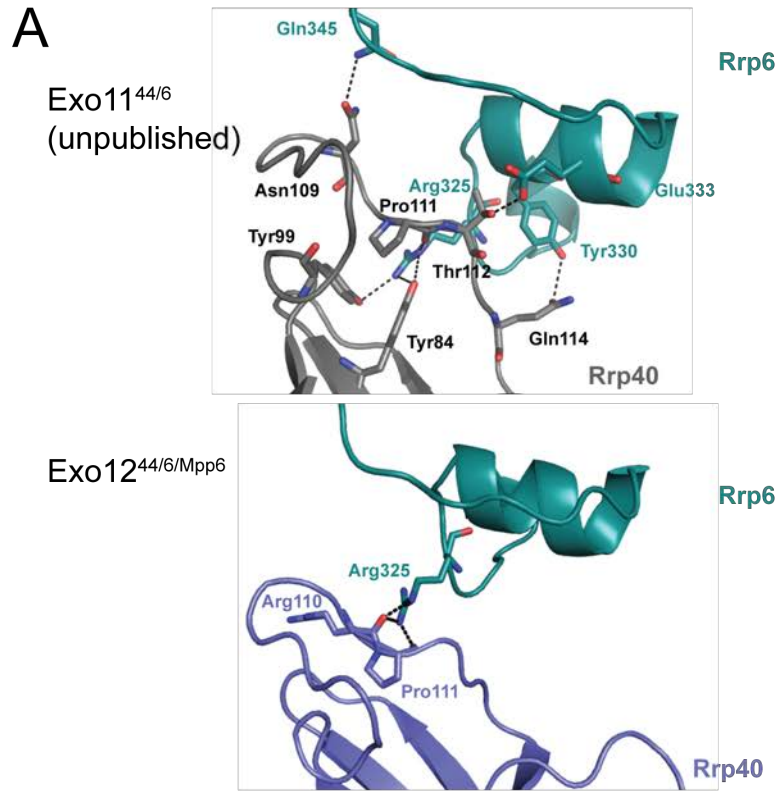


Figure 65. The molecular basis for the Rrp6 catalytic module conformational change upon Mpp6 association.

Polar contacts between a loop and helix of the Rrp6 EXO domain and the S1 domain of Rrp40 upon Mpp6 association in Exo12^{44/6/Mpp6} (A) and Exo11^{6/Mpp6} (B). Residues and contacts are indicated. Figures prepared with Pymol⁷⁷.

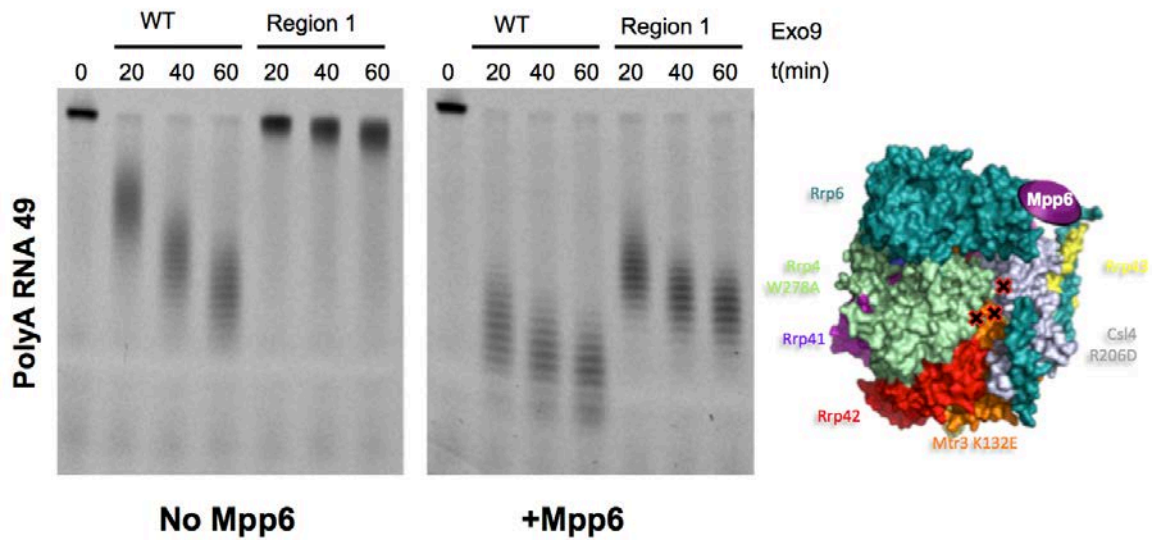
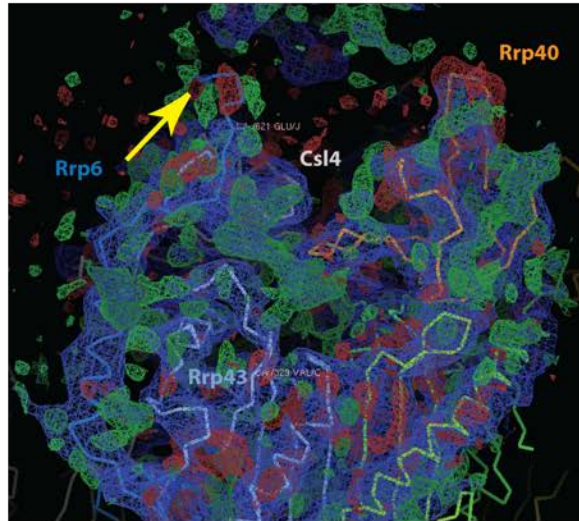


Figure 66. Mpp6 can bypass inhibitory mutations in the Rrp4/Mtr3/Rrp42/Csl4 region of Exo9.

Exoribonuclease assays of Exo10⁶ on 5' fluorescein single-stranded polyA 49 nt RNA reconstituted with WT Exo9 or the Region 1 Exo9 triple mutant described in Figure 46, Chapter 3. Mpp6 alleviates the inhibition caused by these mutations.

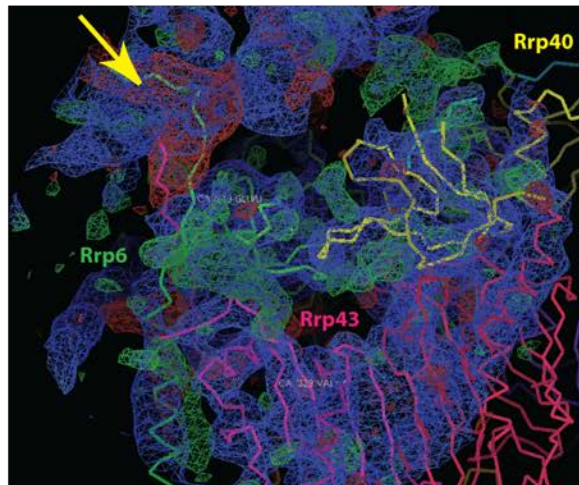
A

Exo12^{44/6}/Mpp6
(P212121)



B

Exo11⁶/Mpp6
(P32)



C

Exo11⁶/Mpp6
(P1211)

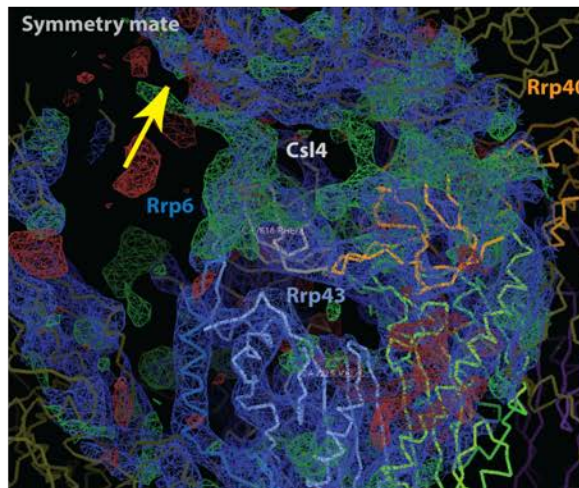


Figure 67. The Rrp6 CTD/Rrp43 NTD interaction takes an alternative route in crystal structures of Mpp6 exosomes.

Unmodeled density (green) showing the Rrp6 lasso/Rrp43 NTD in three different crystal forms of Mpp6-associated exosomes (A,B,C) adopts a different configuration from previously published Exo10⁶ lacking Mpp6 (PDB: 4OO1). 2Fo-Fc feature enhanced map in blue, contoured at 1.5 RMSD; Fo-Fc map in green and red, contoured at 2.0 RMSD. Yellow arrow indicates direction of the Rrp6 CTD/Rrp43 NTD in PDB 4OO1. Density viewed in Coot⁸⁹.

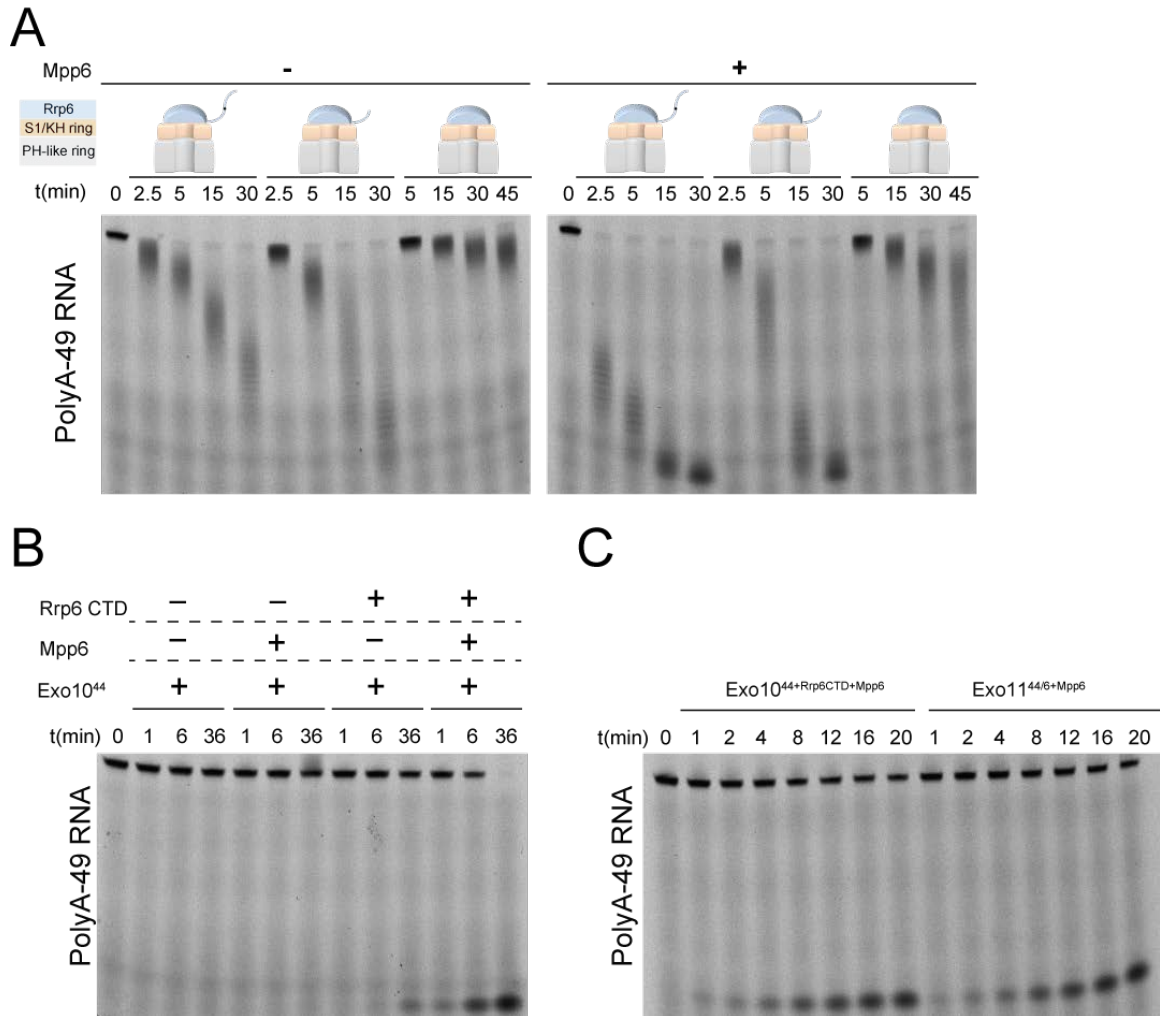
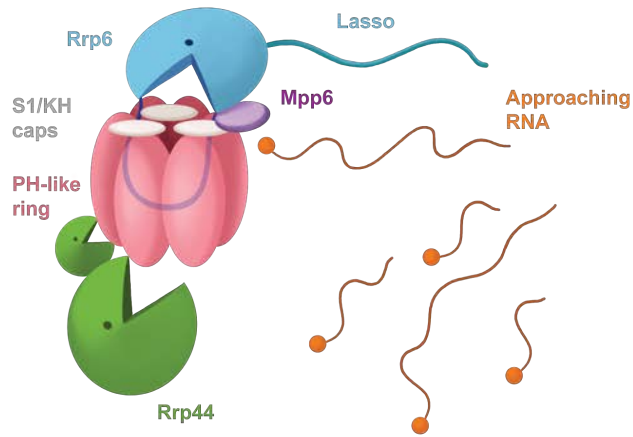


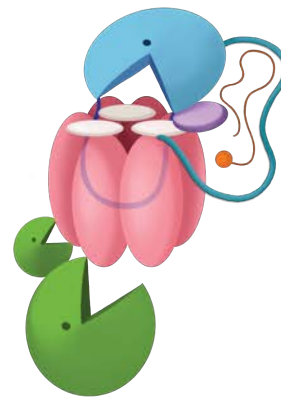
Figure 68. The Rrp6 lasso and Mpp6 cooperatively stimulate Rrp6 and Rrp44 exoribonuclease activities.

(A) Exoribonuclease assays monitoring decay of 5' fluorescein polyA RNA by Exo10⁶ with different lasso variants (intact, partial, lassoless) without (left) and with (right) Mpp6. Lasso deletion severely compromises the magnitude of Mpp6-mediated stimulation. (B) Exoribonuclease assays of Exo10⁴⁴. The combination of the Rrp6 CTD (EAR+intact lasso) and Mpp6, but neither in isolation, results in activation of Rrp44 activity on polyA RNA. (C) The activation of Exo10⁴⁴ activity observed with the combination of Mpp6 and the Rrp6 CTD results in the same activity as Mpp6-mediated stimulation of Exo11^{44/6}.

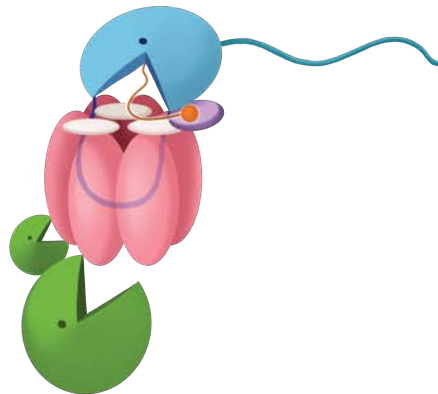
Step 1: Longer RNAs approach the exosome for decay



Step 2: RNA is recruited by the Rrp6 lasso and Mpp6



Step 3a: Decay by Rrp6 through the S1/KH ring



Step 3b: Decay by Rrp44 through the entire Exo9 channel

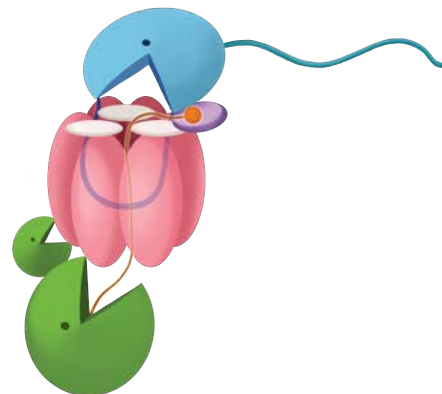


Figure 69. Model of RNA decay by the Mpp6-associated nuclear exosome.

Artwork by A. Wasmuth.

DISCUSSION

The biochemical, genetic, and structural findings described in this dissertation shed light on long-standing questions in the field of exosome and RNA biology – namely, how are the different activities of the exosome coordinated in and out of the Exo9 core; how is the central channel involved in modulating these associated ribonuclease activities, and what are the role of protein cofactors of the exosome on a molecular level?

Nevertheless, many questions still remain outside of those posed at the end of the respective chapters. A benefit and a caveat of the pre-existing experiments is that they essentially represent “naked” exosomes. No evidence exists to support that the “nuclear exosome” consists solely of Rrp44, Rrp6, and Exo9, for example. Indeed, mass spectrometry of endogenous exosomes in yeast suggests that the nuclear exosome is constitutively associated with its cofactors Mpp6 and Rrp47, and likely the TRAMP complex. Conversely, the “cytoplasmic exosome” is not only composed of Rrp44 and Exo9, but Ski7, and the Ski complex. These 13- to 16-subunit exosomes are more representative of what would be recruited to sites of RNA degradation or processing in various cellular contexts. As such, dissection of the molecular interplay between the Ski complex and the exosome in cytoplasmic decay, and the TRAMP complex in nuclear RNA processing and quality control using approaches similar to those described in this dissertation would be of interest. The isolation and understanding of these complexes would facilitate future studies of the exosome’s interactions and roles in mRNA turnover and quality control with the ribosome, and transcriptional termination with RNA polymerase.

BIBLIOGRAPHY

1. Mitchell, P., Petfalski, E., Tollervey, D. (1996). The 3' end of yeast 5.8S rRNA is generated by an exonuclease processing mechanism. *Genes Dev.* 10, 502-513.
2. Houseley, J., LaCava, J., Tollervey, D. (2006). RNA-quality control by the exosome. *Nat. Rev. Mol. Cell. Biol.* 7, 529-539.
3. Allmang, C., Petfalski, E., Podtelejnikov, A., Mann, M., Tollervey, D., Mitchell, P. (1999). The yeast exosome and human PM-Scl are related complexes of 3' → 5' exonucleases. *Genes Dev.* 13, 2148-2158.
4. Schneider, C., Anderson, J.T., Tollervey, D. (2007). The exosome subunit Rrp44 plays a direct role in RNA substrate recognition. *Mol. Cell* 27, 324-331.
5. Graham, A.C., Kiss, D.L., Andrulis, E.D. (2006). Differential distribution of exosome subunits at the nuclear lamina and in cytoplasmic foci. *Mol. Biol. Cell* 17, 1399-1409.
6. Mitchell, P., Petfalski, E., Shevchenko, A., Mann, M., Tollervey, D. (1997). The exosome: a conserved eukaryotic RNA processing complex containing multiple 3' → 5' exoribonucleases. *Cell* 91, 457-466.
7. Tomecki, R., Kristiansen, M.S., Lykke-Andersen, S., Chlebowski, A., Larsen, K.M., Szczesny, R.J., Draskowska, K., Pastula, A., Andersen, J.S., Stepien, P.P., Dziembowski, A., Jensen, T.H. (2010). The human core exosome interacts with differentially localized processive RNases: hDIS3 and hDIS3L. *EMBO J.* 29, 2342-2357.
8. Carpousis, A.J. (2002). The Escherichia coli RNA degradosome: structure, function and relationship in other ribonucleolytic multienzyme complexes. *Biochem. Soc. Trans.* 30, 150-155.
9. Symmons, M.F., Jones, G.H., Luisi, B.F. (2000). A duplicated fold is the structural basis for polynucleotide phosphorylase catalytic activity, processivity, and regulation. *Structure* 8, 1215-1226.
10. Nurmohamed, S., Vaidialingam, B., Callaghan, A.J., Luisi, B.F. (2009). Crystal structure of Escherichia coli polynucleotide phosphorylase core bound to RNase E, RNA and manganese: implications for catalytic mechanism and RNA degradosome assembly. *J. Mol. Biol.* 389, 17-33.
11. Evguenieva-Hackenberg, E., Walter, P., Hochleitner, E., Lottspeich, F., Klug, G. (2003). An exosome-like complex in *Sulfolobus solfataricus*. *EMBO Rep.* 4, 889-893.
12. Lorentzen, E., Walter, P., Fribourg, S., Evguenieva-Hackenberg, E., Klug, G., Conti, E. (2005). The archaeal exosome core is a hexameric ring structure with three catalytic subunits. *Nat. Struct. Mol. Biol.* 12, 575-581.
13. Büttner, K., Wenig, K., Hopfner, K.P. (2005). Structural framework for the mechanism of archaeal exosomes in RNA processing. *Mol. Cell* 20, 461-471.
14. Mian, I.S. (1997). Comparative sequence analysis of ribonucleases HII, III, II PH and D. *Nucleic Acids Res.* 25, 3187-95.
15. Zuo, Y., Deutscher, P. (2001). Exoribonuclease superfamilies: structural analysis and phylogenetic distribution. *Nucleic Acids Res.* 29, 1017-1026.
16. Lorentzen, E., Dziembowski, A., Lindner, D., Seraphin, B., Conti, E. (2007). RNA channelling by the archaeal exosome. *EMBO Rep.* 8, 470-476.
17. Liu, Q., Greimann, J.C., Lima, C.D. (2006). Reconstitution, activities, and structure of the eukaryotic RNA exosome. *Cell* 127, 1223-1237.
18. Dziembowski, A., Lorentzen, E., Conti, E., Séraphin, B. (2007). A single subunit, Dis3, is essentially responsible for yeast exosome core activity. *Nat. Struct. Mol. Biol.* 14, 15-22.
19. Januszyk, K., Lima, C.D. (2010). In "RNA Exosome" (T.H. Jensen, ed.) Vol. 702, pp. 9-28. Landes Bioscience and Springer Science, New York.

20. Ishii, R., Nureki O, Yokoyama S. (2003). Crystal structure of the tRNA processing enzyme RNase PH from *Aquifex aeolicus*. *J. Biol. Chem.* 278, 32397-32404.
21. Harlow, L.S., Kadziola, A., Jensen, K.F., Larsen, S. (2004). Crystal structure of the phosphorolytic exoribonuclease RNase PH from *Bacillus subtilis* and implications for its quaternary structure and tRNA binding. *Protein Sci.* 13, 668-677.
22. Shi, Z., Yang, W.Z., Lin-Chao, S., Chak, K.F., Yuan, H.S. (2008). Crystal structure of *Escherichia coli* PNPase: central channel residues are involved in processive RNA degradation. *RNA* 14, 2361-2371.
23. Brouwer, R., Allmang, C., Raijmakers, R., van Aarsen, Y., Egberts, W.V., Petfalski, E., van Venrooij, W.J., Tollervey, D., Pruijn, G.J. (2001). Three novel components of the human exosome. *J. Biol. Chem.* 276, 6177-6184.
24. Mitchell, P., Tollervey, D. (2000). Musing on the structural organization of the exosome complex. *Nat. Struct. Mol. Biol.* 7, 843-846.
25. Bonneau, F., Basquin, J., Ebert, J., Lorentzen, E., Conti, E. (2009). The yeast exosome functions as a macromolecular cage to channel RNA substrates for degradation. *Cell* 139, 547-559.
26. Siomi, H., Matunis, M.J., Michael, W.M., Dreyfuss, G. (1993). The pre-mRNA binding K protein contains a novel evolutionarily conserved motif. *Nucleic Acids Res.* 21, 1193-1198.
27. Valverde, R., Edwards, L., Regan, L. (2008). Structure and function of KH domains. *FEBS J.* 275, 2712-2726.
28. Subramanian, A.R. (1983). Structure and functions of ribosomal protein S1. *Prog. Nucleic Acid Res. Mol. Biol.* 28, 101-142.
29. Worbs, M., Bourenkov, G.P., Bartunik, H.D., Huber, R., Wahl, M.C. (2001). An extended RNA binding surface through arrayed S1 and KH domains in transcription factor NusA. *Mol. Cell* 7, 1177-1189.
30. Schubert, M., Edge, R.E., Lario, P., Cook, M.A., Strynadka, N.C., Mackie, G.A., McIntosh, L.P. (2004). Structural characterization of the RNase E S1 domain and identification of its oligonucleotide-binding and dimerization interfaces. *J. Mol. Biol.* 341, 37-54.
31. Oddone, A., Lorentzen, E., Basquin, J., Gasch, A., Rybin, V., Conti, E., Sattler, M. (2007). Structural and biochemical characterization of the yeast exosome component Rrp40. *EMBO Rep.* 8, 63-69.
32. Schaeffer, D., Tsanova, B., Barbas, A., Reis, F.P., Dastidar, E.G., Sanchez-Rotunno, M., Arraiano, C.M., van Hoof, A. (2009). The exosome contains domains with specific endoribonuclease, exoribonuclease and cytoplasmic mRNA decay activities. *Nat Struct Mol. Biol.* 16, 56-62.
33. Malet, H., Topf, M., Clare, D.K., Ebert, J., Bonneau, F., Basquin, J., Drazkowska, K., Tomecki, R., Dziembowski, A., Conti, E., Saibil, H.R., Lorentzen, E. (2010). RNA channelling by the eukaryotic exosome. *EMBO Rep.* 11, 936-942.
34. Lu, C., Ding, F., Ke, A. (2010). Crystal structure of the *S. solfataricus* archaeal exosome reveals conformational flexibility in the RNA-binding ring. *PLoS One* 5 e8739.
35. Lebreton, A., Tomecki, R., Dziembowski, A., Séraphin, B. (2008). Endonucleolytic RNA cleavage by a eukaryotic exosome. *Nature* 456, 993-996.
36. Staals, R.H., Bronkhorst, A.W., Schilders, G., Slomovic, S., Schuster, G., Heck, A.J., Raijmakers, R., Pruijn, G.J. (2010). Dis3-like 1: a novel exoribonuclease associated with the human exosome. *EMBO J.* 29, 2358-2367.
37. Cheng, Z.F., Deutscher, M.P. (2002). Purification and characterization of the *Escherichia coli* exoribonuclease RNase R. Comparison with RNase II. *J. Biol. Chem.* 277, 21624-21629.

38. Chang, H.M., et. al. (2013). A role for the Perlman syndrome exonuclease Dis3L2 in the Lin28-let-7 pathway. *Nature*. 497, 244-248.
39. Malecki, M., et. al. (2013). The exoribonuclease Dis3L2 defines a novel eukaryotic RNA degradation pathway. *EMBO J.* 32, 1843-1854.
40. Astuti, D., et. al. (2012). Germline mutations in DIS3L2 cause the Perlman syndrome of overgrowth and Wilms tumor susceptibility. *Nature Genetics*. 44, 277-284.
41. Faehnle, C.R., Walleshauser, J., Joshua-Tor, L. Mechanism of Dis3L2 substrate recognition in the Lin28-let-7 pathway. *Nature*. 514, 252-256.
42. Lorentzen, E., Basquin, J., Tomecki, R., Dziembowski, A., Conti, E. (2008). Structure of the active subunit of the yeast exosome core, Rrp44: diverse modes of substrate recruitment in the RNase II nuclease family. *Mol. Cell* 29, 717-728.
43. Frazão, C., McVey, C.E., Amblar, M., Barbas, A., Vornrhein, C., Arraiano, C.M., Carrondo, M.A. (2006). Unravelling the dynamics of RNA degradation by ribonuclease II and its RNA-bound complex. *Nature* 443, 110-114.
44. Vincent, H.A., Deutscher, M.P. (2009). Insights into how RNase R degrades structured RNA: analysis of the nuclease domain. *J. Mol. Bio.* 387, 570-583.
45. Arcus, V.L., Bäckbro, K., Roos, A., Daniel, E.L., Baker, E.N. (2004). Distant structural homology leads to the functional characterization of an archaeal PIN domain as an exonuclease. *J. Biol. Chem.* 279, 16471-16478.
46. Nowotny, M., Gaidamakov, S.A., Crouch, R.J., Yang, W. (2005). Crystal structures of RNase H bound to an RNA/DNA hybrid: substrate specificity and metal-dependent catalysis. *Cell* 121, 1005-1016.
47. Steitz, T.A., Steitz, J.A. (1993). A general two-metal-ion mechanism for catalytic RNA. *Proc Natl Acad Sci U S A.* 90, 6498-6502.
48. De Vivo, M., Dal Peraro, M., Klein, M.L. (2008). Phosphodiester cleavage in ribonuclease H occurs via an associative two-metal-aided catalytic mechanism. *J. Am. Chem. Soc.* 130, 10955-10962.
49. Huntzinger, E., Kashima, I., Fauser, M., Saulière, J., Izaurralde, E. (2008). SMG6 is the catalytic endonuclease that cleaves mRNAs containing nonsense codons in metazoan. *RNA* 14, 2609-2617.
50. Eberle, A.B., Lykke-Andersen, S., Mühlemann, O., Jensen, T.H. (2009). SMG6 promotes endonucleolytic cleavage of nonsense mRNA in human cells. *Nat. Struct. Mol. Biol.* 16, 49-55.
51. Wang, H.W., Wang, J., Ding, F., Callahan, K., Bratkowski, M.A., Butler, J.S., Nogales, E., Ke, A. (2007). Architecture of the yeast Rrp44 exosome complex suggests routes of RNA recruitment for 3' end processing. *Proc. Natl. Acad. Sci. U.S.A.* 104, 16844-16849.
52. Makino, D.L., Baumgärtner, M. & Conti, E. Crystal structure of an RNA-bound 11-subunit eukaryotic exosome complex. *Nature* 495, 70-75 (2013).
53. Kim, D.U., Hayles, J., Kim, D., Wood, V., Park, H.O., Won, M., Yoo, H.S., Duhig, T., Nam, M., Palmer, G., Han, S., Jeffery, L., Baek, S.T., Lee, H., Shim, Y.S., Lee, M., Kim, L., Heo, K.S., Noh, E.J., Lee, A.R., Jang, Y.J., Chung, K.S., Choi, S.J., Park, J.Y., Park, Y., Kim, H.M., Park, S.K., Park, H.J., Kang, E.J., Kim, H.B., Kang, H.S., Park, H.M., Kim, K., Song, K., Song, K.B., Nurse, P., Hoe, K.L. (2010). Analysis of a genome-wide set of gene deletions in the fission yeast *Schizosaccharomyces pombe*. *Nat Biotechnol.* 28, 617-623.
54. Allmang, C., Kufel, J., Chanfreau, G., Mitchell, P., Petfalski, E., Tollervey, D. (1999). Functions of the exosome in rRNA, snoRNA and snRNA synthesis. *EMBO J.* 18, 5399-410.

55. van Hoof, A., Lennertz, P., Parker, R. (2000). Yeast exosome mutants accumulate 3'-extended polyadenylated forms of U4 small nuclear RNA and small nucleolar RNAs. *Mol. Cell. Biol.* 20, 441-452.
56. Allmang, C., Mitchell, P., Petfalski, E., Tollervey, D. (2000). Degradation of ribosomal RNA precursors by the exosome. *Nucleic Acids Res.* 28,1684-1691.
57. Neil, H., Malabat, C., d'Aubenton-Carafa, Y., Xu, Z., Steinmetz, L.M., Jacquier, A. (2009). Widespread bidirectional promoters are the major source of cryptic transcripts in yeast. *Nature* 457,1038-1042.
58. Wyers, F., Rougemaille, M., Badis, G., Rousselle, J.C., Dufour, M.E., Boulay, J., Régnault, B., Devaux, F., Namane, A., Séraphin, B., Libri, D., Jacquier, A. (2005). Cryptic pol II transcripts are degraded by a nuclear quality control pathway involving a new poly(A)polymerase. *Cell*, 121, 725-737.
59. Bühler, M., Haas, W., Gygi, S.P., Moazed, D. (2007). RNAi-dependent and -independent RNA turnover mechanisms contribute to heterochromatic gene silencing. *Cell* 129, 707-721.
60. Reyes-Turcu, F.E., Zhang, K., Zofall, M., Chen, E., Grewal, S.I. (2011). Defects in RNA quality control factors reveal RNAi-independent nucleation of heterochromatin. *Nat. Struct. Mol. Biol.* 18, 1132-1138.
61. Harigaya, Y., Tanaka, H., Yamanaka, S., Tanaka, K., Watanabe, Y., Tsutsumi, C., Chikashige, Y., Hiraoka, Y., Yamashita, A., Yamamoto, M. (2006). Selective elimination of messenger RNA prevents an incidence of untimely meiosis. *Nature* 442, 45–50.
62. Zofall, M., Yamanaka, S., Reyes-Turcu, F.E., Zhang, K., Rubin, C., Grewal, S.I. (2012). RNA elimination machinery targeting meiotic mRNAs promotes facultative heterochromatin formation. *Science* 335, 96–100.
63. Callahan, K.P., Butler, J.S. (2008). Evidence for core exosome independent function of the nuclear exoribonuclease Rrp6p. *Nucleic Acids Res.* 36, 6645-55.
64. Callahan, K.P., Butler, J.S. (2010). TRAMP complex enhances RNA degradation by the nuclear exosome component Rrp6. *J. Biol. Chem.* 285, 3540-3547.
65. Haile, S., Cristodero, M., Clayton, C., Estévez, A.M. (2007). The subcellular localisation of trypanosome RRP6 and its association with the exosome. *Mol Biochem Parasitol.* 151, 52-58.
66. Lejeune, F., Li, X., Maquat, L.E. (2003). Nonsense-mediated mRNA decay in mammalian cells involves decapping, deadenylation, and exonucleolytic activities. *Mol. Cell* 12, 675-687.
67. Stead, J.A., Costello, J.L., Livingstone, M.J., Mitchell, P. (2007). The PMC2NT domain of the catalytic exosome subunit Rrp6p provides the interface for binding with its cofactor Rrp47p, a nucleic acid-binding protein. *Nucleic Acids Res.* 35, 5556-5567.
68. Feigenbutz, M., Garland, W., Turner, M., Mitchell, P. (2013). The exosome cofactor Rrp47 is critical for the stability and normal expression of its associated exoribonuclease Rrp6 in *Saccharomyces cerevisiae*. *PLoS One.* 8, e80752.
69. Midtgaard, S.F., Assenholt, J., Jonstrup, A.T., Van, L.B., Jensen, T.H., Brodersen, D.E. (2006). Structure of the nuclear exosome component Rrp6p reveals an interplay between the active site and the HRDC domain. *Proc. Natl. Acad. Sci. U.S.A.* 103, 11898-11903.
70. Januszyk, K., Liu, Q., Lima, C.D. (2011). Activities of human RRP6 and structure of the human RRP6 catalytic domain. *RNA* 17, 1566-1577.
71. Schuch, B. et al. (2014). The exosome-binding factors Rrp6 and Rrp47 form a composite surface for recruiting the Mtr4 helicase. *EMBO J* 33, 2829-2846.

72. Ollis, D.L., Brick, P., Hamlin, R., Xuong, N.G., Steitz, T.A. (1985). Structure of large fragment of *Escherichia coli* DNA polymerase I complexed with dTMP. *Nature* 313, 762-766.
73. Assenholt, J., Mouaikel, J., Andersen, K.R., Brodersen, D.E., Libri, D., Jensen, T.H. (2008). Exonucleolysis is required for nuclear mRNA quality control in yeast THO mutants. *RNA* 14, 2305-2313.
74. Zuo, Y., Wang, Y., Malhotra, A. (2005). Crystal structure of *Escherichia coli* RNase D, an exoribonuclease involved in structured RNA processing. *Structure* 13, 973-984.
75. Phillips, S., Butler, J.S. (2003). Contribution of domain structure to the RNA 3' end processing and degradation functions of the nuclear exosome subunit Rrp6p. *RNA* 9, 1098-1107.
76. Januszzyk, K., Lima, C.D. (2014). The eukaryotic exosome. *Curr. Opin. Struct. Biol.* 24, 132-140.
77. Delano, W.L. The PyMOL Molecular Graphics System. (<http://www.pymol.org>). DeLano Scientific, San Carlos, CA.
78. Landau, M., Mayrose, I., Rosenberg, Y., Glaser, F., Martz, E., Pupko, T., and Ben-Tal, N. (2005). ConSurf 2005: the projection of evolutionary conservation scores of residues on protein structures. *Nucleic Acids Res.* 33, W299-W302.
79. Mossessova, E., and Lima, C.D. (2000). Ulp1-SUMO crystal structure and genetic analysis reveal conserved interactions and a regulatory element essential for cell growth in yeast. *Mol Cell* 5, 865-876.
80. Greimann, J.C., Lima, C.D. (2008). Reconstitution of RNA exosomes from human and *Saccharomyces cerevisiae* cloning, expression, purification, and activity assays. *Methods Enzymol.* 448, 185-210.
81. Abruzzi, K., et al. (2007). A novel plasmid-based microarray screen identifies suppressors of rrp6Delta in *Saccharomyces cerevisiae*. *Mol. Cell. Biol.* 27, 1044-1055.
82. Puig, O., Caspary, F., Rigaut, G., Rutz, B., Bouveret, E., Bragado-Nilsson, E., Wilm, M., Séraphin, B. (2001). The tandem affinity purification (TAP) method: a general procedure of protein complex purification. *Methods* 24, 218-229.
83. Tollervey, D., Mattaj, I.W. (1987). Fungal small nuclear ribonucleoproteins share properties with plant and vertebrate U-snRNPs. *EMBO J.* 6, 469-76.
84. Livak, K.J., and Schmittgen, T.D. (2001). Analysis and relative gene expression data using real-time quantitative PCR and the 2- $\Delta\Delta$ CT method. *Methods* 25, 402-408.
85. Otwinowski, Z. & Minor, W. in *Methods in Enzymology* vol. 276 (eds Carter, C. W. Jr. & Sweet, R. M.) 307–326 (Academic Press, 1997).
86. McCoy, A. J. et al. Phaser crystallographic software. *J. Appl. Crystallogr.* 40, 658–674 (2007).
87. Adams, P. D. et al. PHENIX: a comprehensive Python-based system for macromolecular structure solution. *Acta Crystallogr. D* 66, 213–221 (2010).
88. Jones, T. A., Zou, J. Y., Cowan, S. W. & Kjeldgaard, M. Improved methods for building protein models in electron density maps and the location of errors in these models. *Acta Crystallogr. A* 47, 110–119 (1991).
89. Emsley, P., Lohkamp, B., Scott, W.G. & Cowtan, K. Features and development of Coot. *Acta Crystallogr. D* 66, 486–581 (2010).
90. Baker NA, Sept D, Joseph S, Holst MJ, McCammon JA. Electrostatics of nanosystems: application to microtubules and the ribosome. *Proc. Natl. Acad. Sci. USA* 98, 10037-10041 2001.
91. Chen, V.B. et al. MolProbity: all-atom structure validation for macromolecular crystallography. *Acta Crystallogr. D Biol. Crystallogr.* 66, 12-21 (2010).

92. Larimer, F.W., Stevens, A. (1990). Disruption of the gene XRN1, coding for a 5' to 3' exoribonuclease, restricts yeast cell growth. *Gene* 95, 85-90.
93. Anderson, J.S., Parker, R.P. (1998). The 3' to 5' degradation of yeast mRNAs is a general mechanism for mRNA turnover that requires the SKI2 DEVH box protein and 3' to 5' exonucleases of the exosome complex. *EMBO J.* 17, 1497-506.
94. Davis, C.A., Ares M. Jr. (2006). Accumulation of unstable promoter-associated transcripts upon loss of the nuclear exosome subunit Rrp6p in *Saccharomyces cerevisiae*. *Proc. Natl. Acad. Sci. USA.* 103, 3262-7.
95. Orban, T.I., Izaurrealde, E. (2005). Decay of mRNAs targeted by RISC requires XRN1, the Ski complex, and the exosome. *RNA* 11, 459-69.
96. Bühler, M., Haas, W., Gygi, S.P., Moazed, D. (2007). RNAi-dependent and – independent RNA turnover mechanisms contribute to heterochromatic gene silencing. *Cell* 129, 707-21.
97. Flynt, A.S., Greimann, J.C., Chung, W.J., Lima, C.D., Lai, E.C. (2010). MicroRNA biogenesis via splicing and exosome-mediated trimming in *Drosophila*. *Mol. Cell* 38, 900-7.
98. Basu, U., Meng, F.L., Keim, C., Grinstead, V., Pefanis, E., Eccleston, J., Zhang, T., Myers, D., Wasserman, C.R., Wesemann, D.R., Januszyk, K., Gregory, R.I., Deng, H., Lima, C.D., Alt, F.W. (2011). The RNA exosome targets the AID cytidine deaminase to both strands of transcribed duplex DNA substrates. *Cell* 144, 353-63.
99. Pefanis, E., et al. (2014) Noncoding RNA transcription targets AID to divergently transcribed loci in B cells. *Nature* 514, 389-393.
100. van Hoof, A., Frischmeyer, P.A., Dietz, H.C., Parker, R. (2002). Exosome-mediated recognition and degradation of mRNAs lacking a termination codon. *Science* 295, 2262-4.
101. Doma, M.K., Parker, R. (2006). Endonucleolytic cleavage of eukaryotic mRNAs with stalls in translation elongation. *Nature* 440, 561-4.
102. Lorentzen, E., Conti, E. (2006). The exosome and the proteasome: nano-compartments for degradation. *Cell* 125, 651-4.
103. Schneider, C., Leung, E., Brown, J., Tollervey, D. (2009). The N-terminal PIN domain of the exosome subunit Rrp44 harbors endonuclease activity and tethers Rrp44 to the yeast core exosome. *Nucleic Acids Res.* 37, 1127-40.
104. Butler, J.S., Mitchell, P. (2010). Rrp6, Rrp47 and cofactors of the nuclear exosome. In *RNA Exosome*, T.H. Jensen, ed. (New York: Landes Bioscience and Springer Science). *Adv. Exp. Med. Biol.* 702, 91-104.
105. Seol, Y., Skinner, G.M., Visscher, K. (2004). Elastic properties of a single-stranded charged homopolymeric ribonucleotide. *Phys. Rev. Lett.* 93, 118102.
106. Seol, Y., Skinner, G.M., Visscher, K., Buhot, A., Halperin, A. (2007). Stretching of homopolymers reveals single-stranded helices and base-stacking. *Phys. Rev. Lett.* 98, 158103.
107. Xu, Z., Wei, W., Gagneur, J., Perocchi, F., Clauder-Munster, S., Camblong, J., Guffanti, E., Stutz, F., Huber, W., Steinmetz, L.M. (2009). Bidirectional promoters generate pervasive transcription in yeast. *Nature* 457, 1033-7.
108. Schaeffer, D., van Hoof, A. (2011). Different nuclease requirements for the exosome-mediated degradation of normal and nonstop mRNAs. *Proc. Natl. Acad. Sci. USA.* 108, 2366-71.
109. Abramoff, M.D., Magalhaes, P.J., Ram, S.J. (2004). Image processing with ImageJ. *Biophotonics International* 11, 36-42.
110. Smart, O.S., Neduvilil, J.G., Wang, X., Wallace, B.A., Sansom, M.S. (1996). HOLE: a program for the analysis of the pore dimensions of ion channel structural models. *J. Mol. Graph.* 14, 354-60.

111. Wasmuth, E.V. & Lima, C.D. Structure and activities of the eukaryotic RNA exosome. Chanfreau, G.F. & Tamanoi, F., ed. (San Diego: Elsevier). *The Enzymes* 31, 53-76 (2012).
112. Houseley, J. & Tollervey, D. The many pathways of RNA degradation. *Cell* 136, 763-776 (2009).
113. Briggs, M.W., Burkard, K.T. & Butler, J.S. Rrp6p, the yeast homologue of the human PM-Scl 100-kDa autoantigen, is essential for efficient 5.8 S rRNA 3' end formation. *J. Biol. Chem.* 273, 13255-13263 (1998).
114. Yang, W., Lee, J.Y. & Nowotny, M. Making and breaking nucleic acids: two-Mg+2 ion catalysis and substrate specificity. *Mol. Cell* 22, 5-13 (2006).
115. Beese, L.S., Steitz, T.A. Structural basis for the 3'-5' exonuclease activity of Escherichia coli DNA polymerase I: a two metal ion mechanism. *EMBO J.* 10, 25-33 (1991).
116. Wasmuth, E.V. & Lima, C.D. Exo- and endoribonucleolytic activities of yeast cytoplasmic and nuclear RNA exosomes are dependent on the noncatalytic core and central channel. *Mol. Cell* 48, 133-144 (2012).
117. Drązkowski, K. et al. The RNA exosome complex central channel controls both exonuclease and endonuclease Dis3 activities in vivo and in vitro. *Nucleic Acids Res.* 41, 3845-3858 (2013).
118. Liu, J.J. et al. Visualization of distinct substrate-recruitment pathways in the yeast exosome by EM. *Nature Struct. Mol. Biol.* 21, 95-102 (2013).
119. Milligan, L. et al. A yeast exosome cofactor, Mpp6, functions in RNA surveillance and in the degradation of noncoding RNA transcripts. *Mol. Cell. Biol.* 28, 5446-5457 (2008).
120. LaCava, J. et al. RNA degradation by the exosome is promoted by a nuclear polyadenylation complex. *Cell* 121, 713-724 (2005).
121. Makino, D.L., Halbach, F. & Conti, E. The RNA exosome and proteasome: common principles of degradation control. *Nat. Rev. Mol. Cell. Biol.* 14, 654-660 (2013).
122. Kish-Trier, E. & Hill, C.P. Structural biology of the proteasome. *Annu. Rev. Biophys.* 43, 29-49 (2013).
123. Sen, M. et al. The ClpXP protease unfolds substrates using a constant rate of pulling but different gears. *Cell* 155, 636-646 (2013).
124. Effantin, G., Maurizi, M.R. & Steven, A.C. Binding of the ClpA unfoldase opens the axial gate of ClpP peptidase. *J. Biol. Chem.* 285, 14834-14840 (2010).
125. Cha, S.S. et al. Crystal structure of Lon protease: molecular architecture of gated entry to a sequestered degradation chamber. *EMBO J.* 29, 3520-3530 (2010).
126. Wasmuth, E.V., Januszyk, K.J., Lima, C.D. Structure of an Rrp6-RNA exosome complex bound to poly(A) RNA. *Nature* 511, 435-439.
127. Lemay, J.F., et al. The RNA exosome promotes transcription termination of backtracked RNA polymerase II. *Nat. Struct. Mol. Biol.* 21, 919-926 (2014).
128. Klauer, A.A., van Hoof, A. Genetic interactions suggest multiple distinct roles of the arch and core helicase domains of Mtr4 in Rrp6 and exosome function. *Nucleic Acids Res.* 41, 533-541 (2013).
129. Castelnovo, M., et al. Bimodal expression of PHO84 is modulated by early termination of antisense transcription. *Nat. Struct. Mol. Biol.* 20, 851-858 (2013).
130. Tsanova, B., et al. The RNA exosome affects iron response and sensitivity to oxidative stress. *RNA* 20, 1057-1067 (2014).
131. Melnikov, S., et al. Insights into the origin of the nuclear localization signals in conserved ribosomal proteins. *Nat. Comm.* 6, doi: 10.1038/ncomms8382 (2015).

132. Tomko, R.J. Jr., Hochstrasser, M. The intrinsically disordered Sem1 protein functions as a molecular tether during proteasome lid biogenesis. *Mol. Cell* 53, 433-443 (2014).
133. Kucera, N.J., Hodsdon, M.E., Wolin, S.L. An intrinsically disordered C terminus allows the La protein to assist the biogenesis of diverse noncoding RNA precursors. *Proc. Natl. Acad. Sci.* 108, 1308-1313 (2011).
134. Garland, W., et al. Rrp47 functions in RNA surveillance and stable RNA processing when divorced from the exoribonuclease and exosome-binding domains of Rrp6. *RNA* 19, 1659-1668 (2013).
135. Decourty, L., et al. Linking functionally related genes by sensitive and quantitative characterization of genetic interaction profiles. *Proc. Natl. Acad. Sci.* 105, 5821-5826 (2008).
136. Schilders, G., R. Raijmakers, J. M. Raats, and G. J. Pruijn. MPP6 is an exosome-associated RNA-binding protein involved in 5.8S rRNA maturation. *Nucleic Acids Res.* 33, 6795-6804 (2005).
137. Vanacova, S., et al. A new yeast poly(A) polymerase complex involved in RNA quality control. *PLoS Biol* 3, e189. (2005).
138. Mullen, T.E., Marzluff, W.F. Degradation of histone mRNA requires oligouridylation followed by decapping and simultaneous degradation of the mRNA both 5' to 3' and 3' to 5'. *Genes Dev* 22, 50-65 (2008).
139. Choi, Y.S., et al. Widespread RNA 3'-end oligouridylation in mammals. *RNA* 18, 394-401 (2012).
140. Lee, M., Kim, B., Kim, V.N. Emerging roles of RNA modification: m(6)A and U-tail. *Cell* 158, 980-987 (2014).
141. Hendrickson, W.A., Horton, J.R., LeMaster, D.M. Selenomethionyl proteins produced for analysis by multiwavelength anomalous diffraction (MAD): a vehicle for direct determination of three-dimensional structure. *EMBO J* 9, 1665-1672 (1990).
142. Dong, A., et al. In situ proteolysis for protein crystallization and structure determination. *Nat Methods* 4, 1019-1021 (2007).
143. McPherson, A., Cudney, B. Searching for silver bullets: an alternative strategy for crystallizing macromolecules. *J Struct Biol* 156, 387-406 (2006).
144. Shaw Stewart, P.D., et al. Random microseeding: a theoretical and practical exploration of seed stability and seeding techniques for successful protein crystallization. *Cryst Growth Des* 11, 3432-3441 (2011).
145. Quiocho, F.A., Richards, F.M. Intermolecular cross linking of a protein in the crystalline state: carboxypeptidase-A. *Proc Natl Acad Sci* 52, 833-839 (1964).
146. Paredes, E., Das, S.R. Click chemistry for rapid labeling and ligation of RNA. *ChemBiochem.* 12, 125-131 (2011).
147. Cole C, Barber JD and Barton GJ. (2008) The Jpred 3 secondary structure prediction server, *Nucleic Acids Res.* 36 (suppl. 2): W197-W201